Dx 235166

Modelling the Ultrasonically Assisted Turning of High-Strength Alloys

by Alexander Mitrofanov

A Doctoral Thesis

Submitted in partial fulfilment of the requirements for the award of Doctor of Philosophy of Loughborough University

April 2004

Abstract

The thesis deals with a novel machining technique - ultrasonically assisted turning (UAT) -- and its comparison with conventional turning (CT). The main objective of the research is a detailed analysis of various features of both processes, especially the deformational and thermomechanical behaviour of the treated material. The main emphasis here is on the superalloy Inconel 718 due to the industrial demand.

A thorough analysis of the cutting techniques is possible only with the use of advanced finite-element numerical simulations validated by a range of experimental methods (mechanical, optical, microstructural and thermal). Various effects of technological parameters (lubrication, thermal contact conditions, etc.) on deformational processes, stresses and chip formation are studied.

High-speed filming of the cutter — workpiece interaction zone is conducted to compare chip formation processes for both technologies. Light microscopy, scanning electron microscopy (SEM) and nanoindentation analyses are employed to study the differences in the microstructure of surface layers of machined workpieces. Cutting-force measurements and infrared thermography when turning with and without ultrasonic assistance are also carried out.

The two-dimensional finite-element (FE) model is developed with MSC MARC general FE code and provides a transient, fully coupled thermomechanical analysis of both ultrasonic and conventional turning of Inconel 718. A detailed study of the UAT process is performed, including specificity of the single cycle of ultrasonic vibration. Differences between thermal and deformation processes for UAT and CT, effects of application coolant/lubricant, various friction conditions, and specific features of the heat conduction between chip and cutting tool are examined.

For the first time, thermomechanics of UAT has been thoroughly analysed. The main outcome of the thesis is an in-depth understanding of the UAT process, and of its advantages and disadvantages in comparison to CT. Recommendations on further research development are also suggested.

Acknowledgements

I would like to express my deep sense of gratitude and appreciation to my supervisor, Prof. Vadim V. Silberschmidt, for his expert guidance and mentorship, and for his encouragement and support at all levels. His vital advice played a crucial role in my work throughout the PhD, and without it this thesis would have never materialized in the present form. I really appreciate his always-ready-to-help attitude, which was a constant motivating factor for me to complete this thesis.

I also extend my sincere thanks to my second supervisor, Prof. Vladimir I. Babitsky, for his invaluable comments and permanent support, which have been of greatest help at all times.

I would like to thank my Director of Research, Prof. Colin Garner, for his encouraging attitude and his advice on thesis planning.

I would like to express my sincere thanks to Dr. Graham K. Hargrave, Loughborough University, for developing and providing the optical part of the high-speed filming experiments. Special thanks goes to Mr. Peter Wileman for his trust and patience, as well as for his practical help and assistance with high-speed filming and other experiments.

I acknowledge with much appreciation the role of academic and technical staff of the Wolfson School of Mechanical and Manufacturing Engineering. Special thanks are due to Dr. Allan Meadows for his advice, useful suggestions and assistance in operating the ultrasonic turning system, and to Mr. Terry Smith, Mr. Andy Sandavar and Dr. Z. Zheng for their help with light microscopy and nanoindentation experiments.

I express my sincere gratitude to Head of Department, Prof. Ewald Werner, and the staff of Technical University of Munich, including Dr. Christian Krempaszky, Mr. Christof Messner and Mr. Lars Renhof, for their valuable ideas on numerical modelling and thermomechanics of ultrasonic turning. I am especially grateful to Dr. Susana Gruber, for the SEM analysis of the machined samples and her assistance with the result interpretation. I also wish to acknowledge Dr. Martin Baeker, TU Braunschweig, Germany, for his critical comments on the numerical simulations of the machining techniques.

I would like to thank my colleagues, Dr. Ilya Sokolov, Dr. Eugenia Golycheva, Dr. Vladimir Doubrovsky and Mr. Peter Thomas, for a friendly office atmosphere and for their help and advice on different issues. I am thankful to Dr. Andre Batako for his emotional support and wise advice, which were of a great help in adapting quickly to academic life in England.

I am very grateful to my NLP trainer and friend, Ms. Svetlana Alekseevitch, for her assistance in keeping my motivation high, and for her wisdom and advice on tackling the challenges of everyday life. Finally, I would like to thank my mother for her life-long love and her utter belief in my abilities.

Many more persons participated in various ways to ensure my research succeeded than those I have mentioned, and I am thankful to them all.

Publications

The research undertaken during the course of this project has given rise to publications listed below.

1. Mitrofanov, A.V., V.I. Babitsky and V.V. Silberschmidt, Finite element simulations of ultrasonically assisted machining. *Computational Materials Science*, 2003, 28 (3-4), pp. 645-653.

2. Babitsky, V.I., A.V. Mitrofanov and V.V. Silberschmidt. Ultrasonically Assisted Turning of Aviation Materials: Simulations and Experimental Study. *Ultrasonics*, 2004, 42 (1-9), pp. 81-86.

3. Mitrofanov, A.V., V.I. Babitsky and V.V. Silberschmidt, Finite element analysis of ultrasonically assisted turning of Inconel 718. *Journal of Materials Processing Technology*, 2004, to appear.

4. Mitrofanov, A.V., V.I. Babitsky and V.V. Silberschmidt. Thermomechanical finite element simulations of ultrasonically assisted machining. In *5th International Congress on Thermal Stresses and Related Topics*, 2003. Blacksburg, USA, pp. 1031-1034.

5. Mitrofanov, A.V., V.I. Babitsky and V.V. Silberschmidt. Finite element simulations of ultrasonically assisted turning of Inconel 718. In *International Conference on Advances in Materials and Processing Technologies (AMPT 2003)*. Dublin, Ireland, pp. 317-320.

6. Mitrofanov, A.V., V.I. Babitsky and V.V. Silberschmidt, Thermomechanical finite element simulations of ultrasonically assisted turning. *Computational Materials Science*, submitted.

Notation and abbreviations

Symbols

Symbol	Meaning
a	Amplitude of vibration, μm
A	Projected indentation area, nm^2
C	Specific heat, J/kg K
d	Depth of cut, mm
D	Workpiece diameter, mm
E	Young's modulus, GPa
E_i	Young's modulus of the indenter, GPa
E_s	Young's modulus of the sample, GPa
f	Frequency of vibration, Hz
F	Cutting force, N
h	Convective heat transfer coefficient, W/m^{2}K
h_c	True contact depth, nm
h_{max}	Maximum penetration depth, nm
H	Contact heat conduction coefficient, W/m^{2}K, (or Hardness, GPa, in Section 5.4.3)
k	Shear yield strength, MPa
K	Thermal conductivity, W/m K
K_Y	Coefficient of plastic resistance, MPa
K_{IC}	Material's fracture toughness, N m$^{-3/2}$
l	Distance ahead of the crack tip, mm
L_C	Contact length, mm
m	Distributed heat source density, J/m^3 s
M_Y	Hardening exponent
n	Rotational speed, rev/min
F_T	Main cutting force, N

F_p	Thrust force, N
F_f	Feed force, N
F_{CT}	Cutting force in CT, N
F_{UAT}	Cutting force in UAT, N
P_{max}	Maximum load, mN
r	Chip thickness ratio
R	Chip's radius of curvature, mm
s	Feed rate, mm/rev
S	Contact compliance, nm/N
t	Time, s
t_1	Uncut chip thickness, mm
t_2	Deformed chip thickness, mm
$\mathbf{t}$	Contact traction, N
T	Temperature, °C
T_{melt}	Melting temperature, °C
T_∞	Room temperature, °C
V_C	Cutting speed, m/min
$\mathbf{v}_r$	Velocity jump across the contact, m/s
$\dot{W}^p$	Plastic power per unit deformed volume, J/m^3 s
α	Coefficient of thermal expansion, °C^{-1}
β	Taylor-Quinney coefficient
γ	Rake angle, °
ε_{ij}	Components of the strain tensor
$\dot{\varepsilon}$	Strain rate, s^{-1}
$\bar{\varepsilon}^p$	Equivalent plastic strain
$\dot{\varepsilon}^p$	Plastic strain rate, s^{-1}
$\dot{\bar{\varepsilon}}^p$	Equivalent plastic strain rate, s^{-1}
$\dot{\varepsilon}_0$	Initial strain rate, s^{-1}
φ	Shear angle, °
μ	Friction coefficient
ν	Poisson's ratio

ν_i	Poisson's ratio of the indenter
ν_s	Poisson's ratio of the sample
ρ	Mass density, kg/m^3
σ_{ij}	Components of the Cauchy stress tensor, MPa
σ_d	Dynamic yield strength, MPa
σ_f	Critical fracture stress, MPa
σ_Y	Yield strength, MPa
σ_{Y_0}	Initial yield strength, MPa
$\bar{\sigma}$	Equivalent stress, MPa
ω	Angular frequency, rad/s

Abbreviations

Abbreviation	Meaning
CNC	Computer numerical control
CT	Conventional turning
FE	Finite element
FEA	Finite element analysis
FEM	Finite element modelling
HS	High-speed
IR	Infrared
SEM	Scanning electron microscope
TEM	Transmission electron microscope
UAT	Ultrasonically assisted turning
UTS	Ultimate tensile strength

Table of Contents

Chapter 1 Introduction

1.1 General introduction

Modern industrial manufacture often requires a material to be removed from initial shapes in order to produce final components. Metal cutting is used extensively for this purpose in a broad spectrum of industries. Cutting operations include turning, milling, drilling, and a range of other processes designated for various types of material shaping. This research is focused on one particular kind of metal cutting – turning.

Turning has been used extensively for decades, and vast experience has been accumulated in industry and through research concerning its different aspects. This led to a considerable advance in both practical technology and theoretical understanding of turning. Sophisticated CNC (computer numerical control) machines allowing considerable automation of the process, have been developed. Advanced materials for cutting edges, such as coated carbide and cubic boron nitride inserts, have been introduced. High-speed machining has permitted a significant increase in material removal rates. The metal cutting science is presently a complex mechanical discipline that includes various theoretical models of cutting and allows us to study its different features, such as chip formation, heat transfer and tool wear processes.

Modern turning techniques (e.g. high-speed machining) usually bring a desired outcome in cutting standard metal alloys, for example, engineering structural steels. However, some intractable materials, namely Ni-, Ti- and Cr-based alloys, that are widely used in aerospace applications, require the development of new machining techniques. When machined conventionally, these alloys cause fast wear of cutting edges due to their high strength and abrasivity even at relatively low cutting speeds. Machining such alloys also creates large cutting forces and high working temperatures, and often results in poor surface finish. New methods of machining are also needed for ceramics, glass and other brittle materials, which presently require prolonged and expensive post-processing operations, such as grinding and polishing, to obtain desired surface finish. Hence, a lot of activity in the development of turning is directed at improving the characteristics of machining for such intractable

materials.

Ultrasonically assisted turning (UAT) is one of the most promising techniques invented for machining high-strength alloys. In conventional turning (CT) process a specimen is held in the chuck of the lathe and rotated; the tool moves with a constant velocity in the feed direction, cutting away a layer of the material and forming a cylindrical surface. In UAT, high-frequency vibration ($f \approx 20\,\text{kHz}$) with amplitude $a \approx 20 \div 30$ μm is superimposed on this tool movement, transforming the process of cutting into one with a multiple-impact interaction between the tool and the formed chip. Compared to CT, this technique demonstrates the following benefits in machining intractable alloys: a decrease in cutting forces in up to several times, improvement in surface finish by 50 % and workpiece roundness by 40 %, as well as noise reduction (see, for example, [1, 2]).

Although the UAT technique was invented in 1960s, it has not been introduced into industry since. The main reason for that has been instability of the vibration process and of produced results of turning. This problem has been recently eliminated with an invention of the autoresonant control system that allows to stabilise the cutting process and makes the vibration regular. This control system has been designed and assembled at Loughborough University together with the original test rig for UAT. A range of experiments has been performed on these in-house facilities at Loughborough University confirming the advantages of UAT in comparison to CT. Ultimately, an introduction of the autoresonant control system has become a major breakthrough that permits successful industrial introduction of UAT.

Still, thermomechanics of UAT has not been studied with an appropriate level of detail, and only a basic level of its understanding has been achieved, thus preventing the technique from purposeful development. Various attempts have been carried out, and lately non-linear dynamic characteristics of an ultrasonic machining system, such as cutting forces and the amplitude response of the cutting tool under load, have been studied for the first time by the Non-linear Dynamics Research Group at Loughborough University. However, thermomechanics of the material response to UAT is not clearly understood, and only a little information is available on it. It is believed that better understanding of the heat transfer and mechanical processes involved in UAT would allow the optimisation of this advanced technique and extend the range of its application onto different material types. Such optimisation, in

its turn, would make the technique even more competitive and attractive for manufacturing industries, and thus would accelerate the process of its industrial introduction.

A holistic analysis of the UAT process necessitates a combination of experimental studies and numerical simulations of the cutting tool – workpiece interaction. Both approaches are employed in the present thesis in order to investigate microstructural and thermal processes involved in UAT. Since the ultrasonically assisted technique was proposed as an enhancement of the existing CT methods, the comparison is naturally performed with CT at each stage of the research. Besides, CT has been studied for many decades and its theory is well developed, hence its comparative analysis with UAT may reveal peculiarities of the latter, allowing better understanding of the nature of the obtained improvements in cutting.

1.2 Aims and objectives of this research

The purpose of this research is to investigate microstructural and thermal processes in the tool–chip interaction zone. A fundamental mechanical study, which includes numerical (FE) modelling of the chip separation process and various experiments with the UAT prototype, can significantly improve the understanding of the UAT process. It is hoped that the results of this research will be useful for the optimisation of the ultrasonic cutting procedure and extension of the ultrasonically supported technology to different types of materials.

It is worth pointing out that the experiments carried out in this thesis are largely focused on the study of thermomechanics of the tool–chip interaction and not on producing the best possible cut. Most of the experiments described here are unique (to the author's knowledge) and aimed at gaining advanced understanding of the UAT process.

Finite element (FE) modelling can provide detailed spatial and temporal information on the mechanical and thermal features of the cutting process, and it has become a main computational tool to study metal cutting in the last decades. Nevertheless, to the author' knowledge, no FE models for UAT have been suggested yet. Hence, one of the objectives of the research is to develop a FE model of UAT, which would adequately describe the real cutting process and allow its comparison with CT. The model will be used to study and compare specific features of the

thermal and deformation processes for the two cutting techniques – CT and UAT, as well as investigate the influence of frictional contact interaction at the tool–chip interface on the chip formation.

The objectives of the thesis are therefore:

- To study the application of FEM to modelling of metal cutting (see Chapter 3)

- To study the historical development of UAT and state of the art in this area (see Chapter 4)

- To undertake a comparative experimental analysis of the following features of two cutting techniques (see Chapter 5):

  - ➢ Thermomechanics of deformation processes and dynamics of the tool–workpiece interaction (using high-speed photography experiments and analyses of microstructure of chips obtained in turning)

  - ➢ Influence of the cutting process on the properties of treated materials (on the basis of light microscopy, scanning electron microscopy (SEM), and nanoindentation experiments)

  - ➢ Heat transfer in the workpiece material and into the cutting tool (based on infrared thermography tests)

  - ➢ Cutting forces

- To develop a working two-dimensional FE model of UAT and study the following features of UAT in comparison to CT (see uncoupled and thermomechanically–coupled FE simulations described in Chapters 6 and 7, respectively):

  - ➢ Mechanics of the of the tool–chip interaction

  - ➢ Stress-strain distributions in the cutting region

  - ➢ Heat-transfer in the workpiece material and into the cutting tool

  - ➢ Cutting forces

- To validate that developed FE models adequately reflect experimental results (a comparison between experimental and numerical (FE) results is performed in Chapters 6 and 7)

1.3 Outline of the thesis

The rest of the thesis is organised into the following chapters.

Chapter 2 introduces the basic concepts of the mechanics of cutting, its nomenclature, chip formation fundamentals and experimental methods of research. It provides an essential background for the description and study of the ultrasonically assisted cutting process.

Chapter 3 describes various aspects of the FEM application to modelling of metal cutting, reviews the historical development of FE models, and studies recent modelling publications relevant to the current study.

Chapter 4 outlines the principles of UAT and its application to turning operations, characterises specific features of a prototype of the ultrasonic vibration system, used in all experiments, and reviews the development of UAT and achievements that have been made in this area.

Chapter 5 specifies thermal and mechanical properties of the employed material (Inconel 718) and gives the details of the experimental work carried out, including microstructural studies of the workpiece and chip, high-speed filming, infrared thermography, and measurements of cutting forces.

Chapter 6 introduces a mechanical FE model of contact interaction between the workpiece material and cutting tool for both CT and UAT. Various stages of the single cycle of ultrasonic vibration are described. A detailed comparison of CT and UAT is provided, based on the analysis of distribution of stresses, plastic strains and strain rates.

Chapter 7 presents an enhanced, fully thermomechanically coupled model of the UAT. The description of the model, results of various numerical case studies and comparison with experiments are given.

Chapter 8 summarizes the outcome of the research, presents conclusions drawn on the basis of the experimental results and numerical simulations, and recommends possible further work on the topic.

Chapter 2 Mechanics of cutting

2.1 Parameters of turning

This chapter introduces the nomenclature of the mechanics of cutting and its basic concepts. Experimental and analytical methods for studying various cutting parameters, such as forces and temperatures, are described. These serve as a basis to characterise the ultrasonically assisted cutting process using experimental and numerical techniques.

In the conventional turning process the workpiece material is gripped in the chuck of a lathe (Figure 2.1) and rotated. The tool is held in a tool post and moved at a constant rate along the axis of the workpiece, cutting away a layer of material to form a cylindrical surface, as shown schematically in Figure 2.2.
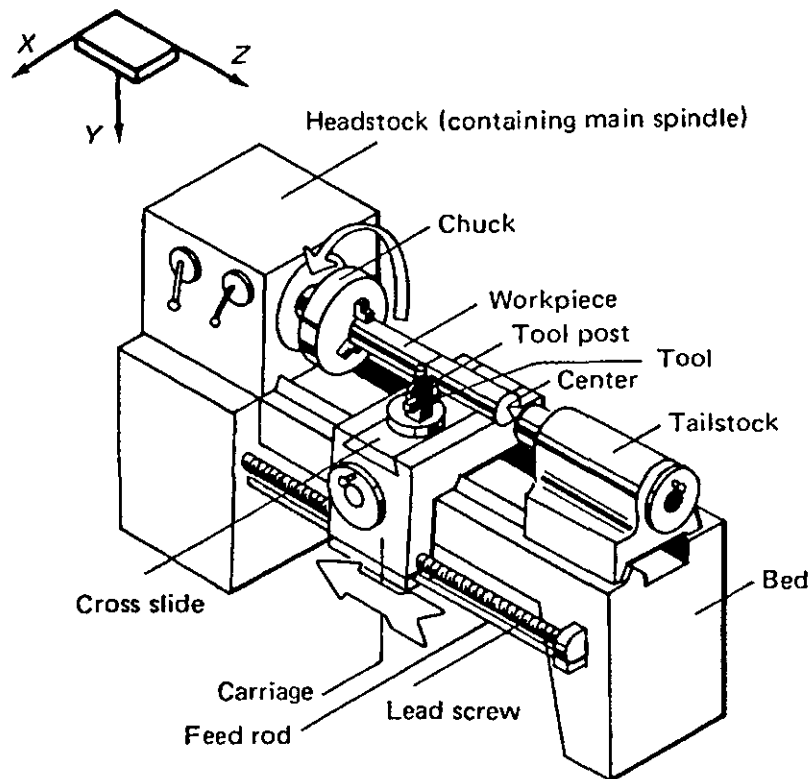
Figure 2.1 A centre lathe (reproduced from [3])

The cutting speed v is the rate at which the surface of the workpiece passes the cutting edge of the tool, usually expressed in m/min. The feed rate s is the distance moved by the tool in an axial direction at each revolution of the workpiece (expressed in mm/rev). The depth of cut d is the thickness of the material removed from the bar, measured in a radial direction. The cutting speed, feed rate and depth of cut are parameters that can be adjusted by the operator to achieve optimum cutting conditions.
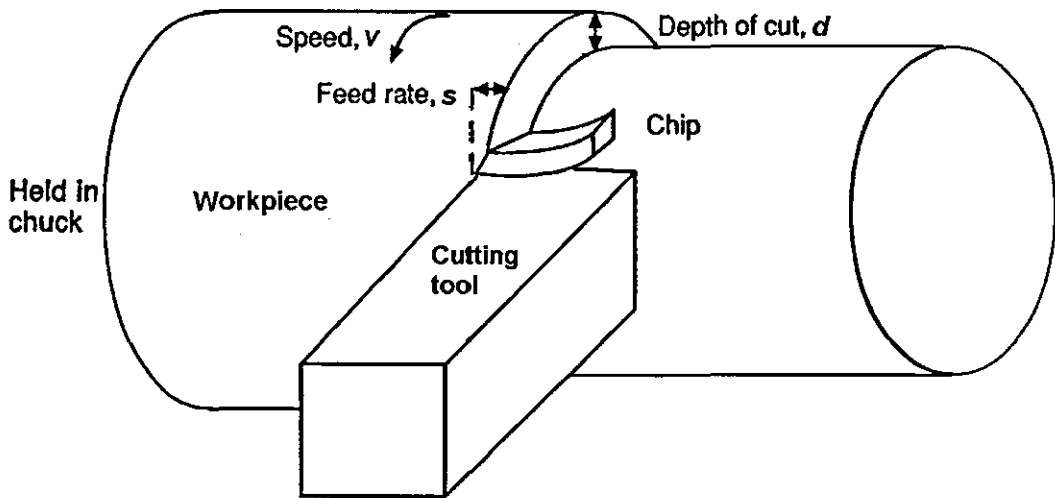
Figure 2.2 Lathe turning (from [4])

The rotational speed n of the spindle (expressed in rev/min) is usually constant during a single operation, so that during cutting the cutting speed varies as the diameter D reduces with the workpiece material being gradually removed.

The surface of the tool over which the chip flows in the cutting process is known as the rake face of the tool (Figure 2.3). The cutting edge is formed by the intersection of the rake face with the clearance face (or flank) of the tool. The tool is so designed and inclined at such an angle that the clearance face does not rub against the freshly cut metal surface. The clearance angle γ is variable but it is often of the order of 6-10°. The rake face is inclined at an angle to the axis of the workpiece and this angle can be adjusted to achieve optimum cutting performance for particular tool / workpiece materials and cutting conditions. The rake angle α is measured from a line parallel to the axis of rotation of the workpiece. The rake angle can take values

from about 30° to negative values of 5 or 6°. Although the cutting edge is considerably sharper for big positive values of α, it is easily worn, hence the tools with a zero or negative rake angle are often used to decrease wear, as they are more robust. The third face of the tool is called an end clearance face, and it is also inclined at such an angle as to avoid rubbing against the freshly cut surface of the workpiece. The intersection of all three faces is known as the nose of the tool, and a radius of curvature between the two clearance faces is called a nose radius R_n. The orientation of the cutting edge relatively to the axis of the workpiece is specified by a major cutting edge angle k_r.
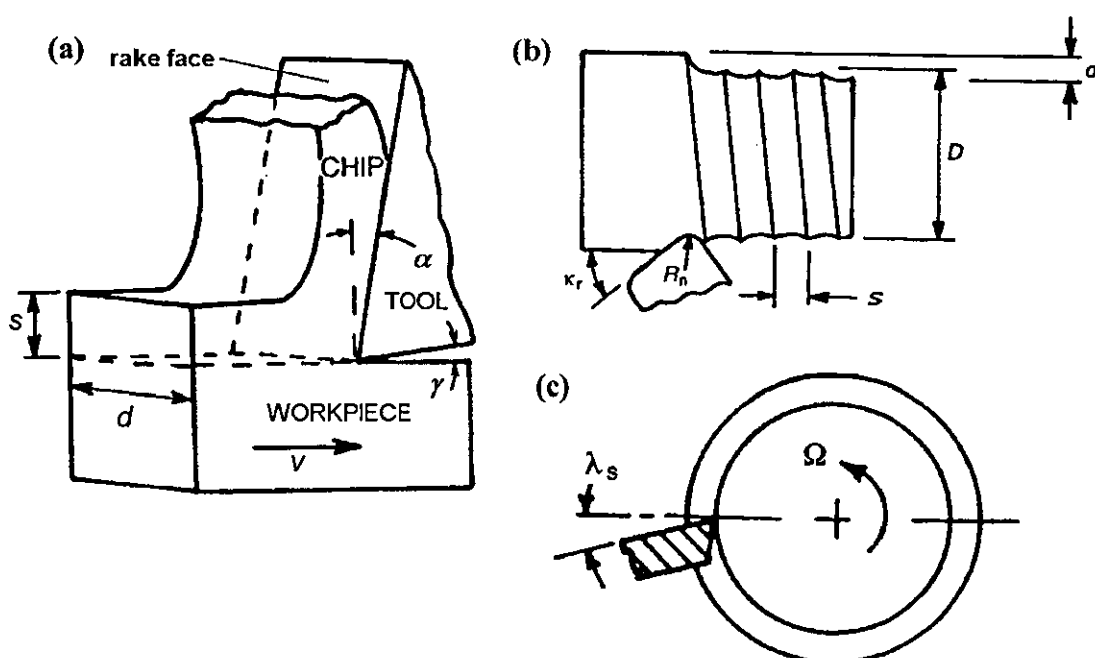
Figure 2.3 Parameters of turning (from [5])

2.2 Chip formation

2.2.1 Orthogonal vs. non-orthogonal cutting

In an orthogonal turning process, the cutting edge AD of the tool rake face ABCD is perpendicular to the direction of v (Figure 2.4a). The chip that is formed during cutting flows with some velocity v_{chip}, which is perpendicular to the cutting edge. All relative motions in orthogonal turning occur in the plane normal to the cutting edge, and the problem becomes two-dimensional. It largely simplifies the formulation of

the problem and eliminates many variables present in the general case of cutting. The orthogonal formulation is therefore widely used in research studies, where it is desirable to reduce the complexity of the process, and is analysed by analytical methods and numerical calculations.
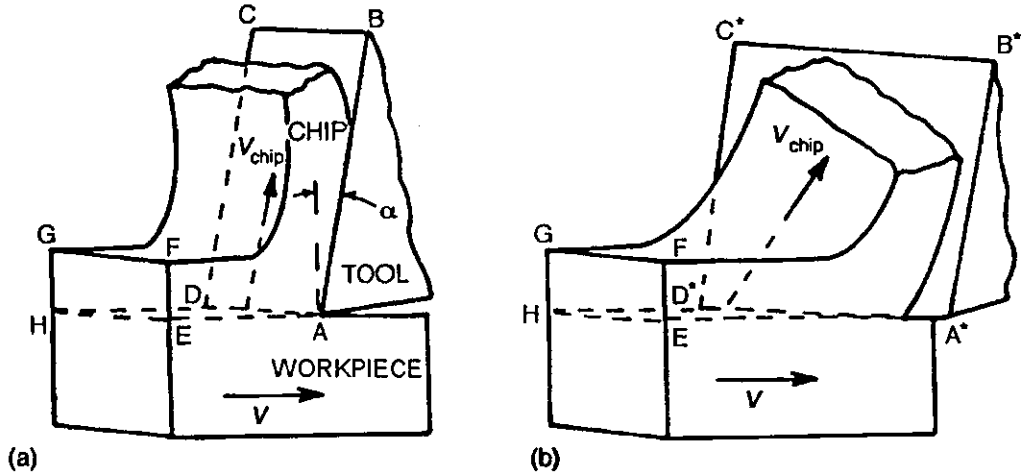
Figure 2.4 Orthogonal (a) and non-orthogonal (b) chip formation (from [5])

In the general case of cutting, which is known as non-orthogonal (or oblique) cutting, the cutting edge A*D* is perpendicular neither to v nor to v_{chip} (Figure 2.4b). The angle between AD and A*D* is called the cutting edge inclination angle (λ_s) (Figure 2.3c). Geometry of the non-orthogonal chip formation is more complicated than that of the orthogonal one, thus making mechanics of the process more difficult to analyse. The analysis of the problem in this case is essentially three-dimensional that complicates both experimental and theoretical studies of the processes in the cutting zone. The chip formation processes described in this research are largely considered for the case of orthogonal cutting conditions

2.2.2 Chip formation

A complete description of a chip formation in oblique cutting is a very difficult task, and, for the purposes of analysis of stresses and strains in cutting, many details are ignored and simplified models are usually assumed. An important simplification is to ignore the irregular cross-section of real chips, and to assume a rectangular

cross-section, which height is equal to the measured mean thickness of the chip, and width is equal to the cutting edge engagement length. The latter corresponds to the depth of cut d (Figure 2.2). With these assumptions, the formation of chips is considered in terms of the simplified diagram, Figure 2.5, presenting an idealised chip formation process in the plane normal to the cutting edge of a tool.
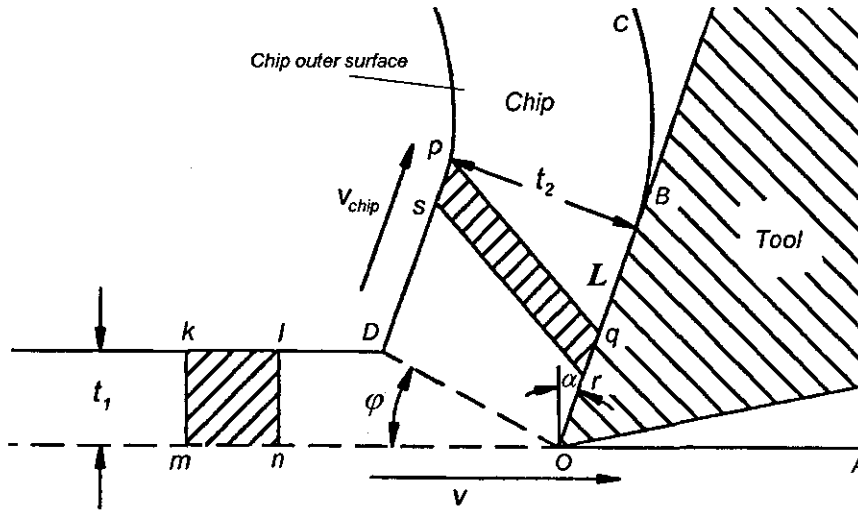
Figure 2.5 Chip formation diagram (from [4])

Figure 2.5 illustrates how the chip of thickness t_2 is being formed from an undeformed layer of thickness t_1 equal to the feed rate s (described in Section 2.1.) by the action of a tool with the rake angle α. Two new surfaces are formed in this process, the new surface of the workpiece OA and that of the chip OC. The main deformation region is situated in the zone around line OD going from the tool edge to the position where the chip leaves the workpiece surface and known as a primary shear zone. Hence, for the purpose of simple analysis, the chip is assumed to be formed by shear along the shear plane OD. Secondary shear zone is observed along the rake face of the tool, where a seizure often occurs at the interface between the chip and tool along a contact length L_C (OB in Figure 2.5). A simplified flow model neglects additional deformation in the secondary shear zone, although the material there may still be at the plastic limit [5]. Instead, a sliding contact with Coulomb friction with the averaged friction coefficient μ is presupposed along the contact length OB. The shear plane OD is inclined at the shear angle φ to the cutting

direction OA; the shear angle is an important parameter in chip formation mechanics and various models are employed in order to predict it (see below).

It is also usually assumed that the workpiece material is incompressible and no side spread of the material occurs [4]. As any volume of material, e.g. *klmn* (Figure 2.5) passes through the shear zone, it is plastically deformed into a new shape – *pqrs*. The deformed chip thickness t_2 is related to the tool rake angle α and the shear plane angle ϕ. From the geometry of the cut (see Figure 2.5), it can be shown [4] that

$$OD = \frac{t_1}{\sin\phi} = \frac{t_2}{\cos(\phi-\alpha)}, \text{ or } \frac{t_1}{\sin\phi} = \frac{t_2}{\cos\phi\cos\alpha + \sin\phi\sin\alpha}.$$

Hence,

$$t_2 = \frac{\cos(\varphi-\alpha)}{\sin\varphi} t_1$$

and shear angle φ can be found from

$$\tan\phi = \frac{r\cos\alpha}{1 - r\sin\alpha}, \tag{2.1}$$

where the value of r, called the chip thickness ratio, is the ratio of the undeformed chip thickness to the deformed chip thickness $r = t_1/t_2$, with $r < 1$.

The chip speed v_{chip} can be found from the cutting speed v as follows [4]:

$$v_{chip} = \frac{\sin\phi}{\cos(\phi-\alpha)} v. \tag{2.2}$$

It should be pointed out that the terminology of cutting can be considered from two different points of view: the tool movements and chip formation process. Feed rate and depth of cut refer to the former point of view. Uncut chip thickness and cutting edge engagement length directly correspond to feed rate and depth of cut, respectively, but from the point of view of the chip formation process, there is no difference between these parameters if the major cutting edge angle $k_r = 90°$ [5]. In the present work, chips are considered to be formed at a feed rate (uncut chip thickness) s and depth of cut (cutting edge engagement length) d.

It is worth noticing that formation of new surfaces requires certain energy, but in metal cutting the theoretical energy of free surface formation is an insignificant proportion of the plastic deformation energy needed to shear the whole volume of the metal in the shear zone. However, although the surface free energy is negligible indeed, the specific work of fracture in the vicinity of the cutting tool tip is in most

cases at least three orders of magnitude higher than that, and thus should not be overlooked [6].

2.2.3 Chip types

The cross section of the chip is not strictly rectangular even in the case of orthogonal cutting. Since the material is constrained only by the rake face of the tool, it is free to move in all other directions as it is formed into the chip. The chip tends to spread sideways, so that the maximum width of it is somewhat greater than the original depth of cut d [4].

The chip formation involves separation of the workpiece material in the vicinity of the cutting edge and its subsequent shearing in the primary shear zone near the shear plane (OD in Figure 2.5). Extensive amount of deformation takes place in this region at very high strain rates, and for some materials and under certain cutting conditions this leads to catastrophic shear and fracture that causes discontinuous chips to be produced. Such fragmented chips are one of the principal classes of a chip form. However, under the majority of cutting conditions, ductile materials do not fracture on the shear plane and a continuous chip is produced. There is no sharp boundary between continuous and discontinuous chips and various shades of gradation between the two types can be observed. Even in a continuous chip, periodic small corrugations, cracks or steps are often observed at the outer surface of the chip (Figure 2.5), breaking it into a series of segments [4].

There is a variety of shapes for the continuous chips; they can be straight, tangled or, more often, have a helix shape. Helix chips were produced for majority of the cutting conditions described in the experimental part of this thesis.

2.3 Forces and stresses in turning

Forces acting on the cutting tool are important parameters in turning and have a primary influence upon the tool wear and required power [4]. Research analysis of turning essentially includes a study of the cutting forces acting on the tool.

There are three mutually orthogonal components of cutting forces. The component of the force acting on the rake face of the tool in the direction of the cutting velocity is called the main cutting force (F_T) (Figure 2.6). This is usually the

largest of the three force components. The second component, acting along OX and parallel to the feed direction, is known as the feed force (F_f). The third component, referred to as the thrust force (F_p), tends to push the tool away from the workpiece in a radial direction. This is the smallest of the force components and is usually neglected. The absolute values of forces in metal cutting are comparatively low compared to those in forging or forming processes and usually are not greater than several tens or hundreds of kilograms. However, stresses acting in the cutting tool are quite large due to the small contact area between the tool and workpiece [4].

Methods for measuring the forces acting on the cutting tool are reviewed in Section 2.6.2.
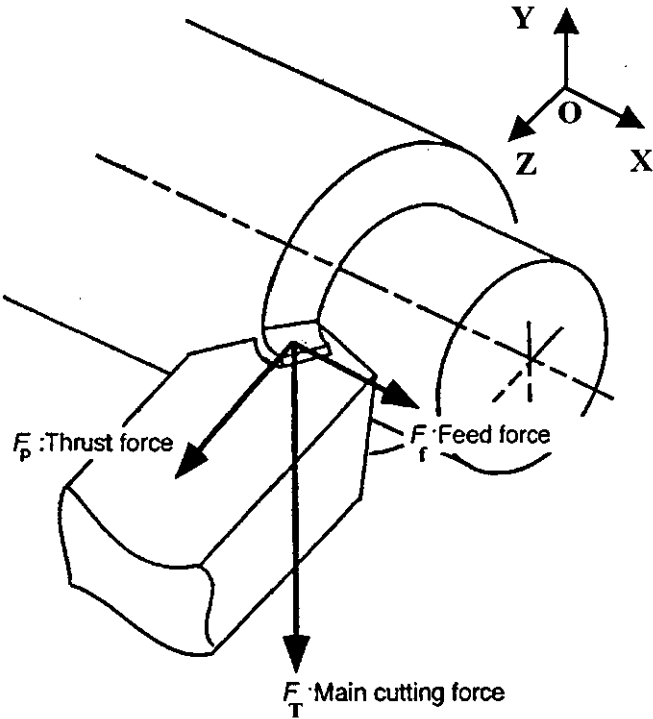
Figure 2.6 Forces acting on the cutting tool (from [5])

In the classic Merchant model [7], shear processes are limited to the shear plane and the chip moves along the tool face with sliding friction, defined by the average friction coefficient μ. This model cannot predict the influence of process parameters, such as the cutting speed, on the material behaviour. Another drawback of this scheme is an oversimplified friction model, not accounting for the influence of the contact area between the tool and chip on the cutting process [4]. However,

Merchant's force circle allows to establish approximate interrelation between various components of forces in the orthogonal turning model.

In the Merchant's force circle (Figure 2.7) (as described in [4]), R is the resultant force in cutting and it can be decomposed into components acting along different axes. Firstly, it can be obtained as a combination of the main cutting force F_T and feed force F_f. Secondly, it is can be projected onto the rake face and normal to the rake face directions, becoming a combination of friction force F and normal force N on the rake face. Since friction coefficient $\mu = F/N = \tan \lambda$, the resultant force R is inclined at the friction angle λ to the direction normal to the rake face. Finally, R can be given as a combination of forces F_S and F_N acting along the shear plane and normal to it, respectively.
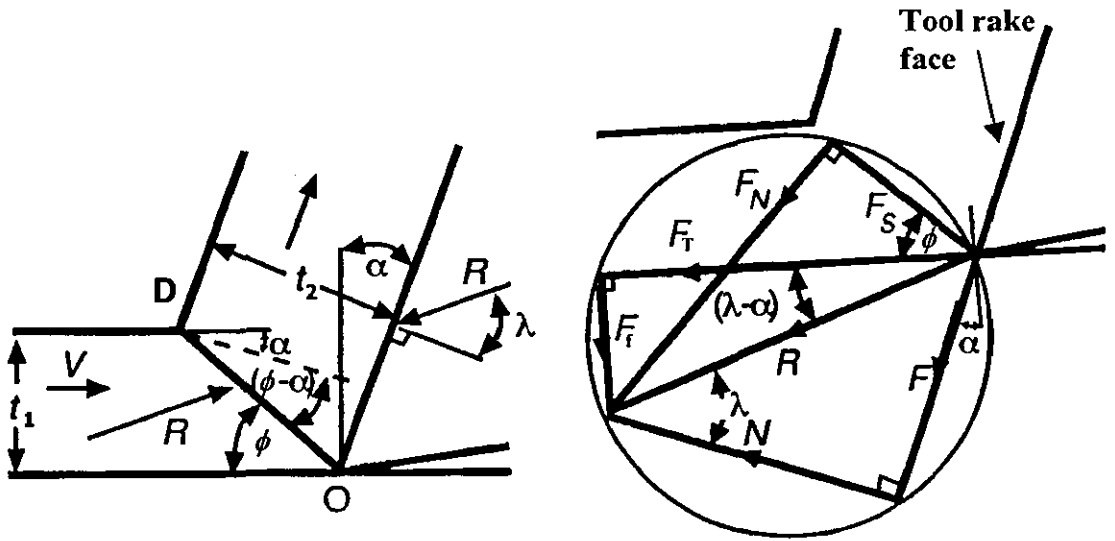
Figure 2.7 Merchant's force circle (from [4])

The stresses acting in the shear plane are equal to the shear strength k_S of the workpiece material in that area, thus $F_S = k_S A_S = \dfrac{k_S dt_1}{\sin \varphi}$, where A_S is the area of the shear plane and d is its width (depth of cut). Hence, the resultant force R can be found as

$$R = \frac{F_S}{\cos(\varphi + \lambda - \alpha)} = \frac{k_S dt_1}{\sin\varphi \cos(\varphi + \lambda - \alpha)}. \qquad (2.3)$$

This allows to find the main and feed cutting forces:

$$F_T = R\cos(\lambda - \alpha) = \frac{k_S dt_1 \cos(\lambda - \alpha)}{\sin\varphi\cos(\varphi + \lambda - \alpha)}, \tag{2.4}$$

$$F_f = R\cos(\lambda - \alpha) = \frac{k_S dt_1 \sin(\lambda - \alpha)}{\sin\varphi\cos(\varphi + \lambda - \alpha)}. \tag{2.5}$$

Selecting shear angle φ, which minimises the expenditure of work in cutting, gives:

$$\frac{dF_T}{d\varphi} = \frac{k_S t_1 d \cos(\lambda - \alpha)\cos(2\varphi + \lambda - \alpha)}{\sin^2\varphi\cos^2(\varphi + \lambda - \alpha)} = 0, \quad \text{which leads to the famous}$$

Merchant's equation: $\varphi = \dfrac{\pi}{4} - \dfrac{1}{2}(\lambda - \alpha)$. $\tag{2.6}$

Substituting this expression for φ into (2.4) and (2.5) allows cutting forces to be rewritten:

$$F_T = \frac{k_S dt_1 \cos(\lambda - \alpha)}{\sin\left[\frac{\pi}{4} - \frac{1}{2}(\lambda - \alpha)\right]\cos\left[\frac{\pi}{4} + \frac{1}{2}(\lambda - \alpha)\right]} \quad \text{or } F_T = 2k_S dt_1 \cot\varphi, \tag{2.7}$$

$$F_f = \frac{k_S dt_1 \sin(\lambda - \alpha)}{\sin\left[\frac{\pi}{4} - \frac{1}{2}(\lambda - \alpha)\right]\cos\left[\frac{\pi}{4} + \frac{1}{2}(\lambda - \alpha)\right]} \quad \text{or } F_f = k_S dt_1\left(\cot^2\varphi - 1\right). \tag{2.8}$$

From the force diagram (Figure 2.7), the forces acting in the shear plane can be expressed as:

$$F_S = F_T \cos\varphi - F_f \sin\varphi, \quad F_N = F_T \sin\varphi + F_f \cos\varphi. \tag{2.9}$$

Hence, shear stress k_S and normal stress σ can be given as

$$k_S = \frac{F_S}{A_S} = \frac{(F_T\cos\varphi - F_f\sin\varphi)\sin\varphi}{dt_1}, \quad \sigma = \frac{(F_T\sin\varphi + F_f\cos\varphi)\sin\varphi}{dt_1}. \tag{2.10}$$

Finally, the coefficient of friction at the tool–chip interface can be written as:

$$\mu = \frac{F}{N} = \frac{F_T\sin\alpha + F_f\cos\alpha}{F_T\cos\alpha - F_f\sin\alpha}. \tag{2.11}$$

It is worth noticing that the friction model used for this derivation, implies that friction force F and normal force N are uniformly distributed along the sliding interface and that F is proportional to N. This is an oversimplified approach, which cannot adequately describe seizure conditions at the interface and also leads to unrealistically high friction forces for extremely high contact pressures occurring in

cutting. A shear friction model allows to limit the friction force at the tool–chip interface and will be described below.

The forces related to deformations in the shear plane and the chip movement along the rake face are the only forces to be considered in cutting if the cutting tool is sharp. An additional force may appear due to pressure of the workpiece material against a small contact area on the clearance face of the tool underneath the cutting edge; it can, however, be neglected if the tool is sharp and the contact area on the clearance face is small.

The forces in turning increase proportionally with an increase in the feed rate and depth of cut, which are parameters, set by the operator. Nevertheless, the shear angle φ is not in the direct control of the operator and varies considerably for different cutting conditions. The shear angle influences greatly the cutting forces: for the same material shearing force F_{s} can be more than five times higher for small values of φ ($\varphi = 5°$) than for $\varphi = 45°$.

Last but not least, the Merchant's formula for the shear angle allows its straightforward estimation, in contrast to other predictions, which require the use of parameters hardly definable for the case of UAT. For example, according to the Oxley's shear zone analysis [8] (described in [4]), based on selecting the shear angle ϕ so that resultant forces in the shear plane and the tool–chip interface are in equilibrium:

$$\tan\theta = 1 + 2\left(\frac{1}{4}\pi - \varphi\right) - Cn,\qquad(2.12)$$

where $\theta = \varphi + \lambda - \alpha$, and C and n are constants. Parameter C is defined from the empirical strain-rate relation $\dot{\gamma}_{\mathrm{p}} = CV_{\mathrm{p}}/b$, where $\dot{\gamma}_{\mathrm{p}}$ and V_{p} are the maximum shear strain rate and shear velocity in the shear plane, respectively, and b is the length of the shear plane. However, estimations of C for UAT are cumbersome, since the strain rate at the shear plane changes considerably within a cycle of ultrasonic vibration.

In another model proposed by Rowe and Spick [9], the shear angle is chosen so as to minimise the total energy expended in the system, i.e. the energy both in the shear plane and at the rake face. According to this model:

$$\beta \sin^2 \varphi = \frac{1}{\chi}\cos\alpha\cos(2\varphi - \alpha),\qquad(2.13)$$

where β is the constant between zero and unity, defined by the proportion of sliding/seizure on the tool–chip interface, and $\chi = L_c/OP$ with OP being equal to the projected contact length (Figure 2.8). The parameter χ could not be used in our studies of the UAT process since the contact length changes from zero to L_c at every cycle of ultrasonic vibration.
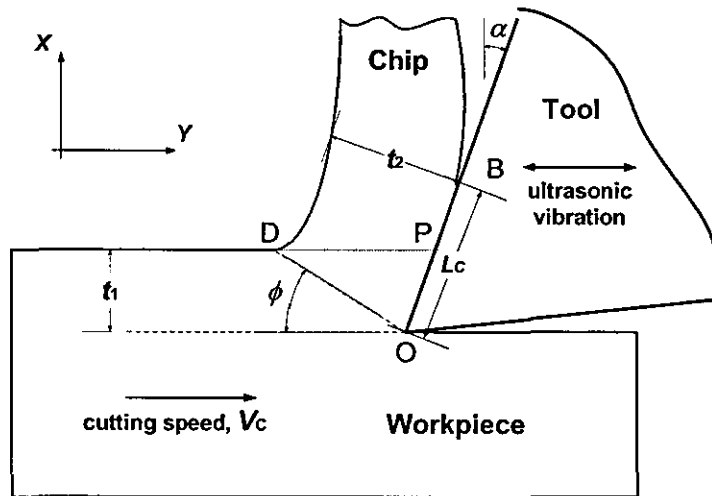
Figure 2.8 Projected contact length (OP)

2.4 Contact conditions at the tool–chip interface

During the chip formation by shearing, the chip separated from the workpiece material slides along the rake face of the tool. Under real-life cutting conditions, the bonding between the tool and workpiece often occurs within the significant part of the contact length L_c (OB in Figure 2.5). In the area of such seized contact, tool and workpiece materials effectively become one piece of metal; the bonded area can occupy up to 80% of the contact length [4]. Alternatively, formation of the so-called built-up edge (BUE) takes place, when material cyclically builds up and breaks away from the cutting edge, hence the chip flows over the modified shape of the cutting tool defined by the built-up edge. The seizure / BUE occurs over a large part of the chip-tool interface, and only insignificant part of the interface is in the condition of sliding friction between the chip and tool rake face. This leads to stresses acting in the biggest part of the interface between the tool and chip being close to the shear yield strength of the workpiece material. Such contact conditions seriously

complicate the contact problem at the interface, and, in order to simplify the analysis of forces and heat transfer, the idealised case is usually considered, with the sliding contact conditions being assumed along the whole tool–chip interface, as it was described in Section 2.2.2.

The chip thickness and radius of curvature are strongly affected by the lubrication introduced in the cutting region; this was already established in the XIX century [10]. Adding lubricants causes the chip to become thinner and more curled, as observed in the experimental part of this research. Influence of lubricants also depends on the cutting speed, feed rate and rake angle.

The question how the lubricant can penetrate the contact area between the chip and tool at the rake face lies in the field of contact mechanics. It is generally agreed [5] that no lubricant can penetrate the contact area where normal stresses between chip and tool at the interface are high. However, lubricants can infiltrate along the non-contact channels due to the surface roughness of the rake face. The length of these channels generally varies from half to one chip thickness. When the lubricant reacts with the chip in the region of these channels, the resistance to chip flow is reduced, and that increases the shear plane angle. Consequently, the chip becomes thinner and unpeels from the tool surface. Hence, the lubricant does not have to penetrate the whole contact distance at the rake face to reduce the contact area, its influence at the edge of the contact length (next to point B in Figure 2.5) is enough. The nature of lubrication processes in UAT has not been studied yet. Nevertheless, the intermittent contact nature at the rake face of the tool in this case should allow gaseous or liquid lubricants to penetrate deep inside the contact area down to the very cutting edge. It is believed that this should further increase the shear angle, and decrease the chip thickness. The attempt to study the influence of the lubrication on the UAT in comparison to CT is described in the experimental part of this thesis (see Section 5.4.2).

In the friction model described in the previous section, it was assumed that the friction stress is proportional to the normal stress on the rake face with a friction coefficient $\mu = \tan \lambda$. This assumption leads to deductions of peak normal stresses at the interface of up to three times k (k being shear yield strength), and of peak friction stresses for such a friction law of up to two k. This, of course, is not physically realistic, as a metal is not able to transmit a shear stress greater than its

shear yield strength [5]. Hence, more advanced friction models are required for a trustworthy description of the friction on the tool's rake face.

Experimental studies of the friction force at the rake face indicate a nearly proportional dependence for low normal stresses (with μ as a coefficient of proportionality), changing into a plateau with friction stresses $\tau = mk$, where $m \leq 1$, for normal stresses σ_N greater than k [5]. The friction stress along contact length L_C also increases towards the cutting edge, but it is still limited by a value of k. Alternative friction models, which are in agreement with these experimental observations, were first disseminated by Shaw [11]. In these models, the friction force depends on the fraction of the material's shear yield strength rather than the normal force as in the Coulomb friction model.

The simplest of such friction models neglects the friction stress variation with σ_N for its low values, and defines the friction stress as $\tau = mk$. Such an approach is adopted in slip line field modelling. A more advanced model specifies a linear dependence for lower σ_N and limits the friction stress for its higher values [5]:

$$\begin{aligned} \tau &= \mu\sigma_N \quad \text{if} \quad \mu\sigma_N < mk, \\ \tau &= mk \quad \text{if} \quad \mu\sigma_N \geq mk. \end{aligned}$$
(2.14)

A similar friction model introduced in [12] describes the friction law via an exponential function:

$$\tau = mk\left[1 - \exp\left(-\frac{\mu\sigma_N}{mk}\right)\right].$$
(2.15)

In the enhanced variant of this approach, the friction stress depends also on relative sliding velocity v_r between the chip and the tool at their interface. If this velocity is lower than critical sliding velocity v_c, sticking of the chip to the rake face is simulated:

$$\tau = -mk\frac{2}{\pi}\text{sgn}(v_r)\arctan(\frac{v_r}{v_c}).$$
(2.16)

This model is known as shear friction model in commercial FE codes [13] and, it is utilised in FE simulations of UAT and CT described in Chapters 6 and 7.

The area of the contact region at the tool–chip interface in orthogonal cutting is defined by the width of this region, usually equal to depth of cut d and contact length L_C (Figure 2.5). The value of L_C is always greater than uncut chip thickness t_1; it is

uneven along the chip width and the mean value of L_{C} is therefore considered. An estimation of L_{C} was given by Zorev [14] from the moment equilibrium about O (Figure 2.7):

$$L_{\mathrm{C}} = \frac{m}{n} t_2 \left(\mu + \tan(\varphi - \alpha) \right),$$ (2.17)

where $\frac{m}{n} = 1.25 \div 4.5$ for different materials and cutting conditions.

2.5 Cutting tools

There is a variety of modern tool materials used in present-day manufacturing. The main classes are high-speed steel tools, carbides and cermets, and superhard materials, such as polycrystalline diamond (PCD) and cubic boron nitride (CBN). The tools come in different sizes and shapes. For the case of UAT, design of the ultrasonic transducer necessitates the use of insert tools, i.e. relatively small cutting edges fixed to the end of the tool holder. Here, carbides are the natural choice, since they are often used for cutting inserts. These inserts are usually made of tungsten carbide (WC) or a mixture of WC with titanium and tantalum carbides (TiC/TaC). Tungsten carbide inserts are recommended for cutting heat-resistant alloys, such as Inconel 718, and used in all experiments in the present work. Hence, the description of cutting edges is limited to this class of tools.

High temperature can cause a tool to degrade. Firstly, tool can be oxidized by the reaction with the atmosphere (for temperatures greater than 500°C). The chance of oxidization is higher in UAT due to the interrupted contact of the tool with a workpiece; this, however, is not often critical for failure. Secondly, the tool's microstructure changes for temperatures above 900-950°C, when WC starts to dissolve in the cobalt binder that leads to a sudden loss of strength. The temperatures observed in the infrared thermography experiments (see Chapter 5) do not exceed 750°C, hence structural changes in the tool material can be neglected in our study.

For tungsten carbide tools, their thermal conductivity K is several times higher than conductivity of the workpiece material ($K_{\mathrm{WC}} \approx 60$ W/m K compared to $K_{\mathrm{Inconel\,718}} \approx 12$ W/m K), and thus provides an effective heat withdrawal from the cutting region.

The Young's modulus of tungsten carbide is about 650 GPa compared to 200 GPa for Inconel 718. This significant difference allows the cutting tip to be considered rigid in FE simulations (see Chapters 6 and 7).

Cutting tools are often coated to improve their wear resistance by increasing their hardness and toughness. Uncoated tools are, however, used in all the experiments in order to simplify the comparison with the results of the numerical simulations.

2.6 Experimental methods

2.6.1 Techniques for chip formation study

As orthogonal cutting conditions are usually assumed in analytical and numerical models of cutting, experimental studies of chip formation in laboratory conditions should ideally be performed with orthogonal cutting. On a lathe, these cutting conditions are implemented with a workpiece in a form of a tube, whose wall thickness is the depth of cut. However, in many cases the workpiece material is not available in a tube form, and semi-orthogonal cutting conditions are used in this case, where a solid bar is cut with a constant depth of cut. In order to avoid considerable deviations from orthogonal conditions, the major part of the cutting edge should be straight. Fully orthogonal conditions can be achieved on a planning machine, with a workpiece in a form of a plate. For most experimental conditions, and UAT in particular, the lathe method is considerably more convenient. The current design of the ultrasonic system imposes several limitations on the cutting conditions, and semi-orthogonal cutting conditions are therefore used in all tests.

The chip formation is a high-speed process and its real-time observation requires special equipment, such as high-speed cameras (see Chapter 5). The tool–chip interface is not visible due to opaqueness of workpiece and tool materials. This could be overcome with the use of transparent sapphire tools during cutting and observing the interface through the tool, however, it cannot be assumed that the contact conditions at the interface in this case would be the same as for carbide or metallic tool materials [4].

A study of the end of the cutting path, after cutting was stopped in a normal way, by disengaging the feed, cannot produce any useful information about the chip formation process. Nevertheless, important information can be retained after a

sudden stop of the cutting action, which allows to freeze the cutting process (one of such quick-stop devices is described below). The quick-stop technique should, however, be specially adjusted for cutting with superimposed ultrasonic vibration, as the design of the ultrasonic transducer requires special arrangements for quick tool–chip disengagement.

For the external examination of the chip microstructure, the scanning electron microscope (SEM) technique is highly valuable due to its great depth of field. Both light microscopy and SEM are used to study the microstructure of the chip cross-sections after cutting with CT and UAT (see Chapter 5).

Chip thickness measurements

The mean chip thickness can be obtained by measuring the length l and weight W of a piece of the chip. The mean thickness t_2 (Figure 2.5) can be then found as

$$t_2 = \frac{W}{\rho w l},$$
(2.18)

where ρ is the density of the workpiece material and w is the width of the chip (which corresponds to depth of cut d). In practice, the chip is never thinner than the undeformed chip thickness t_1 (Figure 2.5) [4].

The quick-stop technique

HS video cameras have been successfully used to study dynamics of the chip separation processes. It is, however, difficult, to resolve much detail because of the small scale of the cutting region and limitations on the speed of filming. Sometimes microscopic details of the cutting process are more important than such dynamic information, and a "frozen picture" of geometry of the interaction between the tool, chip and workpiece is required for a subsequent microscopic investigation. The quick-stop technique is one of the most popular methods for achieving this goal. In this technique, the cutting process is stopped quickly by moving the tool apart from the workpiece at a speed much greater than the cutting speed. Depending on the seizure conditions on the rake face and strength of the chip and tool, the chip can either stay attached to the workpiece or to the cutting tool. In the former case, a fragment of a cutting edge can be left attached to the chip, especially if a crack or

notch was intentionally introduced in the tool for this purpose in order to preserve the tool–chip interface.

A schematic view of a quick-stop device is illustrated in Figure 2.9 and its description is adapted from [5]. In this device, the tool is supported at a pivot point and by a shear pin; mass M strikes the tool holder with a speed V_M. If the impact force is much greater than needed to break the shear pin, the mass will then cause the tool holder to swing quickly away from the chip. The tool holder's velocity V_T does not instantaneously reach the cutting velocity V that is necessary for cutting to stop, because of its inertia. However, to minimise the retraction time, M and V_M should be made large and inertia of the holder should be small. In practice, to increase V_M, mass M is frequently fired from a gun.
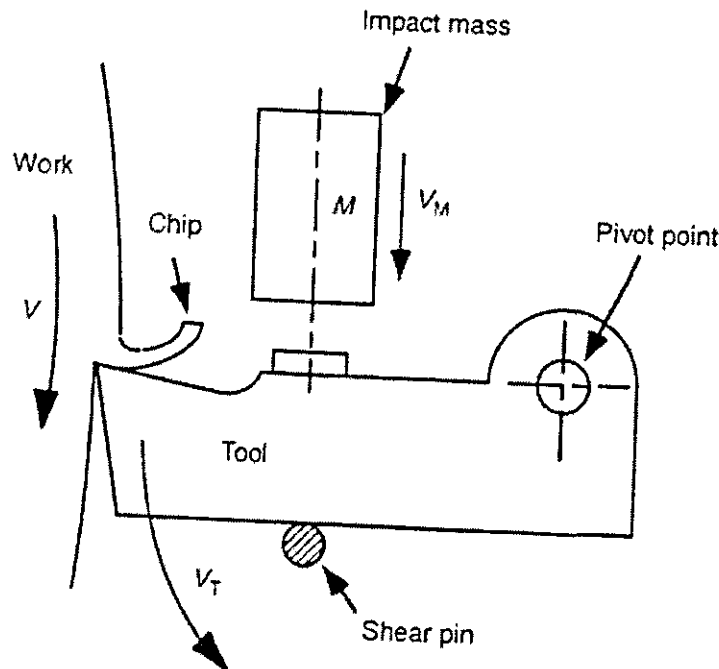

Figure 2.9 A quick-stop device (from [5])

2.6.2 Measurement of forces acting on the cutting tool

Many experimental studies of the metal turning process are done before or after cutting. The number of quantitative observations, which can be done during cutting, is rather limited, with one of the most important measurements of this type being analysis of cutting forces.

There are two main ways of force measurements in metal cutting: direct and indirect. In direct methods, electrical signals proportional to the cutting forces, deflections or strains are measured in elements supporting the cutting tool. These methods provide accurate measurements of forces both in magnitude and direction. In indirect measurements, the forces are deduced from the power used by the lathe motor, which increases with the cutting force [5]. The description in this section is limited to the direct methods, as they are more accurate than the indirect methods.

The force-measurement devices are usually called lathe or tool dynamometers, and there is a number of requirements that a good lathe dynamometer must satisfy: for high sensitivity, rigidity and accuracy [11]. The dynamometer should be sensitive and accurate so that the measurement error does not exceed 1 %. Although some deformation is needed for the operation of the dynamometer, it is should be stiff enough not to affect the rigidity of the tool – workpiece system (and thus deflection measuring device should be capable of measuring small deflections of about 1 μm). Additionally, the natural frequency of the instrument should be at least four times higher than the frequency of the parasitic vibration, such as chatter, frequently found in cutting, in order to minimize the tendency for such vibrations to occur. This will ensure that the recorded force will not be influenced by the vibrating motion of the dynamometer [11]. (It is, however different in case of UAT, as extremely high frequency of the ultrasonic vibration is more than an order of magnitude higher than the natural frequency of the dynamometer and tool – workpiece system, thus it provides the system with high dynamic rigidity.)

A dynamometer should measure at least two components of the cutting forces, or, preferably, all three components. The forces are usually measured relative to a set of rectangular coordinates, and there should be no cross-sensitivity between components, i.e. no influence of the load applied along one axis on the reading in other directions. A dynamometer should be stable with respect to time, temperature and humidity, in other words, it should have a low drift, so that the calibration is required only occasionally [11].

The most common type of the dynamometer uses strain gauges to measure elastic strains caused by the cutting forces [5]. However, a new generation of tool dynamometers is based on the piezoelectric effect. The description here will be limited to this type as they are used in the majority of the modern force measurement experiments.

For piezoelectric materials, such as barium titanate or quartz crystals, deformation of the crystal under the applied mechanical force causes generation of an electrical charge proportional to the force, – this is called the piezoelectric effect [5]. This principle is used for creation of a three-axis force dynamometer. Typically, quartz is used as a piezoelectric material, due to its good dynamic properties. There are several piles of quartz crystals inside a dynamometer (Figure 2.10), each being oriented in its piezoelectric sensitive direction so as to detect one of the respective force components. A produced charge is very small and a charge amplifier is therefore needed to increase the output signal. The natural frequency of such a dynamometer is close to that of quartz crystals and is usually between 2 and 5 kHz [5].
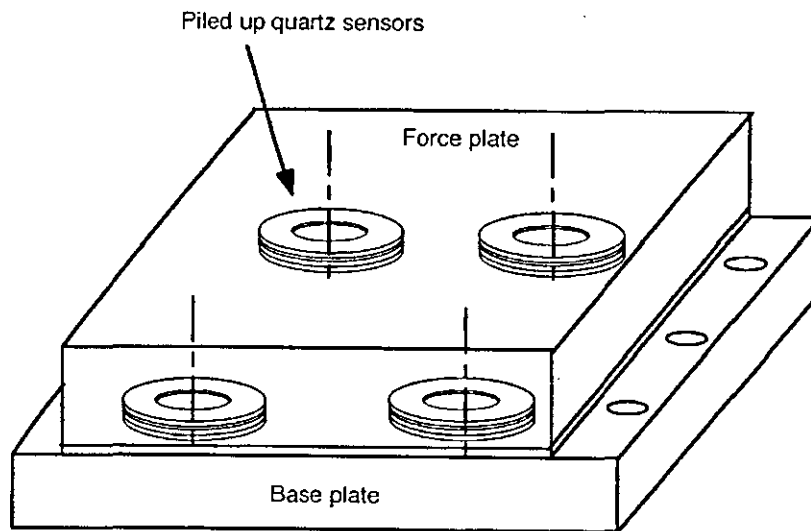
Figure 2.10 A piezoelectric tool dynamometer (from [5])

2.6.3 Temperature measurement

Introduction

During turning, the work of plastic deformation and friction are the main heat sources in the process zone, and can significantly increase temperature in the cutting region. This temperature increase can noticeably affect various mechanical and thermal properties of the workpiece material, leading to material softening (i.e. reduction in the yield stress) and influencing other material properties, such as the coefficient of thermal expansion, specific heat and thermal conductivity. The change of these material parameters, in its turn, influences plastic deformation processes and evolution of stresses in the workpiece [15]. Excessive temperatures can also lead to

premature wear of cutting edges. Hence, temperature in the cutting zone is one of the most important factors in metal turning and significantly affects the cutting process. Analytical and experimental studies of temperature distributions in the workpiece, chip and cutting tool are therefore of high interest, and there is a variety of methods to research temperature, some of which are described below.

There can be several goals for temperature measurements in machining. The first goal is to measure the average temperature at the tool–chip interface. This can be implemented with standard thermocouple methods described below. Another, more ambitious goal is to measure temperature distributions in the cutting region. This is complicated by very high temperature gradients in the cutting region, small volumes with high temperatures and dynamically moving parts [5]. Still, there is a number of ways to measure temperature distributions, such as inserted thermocouples, thermal paints and infrared radiation detection methods. An overview of these various methods is given in this section.

According to the classification given in [16], temperature measurement techniques can be divided into four main groups: (i) measuring radiation emitted from the surface of the body, (ii) using probes such as thermocouples and resistance thermometers, (iii) applying heat-sensitive paints and films and (iv) adding particles with known melting points in order to measure "hot spot" temperature. Each of these methods has its own advantages and disadvantages (see Table 2.1) [16].

Technique (iii) and (iv) are not widely used for measuring temperatures in turning and therefore will not be discussed in the present work. The thermocouples and infrared (IR) radiation methods are described in some detail in the following subsections.

Tool-work thermocouple

Application of tool-work thermocouples is probably the most extensively used method of temperature measurement in the cutting tool.

In the elementary thermocouple two different materials are connected at two junctions (which are called hot and cold junctions) with different temperatures. The electro-motive force (EMF), which is generated in this circuit, depends on the materials used and the difference in the temperatures. Calibrating the generated

EMF, the difference in the temperature between hot and cold junctions can be calculated.

Table 2.1 Advantages and disadvantages of temperature measurement methods

([16])

Advantages	Disadvantages
Infrared radiation measurements	
• non-invasiveness (do not affect temperature distribution being measured) • ability to measure over significant areas of the surface of the body	• comparatively slow response time (recently reduced to microseconds) • temperature measurement only at the surface of a radiating body • difficulties in calibrating the surface emissivity of the object (usually a function of temperature, angle of observation, surface finish and some other parameters)
Thermocouples	
• easy calibration over a wide range of temperatures • ability to measure temperature inside the body	• invasive nature (when inserted into the body may affect temperature distribution being measured) • measurement only in a single point • requirements of a good thermal contact with the surrounding material (even then a finite time is required for heat to diffuse into the thermocouple • easy damage • laboriousness of embedding the thermocouple into the cutting insert (which usually become worn very fast, especially in turning such intractable materials as Inconel 718)
Thermal paints/films	
• ability to measure over the big surface area of the object • registration with usual photography techniques	• invasiveness • easy damage • limited accuracy • limited ability to follow temperature histories

In a tool – workpiece thermocouple, workpiece and tool materials are used as its two elements (Figure 2.11) [5]. The hot junction is the tool – workpiece interface, while electrical connections to the cold part of the cutting tool and to the workpiece form the cold junction. In the latter case, because the workpiece is rotating, a special slip ring system with a liquid mercury contact is utilised to make an electrical connection. Such a contact is used in order to prevent an error resulting from a parasitic EMF, arising in case of the dry rubbing contact between the workpiece and connecting wire. The amplified EMF generated between the tool and workpiece during cutting is measured using a millivoltmeter. The possible error due to the heating of the cutting tool at the cold junction is sometimes compensated with an additional standard thermocouple and a sliding potentiometer system.
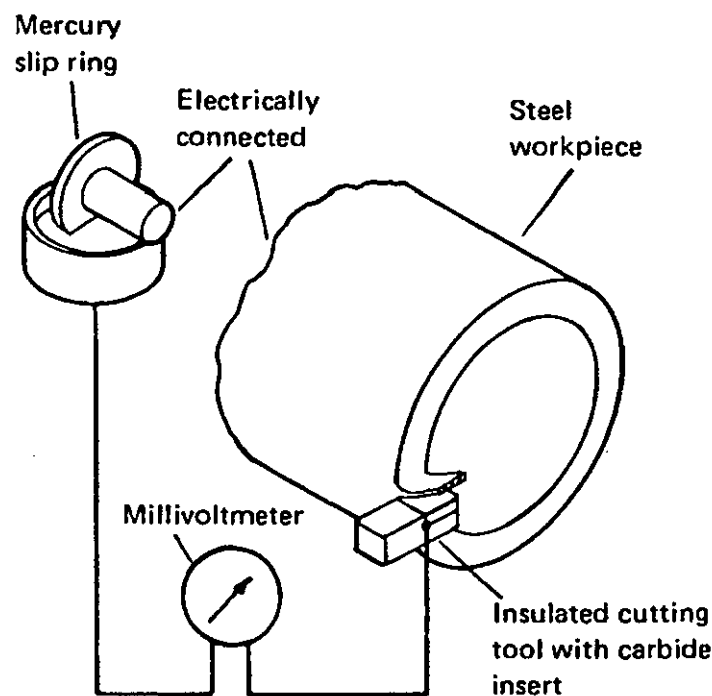

Figure 2.11 Tool-workpiece thermocouple circuit (from [3])

The average value of temperature along the tool–chip interface is measured with this method. While this technique is good to give a basic understanding of the temperature level in the cutting region depending on cutting conditions, it does not provide one with the temperature distribution along the tool rake face.

Inserted thermocouples

To measure the temperature distribution in the tool is more desirable than measuring only the mean temperature along the tool–chip interface. In an attempt to obtain more precise information on the temperature distribution in the tool, a small hole is bored in the tool and a fine thermocouple (or even a special single wire) is inserted into the hole (Figure 2.12) [4]. This allows temperature at the bottom of the hole to be measured. In order to map the temperature gradients, such a procedure should be repeated many times with holes drilled in different places of the tool. There are two main problems arising from this method. The first is that this method is invasive, i.e. the hole with inserted thermocouple affects temperature distribution in the tool. The second source of error is that if the hole is not small enough, the thermocouple reading overlaps a considerable temperature range due to very steep gradients near the edge. Additionally, drilling holes of small diameter in the cutting tool is a tedious job, in particular for the insert tips, made of very hard materials such as tungsten carbide. Besides, such inserts are worn fast in turning of intractable metal alloys. To sum up, this method is also not ideal for taking precise measurements of the temperature distribution in the tool and along its rake face. It is quite laborious and still does not provide a satisfactory temperature distribution picture.
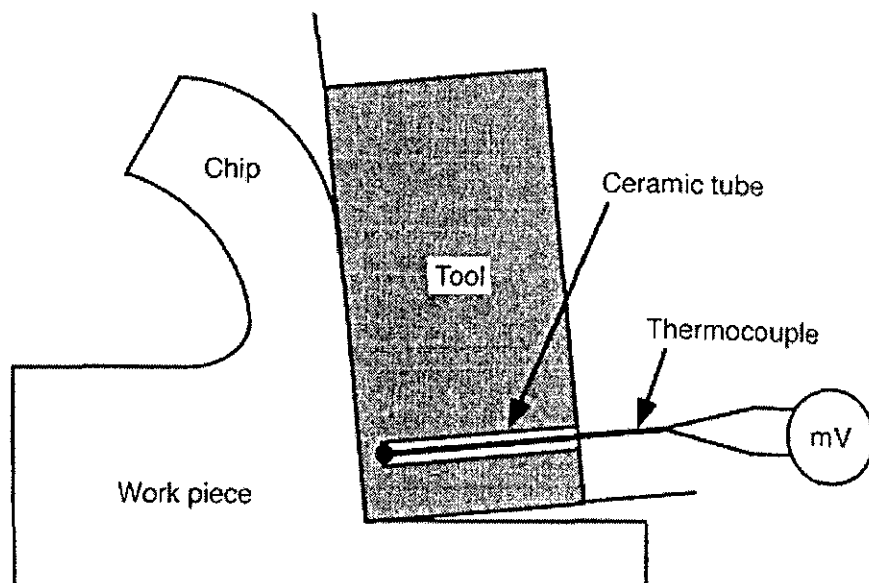

Figure 2.12 Inserted thermocouple (from [5])

IR radiation methods

The techniques described above do not allow straightforward measurements of the temperature distribution in the cutting region. The tool-work thermocouple only determines average temperatures at the tool – workpiece interface, while inserted thermocouples require special changes in cutting tools. Thermal imaging techniques, measuring the infrared radiation from a surface, are non-invasive and have an advantage of measuring temperature distributions over significant surface areas.

There are two main methods to measure infrared radiation from the surface. One is surface photography with the use of special films sensitive to infrared radiation. The intensity of obtained images allows plotting temperature gradients. Another, more modern and promising way is the use of thermal imaging video cameras. Such cameras include an IR detector that absorbs infrared energy within a certain spectral range and converts it into an electrical signal. Since the received radiation has a non-linear relationship to the measured temperature and can be affected by reflected radiation from surrounding objects (namely workpiece and chip) and other factors, calibration and correction procedures should be applied. The main drawback with most thermal detectors is the comparatively slow response time to radiation variations. However, modern thermal cameras allow temperature field measurements at a rate up to about 1000 Hz. Another disadvantage of radiation methods is that information can be only obtained about the temperature at exposed surfaces of the cutting tool. This can be overcome to a certain degree using a very laborious technique based on making holes in the cutting tool and measuring temperature in the created "windows" with an assistance of optical fibres inserted into the holes, thus allowing temperature measurements along the rake face of the tool [17].

Summary of temperature-measurement methods

Among the reviewed methods tool-work thermocouples and IR imaging methods are the most widely used for measuring temperature in metal cutting. The disadvantages of thermocouples are their invasiveness, and difficulty of inserting them into the cutting tools. Additionally, according to Markov [18], thermocouples cannot be used for temperature monitoring in UAT, as there is no constant electrical contact between the tool and workpiece material due to superimposed ultrasonic vibration, thus use of thermocouples can lead to erroneous results of temperature measurements in UAT.

The use of IR radiation methods is therefore a natural choice for UAT also due to their non-invasiveness. Hence, infrared thermography experiments are used to compare temperatures in CT and UAT as described in Section 5.5.

Chapter 3 Application of FEM to simulations of turning

3.1 Introduction

The cutting process during machining is one of material separation at or near the cutting edge tip, therefore consideration of the problem within the framework of material science and interconnection of its dynamic and micromechanical aspects are of significant interest. However, analytical modelling of material separation under the vibro-impact action of a cutter is possible only for partial problems, because of the high level of complexity of the process. It involves three-dimensional geometry, such as a real shape of the cutter and non-orthogonal chip formation with the chip's flow direction being not normal to the cutting edge. Other complications are thermomechanical coupling and strain-rate sensitivity, that is the influence of the process temperature and deformation rates on material properties. Additionally, contact interaction and friction at the tool–chip interface, the influence of the material's microstructure and impact loading (because of the vibrational movement of the cutter) are also important features of the process. The interplay of all these factors determines mechanics of UAT. Hence, numerical modelling of the chip separation and simulations of the tool–chip interaction are probably the only way to analyse UAT processes. Finite element analysis (FEA) is a powerful numerical tool that enables stress and temperature distributions in the tool–chip interaction zone to be obtained and the chip shape during the cutting process to be predicted.

Although there are numerous works utilising the finite element method (FEM) for the analysis of metal cutting, no publication employing this method to study UAT has been found. However, it seems that a substantial number of features inherent in finite element (FE) modelling of CT may be used to development the FE model for UAT. This chapter therefore reviews different aspects of FEA application to CT processes.

3.2 Overview of finite element method

The algorithm of the FEM consists of the following main stages that are described below [4]. A continuous solution region of the boundary-value problem is first discretized into elements by imaginary lines (in two dimensions) or surfaces (in three dimensions). The elements are interconnected at a discrete number of points, which are called the nodes or nodal points. Then the unknown field variable (such as temperature or stress) is expressed in terms of assumed approximating functions within each element. These approximating function are called interpolation functions and defined in terms of the values of the field variable at the nodal points. Typically, polynomials are chosen as interpolation functions due to the ease of their differentiating and integrating. The nodal values of the field variable and the interpolation functions for the elements completely define the behaviour of the field variable within the elements. Together with boundary and initial conditions and constitutive properties of the material, they allow formulation of a discrete-matrix analogue of the boundary-value problem. The nodal values of the field variable become the unknowns in this discrete formation. Once these unknowns are found, the interpolation functions define the field variable throughout the assembly of elements. The choice of the element size and shape and the type of the interpolation function can vary depending on the problem and strongly influence the degree of approximation of the exact solution for the continuous problem. The process is normally based on minimization of the total potential energy of the system, and if the problem is suitably defined, the convergence to the correct result must occur [19].

The choice of FEM for modelling of cutting involves two- or three-dimensional analysis; Eulerian or updated Lagrangian formulation; different material models, such as rigid-plastic or elasto-plastic; structured or adaptive meshes; chip separation criteria; friction and contact conditions at the tool – chip interface and coupled thermomechanical models [5]. The development of FE models for metal cutting and use of particular analysis tools is overviewed in the following sections.

3.3 Development of FE models for turning

Finite element analysis is the main computational tool in the modelling of cutting processes; it has been used to study turning for more than 30 years. A detailed

overview of the development of FE models for turning operations can be found in the monographs [4, 5]. This review follows the exhaustive description of the development of FE models for simulations of cutting until 2000 given in both sources [4, 5] alongside with a review of the most recent papers.

Lagrangian formulation

In FE models of transient processes, there is a choice, in dividing the region of a problem into elements, either to fix the elements to the workpiece or to fix the elements in space. In the former case (the Lagrangian approach), the elements move with the material. In the latter case (the Eulerian approach) the material flows through the immovable elements. Figure 3.1 illustrates these options. In the Eulerian case, attention is drawn to variations in the field variable (in this particular case T) from element to element (for example, elements 1 and 2) at the same time. In the Lagrangian case, attention is focused on changes in the variable at a particular element with time. Each approach has its advantages and disadvantages [5], however, the updated Lagrangian formulation has been used in the majority of publications since mid-1980s (see retrospective review below).
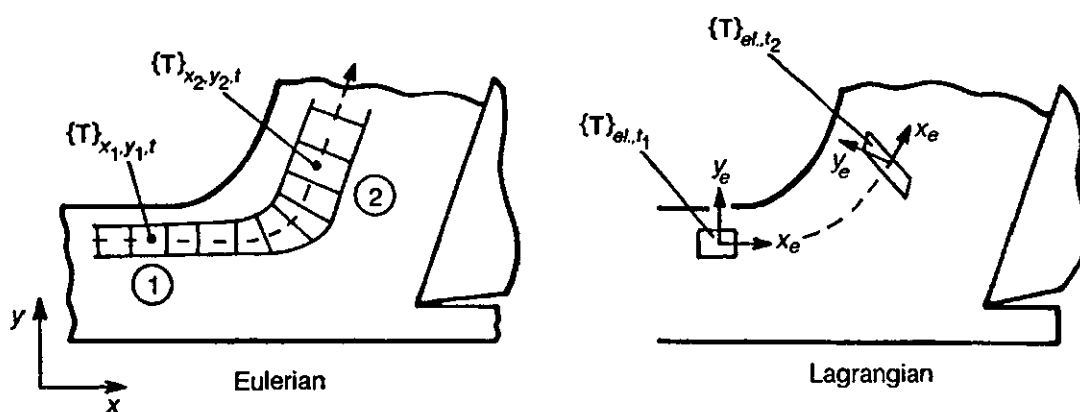

Figure 3.1 Eulerian and Lagrangian formulation (from [5])

In the updated Lagrangian formulation, because elements move with the workpiece, they experience both rigid body motions and large plastic deformations in the direct vicinity of the cutting edge. Under such circumstances, larger

deformations, and changing material properties due to stress and strain in the material, need to be considered [4].

An advantage of the updated Lagrangian formulation is that the cutting can be simulated from the first contact between the tool and workpiece to steady-state cutting conditions. The disadvantage, however, is that large computational times or high computing power are usually required to reach the steady state [4]. In the Lagrangian formulation, material failure and chip-separation mechanisms have to be provided to allow the chip to separate from the workpiece. Various criteria are introduced into modelling schemes in order to describe a condition for the material failure and chip separation from the workpiece [4]. These criteria are based on thresholds for the effective plastic strain [20-23], strain energy density [24, 25], fracture strain (Johnson-Cook model [26]) [27-29], and the critical distance from the cutting edge [30-34]. Several algorithms have been employed to implement the chip formation mechanism when the failure condition is satisfied. In some cases, nodes are separated along a predefined line, so that the line is "unzipped" when the tool tip is sufficiently close, or when another criterion is satisfied [21, 35]. However, such "unzipping" approach, separating nodes along the line (Figure 3.2), makes
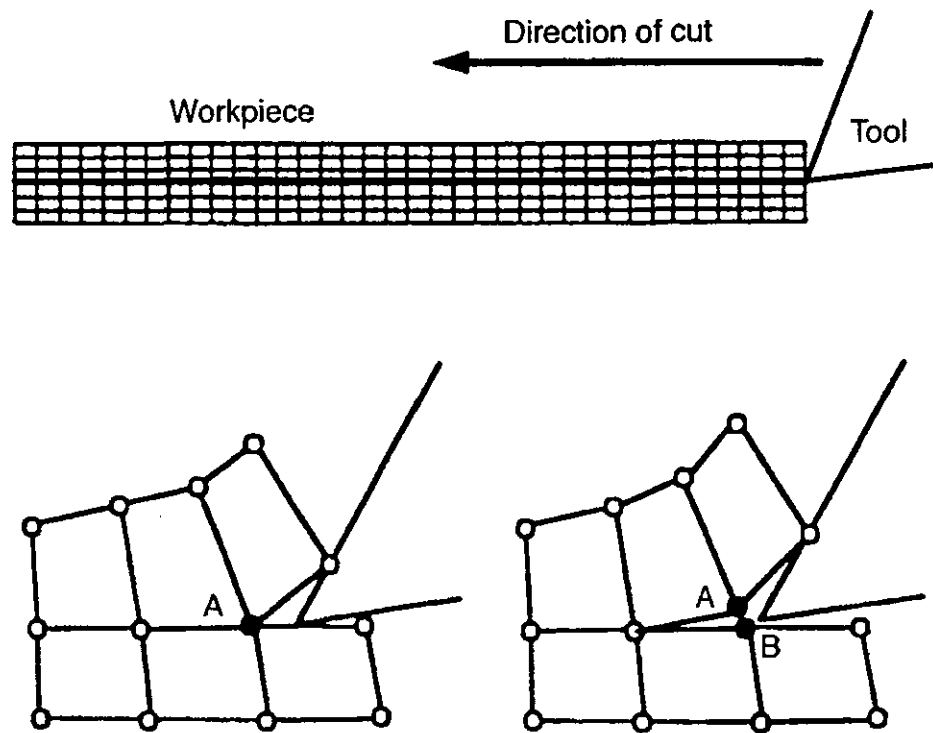

Figure 3.2 Node separation along the predefined line (from [5])

assumptions about both the location and level of the failure stress. Other approaches include element deletion [27-29] and adaptive remeshing [33, 36, 37]. These approaches, by contrast, allow for an arbitrary surface of separation, thus they seem to be preferable, since they more accurately model the cutting process [4]. It is worth mentioning that criteria of chip separation are not needed in Eulerian analyses.

A problem in a Lagrangian formulation is the computational instability due to the large distortion of some elements. The element shape can change significantly during the chip separation process: an element rotates as well as distorts, as it becomes a part of the chip. This problem may cause a degradation of the accuracy and even premature termination of the analysis. It is therefore proved useful to remesh periodically a region with distorted elements, simplifying their shapes, − this process is called rezoning. The rezoning involves state variable mapping algorithms, which interpolates the old solution onto the new mesh [38]. Adaptive remeshing (rezoning) techniques are not needed for the Eulerian scheme, because the element shapes do not change with time [4].

The diversity of mechanically treated materials as well as various magnitudes of technological parameters (cutting speeds, depths of cut, rake angles, etc.), resulting in the considerable variation of cutting forces and induced strains, led to the introduction of different models of material behaviour: elasto-plastic [24, 27, 39] (including the multiplicative decomposition of elastic and plastic strains [40]), rigid-plastic [41] and elasto-visco-plastic [38].

Eulerian formulation

In the Eulerian formulation, the workpiece material is assumed to flow through a meshed volume − the cutting zone. This Eulerian viewpoint focuses attention on a particular point in space and then examines the phenomena occurring there. The cutting process is treated as a large deformation process involving a visco-plastic material. It is assumed that elastic effects are negligible.

The advantage of the Eulerian view is that the shapes of elements do not change with time. However, in cutting modelling, with determination of the chip shape being a part of the problem to be solved, it is not clear where elements should be drawn. Experimental work must be carried out in order to ascertain chip geometry and the shear angle. Furthermore, only continuous chip formation can be modelled [5].

A more general problem of the Eulerian formulation is description of the changes in material's property, such as strain hardening, from element to element. This is not a problem for the Lagrangian scheme, where the state of a material is defined in an element [5].

Review of the development of FE models for metal cutting

The finite element method has been used to model turning operations since the early seventies. The first finite element chip formations studies (Zienkiewicz, 1971) [42] avoided all the problems of large deformation modelling by simulating the loading of a tool against a pre-formed chip, assuming its shape rather than predicting it, as well as neglecting initial stages of the process (i.e. chip separation and residual stresses) in simulations (Figure 3.3). This work had a number of limitations, making it of historical interest only. For example, it neglected friction between the chip and tool and did not consider material yield strength variations with strain rate and temperature. More fundamentally, it assumed the shape of the chip in the first place, whereas the main purpose of chip forming analyses is to predict it.
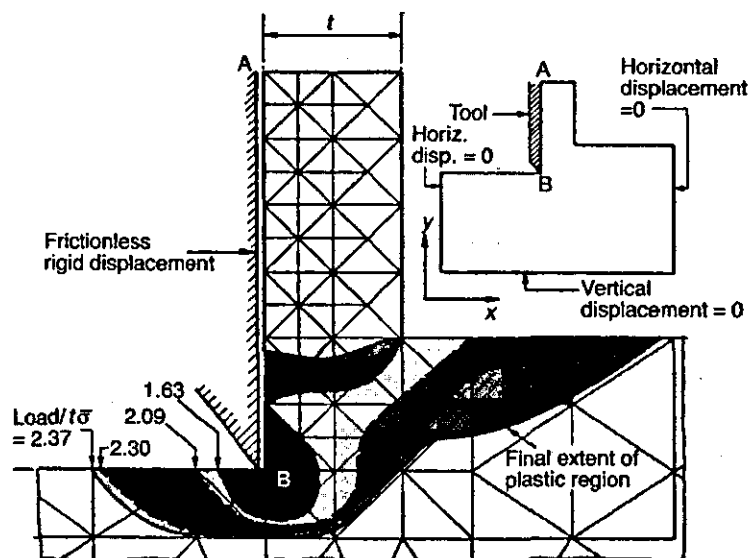

Figure 3.3 Shear zone development, loading a pre-formed chip (from [42])

The limitations of that initial work were removed by Shirakashi and Usui (1976) [43]. While keeping the computational advantages of supposing the tool to move into

a pre-formed chip, they developed an iterative way of changing the shape of the pre-form until the generated plastic flow was consistent with the assumed shape. They also included realistic tool–chip friction conditions obtained experimentally, an analysis of temperatures, and variations of material yield strength with strain, strain rate and temperature. An updated Lagrangian elasto-plastic analysis with three-node triangular elements was performed. The procedure of loading a tool against an already formed chip greatly reduces computational capacity requirements and, in the 1970s, made elasto-plastic analysis possible. This approach has been further developed in the later publications (for example, [44]) and combined with state-of-the-art modelling features of the 2000s.

Steady state rigid-plastic modelling, within a Eulerian framework, was first applied to machining by Iwata et al. (1984) [45], using software developed for metal forming analysis. Their model procedure also adjusted an initially assumed flow field to bring it into agreement with the computed field. The model included friction and work hardening, and also a consideration of chip fracture, but did not include heating and elastic effects.

The development of faster computers in mid-1980s allowed transient simulations of the entire cutting process from the first tool–chip contact to steady-state cutting conditions, as in practical conditions. The updated Lagrangian elasto-plastic analysis was used, and the chip-workpiece separation criterion at the cutting edge became an issue. Figure 3.4 shows the earliest example of such transient simulations (Strenkowski and Carroll, 1985) [35], which used a strain-based separation criterion. At that time, neither a realistic friction model nor coupling of the elasto-plastic analysis to thermal one was included.

There was a further development of non-steady analysis, from transient to discontinuous chip formation, the first three-dimensional schemes and the introduction of adaptive remeshing techniques in the 1990s.

In 1991 Komvopoulos and Erpenbeck [30] used the general-purpose finite element code ABAQUS and an updated Lagrangian formulation to model the cutting process. A distance criterion was used as the chip separation condition. They investigated two possible constitutive deformation laws: (i) elastic-perfectly plastic and (ii) elastic-plastic with isotropic strain hardening and strain-rate sensitivity. A total of five cases with different material models, friction coefficient values and tool

geometries were studied to find their effects on the cutting process. The Coulomb's law was used to model the tool–chip interface friction.
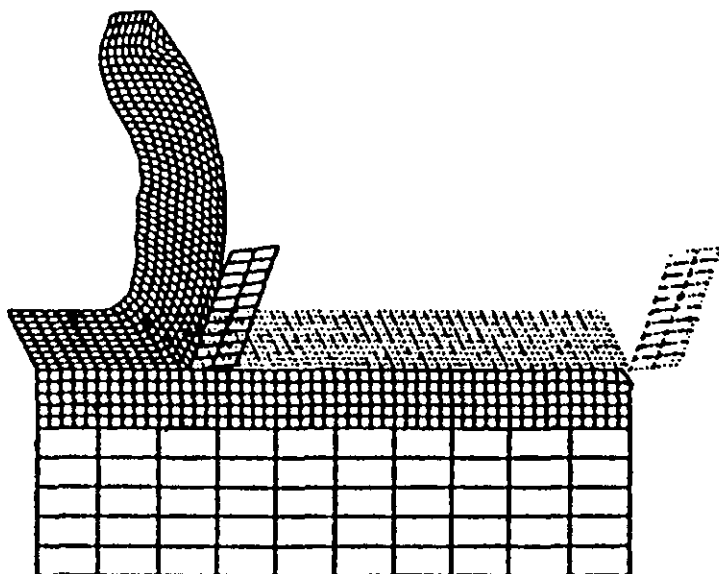

Figure 3.4 An example of non-steady state analysis (from [35])
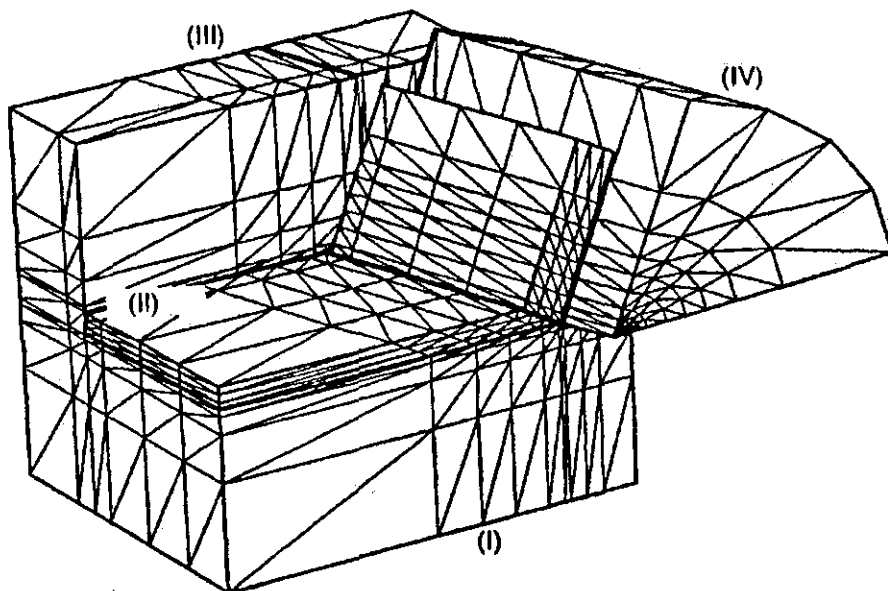

Figure 3.5 Three-dimensional chip formation (from [46])

One of the earliest examples of elasto-plastic three-dimensional analyses was carried out by Maekawa and Maeda (1993) [46](Figure 3.5). Temperature and strain-

rate effects were ignored to reduce computational requirements. This restriction was soon removed: three-dimensional elasto-plastic, thermally coupled simulation was performed by Maekawa et al. (1994) [47].

Marusich with co-workers [33, 40, 48-50] developed specialised software for modelling of metal cutting – MACH2D and, later, AdvantEdge – and used it for modelling high-speed machining. A comprehensive discussion on the numerical techniques employed by them is given in [33]. The Lagrangian model featured adaptive remeshing capabilities, explicit dynamics, multiple-body deformable contact for tool–workpiece interaction, and transient thermal analysis. Two-dimensional, plain-strain orthogonal cutting conditions were considered. The authors, however, argued that, using the orthogonal cutting data, analytical techniques could be used to extend the results to three-dimensional situations, such as oblique cutting. The elastically-deformable cutting tool was parameterised by rake and clearance angles, and the cutting edge radius. A contact between workpiece and cutter with Coulomb friction was considered, as well as conductive heat transfer across the interface. The elasto-plastic material model based on a multiplicative decomposition of the deformation gradient into its elastic and plastic components was employed. The material model accounted for deformation hardening, thermal softening and strain-rate sensitivity, coupled with a transient heat conduction analysis. A fracture criterion based on workpiece fracture toughness and the critical crack distance was employed. The criterion was applied not only to the depth of cut but also within the deformed chip for a given stress magnitude, enabling nucleation and propagation of a crack through the chip. The model allowed prediction of cutting forces, chip breakage, and residual stresses in the work-hardened surface layer of the workpiece. Another major improvement associated with their model was the use of a versatile adaptive continuous remeshing strategy, which eliminated the bulk of the deformation-induced element distortion during machining simulation. A version of Delaunay triangulation algorithm [51] was employed for remeshing, generating six-noded quadratic elements. The workpiece material was allowed to soften and flow around the finite radius of the cutting tool, fracturing only when the respective criterion was satisfied.

Camacho, Marusich and Ortiz (1995) [40] applied this remeshing technique to the model of high-speed machining and ballistic penetration. The Lagrangian model accounted for dynamic effects, heat conduction, mesh-on-mesh contact with friction,

and thermomechanical coupling. Both ductile and brittle fracture initiation and propagation were considered.

Adaptive remeshing software was also developed by Lei, Shin and Incropera (1999) [38]. They used an elasto-visco-plastic material with isotropic strain hardening and took into account thermomechanical coupling and tool–chip contact interaction. An adaptive mesh-regenerating procedure was introduced in [52] based on integrating existing commercial FE codes, such as ABAQUS, I-DEAS and PATRAN, and establishing communication links between these packages.

The work of Ng and Aspinwall (2000) [28] utilised the shear failure criteria and element deletion/adaptive remeshing modules of ABAQUS/Explicit. The Johnson-Cook formulation, including strain-rate and temperature sensitivity effects, was used to model the workpiece material. A two-dimensional, thermally-coupled, elastic-plastic FEM model using ABAQUS/Explicit was proposed in [22] to predict the effect of sequential cuts on the residual stresses in the machined layer. The residual state from the first cut was used as the initial condition for the second cut.

A two-dimensional, thermomechanically coupled model of orthogonal cutting based on MSC/Autoforge was presented in [53]. The Johnson-Cook constitutive equation was used for workpiece material, which was assumed to flow around the cutting tip; the latter was implemented with continuous remeshing of the workpiece and chip material. A stick-slip friction model was utilised, with the friction coefficient determined experimentally. The cutting tool was modelled as elastically-deformable material with temperature-dependent properties.

On balance, the number of studies utilising the Lagrangian formulation have increased recently. With the development of faster processors with larger memory, the model limitations and computational difficulties of the Lagrangian scheme have to some extent been overcome. The advantage that the Lagrangian analysis offers, such as its ability to track material-property changes, outweighs the simplicity of Eulerian computations, which is not fully realised in the large free surface movement conditions of a chip-forming process [5].

The current stage of development of advanced FE schemes for turning is characterized by the introduction of additional process features into consideration, such as thermomechanical coupling and strain-rate sensitivity, i.e. the influence of process temperature and deformation rates on material properties, and more complex frictional contact conditions at the tool–chip interface, e.g. [29, 32, 33, 38]..Specific

features of these advanced simulations are reviewed below. Other interesting developments in numerical modelling of metal cutting are described in [54-64].

As a side note, the only FE analysis, implementing the contact interaction between an ultrasonically-vibrating tool and workpiece for modelling the ultrasonic drawing process, was found in a recent publication [65]. ABAQUS/Standard was employed in this simple model to compare the drawing force between conventional and ultrasonic drawing.

3.4 FE methods in modelling of specific parts of the turning process.

3.4.1 Chip formation: continuous and segmented

Most of the reviewed models, based on commercial FE codes, deal with the continuous chip formation process (for example, [23, 27, 35, 38]). However, in some recent publications discontinuous or segmented chip formation is considered [28, 29, 32, 34, 66].

Ceretti *et al.* [67] studied serrated chip formation in an orthogonal cutting model under different tool geometries and cutting speeds. DEFORM-2D software including the remeshing module was used in simulations. The critical damage criterion was used for ductile fracture modelling with the threshold value evaluated by a uniaxial tensile test.

In the publications of Bäker with co-workers [32, 34, 68, 69], formation of the segmented chip when cutting titanium alloys was implemented in the two-dimensional, thermally-coupled, plain-strain FE model based on the implicit FE code ABAQUS/Standard. A pure deformation process with material flowing around the tool tip was considered, and automatic remeshing with strong mesh refinement in the shear zone was used to track high temperature and stress gradients found there. No crack growth or damage model was assumed in the model, so that chip segmentation was caused entirely by the adiabatic shearing mechanism. According to this mechanism, rapid plastic deformation in front of the tool tip leads to locally-established high temperature gradients, weakening the material by thermal softening; if the rate of thermal softening equals or exceeds the strain-hardening rate, it causes the formation of narrow, heavily deformed shear bands. Such a shearing condition is

known as a catastrophic or adiabatic slip. The influence of thermal conductivity of the workpiece on the width of shear bands and on maximum temperatures was studied in [69].

Ng *et al.* [29] introduced a three-dimensional model for both orthogonal and oblique cutting based on ABAQUS/Explicit FE code. The chip segmentation mechanism was based on the catastrophic slip criteria described above. Segmented chips were produced due to the ductile crack propagation from the free surface of the chip; the crack propagation criterion was based on the attainment of the critical plastic strain, which was the function of the strain, strain rate, temperature and hydrostatic stress. The model was capable of modelling either continuous or segmented chip formation depending on realisations of the catastrophic slip criterion.

3.4.2 Chip separation and direction criteria

If chip separation in metal cutting is considered as a result of material fracture under the action of the cutting tool, it can be modelled as a crack propagation process. A FE method based on Delaunay triangulation [51] was used in [70]. A crack was automatically extended and then remeshing was performed around the crack tip. It was pointed out that criteria for both crack propagation and its direction are needed to predict the crack growth. Various criteria for the crack-propagation direction were discussed that define surface roughness and chip cracking when applied in simulations of cutting. The criteria were divided into explicit and implicit ones. An explicit theory predicts the propagation direction satisfying the postulated criterion based on a physical parameter for the actual crack tip. The crack is advanced in that direction by a small length increment. The following criteria fall into this category: (i) maximum hoop stress ($\sigma_{\theta\theta} \to \max$), (ii) minimum strain energy density ($S \to \min$), (iii) maximum second stress invariant criterion ($I_2 \to \max$). An implicit prediction theory, by contrast, looks for the propagation direction that satisfies the criterion for the new crack tip after the crack is advanced by a small increment. An iterative process is required, and the direction prediction is more accurate in this case. The following implicit criteria were studied: (i) maximum stress intensity factor ($K_1 \to \max$), (ii) maximum energy release rate ($G \to \max$), and (iii) local symmetry criterion ($K_{II} \to 0$).

An extended FE method for cohesive crack growth was presented in [71]. And a meshless (element-free galerkin) approach was used allowing to model displacement discontinuities, which do not conform to interelement surfaces. The crack growth was governed by requiring the stress intensity factors to vanish at the tip of the cohesive zone.

Based on the stress-strain state, metals can fracture in a brittle or ductile manner [49]. Marusich and Ortiz [33] employed fracture criteria allowing for both types of fracture. In their approach, mixed mode fracture conditions, typical for machining, result in a brittle fracture when the hoop stress $\sigma_{\theta\theta}$ reaches a critical value

$$\max_{\theta} \sigma_{\theta\theta}\left(l,\theta\right) = \sigma_f = \frac{K_{IC}}{\sqrt{2\pi l}}, \tag{3.1}$$

where σ_f is the critical fracture stress, K_{IC} is the material's fracture toughness, and l is a distance ahead of the crack tip.

Ductile fracture by void coalescence was implemented by the ductile fracture criterion in terms of the critical effective plastic strain ε_f^p in the following form [33]:

$$\max_{\theta} \varepsilon^p\left(l,\theta\right) = \varepsilon_f^p. \tag{3.2}$$

Ductile crack propagation in relation to metal cutting was discussed by Atkins (2003) [6]. The author argued that the separation criterion has to be employed at the tool tip in order to permit tool movement. This requirement for the extra separation criterion in FEM models of cutting relates to the difference between conventional plastic flow and cutting: the former is found, for example, in forming processes, whereas the formation of new surfaces is essential for metal cutting. Atkins stated that as long as the work of formation of new surfaces is negligible, any separation criterion could be employed in FEM models of cutting. It is, however, best to employ the physics-based criterion, as residual-stress distributions in the machined layer and the distributions of effective plastic strain both in the chip and machined surface depend on the employed criterion. Atkins argued that the work of fracture related to forming new surfaces can be a significant component of the total cutting work under certain cutting conditions even when no obvious cracking is evident, and then this work should be incorporated into FE simulations.

3.4.3 Contact interaction and friction

In many papers the frictional contact at the tool–chip interface is taken into consideration, and various friction models are employed for this purpose. They include the Coulomb friction model, with friction stress being proportional to normal pressure at the interface ($\tau = \mu \sigma_n$) [29, 34, 72]; shear friction model ($\tau = mk$, where k is shear yield strength) [73]; modified shear friction model (2.14) [22], and stress-based polynomial model [23] (see also Section 2.4 for the description of friction models in cutting).

The residual stress sensitivity to friction condition at the tool–chip interface was studied in [22]. It was discovered that as the friction coefficient value changed from 0.3 to 0.5, the residual stress on the machined surface changed from tensile to compressive.

A complex stress-based friction model was employed in [23] for residual stress prediction; the relationship between the friction stress and normal stress was proposed in the form of the 4th order polynomial:

$$\tau = \sum_{k=0}^{k=4} a_k \sigma_n^k ,$$

where a_k is a coefficient.

The authors [23] argued that a conventional force-based friction model, with the coefficient of friction as

$$\mu = b \frac{F_T \sin \alpha + F_f \cos \alpha}{F_T \cos \alpha - F_f \sin \alpha} ,$$

where b is a coefficient, F_T and F_f are main cutting and feed forces, respectively, and α is the tool's rake angle, is inadequate to predict residual stresses induced by a cutting process and that the polynomial friction model could improve residual-stress predictions.

Friction at the cutting tool–chip interface generates heat that should be properly allocated to the tool and chip. The ratio of the heat supply to the tool (h_1) and chip (h_2) can be computed as (see, for example [33]):

$$\frac{h_1}{h_2} = \frac{\sqrt{K_1 \rho_1 C_1}}{\sqrt{K_2 \rho_2 C_2}} , \tag{3.3}$$

where K_i, ρ_i and C_i are, respectively, thermal connectivity, mass density and specific heat of the tool ($i = 1$) and workpiece ($i = 2$). For a more detailed description of tool–chip heat conduction see Section 7.2.

3.4.4 Thermomechanical coupling

Thermomechanical coupling should be an essential part of the numerical description of the metal machining process. During metal cutting the work of plastic deformation and friction between the cutting tool and workpiece are the main heat sources and can result in a significant temperature increase both in the machined material and the cutter. This temperature increase can noticeably affect material properties, such as the yield strength, coefficient of thermal expansion, conductivity and specific heat. The change in these material parameters, in its turn, will influence deformation processes and stress evolution in the workpiece. Excessive temperatures can also lead to premature wear of the cutting edges. Coupled thermomechanical FE models of turning with a non-steady chip formation analysis and elasto-plastic material behaviour were introduced in the beginning of 1990s. Thermal coupling in these approaches is usually modelled with a staggered procedure (see, for example, [33]) where the solution is divided into mechanical and thermal steps, with a non-changing temperature distribution assumed during the mechanical step.

In this procedure, a mechanical step is taken first based on the current distribution of temperatures. The heat generated due to plastic deformation is then found according to the formula:

$$m = \beta \dot{W}^{\mathrm{P}},$$

where m is the distributed heat source density, $\dot{W}^{\mathrm{P}}$ is the plastic power per unit deformed volume, and Taylor-Quinney [74] coefficient β is approximately 0.9. The rate at which heat is generated due to friction is given by

$$h = -\mathbf{t} \cdot \mathbf{v}_r,$$

where $\mathbf{t}$ is the contact traction, and $\mathbf{v}_r$ is the jump in the velocity across the contact. The heat generated by both plastic deformation and friction is used in the thermal analysis where temperatures are recomputed. Resultant temperatures are then incorporated into the thermal expansion and softening of the workpiece material, and

the next mechanical step is then performed, thus completing one cycle of the procedure.

3.4.5 Modelling of the cutting tool

Although many papers focus mostly on stress, strain and temperature distributions in the workpiece and chip, some papers concentrate on the forces acting on the cutting tool, tool temperatures and its wear.

The heat transfer into the rigid cutting tool was investigated, for example, in [75], and factors, influencing the temperature distribution in the cutting tool, were studied. A FEA model employed in [75] was used to validate experimental measurements of temperature in the ceramic tool when turning Inconel 718 and hardened steels in order to predict the influence of various cutting parameters and tool geometries on the tool life.

The tool wear evolution and tool life was studied in [76]. Modifications were made to the commercial FEM code DEFORM-2D in order to allow tool wear calculations and tool geometry updating based on temperatures and stresses acting on the tool face predicted by FE simulations. It was pointed out that tool wear is influenced by the cutting temperature, contact stresses, and relative sliding velocity at the interface, which, in their turn, depend on tool and workpiece materials, tool geometry and coatings, cutting conditions, and use of coolants. The tool wear was related to the predicted process variables in that thermomechanically coupled analysis of orthogonal cutting, and tool rake and flank faces geometry was incrementally updated in simulations. The effect of various tool edge geometries on the process variables, such as cutting forces and chip geometries, was analysed by Lagrangian thermo-viscoplastic cutting simulations in [73]. Tool temperatures and tool stresses on the rake face were predicted, and the effect of the cutting edge radius on the tool–chip interface temperature was studied.

A power flow inside the ultrasonically vibrating tool was estimated by FEM in [77] in order to design the fatigue life of the tool. However, neither interactions with the workpiece material, no chip separation processes were considered.

An elasto-plastic FEA package FORGE-2 was employed in [78] to study the stress distribution for different tool coatings under a range of cutting conditions when cutting Inconel 718. A continuous chip formation during orthogonal cutting was

simulated with a two-dimensional, thermomechanically-coupled model. The results included the stress and temperature distributions at the tool–chip interface and at the coating–substrate boundaries. Tools were modelled as rigid, uncoated deformable solids and coated deformable ones. A standard Coulomb friction model was utilised. A steady-state temperature response in the cutting tool was calculated using NASTRAN, and effects of tool angles, the nose radius and tool materials on the cutting temperature were studied in [79].

3.4.6 Explicit vs. implicit formulation

In different publications, both explicit and implicit integration schemes are used in FE models of cutting, and both schemes have their advantages and drawbacks.

A commercial FE code ABAQUS/Explicit was used in [23]; authors based their selection on the following reasons: (i) the explicit method is advantageous in modelling complex contact problems and materials with degradation and failure, inherent in metal cutting modelling, and (ii) high-speed dynamic problems are extremely costly to analyse using implicit programs, such as ABAQUS/Standard.

A comparison of explicit and implicit methods for the simulations of forming processes was presented in [80]. Both static implicit and dynamic explicit procedures successfully analysed forming processes. The authors stated that the dynamic explicit approach requires less memory and more computationally efficient; however, for some applications it was unable to reduce the computation time because of the stability requirements of the time-step size, requiring a large number of increments. An elastic springback was reported to be successfully modelled using an implicit quasi-static approach, whereas springback calculations using dynamic explicit methods were said to be meaningless due to the artificial vibrations in the workpiece material. The inertia effect in the explicit method was said to play the significant role in affecting results of simulations, whereas the implicit methods did not change physics of the forming process.

Chapter 4 Ultrasonic machining

4.1 Overview of ultrasonic technology

Ultrasonic vibration has been employed with considerable benefits for a variety of manufacturing processes, such as ultrasonic cleaning, welding, cutting, grinding, milling, drilling and turning.

There are two possible applications of the ultrasonic vibrational energy for the machining of materials: (i) indirect utilisation of an ultrasonic transducer to propel abrasive particles suspended in a slurry at the work surface causing slow erosion and (ii) direct application of the vibration to a cutting tip.
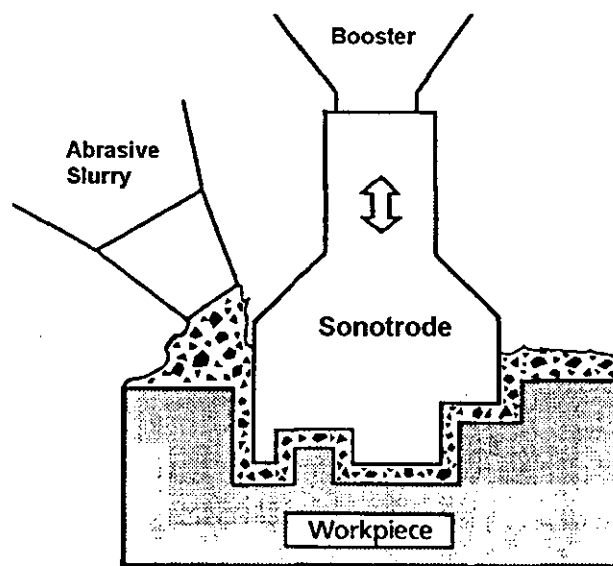
Figure 4.1 Schematic diagram of the ultrasonic erosion process (from [81])

The first process, also called ultrasonic erosion, uses a nonabrasive tool (the sonotrode) made of a hard material, attached to a transducer/booster combination, which vibrates with ultrasonic frequency. A machining action occurs in the following way: the sonotrode vibrates and presses fine abrasive particles flowing throughout the machining gap against the workpiece material. The form tool itself does not abrade the workpiece; the vibrating tool excites the abrasive grains in the flushing

fluid, causing them to wear away the material, leaving a reverse form of the sonotrode shape (Figure 4.1). Such a technique is usually used for machining of brittle workpiece materials, such as engineering ceramics. A good literature review of this form of ultrasonic machining is given in [82].

In the different type of application of ultrasonic energy, a vibrating cutting tool interacts directly with a workpiece and thereby removes the material in a chip form (or cuts it in case of a knife-like system). This approach can be basically associated with any conventional metal removing process, for example turning, drilling, milling and grinding. The advantages of this method, which is usually referred to as ultrasonic vibration cutting/machining, are not obvious, because machine-tool vibration has to be vigorously suppressed in most cases. However, different studies (which are discussed in Section 4.2.3) have reported significant improvements in surface finish, noise and tool wear reduction etc., when ultrasonic vibration is applied during machining operations.

An example of application of ultrasonic vibration for machining operations is ultrasonically assisted drilling. A prototype of an ultrasonic drilling system has been designed in the Wolfson School of Mechanical and Manufacturing Engineering, Loughborough University. The system employs an autoresonant control system, described in Section 4.2.4, to stabilise the drilling process. A reduction in the cutting forces, an increase in the penetration speed, and elimination of burrs are among the benefits of drilling with ultrasonic assistance. Figure 4.2 demonstrates considerable changes in levels of acting forces (a) and penetration speed (b) when ultrasonic vibration is switched on and off (denoted as "US on" and "US off", respectively, in figures).

Although different machining operations supported by ultrasonic vibration, for example, ultrasonic turning, drilling and milling, appear to have much in common, there are still large differences in the deformation processes in machined materials for these applications. An experimental analysis of ultrasonic drilling and milling is further complicated by the cutting tool being shielded by the workpiece, thus making direct optical observation of the process nearly impossible. This research will concentrate on the study of the ultrasonically assisted turning (UAT) process, described in detail in following sections.
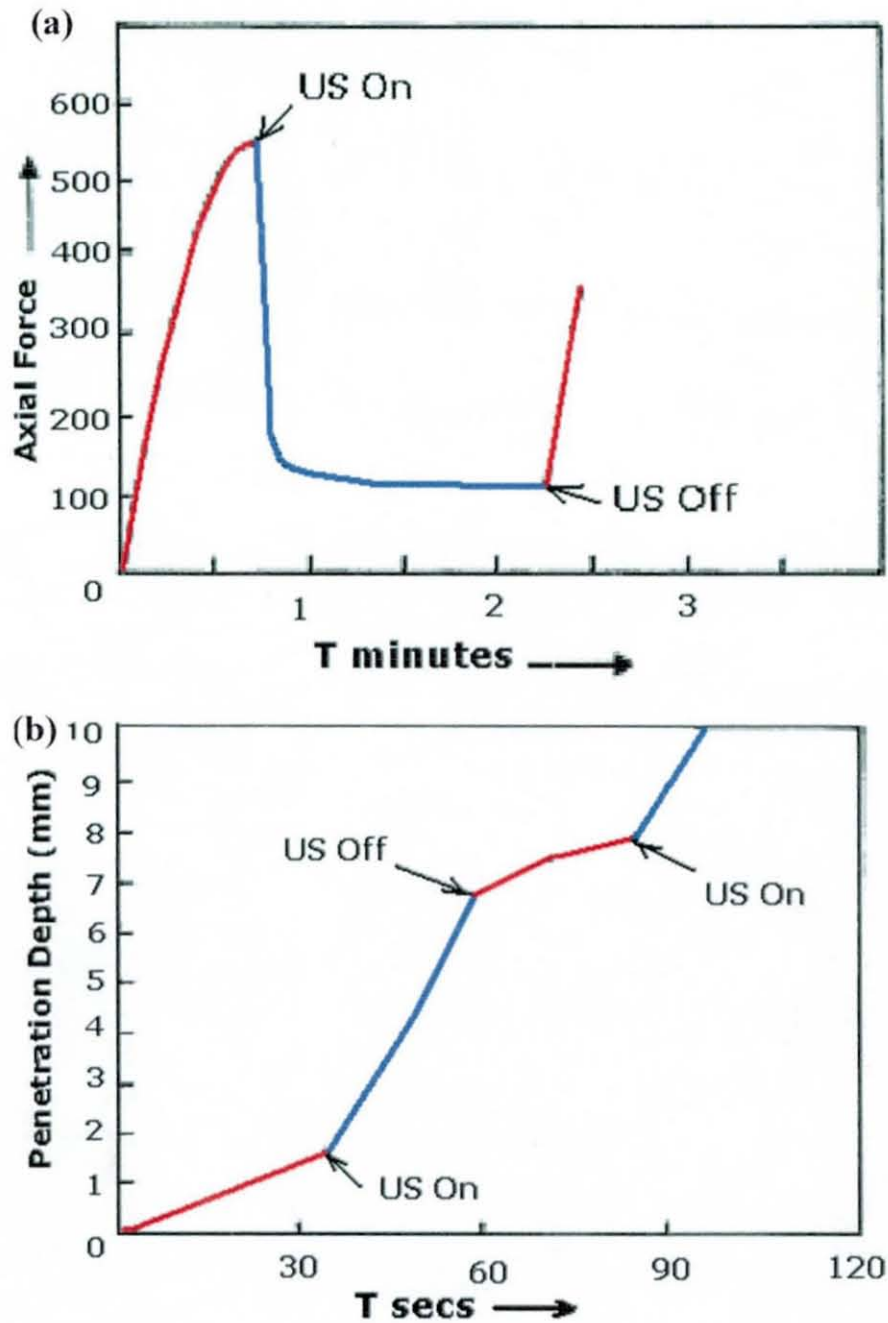
Figure 4.2 Effect of ultrasonic assistance on drilling: (a) a reduction in the cutting force, and (b) an increase in the penetration speed

4.2 Ultrasonically assisted turning

4.2.1 Vibration specification

There are three independent principal directions in which ultrasonic vibration can be imposed during the turning process: the feed direction, the tangential direction (or

the direction of cutting velocity) and the radial direction (Figure 4.3). Vibration in the tangential direction is the most widespread due to the relative ease of implementation, whereas vibration in the feed direction either has a limited run when turning with a commercial ultrasonic transducer or requires a specially designed transducer. Vibration in the radial direction usually results in the deterioration of the surface finish. All our experiments and numerical simulations study vibration in the tangential direction, and thus the description below is limited to this kind of vibration.
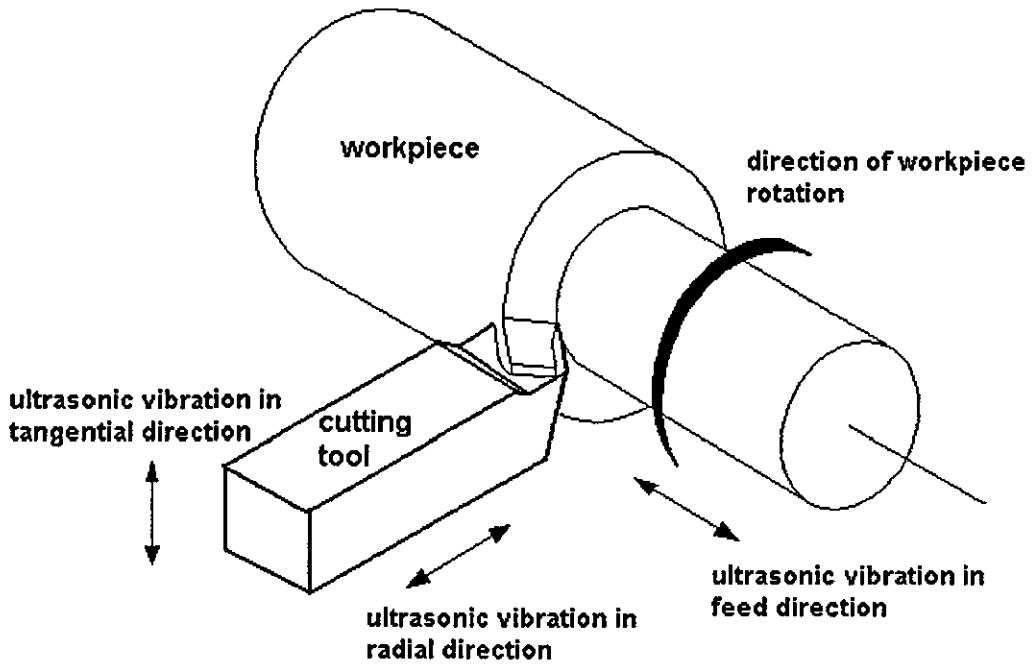
Figure 4.3 Principal vibration directions during ultrasonically assisted turning (from [1])

Consider vibrations in the direction of the cutting velocity (tangential direction). Figure 4.4 shows relative movement of the specimen and cutting tool in this case. The plane of the figure is normal to the cutting edge of a tool, and the axis Y is aligned along the axis of the rotating workpiece.

The periodic movement of the cutting tool can be approximated by the following relation:

$$u^0(t) = a \cos \omega t, \qquad (4.1)$$

where a is the amplitude of vibration, ω is the angular frequency (expressed in rad/s).

The speed of the cutter equals

$$\dot{u}^0(t) = -a\omega \sin \omega t = -2\pi a f \sin \omega t ,$$ (4.2)

where f is the frequency of vibration in Hz.
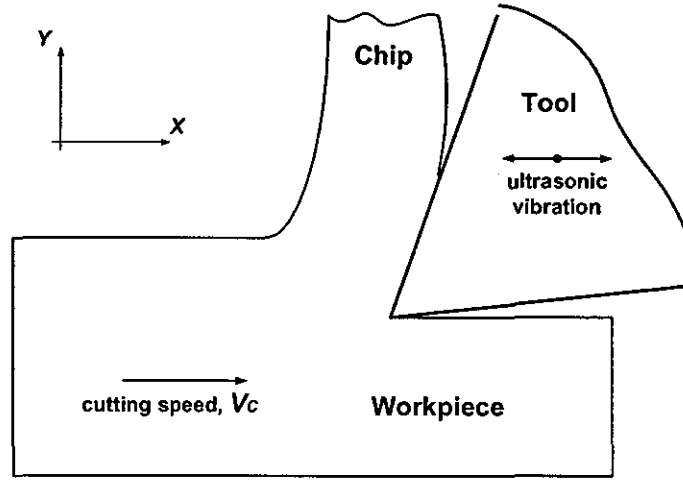
Figure 4.4 Relative movement of the workpiece and cutting tool

When ultrasonic vibration is applied, the nature of the interaction between the cutting tip and workpiece changes: instead of the usual CT continuous contact, it becomes an intermittent one. This means that the cutting tool fully separates from the chip at each cycle of ultrasonic vibration, while it remains in contact with the workpiece surface. The intermittent cutting conditions at UAT take place provided that the velocity of the vibrating tool exceeds the cutting speed:

$$v_t = 2\pi a f > V_C = \pi n D ,$$ (4.3)

where V_C is the cutting speed, n is the rotational speed, D is the diameter of the workpiece, v_t is referred to as the critical cutting speed for a given frequency.

Calculations show that for $f \approx 20 kHz$, $2a \approx 30 \mu m$ (standard parameters of cutting in our experiments) the cutting tip velocity does not exceed 120 m/min. Moreover, reduction of tip vibration velocity also occurs during the cutting process due to the cutting tool–workpiece interaction (Skelton, 1969), so the upper limit on cutting speed is further reduced (investigation of loaded vibration amplitude is given

below in Section 4.2.4). Hence, efficient UAT with vibration applied in the tangential direction is subject to the condition

$$v_t = kV_C, \quad k > 1, \tag{4.4}$$

which can be achieved only for low diameter workpieces or low rotational speeds. For example, n is limited to 150 rev/min for $D = 50$ mm and $k = 5$.

4.2.2 UAT apparatus

A typical arrangement for applying ultrasonic vibration to the cutting tool is shown schematically in Figure 4.5. The main elements of the UAT system are: (i) a high frequency generator, (ii) a transducer, which utilises the piezoelectric or magnetostrictive effect, (iii) a concentrator, which is shaped to amplify the vibration output of the transducer, (iv) a tool holder and (v) a tool. These parts of the ultrasonic vibration system are specified below.
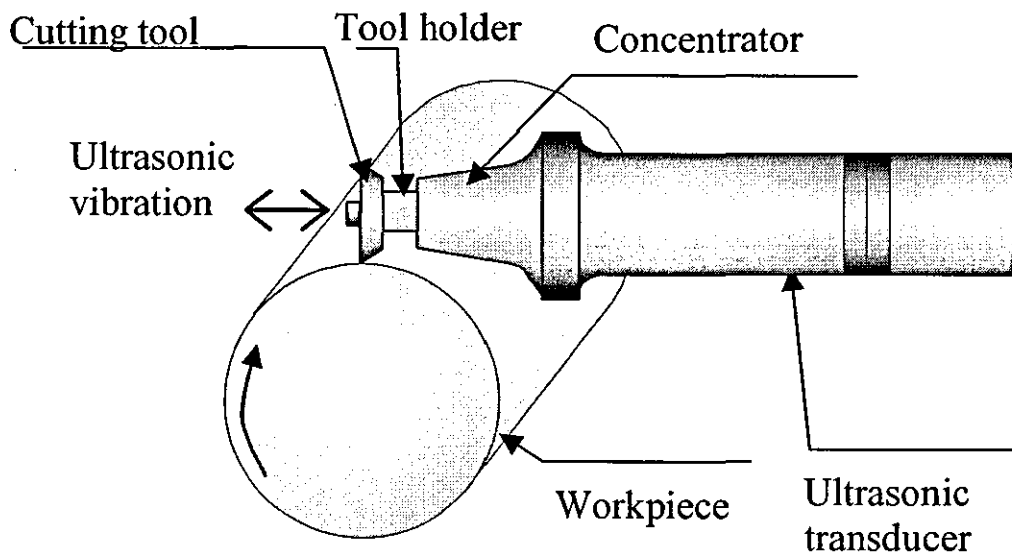

Figure 4.5 A schematic diagram of the UAT apparatus

Transducers

By definition, a transducer converts energy from one form to another. Transducers used in ultrasonic machining convert electrical energy into mechanical motion, and they are based on piezoelectric or magnetostrictive principles. The amplitude of

vibration depends on the length of the transducer and the strength of the material used, the practical limit being approximately 40 µm.

The work of magnetostrictive transducers is based on the phenomenon that magnetised ferromagnetic materials (e.g. nickel and nickel alloys) expand. Application of an alternating current to coils surrounding the material (Figure 4.6) causes vibration at the applied frequency. The magnetic material is laminated to reduce eddy current losses, but the energy conversion efficiency is only 20 to 35 percent; consequently, water cooling is required to remove waste heat from the transducer [3].
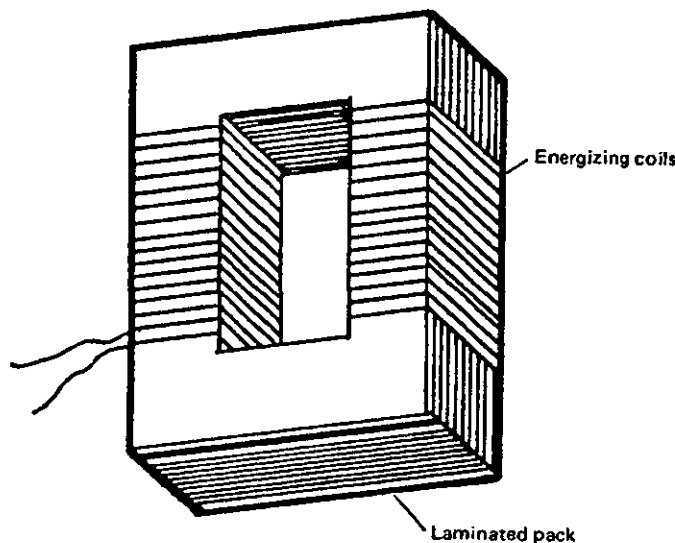
Figure 4.6 Magnetostrictive ultrasonic transducers (from [3])

Another physical phenomenon that can be used for the design of an ultrasonic transducer is piezoelectricity. Certain crystals, such as quartz, undergo small dimensional changes when subjected to a changing electrical current. Application of an alternating voltage to such a crystal causes vibration; its amplitude is greatest at the resonant frequency of the crystal. For resonance, the length of the crystal must be equal to half the wavelength of sound in the crystal. Polycrystalline ceramics, such as barium titanate, are also used as transducers; they have a sandwich construction and lengths of 75 to 100 mm. A typical transducer (Figure 4.7) consists of a stack of ceramic disks, sandwiched between a high-density base and a lower-density block of the material, which forms the radiating face of the transducer. The action of the transducer is based on the fact that, from momentum conservation, the velocity and

amplitude of vibration are high in a lower density material. Such transducers are capable of converting electrical energy into vibrational energy at 96 percent efficiency and, consequently, do not require cooling [3].
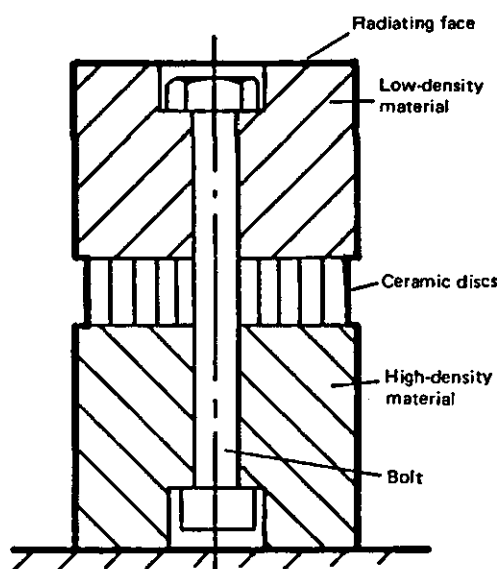
Figure 4.7 Piezoelectric ultrasonic transducers (from [3])

Concentrator and tool holder

The purpose of the concentrator in ultrasonic machining is to increase the vibration amplitude. The concentrator's length is a multiple to half the wavelength of sound in the concentrator's material. The reduction in the cross-sectional area causes amplification of vibration, which increases in inverse proportion to the ratio between the areas of the opposite ends of the concentrator. A sevenfold increase in vibration amplitude may be obtained with a suitably shaped concentrator. An additional increase in amplitude at the tool face can occur in the tool holder, and final amplitudes at the tool face can range from some micrometers to 0.1 mm [3].

4.2.3 Literature review: historical development of UAT

First attempts to employ the ultrasonic power for cutting hard and brittle materials were made independently by Russian [18, 83] and Japanese [84, 85] researchers.

Kumabe [85] in his monograph summarised some of research results up to the time of his publication and also presented the outcomes of his own experiments on the application of ultrasonic vibrations for various conventional material removal

processes. Kumabe emphasized that in CT the cutting tool is not immovable, but oscillates with a variable frequency and amplitude, thus the idea of UAT is to change the character of the workpiece – tool interaction and to regularise these oscillations. Kumabe stated that high-speed photography and study of the chip shape and surface finish are useful tools for the analysis of UAT. He also studied the advantages and shortcomings of using various vibration directions that are summarised in Table 4.1.

Table 4.1 Advantages and shortcomings of various vibration directions ([85])

Processes	Features
Vibration in the feed direction	Advantages: • Sharpening of the cutting edge (introduction of ultrasonic vibration leads to an increase in an equivalent rake angle) • Sinusoidal oscillations of the cutting force • Reduction in average cutting forces Shortcomings: • Increase in friction at the cutting tip leading to temperature growth and subsequent fast wear of the cutting edge (use of ceramic cutting edges is recommended)
Vibration in the radial direction	Advantages: • Extremely thin chip can be obtained ($t_1 \approx t_2$) • Sinusoidal oscillations of the cutting force • Reduction in average cutting forces Shortcomings: • Fast wear at the rake and clearance faces of the cutting tool
Vibration in the tangential direction	Advantages: • Reduction in average cutting forces • High precision of the machining operation • Low temperature of cutting (nearly room temperature) • Abolition of the built-up edge • Improvement in the lubricating and cooling action of lubricants • Increased wear and corrosion resistance of the machined workpieces • Increase in the tool life

It is important to note that all his experiments were carried out with magnetostrictive vibrators specially designed for the generation of ultrasonic vibration. Kumabe also suggested that vibration of the cutting tool in the direction of the cutting velocity might give better results than the application of the vibration in the radial and feed directions. Kumabe pointed out that the actual cutting speed V_c should be less than the critical cutting speed v_t (see Eq. 4.4), otherwise the mechanism of cutting is similar to the conventional. He observed the following general advantages of ultrasonic machining: a rise in machining accuracy due to the increase in the dynamic rigidity of the system, a reduction in cutting temperature, the abolition of the built-up edge, the elimination of burrs (in drilling), a smooth formation of chips, an improvement in the lubrication and cooling properties of lubricants, and an increase in the tool life and in wear and corrosion resistance of machined surfaces [85].

Kumabe discussed residual stresses in the machined layer of carbon steel. For CT, these residual stresses were tensile and the hardened layer is quite deep, whereas for UAT the residual stresses were small and compressive, and the hardened layer is narrow. The author argued that deformation processes in CT engulf a big area in the surface layer when cutting, whereas the deformation is concentrated in the vicinity of the cutting edge in UAT. Consequently, the metallographic structure of the surface layers in UAT remains nearly the same as in the bulk of the material, and such workpieces possess higher wear and corrosion resistance.

Markov [18, 86] in his book "Ultrasonic machining of intractable materials" described the use of ultrasonic vibration in turning of heat-resistant alloys. Vibration in his experiments was applied in the radial–tangential direction with the help of a magnetostrictive transducer. The effects of ultrasonic vibration on the tool life, surface finish, deformation of the cut layer were studied in the book. It was found that during turning the reaction force in the workpiece greatly reduced the amplitude of ultrasonic vibration of the tool and slightly lowered its frequency. Calibration of the tool vibration amplitude was performed under various static loads and used to predict amplitude levels during actual cutting.

The relation between the tool life and ultrasonic vibration was studied in turning heat-resistant alloy grade E1437B for cutting conditions $v = 10$ m/min, $s = 0.2$ mm/rev, $d = 0.5$ mm and high-speed tools. It was found that high intensity vibrations

($2a > 13\,\mu$m, according to Markov's classification) shortened tool life, whereas low intensity vibrations ($2a < 8$ μm) lengthened it. Low amplitude axial vibrations were also found to lengthen the tool life. On the other hand, ultrasonic vibration shortened the tool life for hard alloy tips (grade VK8). The author suggested that the influence of the ultrasonic vibration on the cutting process was very complex. An increase/decrease in the tool life depended on the intensity (amplitude) of the vibration as well as on the material of the cutting tip, thus depending on the tool material and amplitude of vibration, its effect on the tool life could be either beneficial or harmful.

Shortening of the tool life for high amplitudes of vibration, according to Markov, could be linked to changes in frictional conditions between the working surface of the tool and workpiece, due to additional frictional forces introduced, which vary harmonically. The heat generated by ultrasonic vibration flows not only into the workpiece but also into the tool, leading to high temperatures in the contact area between the chip and tool; this causes premature wear of the cutting edge. Markov suggested that a use of hard-alloy cutters was unjustified for UAT due to their fast fatigue fracture and recommended using of tools with high fatigue resistance.

Markov also noted that ultrasonic vibration affected the character of the machined surface. In the absence of ultrasonic vibration, the surface of the heat-resistant alloy was reported lustrous, whereas with vibration, especially of a high amplitude, it became matt. Roughness measurements showed that radial ultrasonic vibration had a negligible or negative effect on the surface finish compared to that of CT for one design of the ultrasonic system, whereas the roughness was improved up to three times for another design. Tangential vibration had also improved the surface finish in turning grade St3 steel. It was noted that the greatest effect on the surface finish was achieved at low cutting speeds. The change in the rake angle from -40° to +30° had a very little effect on the cutting force, chip properties and surface finish.

An important change in deformation processes in the cutting region was noticed. Microhardness of the chips and machined layer was considerably lower compared to that of CT, and the deformed surface layer was much thinner.

In cutting steel, grade 45, with amplitude of vibration $2a = 30\,\mu$m, the cutting forces were reported to reduce by a factor of 5 of 6 for slow cutting speeds ($v = 1\text{-}5$ m/min). The measured temperature was higher for UAT and explained by dissipation

of the ultrasonic energy. However, temperature measurements were very approximate, as tool-workpiece thermocouple method was used, and, in Markov's opinion [18], this method was not sufficiently reliable under conditions of dynamic load, when the cutting tool periodically moves away from the chip. The tests also showed that increasing the amplitude of ultrasonic vibration extended the range of cutting speeds for which ultrasonic vibration had a noticeable effect on the cutting process. Increasing the area of the cut layer reduced the effect of ultrasonic vibration.

Markov emphasized that rigidity of the system comprising a machine tool, fitting, cutting tool and workpiece is important: if the rigidity of this system is not high enough, the tool life is shortened and the overall advantage of UAT may be small.

Finally, Markov [86] suggested that the influence of ultrasonic vibration on the turning process could be explained by the thermal effects, which cause softening and micro-melting of the deformed material in the contact points with the cutting tip and considerably affect the nature of frictional processes at the tool–chip interface.

In more recent publications [87, 88], Markov pointed out that there is a clearly expressed optimum amplitude of ultrasonic vibration, which depends on the tool dimensions as well as physico-mechanical and thermophysical properties of workpiece and tool materials. Markov argued that ultrasonic vibration with amplitude exceeding the threshold value significantly accelerates the motion of dislocations and the formation of new dislocations, thus allowing plastic deformation at a lower load. An optimum vibration amplitude that provides the biggest friction reduction was reported to be experimentally found. Ultrasonic vibration with very high amplitude was considered less effective due to extensive heat generation and increase in the tool wear. Markov stated that in order to obtain a stable positive result in UAT an automatic control system is required. He also proposed a method of controlling UAT based on the resonant character of the amplitude-frequency characteristic and its dependence on the radial force.

The works of Kumabe [85] and Markov [18, 86] are among few reports containing attempts to describe the physics of the ultrasonic process. The majority of the following references include mostly results of the practical implementation of ultrasonic technology with some observations of the attendant phenomena.

Weber et al. (1984) [89] utilised ultrasonic vibration in the direction of the cutting velocity in turning a C60 steel and a X5CrNiMo 18.11 alloy, which are difficult to machine. A decrease in the surface roughness of the workpiece was obtained for

cutting speeds less than 90 m/min. It was also observed that formation of the built-up edge, which was very typical for that range of cutting velocities in CT, did not occur in the case of the ultrasonically assisted procedure. Experiments with a VKB-MgO glass ceramic machined with a K10/GH 012 carbide tool led them to the conclusion that the tool life can be increased up to 20 times by superimposing tangential-radial ultrasonic vibrations on the tool movement. In these experiments the tool vibrated with frequency of about 20 kHz both in tangential (a = 8-12 μm) and radial (a = 2-6 μm) directions.

Moriwaki, Shamoto and their co-workers [90-92] explored ultra-precision diamond turning of glass and SU303Se -JIS stainless steel by applying ultrasonic vibration (f = 40 kHz, a = 3 μm) to a single crystal diamond tool in the direction of cutting velocity. They argued that an increase in vibration frequency reduced generation of vibration marks at the finished surface. These experiments were carried out on an ultraprecision turning machine and a mirror-like finish of the stainless steel with a surface roughness of 0.026 μm was obtained. An increased tool life was reported due to a reduction in both crater and flank wear.

An UAT process with vibration in the tangential direction and the cutting speed exceeding the critical level was discussed in [93]. Although the tool did not separate from the chip in this case, such a technique demonstrated several advantages, namely, a decrease in the size of a buildup edge and chatter reduction. An application of UAT for cutting carbon-fibre reinforced aluminum matrix composites was studied in [94]. A fivefold increase in a diamond-tool life was reported together with fourfold improvement in the surface finish.

The ultrasonic vibration system used by Kim and Lee (1996) [95] in their experiments on the cutting of Carbon-Fibre Reinforced Plastics (CFRP) had frequency of 19.5 kHz and amplitude of 15 μm (vibration was applied in the tangential direction). It was concluded that ultrasonic cutting produced a better surface than CT when the cutting speed was less than the critical one. The surface quality of CFRP was not connected with the depth of cut but was closely related to the cutting speed and feed rate. They also observed that the cutting force generated during UAT was less than that generated in CT for all cutting tool/workpiece combinations.

Further studies carried out by Kim and Choi [96] on brittle optical plastics (CR-39) investigated the possibility of utilising UAT ($f = 20$ kHz, $a = 26.4$ μm) as a substitute for micro-surface machining which is used in manufacturing of precision optical parts. It was confirmed that surfaces in the ductile mode of cutting were obtained for depths of cut less than 2.7 μm. It was also found that an ultrasonically excited tool contributed to an improvement in both waviness and roughness of the machined surface. Moreover, they [97] tested the UAT with the same parameters at the extremely low cutting velocity for precision machining of CR-39. They concluded that such cutting velocities maximised the non-contact interval between the chip and the tool face and induced aerodynamic lubrication, which greatly reduced the friction force and the instantaneous cutting force. They obtained chips generated by ductile-mode cutting when the cutting speed was as low as 1/40 of the critical speed of the UAT system.

The attempt to prevent chipping of the cutting tool when cutting hardened steels was taken in [98]. The authors considered that the chipping was caused by a collision between the flank face of a cutting tool and the machined surface of a workpiece due to a vibrational movement of the tool. Countermeasures proposed were increasing of the rigidity and stability of the ultrasonic system and inclination of the vibrational direction by 10-30° from the principal cutting direction toward the workpiece.

The influence of tool-nose radius on chatter vibration, cutting forces and the surface roughness when cutting Inconel 600 was investigated in [99] both analytically, with a dynamics model, and experimentally. It was concluded that larger tool-nose radii could be used in UAT without causing chatter vibration compared to those in CT. The optimum tool-nose radius was found for studied cutting conditions, and larger radii were reported to increase surface roughness and cutting forces.

In a recent work by Klocke and Rübenach [100], application of UAT ($f = 40$ kHz, $a = 3.5 \div 5$ μm) using synthetic single crystal diamond tools to manufacture ultraprecision optical parts was further studied. It was reported that the level of the resultant surface quality of workpieces when machined with hard-metal tools was limited by the polycrystalline structure of the cutting edges, thus a use of diamond tools was necessary. Vibration was applied in the direction of the cut (i.e. tangential direction). The main focus of this study was an extension of the tool life with

assistance of ultrasonic vibration: extremely fast tool wear was reported for CT, and was extended by 4-5 times when using an ultrasonic-assisted process for machining C60 steel. The ductile mode in glass machining was investigated, and material removal was found to be dependent on the vibration amplitude. For required high levels or accuracy (R_a < 10 nm and peak-to-valley value of roundness less than 1 µm), the roughness of machined surface was largely dependent of the size of material's particles/grains (the depth of cut and feed rate were in the micron range). However, the tool wear in machining steel materials was determined primarily by the hardness of the material and to a much lesser degree by its microstructure. Finally, it was stated that a delay in industrial application of UAT was connected with unsatisfactory explanation for effects of decisive factors on the UAT process and with absence of an UAT system suitable for industrial use.

In another recent publication, Sharman et al. [2] studied machining of gamma titanium aluminides (γ-TiAl) – which are considerably more difficult to machine than conventional titanium alloys – with UAT ($f \approx 20$ kHz, unloaded $2a = 30$ µm). A high-circle fatigue load imposed on the tool edge due to ultrasonic vibration was reported to cause micro-cracking and chipping and significantly reduced tool life (typically 5 –15 minutes), compared to CT, for used uncoated tungsten carbide (WC) insert tools (grade K10). The nature of tool failure was unpredictable and catastrophic. However, an increase in the cutting speed generally resulted in longer tool lives when UAT; that was explained by the reduced non-contact time producing lower fatigue stresses on the tool edge. An increase in the depth of cut reduced the tool life due to the higher load imposed on the cutting edge. The cutting forces were 12% of those in CT for similar cutting parameters. This was explained by the reduced material strength in the shear zone due to formation of cracks caused by an impact motion of the tool. A change in the rake angle did not have any noticeable effect on the cutting force. Additionally, superposition of ultrasonic vibration led to a transition from partly discontinuous needle chips to long helical chips (~ 25 mm). An explanation of the latter phenomenon was that a reduction in cutting forces prevented unstable crack propagation from the tool tip.

Many authors reported that UAT resulted in improved workpiece finish, reduction in average cutting forces or elimination of the build-up edge [101-104]. In contrast to

the most of above-listed studies, the papers that follow contain some theoretical explanations and modelling of the ultrasonic cutting process.

A rheological model of ultrasonic vibrational cutting proposed by Astashev [105] and subsequent experiments confirmed a noticeable reduction in the cutting force for ultrasonic cutting with vibration in the tangential direction (f = 20 kHz, a = 10 μm). It was also established that the cutting force reduction was less at higher cutting speeds and, with a cutting speed exceeding a certain level ($v > a\omega$, where ω is the angular frequency), vibration did not affect the cutting force. The resistance forces were considered to be caused by plastic deformation of the layer being cut off and by frictional forces acting on the working faces of the cutting tool.

These experimental results have been explained theoretically by Astashev and Babitsky [106] within the framework of rheological models. Reduction in the cutting force caused by superimposition of ultrasonic vibration was derived for the elasto-plastic material model. It was concluded that the vibrating process transforms and reduces the friction force due to the effect of dynamic fluidisation of dry friction. Dynamic characteristics of transformed machining processes were obtained, including the dependence of reduced cutting forces on the material and vibration parameters. Dynamics of an ultrasonic cutting machine under technological load was investigated and the nonlinear amplitude response of the vibrating tool in the process of cutting was obtained. The autoresonant control system keeping the resonant conditions of excitation under variable technological loads was constructed.

Babitsky et al. [1] have developed an elaborated autoresonant system, maintaining a constant level of vibration provided by the transducer and therefore improving the accuracy of ultrasonic machining. Vibration in the feed direction was studied. It was pointed out that application of ultrasonic vibration along the feed direction enables overcoming the restriction on the level of rotational speeds, which is of great importance for industrial UAT requiring high levels of productivity.

The majority of research on UAT has been focused on technological aspects of the problem, such as frequencies, amplitudes and directions of vibration, depths of cut, feed rates, and cutting velocities. However, there is little information available on mechanical processes involved in ultrasonic cutting. Studies by Babitsky and co-workers [1, 105-107] are the starting points of the current research. Although uniaxial rheological models [106] cannot predict stress and strain fields at the workpiece − cutting tool interface, they allow dynamical characteristics of the

ultrasonic vibration system, such as the amplitude response of the tool under technological load, to be obtained.

4.2.4 Autoresonant UAT prototype and results of turning tests at Loughborough University

An original test rig for ultrasonically assisted turning with autoresonant control system has been designed by Nonlinear Dynamics Group, Wolfson School of Mechanical and Manufacturing Engineering, Loughborough University, UK. This test rig uses a standard lathe with a specially designed ultrasonic attachment, and it effectively serves as a prototype of the machine tool for UAT. For the case of simplicity, it will be referred to as a "prototype" below. This prototype is used in all our experiments for turning Ni- and Ti-base superalloys, widely used in the aerospace industry, as well as for many other materials. The complete description of the experimental arrangement is given in [1, 107].

Figure 4.8 shows a schematic diagram of the UAT system. A workpiece is clamped in the three-jaw chuck of a *Harrison 300* universal lathe and rotates
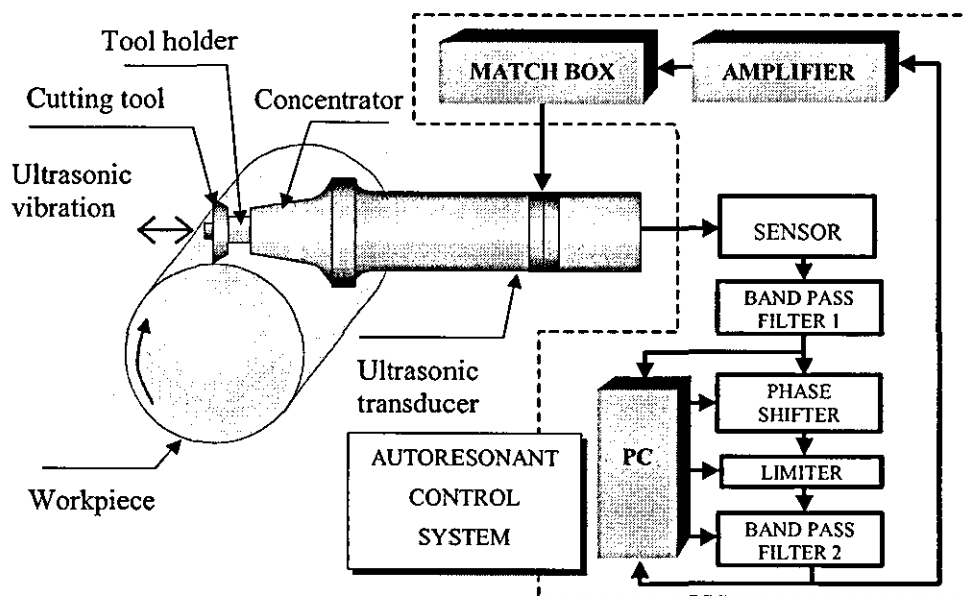

Figure 4.8 Autoresonant control system for the UAT prototype

with a constant speed. A commercial ultrasonic piezoelectric transducer (unloaded resonant frequency $f \approx 20$ kHz) is used to provide vibration. The transducer is fixed

in the cross slide of the lathe by a specially designed tool post attachment, so that it is possible to apply ultrasonic vibration either in the direction tangential to the surface of the workpiece (parallel to the Z-axis, Figure 4.9), or in the feed direction, i.e. along the axis of the workpiece (X-axis, Figure 4.9).
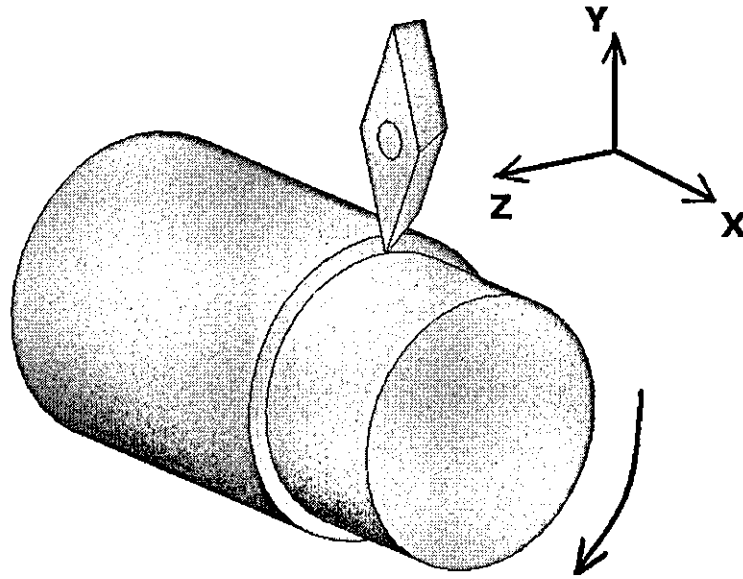
Figure 4.9 Relative position of the workpiece and cutting tool

Experimental setups for UAT with vibration in the tangential and feed direction are demonstrated in Figure 4.10a and Figure 4.10b, respectively. The vibration amplitude is intensified in the concentrator and transmitted to the tool holder at the thin end of the concentrator. Resultant vibration of the cutting tip fixed in the tool holder usually reaches 15 μm (i.e. 30 μm peak-to-peak) at a frequency of about 20 kHz; however, the exact vibration amplitude depends on the tool holder shape and material (titanium, aluminium or stainless steel) and ranged in different tests from 20 to 40 μm peak-to-peak. This level of vibration is comparable with levels used by other researchers [97, 108, 109]. Vibration is measured by a laser vibrometer (*Polytec OFV-3001*), and the signal is processed by a phase shifter, limiter and band pass filter to form an autoresonant control [110]. These devices are controlled by a

Figure 4.10 Experimental setup for UAT with vibration in tangential (a) and feed (b) directions

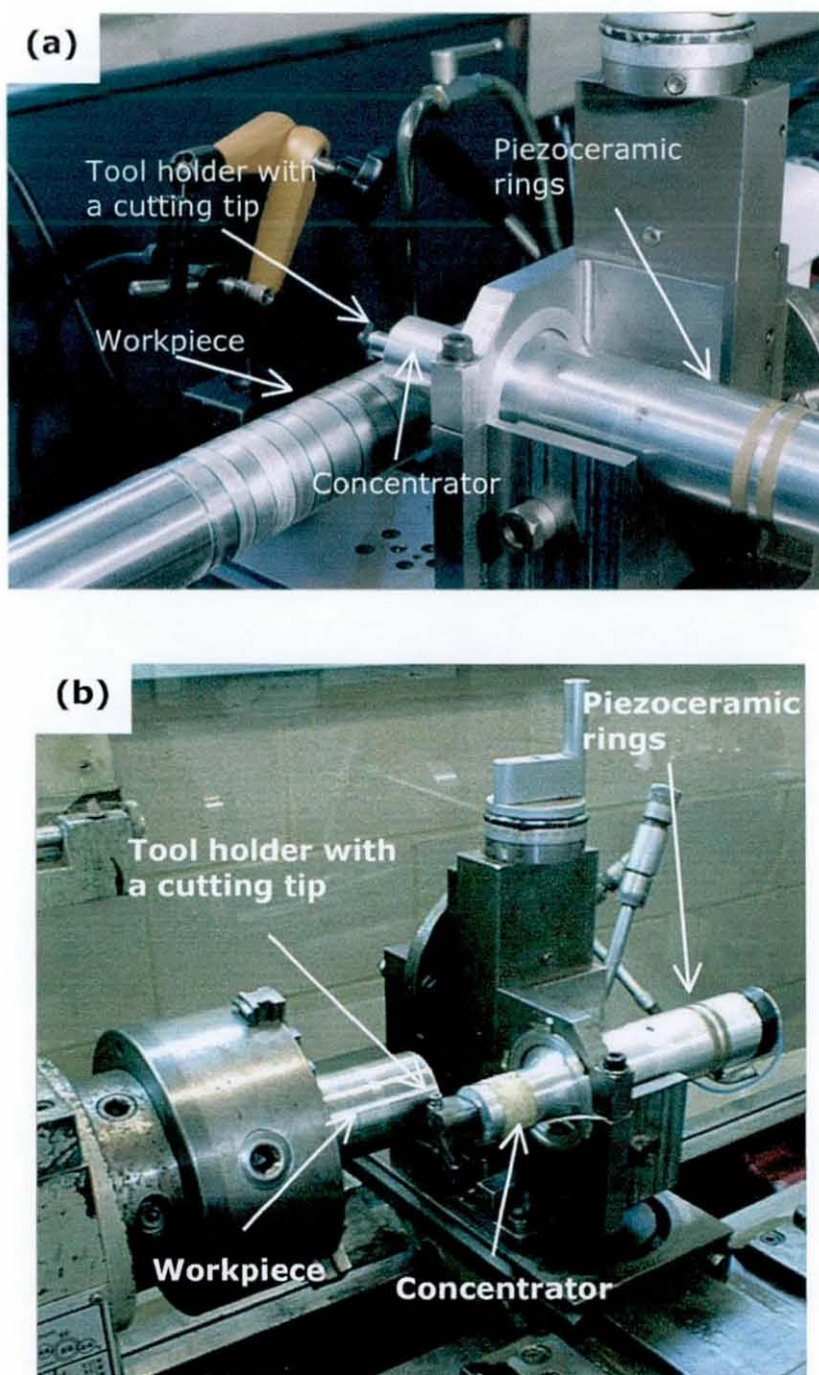PC, and signal parameters are monitored and recorded. The control signal from the computer is amplified using a 250 W MOSFET amplifier and fed into the transducer via a passive matching unit (matchbox). This causes the transducer to vibrate at its

resonant frequency. The autoresonant system maintains a self-sustained resonant mode of vibration of this cutting system during the dynamic changes of the load.

A range of turning tests has been conducted to compare the use of UAT and CT for machining aviation materials. The detailed description of these tests can be found in [1], however, the main results are outlined here. Among the materials used in tests is Inconel 718 – a high-grade heat-resistant Ni-based superalloy widely used in the aerospace industry (described in detail in Chapter 5). This material is very abrasive and causes tool blunting and high cutting temperatures when machined conventionally.

The surface quality obtained by turning is one of the crucial factors in metal cutting and is extremely sensitive to any changes in the machining process. The surface finish of specimens is compared in terms of average roughness measurement (R_a) and measurement of roundness (the peak-to-valley measure), using the *Taylor Hobson – Talysurf 4* surface measurement instrument. The following cutting parameters are used to machine tested specimens: depth of cut $d = 0.8$ mm, feed rate $s = 0.05$ mm/rev, and cutting speed $v = 17$ m/min. The same parameters are used for both UAT and CT, with superimposed ultrasonic vibration in the feed direction applied in the case of UAT.

Figure 4.11a shows representative axial profiles of the machined surface of the Inconel 718. It is obvious that magnitudes of R_a are reduced by nearly 50 % for specimens machined with UAT. Furthermore, the regularity of the surface profile is greatly improved, as the surface becomes smoother in the axial direction. A considerable improvement is also obtained for roundness of machined workpieces (Figure 4.11b): a peak-to-valley value of roundness measures 4.20 μm for CT, whereas it attains only 1.89 μm for UAT. Hence, the roundness is improved by 55% when ultrasonic vibration is superimposed upon the movement of the cutting tool. It is worth noticing that similar results have been obtained by other researchers [97, 109] utilising vibration in the tangential direction. Additionally, a squealing noise from the tool – workpiece contact during machining of mild steel disappears when ultrasonic vibration is applied.

Apparently, the reason for these improvements is the change of the character of the cutting process, which is transformed into the one with multiple-impact high-frequency interaction between the cutting tool and chip due to applied ultrasonic

vibration. This leads to changes in material deformation processes and friction forces, and increase in the dynamic stiffness of the lathe-tool-workpiece system [85, 106] due to vibration frequency levels considerably exceeding its natural frequency.
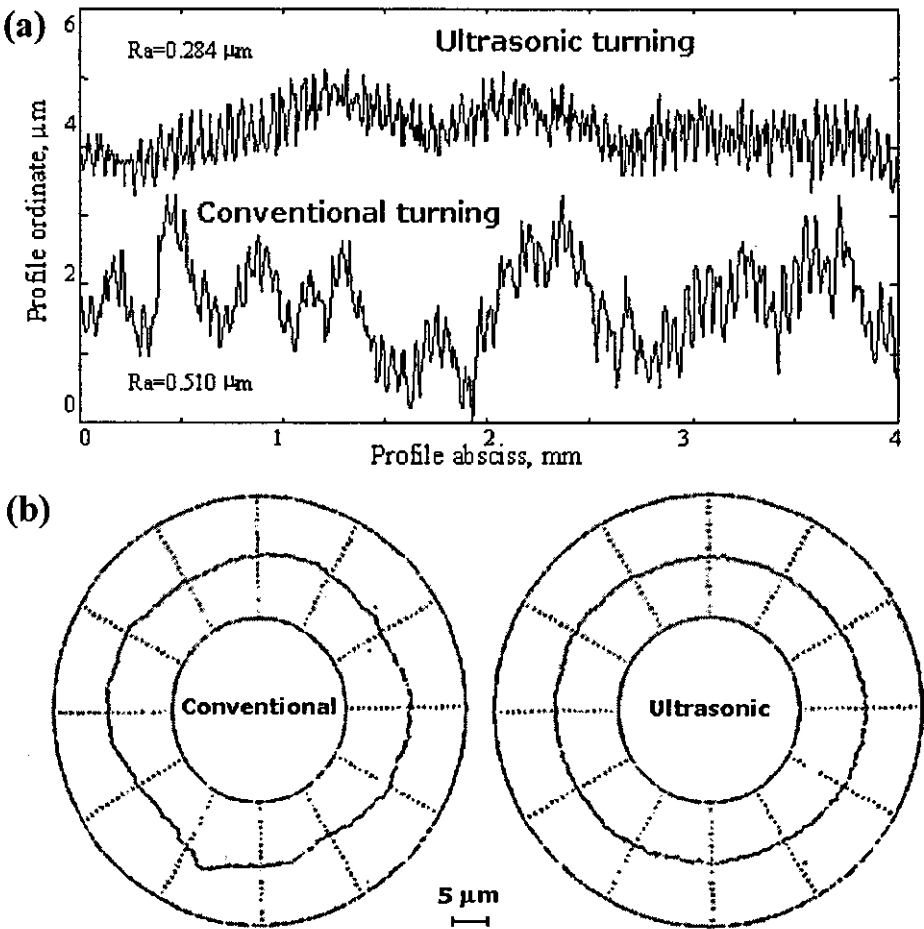
Figure 4.11 Surface quality of Inconel 718 specimens machined with UAT and CT: axial surface profiles (a), roundness profiles (b). Cutting parameters: $d = 0.8$ mm, $s = 0.05$ mm/rev, $v = 17$ m/min (from [111])

According to observations of other researchers [112], the amplitude of ultrasonic vibration drops when load is applied to the cutting tip. Hence, it had to be checked how the amplitude of ultrasonic vibration changes during turning as compared to the no-load operation. Unfortunately, the laser vibrometer could not be used to measure the amplitude at turning, since low-frequency high-amplitude vibration, inherent in

the cutting process on the lathe, hinders such measurements. Therefore, another method is used: the static load equal to the cutting force is applied to the cutting tip; such load did not interfere with normal operation of laser vibrometer. The magnitude of the applied force is up to 200 N corresponding to the force levels found in the experiment (Section 5.6). The amplitude of ultrasonic vibration in no-load operation is 40 µm (peak-to-peak). After application of the maximum static force, the amplitude reduced to 32-36 µm, thus the reduction in the vibration amplitude is less than 20% for the highest applied force. Extrapolating this result on the vibration amplitudes in the majority of the previous UAT tests with the vibration levels in no-load operation being 30 µm, it can be concluded that the amplitude of ultrasonic vibration is about 24-27 µm (peak-to-peak), which corresponds to the amplitude of 26 µm used in the FE simulations in Chapter 7.

Chapter 5 Experimental work

5.1 Introduction

Existing experimental studies of UAT could be roughly divided into three main groups: (i) optimisation of technological parameters of UAT, such as directions, frequencies and amplitudes of vibration, (ii) analyses of cutting forces as compared to those of CT, and (iii) surface profile measurements (see, for example [1, 97, 100]).

However, thermomechanics of UAT has not yet been experimentally investigated. There are a number of important issues to be explored: (i) dynamics of chip separation and deformation processes in the material during cutting, (ii) the influence of UAT on material's surface structure, and (iii) heat generation during UAT. All these features should be compared with those of CT. Therefore, the present experimental investigation aims at the comparative analysis of structural and thermal processes during CT and UAT and their influence on machined materials. Microstructural analysis, nanoindentation tests, high-speed filming of the tool–chip interaction zone, and infrared thermography are employed in order to carry out a full-scale study of these processes. Cutting forces are also investigated in order to confirm the multifold reduction in cutting forces in UAT as compared to CT. All these experiments have been performed on the UAT test rig designed at Loughborough University [1].

5.2 Material in turning tests: Inconel 718

Presently, the main area of application for the ultrasonic-supported technology is machining of intractable materials used in the aerospace industry. UAT is considered as one of the promising and competitive technologies for machining high-strength aerospace alloys, namely Ni-, Ti- and Cr- based superalloys. Each of these materials requires separate investigation in order to carry out full-scale research of its machinability with CT/UAT, as well as of the influence of machining on the material microstructure and surface finish. Each material also requires careful formulation of

a material model for numerical simulations. This research is concentrated on one of the modern aerospace alloys: Inconel 718.

Inconel 718 is vacuum-melted, precipitation-hardened nickel-chromium alloy. It also contains significant amounts of iron, niobium and molybdenum along with lesser amounts of aluminium and titanium. Inconel 718 combines corrosion resistance and high strength with outstanding weldability including resistance to postweld cracking. It is also readily formable. The alloy exhibits excellent resistance to creep and stress rupture at temperatures to about 700°C and thus known as heat-resistant. The chemical composition of Inconel 718 is shown in Table 5.1.

Table 5.1 Chemical composition of Inconel 718

Ni	Cr	Fe	Mo	Nb	Ti	C
53.7 %	18.93	17.2 %	3 %	5.26 %	0.97 %	0.026 %
Si	Mn	Al	Cu	Ta	B	P
0.12 %	0.09 %	0.5 %	0.5 %	0.3%	0.004 %	0.007 %
S	Ca	Mg	Mn	Se	Ag	Pb
<0.001 %	<0.001 %	<0.001 %	4.1 ppm	<3 ppm	<0.1 ppm	0.1 ppm

While this material has been used for decades, there is little data available on its thermomechanical behaviour at high strain rates and elevated temperatures. Some parameters, for example, contact heat conduction and friction properties that are important for machining or superelasticity at high temperatures, are not freely available. The data shown below is a result of timely literature survey and includes all known to the author sources of relevant information to date.

5.2.1 Applications of Inconel 718

Inconel 718 has a broad range of applications, such as in space shuttle and aircraft engines, nuclear reactors and pumps. In the following paragraphs examples of the typical Inconel 718 applications will be given.

Inconel 718 is used as a structural material for a variety of components in the main engine of the space shuttle and accounts for more than half of the total weight of this engine. The components of the space shuttle main engine are subjected to

start-up and shutdown transient loads and occasional overloads in addition to high-frequency vibratory loads from routine operation.

Inconel 718 is also used in the blade containment system of the turbine aircraft engines. This system should possess significant strength to withstand high-velocity impact and prevent blade penetration in case of blade failure during engine operation. Due to a high level of temperatures in turbines, it is necessary to utilise heat-resistant alloys, and Inconel 718 is an ideal candidate for this application, as it possesses excellent properties at elevated temperatures. Ballistic penetration behaviour of Inconel 718 is studied in [113].

5.2.2 Properties of Inconel 718

Inconel 718 is classified as difficult-to-machine material due to its high shear strength, strong work hardening, highly abrasive carbide particles in the microstructure causing premature wear of the cutting edges, tendency to form built-up edge and low thermal conductivity leading to very high temperatures in the cutting region. Inconel 718 also tends to maintain its high strength at high temperatures generated during machining. This material is therefore extremely difficult to machine with existing technologies and cutting edges. Machinability of Inconel 718 is studied in many papers, for example [114, 115].

The type of heat treatment affects the deformation behaviour of Inconel 718 that changes dramatically its stress – strain relation. In [116] large differences in static properties were found between the annealed and aged material. Annealed Inconel 718 possesses lower strength and hardness, as well as greater elongation before failure than the aged material (Figure 5.1).

Behaviour of materials at very high strain rates that can be attained in machining (up to 10^5 s^{-1} for cutting and vibration parameters considered in the current work) is usually analysed by means of impact tests. Among these are standard Charpy impact tests, split Hopkinson bar tests [113], as well as ballistic penetration tests with gas gun facility [116, 117]. Strain-rate sensitivity of Inconel 718 was also studied with a high-speed tensile tester [118], however, maximum values of strain rate obtained in their experiment were low: $\dot{\varepsilon} \leq 500$ 1/s.
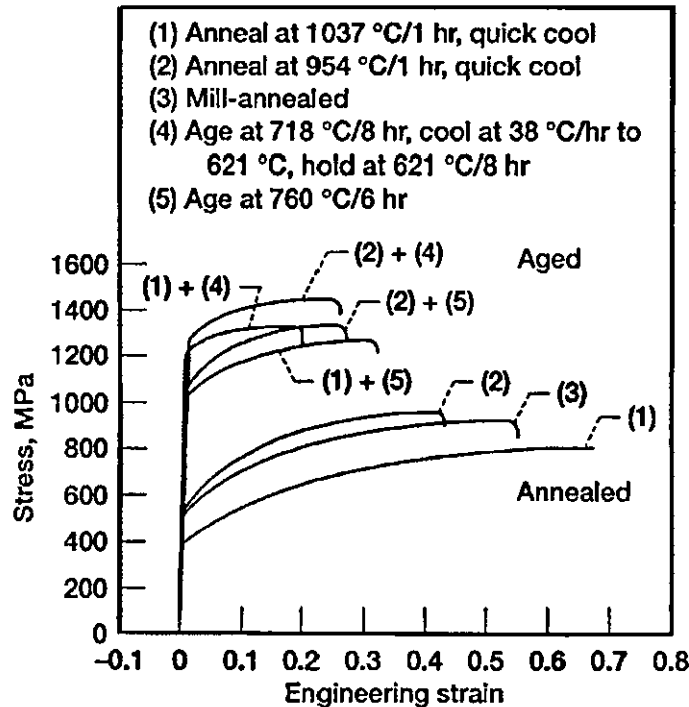
Figure 5.1 Effect of heat treatment on the room temperature tensile behaviour of In-718 specimens (from [116])

Traditional experimental techniques allow to observe deformation behaviour of the materials at strain rates below 10^4 s^{-1}. For numerical simulations of machining this data is usually extrapolated. Figure 5.2 shows the deformation behaviour of Inconel 718 at high strain rates as obtained from experiments at split Hopkinson bar [113]. Stresses reached for the annealed material are about 1000 MPa lower than those for the aged material in the quasistatic mode, but this difference decreases at high strain rates due to the greater hardening of the annealed material. For the annealed material, stresses increase monotonely at all studied strain rates. On the contrary, for the aged material, complex non-monotone behaviour at high strain rates is observed, however, still with a general trend of higher stresses obtained at higher strain rates.

Analysis of the failure mechanisms of Inconel 718 at high strain rates with impact gas gun [116] showed failure resulted from the adiabatic shear. Localized bands of large shear deformations were found both in annealed and aged materials, and microhardness measurements indicated an increase in hardness in these bands compared to the surrounding material. These shear bands were more localized in the

aged material than in the annealed material. Additionally, overall deformation before failure was considerably higher for the annealed specimens.
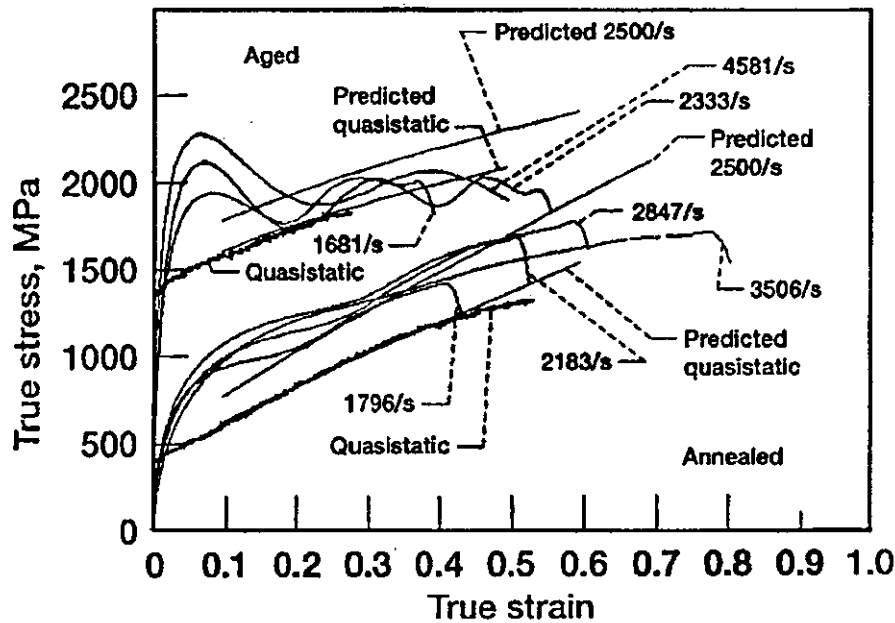
Figure 5.2 Effect of heat treatment on the room temperature quasi-static and high-strain-rate compression behaviour of Inconel 718. Also shown is the stress-strain behaviour of two material conditions predicted by the Johnson –Cook model for the quasi-static case and for a strain rate of 2500 s⁻¹ (from [116]).
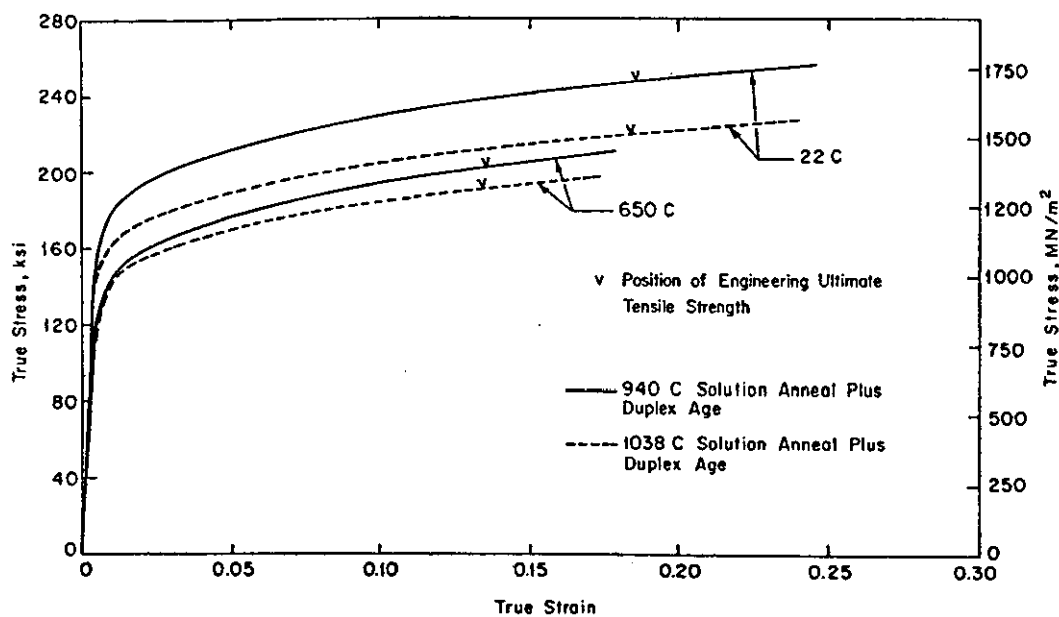

Figure 5.3 Average true stress – true strain curves of Inconel 718 at 22 and 650°C for two heat treatments (from Brinkman and Korth [119])

For Inconel 718 being a heat-resistant alloy, its deformation behaviour does not significantly change within the range 22°C – 650°C (Figure 5.3). The decrease in the yield strength of Inconel 718 for 650°C compared to the room temperature is only about 20 %. It is worth mentioning that the temperatures obtained during machining tests with CT and UAT (see section 5.5) are well within this range.

Elevated temperature also influences such parameters of the material thermomechanical behaviour as thermal conductivity (K), specific heat (C) and the coefficient of thermal expansion α (Figure 5.4).
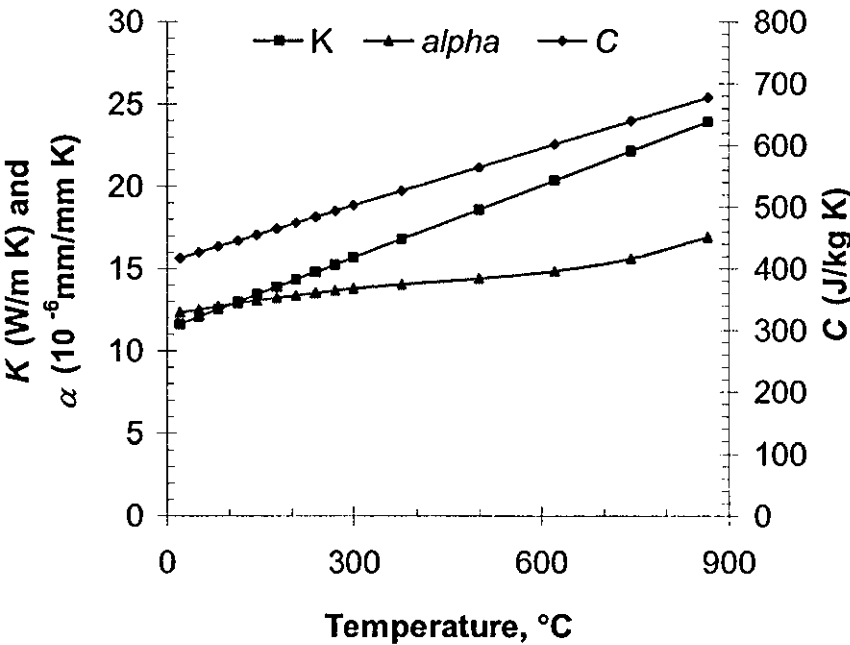
Figure 5.4 Evolution of thermal conductivity (K), specific heat (C) and coefficient of thermal expansion (α) with temperature (from [120])

5.2.3 Material models for Inconel 718

There is a range of material models employed for Inconel 718 in different works. The Ramberg–Osgood equation is capable of describing the non-linear hardening behaviour of Inconel 718:

$$\sigma_Y = \sigma_{Y_0} + K_Y \left(\varepsilon^p\right)^{1/M_Y},$$ (5.1)

where ε^p is plastic strain, σ_{Y_0} is initial yield stress, K_Y is a coefficient of plastic resistance, M_Y is the hardening exponent. Parameters σ_{Y_0}, K_Y, M_Y are determined from hardening test results. According to the model, the plastic flow occurs if

$\sigma = \sigma_Y$. (For more information about the Ramberg-Osgood equation see [121]). The deformation behaviour of annealed Inconel 718 in terms of the Ramberg-Osgood relation is described in [120] and used in the numerical model of cutting described in Chapter 6. However, the Ramberg-Osgood law does not have a direct account for the effect of high strain rates and elevated temperatures on the material deformation behaviour.

Another model for Inconel 718 – the Cowper–Symonds equation – is suggested in [117]. This model describes Inconel 718 behaviour under dynamic loads and high strain rate. The Cowper-Symonds equation correlates the yield strength σ_Y to the dynamic yield strength σ_d, obtained from dynamic experiments with high strain rates:

$$\frac{\sigma_d}{\sigma_Y} = 1 + \left(\frac{\dot{\varepsilon}}{D}\right)^{1/p},$$

where D and p are material constants. The following values for these material constants were found in [117]: $D = 20$ s^{-1} and $p = 15$. However, strain rates considered were only some 500 s^{-1} and heat treatment of Inconel 718, though crucial for material behaviour, was not mentioned.

Another model for Inconel 718 was proposed in [116]. The Johnson-Cook model accounts for strain-rate sensitivity as well as for high temperature softening of the material, and it is frequently used for numerical (FE) modelling of material behaviour during machining:

$$\sigma_Y = \left[A + B\left(\varepsilon^p\right)^n\right]\left[1 + C\ln\left(\frac{\dot{\varepsilon}^p}{\dot{\varepsilon}_0}\right)\right]\left[1 - T^{*m}\right], \tag{5.2}$$

where $T^* = \left(T - T_\infty\right)/\left(T_{melt} - T_\infty\right)$, $\dot{\varepsilon}_p$ is a plastic strain rate, $\dot{\varepsilon}_0$ is an initial strain rate equal to unity, T_∞ and T_{melt} are room and melting temperatures, respectively. Material parameters A, B, n and C are derived from dynamic tests. In [116] the following values of these coefficients were found: for the annealed material $A = 400$ MPa, $B = 1798$ MPa, $n = 0.9143$ and $C = 0.0312$, and for the aged material $A = 1350$ MPa, $B = 1139$ MPa, $n = 0.6522$ and $C = 0.0134$. The latter values are used in the numerical model of UAT and CT for the aged Inconel 718 described in Chapter 7.

In the case of machining, the yield strength should be restricted with ultimate tensile strength (UTS) of Inconel 718, so that to prevent anomalously high stress levels at high values of plastic strains of the order of unity, reached in machining.

Analytical models of rate-dependent flow surface for Inconel 718 are also discussed in [122].

5.3 High-speed photography experiments

Direct observations of the tool–workpiece interaction zone can be very useful to gain an understanding of mechanics of the ultrasonic cutting process. They can give invaluable insight into the process of chip formation and its specific features, such as chip separation mechanisms, shear angle, affected material layers, as well as chip cracking and breakage processes. Additional information can be obtained on cutting tool vibrations, either superimposed intentionally, as in case of UAT, or forced and self-excited, inherent in CT (chatter).

But such observations are very difficult to implement due to a number of reasons. A small area of the process region (about several millimetres squared) and low vibration amplitudes require high-quality telescopic lenses or special microscopic attachments to be used to zoom into the cutting tool – workpiece interaction region with a decent magnification. An intrinsic limitation is the opaque nature of machined metallic materials and used cutting edges, preventing observation of the most interesting processes at the cutter – workpiece interface.

Another difficulty is that the high speed of the processes determined by cutting and vibration speeds necessitates the use of high-speed photography equipment. In the particular case of UAT, with high-frequency ultrasonic vibration of some 20 kHz, the desirable rate of continuous filming should be about 100,000 frames/sec, in order to study a single cycle of ultrasonic vibration. This, in turn, requires extremely short exposure times and fast data storage devices. This limitation has been recently eliminated with the invention of modern high-speed (HS) photography equipment.

5.3.1 Instrumentation

Figure 5.5 shows an experimental arrangement for ultrasonic turning filming. A high-speed digital camera (Kodak Ektapro HS Motion Analyzer, model 4540) is employed for the experiments. The camera is mounted on a lathe by a specially designed holder, enabling the distance to the filmed region to be adjusted. The tool-workpiece interaction zone is illuminated by a laser beam supplied form a high-power laser (3 kW copper vapour laser LS-20-50, manufactured by Oxford Lasers Ltd., Abingdon, UK). The laser pulses are synchronized with the camera operation so that to provide maximum illumination during each subsequent frame exposure time: as exposure time is extremely short, it requires bright illumination of the object. The laser beam is delivered into the cutting region via the fibre-optic cable. The limited size of the camera memory allows storing only short fragments of about 1 s of the
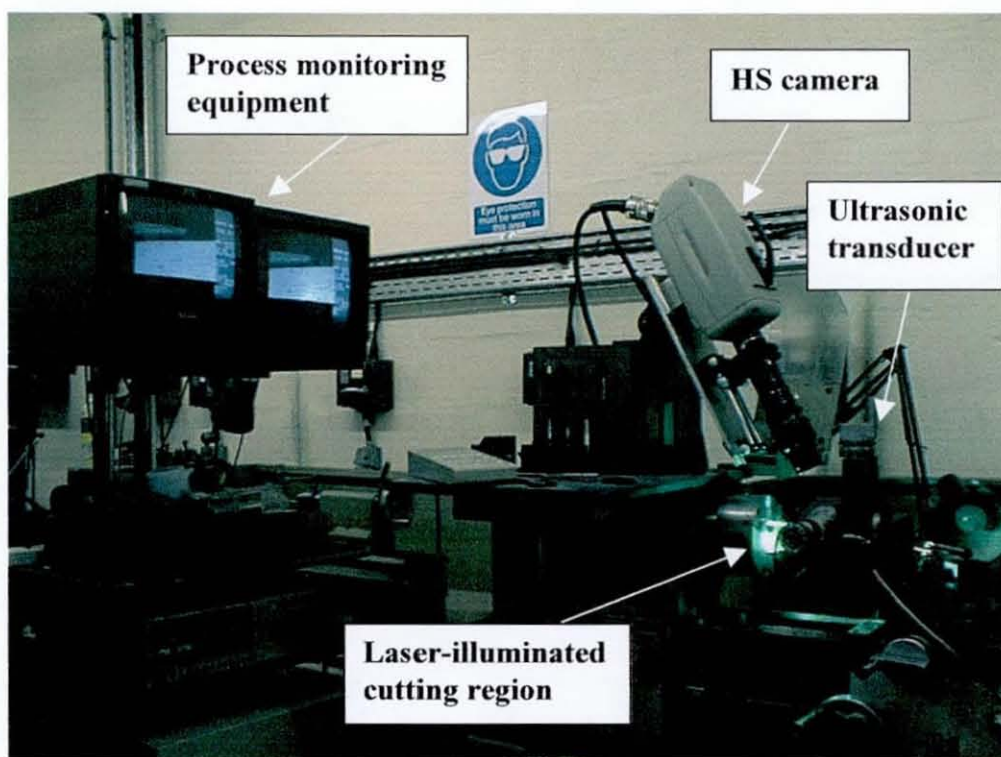
Figure 5.5 An experimental arrangement for the HS photography experiments

cutting process. Although the maximal filming rate of the Kodak 4540 camera is 40,000 frames/sec, the speeds more than 27,000 frames/s cannot be used, due to the limitation caused by required synchronisation with the laser. The data stored in the camera memory is then transferred either onto the VCR tape or the hard drive of a PC. The recorded image is also observed in real time on the TV monitors. A high-

pressure air supply is used to eliminate the metal dust and to remove the chip from the field of view, in order to get a clearer image of the otherwise obscure cutting region. The ultrasonic vibration turning system used for the experiment is specified in Section 4.2.4. The amplitude of ultrasonic vibration is monitored with the laser vibrometer in the no-load operation mode, and then adjusted with a phase-shifter of the autoresonant control system.

5.3.2 Experimental procedure

The filming is conducted for two materials: PMMA (polymethylmethacrylate) and mild steel. PMMA is chosen because it is transparent and easy to machine. It is believed that experiments on PMMA can give the necessary experience for the subsequent experimentation on metallic materials. Round bars 50 mm in diameter are employed for these experiments.

The next stage are experiments on mild steel. This material is also quite easy to machine, although it possesses metal properties, e.g. it is opaque and has polycrystalline grain structure. Round bars of diameter 35 mm are utilised for the experiments.

PMMA filming

The position of the high-speed digital camera for this part of the experiment is shown in Figure 5.5 and Figure 5.7. The observation is done in direction I in Figure 5.6. The dimensions of the region being filmed are about 1.2×2.0 mm. Ultrasonic vibration ($f \approx 20$ kHz, $a \approx 20-30 \, \mu m$) is applied in the tangential direction. The depth of cut and feed rate are kept constant throughout the experiments: $d = 1$ mm, $s = 0.16$ mm/rev.

The first cut is made with rotational speed $n= 40$ rev/min by CT with the filming speed of 9000 frames/sec. Thereupon, the ultrasonic vibration is switched on, and several cuts are made under the same cutting conditions with UAT. The filming speed is 9000, 18000 and 27000 frames/sec. In practice, 18,000 and 27,000 frames/s speeds do not provide much additional information compared to 9,000 frames/sec. Most of the tests are therefore performed with the latter speed. Although the frequency of vibration is in this case higher than the frequency of filming, the vibration of the cutter is still visible in the images due to the stroboscopic effect. In

order to observe dynamics of the cutting process within a single cycle of ultrasonic vibration, a significantly higher filming speed (about 10^5 frames/s) and better lenses allowing higher magnification are required.

The same procedure is repeated for rotational speeds of 125, 260 and 540 rev/min with the filming speed of 9000 frames/sec and for different lighting conditions.
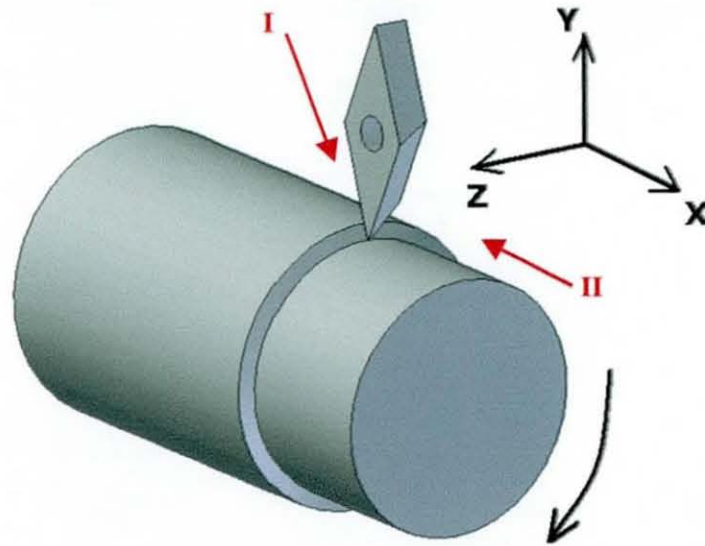
Figure 5.6 Relative position of the workpiece and cutting tool

Mild steel filming

The experiments are continued on mild steel. The size of the image region is 1.5×2.5 mm, and the same cutting conditions are kept: $d=1$ mm, $s= 0.16$ mm/rev, $n=40$ rev/min. UAT and CT cutting processes are recorded with the filming speed of 9000 frames/sec.

Thereafter, the camera is repositioned and mounted on the cross-slide of the lathe (the observation is performed in direction II in Figure 5.6). In such a position, the camera is moving together with the cross-slide during the run, staying all the time focused on the cutter – workpiece interaction region. No refocusing of the camera for each run is needed for such mounting, and it is therefore considerably more convenient than fixing the camera to the immovable parts of the lathe as described above. The filming is conducted at a different angle – nearly along the axis of the workpiece (Figure 5.8) – but for the same cutting parameters and for both UAT and CT cutting procedures.
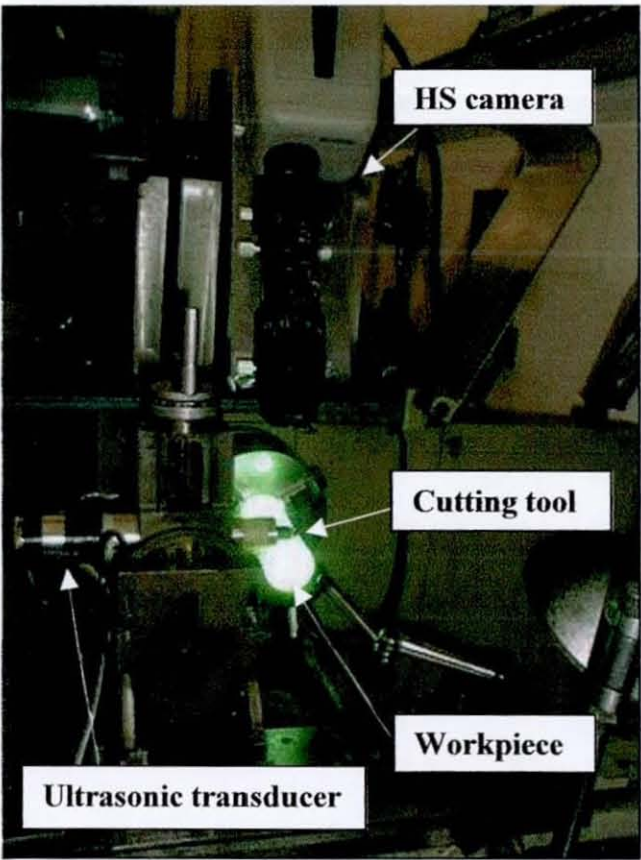
Figure 5.7 A close-up view of the camera–workpiece region

Figure 5.8 Position of the camera in the second part of the experiment

5.3.3 Experimental results and discussion

Significant differences between ultrasonic and conventional processes are observed for both PMMA and mild steel. The distinction is most noticeable for low rotational speed (n= 40 rev/min) and becomes less evident for higher cutting speeds, practically undetectable for rotational speeds greater than n= 125 rev/min. This fact can be explained by exceeding the critical cutting speed limit (see Section 4.2.1) for higher rotation speeds.

The differences between ultrasonic and conventional technology are observed in the chip separation process, namely the size and shape of the process zone, and the type of chip produced. Figure 5.9a and Figure 5.9b show frames from HS video recording of CT and UAT, respectively. The cutting tool, interacting with the

Figure 5.9 Frames from high-speed filming of CT (a) and UAT (b) of mild steel

workpiece and separating a chip, is seen in the images; continuous video recording can also allow estimating the visible size of the process zone, unclear in single frames. For studied cutting conditions, the chip, formed in CT of mild steel, is segmented. Periodic formation of material segments is seen in the fragments of HS video recording. The 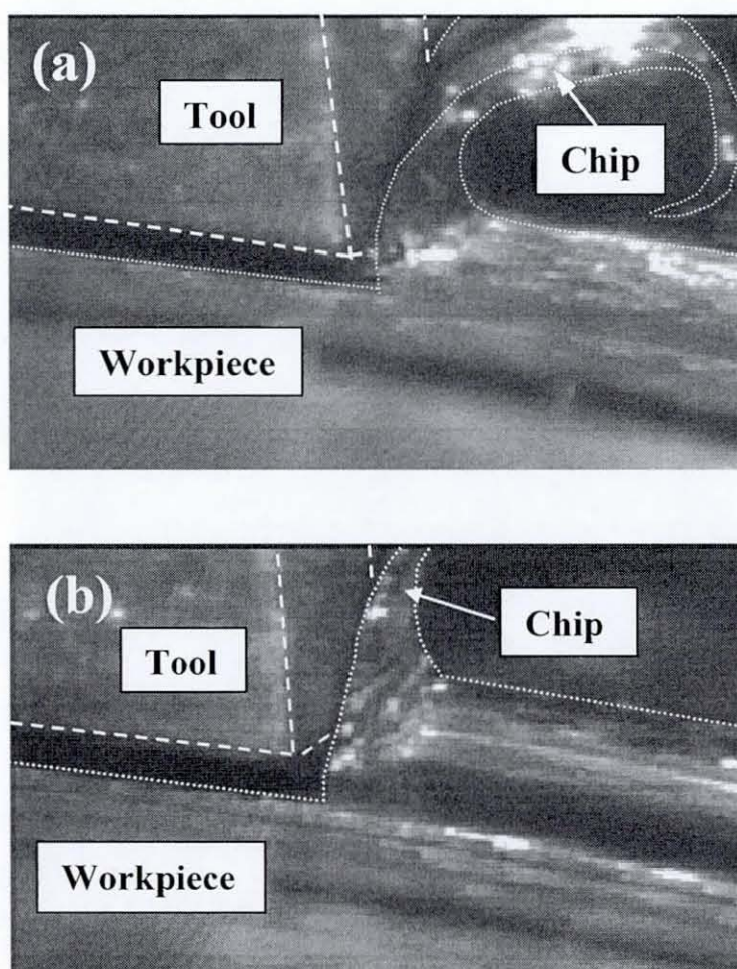segments are torn from the workpiece and slip along the shear plane, with visible levels of deformation between segments being considerably higher than within each segment. Such step-like chip formation is particularly well observed from the first position of the camera (Figure 5.5) allowing material removal in the feed direction to be seen. Higher resolution images are also obtained in the HS photography tests with a different video camera (Phantom HS camera manufactured by Vision research Inc., USA). A frame from HS filming of UAT of mild steel performed with that camera is shown in Figure 5.10.
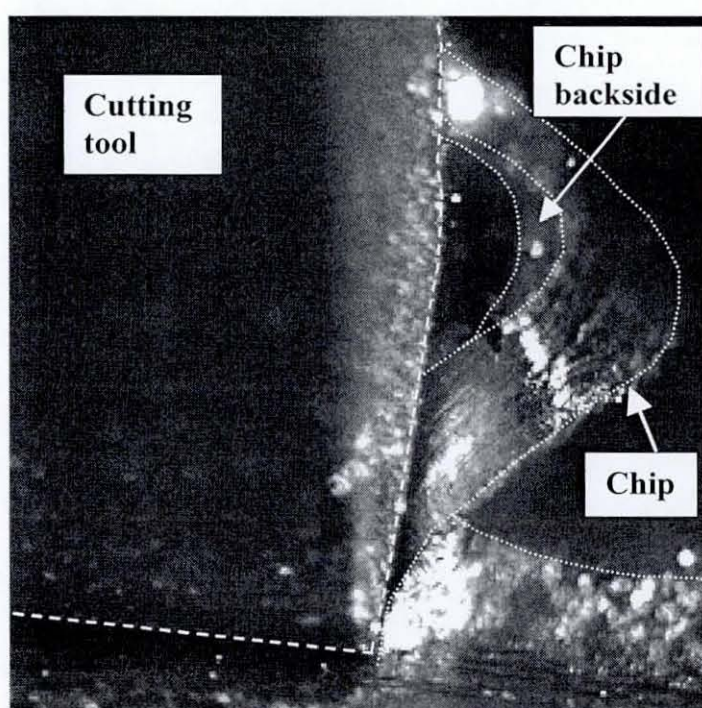
Figure 5.10 A frame from HS filming of UAT of mild steel

Switching on the ultrasonic vibration drastically changes the tool–chip interaction and the process of chip formation. There are no more segments or steps in chip formation, instead, continuous material separation in front of the cutter and slipping of the material along the shear plane with each impact of the cutting tool are observed. The process of UAT appears as the one with completely different nature of

material separation and deformation. The material, separated from a workpiece, looks as considerably more plasticized, i.e. experiencing higher levels of plastic deformation happening throughout the chip volumes. The chip formed in UAT rises nearly in the radial direction very close to the cutting tool surface in the recorded frame (Figure 5.9b), whereas the chip in CT shifts much further from the cutting tool, leading to a more curled chip. This is in good agreement with a subsequent macroscopic chip analysis, indicating the chip radius of curvature being several times greater for UAT than for CT for these cutting conditions.

Differences between two cutting techniques are also observed in shapes as well as in sizes and areas of the process zones. Figure 5.11 and Figure 5.12 show the shape of the visible process zone for CT and UAT of PMMA and mild steel respectively (as being monitored). The area of the visible process zone for UAT and its width in

Figure 5.11 Shape of process zones for CT (a) and UAT (b) of PMMA

Figure 5.12 Shape of process zones for CT (a) and UAT (b) of mild steel

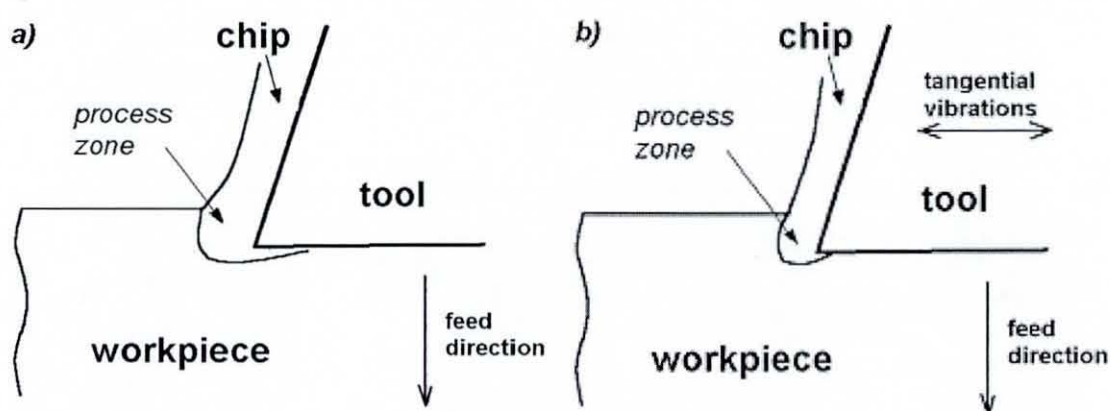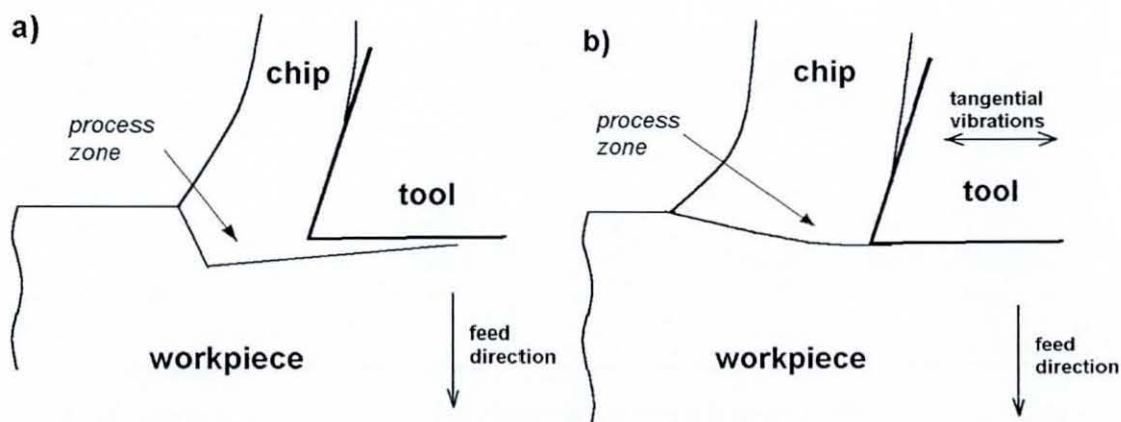the radial direction are considerably smaller than those for CT. Deformation processes for the ultrasonic process are localized in the direct vicinity of the cutting edge along the surface of the workpiece and are not observed underneath the clearance face of the tool at the newly formed surface layer, in contrast to the CT process.

5.3.4 Overview of different HS photography trials and outlook

HS photography was also attempted with a Kodak Megaplus camera (model ES.1.0), producing high quality pictures (single frames). The resolution of the images was considerably better than those of the video camera. The images were planned to take at a regular intervals during a single cycle of ultrasonic vibration, so that to have information about important changes in the chip formation and processes in the cutting zone during the cycle. The experiment required a triggering signal form the ultrasonic control system, indicating a certain moment in the cycle of vibration. The camera also needed synchronising with the laser, for the laser to illuminate the cutting region at the moments when images were being taken. The experiment, however, did not produce any usable results. The following problems arose during the trial experiment: (i) higher specification lenses needed to zoom into the small region of several millimetres in diameter, and it was not possible to focus properly with the available lenses; (ii) reflections from the surface of the Inconel 718 workpiece were too bright and necessitated either use of lenses with anti-reflective coating, special directing of the laser beam to avoid the reflections, or use of non-reflective materials.

The HS equipment develops very dynamically, and it is believed that in the nearest future some even more insightful experiments can be performed on the basis of the tests described in this section. It would be of interest to carry out the experiments with higher magnification lenses to resolve smaller details of the chip formation mechanisms. Recently, the HS cameras have become commercially available with higher filming rate of about 10^5 frames/s; such cameras would allow observation of different stages of the cycle of ultrasonic vibration, what would provide a valuable insight into the UAT cutting process. High-speed filming of Inconel 718 would also be of significant interest, in order to ensure that the main

features of the chip formation mechanism in UAT of Inconel 718 are the same as those observed in machining mild steel.

5.4 Analyses of microstructure of machined materials

5.4.1 Microscopy analyses of the surface structure

Introduction

The study of the material microstructure helps to reveal specific features of the deformational and thermal processes in the workpiece material resulted from different material treatment, namely CT and UAT, and thus allows better understanding of the micromechanics of these machining technologies. Changes in the alloy grain structure reflect material hardening and residual stresses induced to the workpiece material during the machining procedure. These changes can be observed with different optical techniques, such as light microscopy, SEM (scanning electron microscopy), TEM (transmission electron microscopy) and measured quantitatively with various indentation techniques, such as nanoindentation tests. Width and hardness of hardened surface layers are evaluated in these experiments, thus providing detailed information on the influence of machining on the surface structure of the machined material.

All experiments described in this section are conducted on solution-treated and aged Inconel 718 rods ($D = 45$ mm).

Initial experimentation

The aim of initial experiments is to investigate potential radial changes in the material's grain structure. A 20 mm-long piece is cut off from an Inconel rod (the rod was in the delivery state). The face is polished and etched, and then the grain structure is observed employing a "Nikon Optiphot" metallurgical microscope.

The results of the microscopy analysis show that the grain structure in the centre of the cross-section and at the outer edge is different (Figure 5.13). Grains found in the areas of the cross-section distant from the outer edge are some three times larger than those in the outer layer. The transition between the areas with "big" and "small" grain sizes is not gradual, but an evident boundary between the areas with different grain sizes has been found about 400 μm from the surface of the workpiece (Figure

5.14). Such a sharp transition can only be attributed to initial material shaping
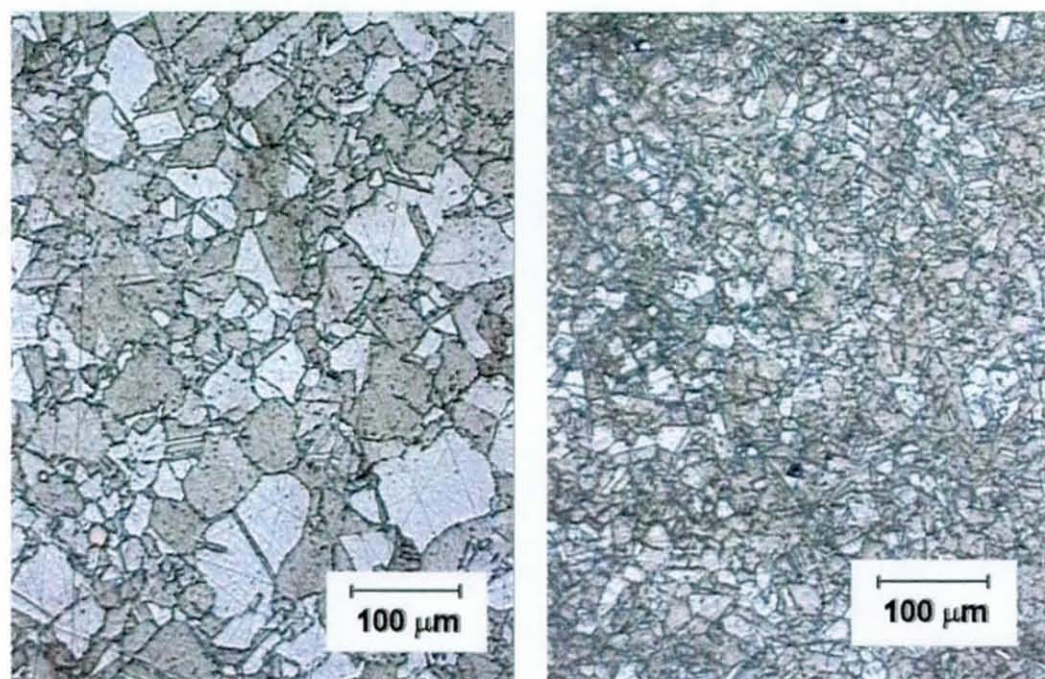

Figure 5.13 Grain structure of the Inconel 718: in the centre of the cross-section (left) and at the outer edge (right)
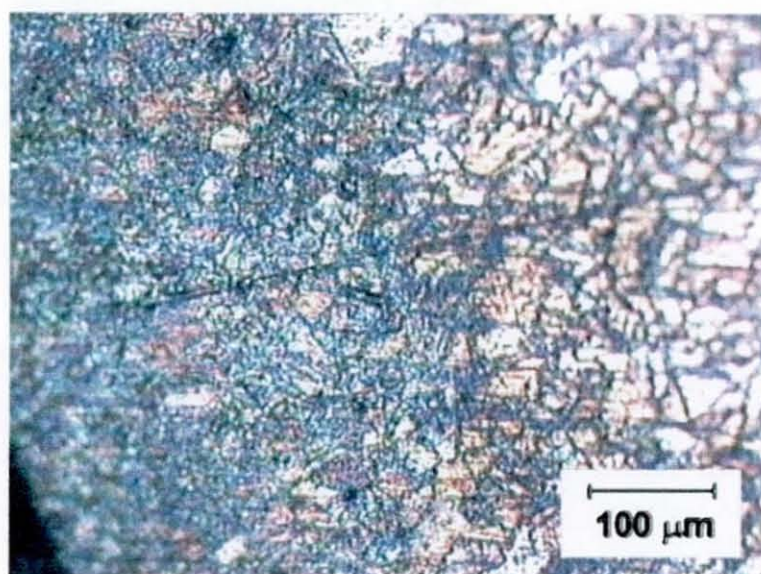

Figure 5.14 A boundary between the areas with different grain structure (Inconel 718)]

processes, namely machining of the workpieces prior to delivery. The surface layer with smaller grain size is obviously a hardened layer, i.e. the layer of the material that has been affected by thermal and deformation processes during machining.

Workpiece preparation and processing

In order to eliminate the effects of initial (manufacturing) material processing, the Inconel rod of 45 mm diameter is turned down to 33 mm by CT ($n = 160$ rev/min, $s = 0.11$ mm/rev, d=0.5 mm).

Subsequently, the workpiece is turned down to 30.5 mm diameter by CT with slow rotational speed ($n = 40$ rev/min or cutting speed $V_C = 60$ mm/s, $s = 0.03$ mm/rev, $d = 0.3$ mm) to eliminate the potential influence of high temperature during the previous turning operation on the material surface structure.

Finally, two cuts with very small depth of cut are performed ($n = 40$ rev/min, $s = 0.03$ mm/rev, $d = 0.1$ mm). The first cut is made with the application of ultrasonic vibration in the tangential direction, and as soon as the tool had traversed 10 mm the vibration is switched off thus allowing the second cut to proceed under the same cutting conditions but without ultrasonic vibrations. The procedure is repeated five times, each time starting at the same place. Hence, surfaces machined ultrasonically and conventionally under the same cutting conditions for 0.5 mm ($5*d = 0.5$ mm) of depth are obtained.

The pieces of the workpiece containing surfaces obtained by CT and UAT are cut off, and then potted into plastic (epoxy resin). The faces of the specimens are polished and etched (utilising stainless-steel etchant ASTM E407). After that the mould next to the machined surface is broken in order to obtain a better picture of the surface layers otherwise obscured by the products of etching coming out of the gap between the plastic and metal. Having made these preparations, surface layers of Inconel 718 directly under the machined surface are observed with SEM and light microscopy.

Experimental results and discussion

Figure 5.15a and Figure 5.15b show characteristic micrographs of the surface layers of Inconel 718 machined with CT and UAT respectively as obtained from light microscopy tests. A hardened surface layer (measuring some 15 μm thick) is

observed for the surface machined with UAT. This deformation zone manifests in the alignment of the grain boundaries along the preferred direction. This direction indicates orientation of residual deformation. It is worth noticing that we consider here that precipitates (here seen as black lines in micrographs) are aligned along grain boundaries.
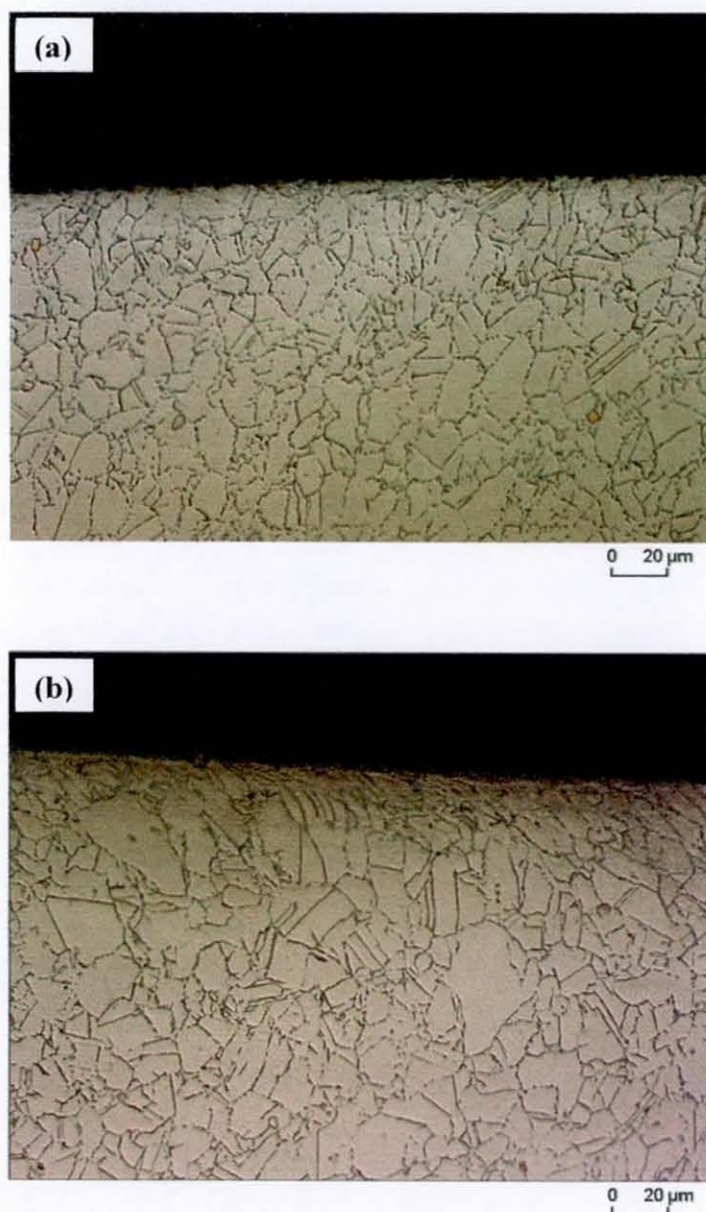
Figure 5.15 Light microscopy of the surface layers of Inconel 718 after CT (a) and UAT (b)

By contrast, there are no visible alterations in the grain structure of the surface layers for the workpiece machined with CT. No deformation or alignment of grain boundaries can be seen form the CT micrographs: the grain boundaries are randomly oriented in all regions of the specimen up to its edge. Because of the mounting and etching procedure, the water is coming out of the gap between the metal part and mould, and the edge of the metal workpiece is not sharp due to this phenomenon. Still, even though the image is slightly unclear in this edge area, no visible deformation at the surface can be observed. Having said that, in case of insignificant compressive residual stresses in the surface layer, no deformation will be seen either.

Following the light microscopy tests, the same specimens are examined with SEM in order to retrieve more detailed information about microstructure of the machined workpieces. The results of the SEM tests are in good agreement with the light-microscopy results.

Figure 5.16 shows a characteristic micrograph of the surface layers of Inconel 718 machined with UAT as obtained from SEM tests. A layer with different etching behaviour (most likely corresponding to the region of high deformation) of about 30 to 40 μm can be observed. A close-up of this layer (Figure 5.17) demonstrates that it
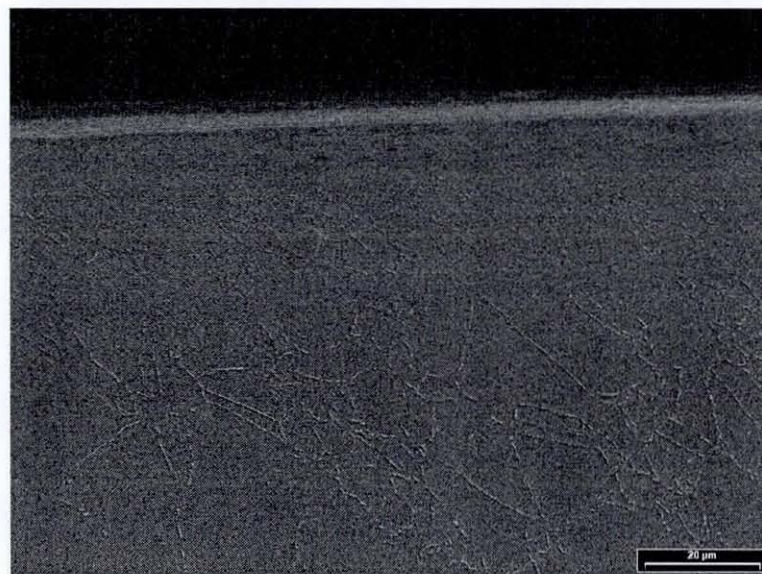
Figure 5.16 SEM of the surface layers of Inconel 718 after UAT

comprises two parts. The first part is a thin surface layer of about 10 μm: no alignment of precipitates and, in fact, no grain boundaries can be seen in this highly

deformed layer. Deeper into the material, the second part is discovered (some 20 μm thick): it is characterised by the alignment of grain boundaries in one preferred direction corresponding to the direction of deformation. Here again it is considered that precipitates most likely coincide with grain boundaries. The high degree of deformation destroys such alignment of precipitates in the first part of the layer.
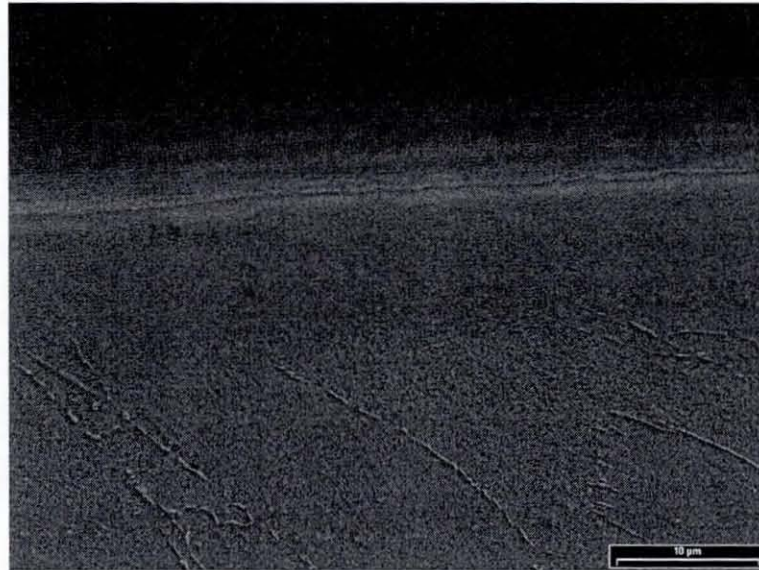
Figure 5.17 A close-up of the layer with different etching behaviour for the UAT-machined specimen

In the SEM analysis of CT-machined specimens, there are no visible changes (Figure 5.18) of the microstructure of the machined surface layers: as in the case of the light-microscopy tests the grain boundaries are randomly oriented throughout the entire specimen, thus indicating no changes in the microstructure due to machining. However, a very thin layer (about 3 μm) with different etching behaviour can be seen in Figure 5.18, apparently indicating high deformation in this area. The thickness of this layer is some 10 times smaller than that of the layer found in the UAT-machined specimen.

The observed phenomena are a clear indication of the differences in thermal and deformation processes between UAT and CT procedures and their subsequent influence on the microstructure of the surface layers of the machined workpieces. Nevertheless, a final conclusion on the changes in the material microstructure due to different machining procedures cannot be drawn only from the observations of

microstructure, as it is possible that actual sizes of the hardened surface layers are greater than those detectable through different microscopy techniques. (It is worth noticing, though, that if there is some deformation undetectable by the used techniques, it does not influence the orientation of precipitates and grain boundaries in the microstructure of the machined workpieces.) Therefore, the next logical stage of experimental investigation is a quantitative analysis of mechanical properties of the machined surfaces. Nanoindentation tests are employed for this quantitative comparison of the effect of CT and UAT on microstructure of the machined workpieces (see Section 5.4.3).
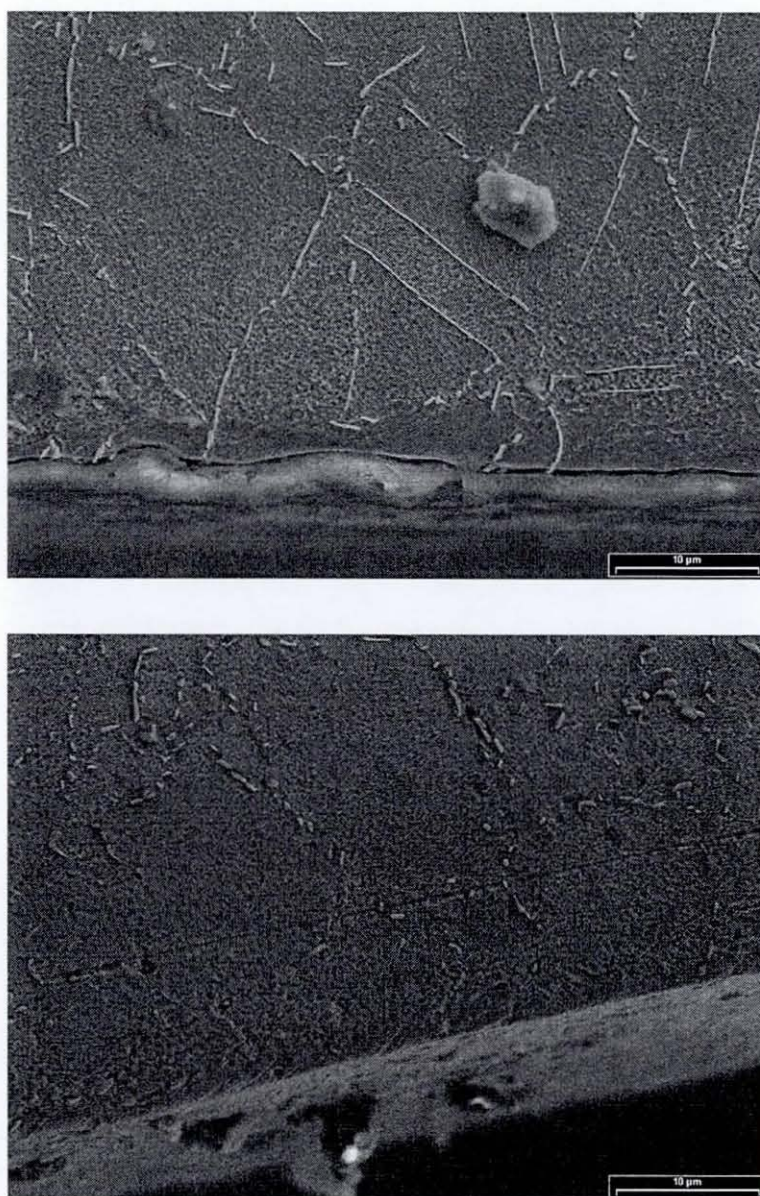
Figure 5.18 SEM of the surface layers of Inconel 718 after CT (2 examples)

5.4.2 Chips: unmagnified observations, light microscopy and SEM analysis

Detailed information on the chip shapes and external/internal structure can provide an invaluable insight into specific features of the cutting process during turning. Particularly precious information on the specific features of the turning process can be obtained via analysis of the chip cross-sections. This information includes shear angle, chip formation mechanisms and segmentation degree, material deformation features and change in the grain structure. This data can be used to study and compare mechanics of various turning procedures and define the proper chip formation mechanisms for an input to the FE model. Such experimental data can also be used to verify the results of the numerical modelling and enable the creation of a realistic FE model of the chip formation reflecting better the complexities of the cutting process.

Light microscopy and SEM have been used for a study of the external structure and cross-sectional analysis of chips produced during CT and UAT. The experimental procedure together with results and discussion of the observations are described in this section.

Preparation procedure

The chips produced during CT and UAT tests under different cutting conditions are collected for further investigation. The various cutting conditions used during turning are shown in Table 5.2. The chip structure is then analysed with an unaided eye as well as with microscopy techniques.

Table 5.2 Cutting conditions in turning tests for chip analyses

Workpiece material	Depth of cut d, mm	Cutting speed n, rev/min	Feed rate s, mm/rev	Diameter of the workpiece D, mm
Mild steel	1	40	0.16	30
	0.1	40	0.2	50
Inconel 718	0.1, 0.2	40, 85, 125	0.03, 0.05, 0.1	40
	0.3	32	0.28	40

Unmagnified observations

In the turning experiments, the runs usually are started with a non-vibrating cutting tip, thus implementing a CT procedure. The chips produced at this stage are discontinuous for a range of cutting conditions and various tested materials (PMMA and mild steel). A drastic change occurs when ultrasonic vibration is switched on. If the chip formation is discontinuous, it nearly immediately transforms into continuous, producing very long chips, typically several decimetres long. The radius of curvature of the chip R usually changes too when ultrasonic vibration switched on. The radius of curvature R depends on a wide range of parameters, such as cutting speed, feed rate, cutter geometry and use of lubrication. These factors complicate the consistent comparison of R between CT and UAT. Additionally, precise measurements of R are difficult because of the essentially three-dimensional geometry of the chip and its small dimensions (fractions of millimetre in many cases).

The chips are assumed to have an ideal helical shape (an example of the helical chip produced during turning tests is shown in Figure 5.19). As it is known from
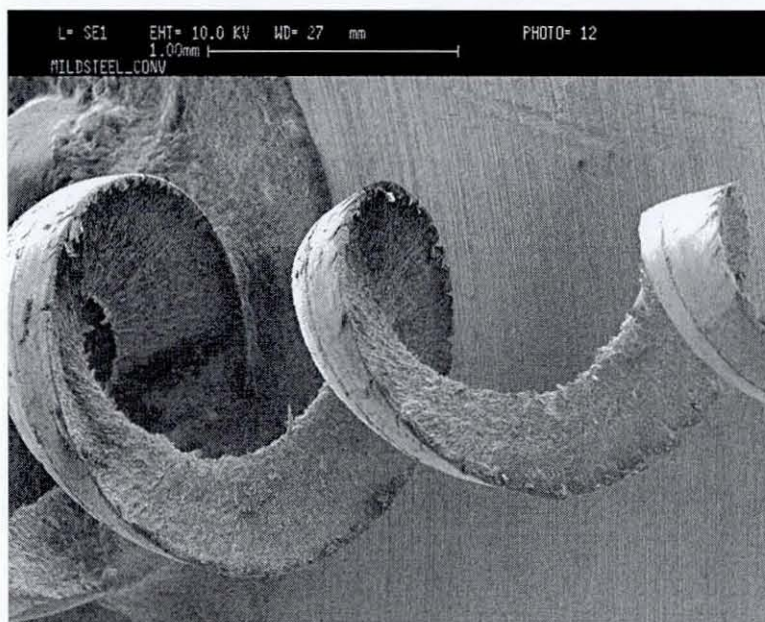

Figure 5.19 A fragment of the chip produced during the turning tests with mild steel

mathematics, for a helix with a path confined to a circular cylinder of radius r_c, its radius of curvature R (which is constant) can be calculated as follows:

$$R = \frac{r_c}{\cos^2 \beta},$$

where β is the angle of ascension, that is the angle made by the helical path with a plane that is orthogonal to the length of the cylinder. Hence, the value of R is calculated by the measured values of the diameter of the chip and its angle of ascension.

For some combinations of cutting parameters, the difference between radius of curvature R between CT and UAT is insignificant, with somewhat bigger values of R for UAT produced chips. However, in most of cases studied superimposition of ultrasonic vibration considerably influences the R-value, and some general tendencies were noticed. Typically, for dry turning conditions the difference between CT and UAT produced chips is mostly noticeable, with higher values of r_c and the angle of ascension β, resulting in the ratio R_{UAT}/R_{CT} being from about 1.25 to 2. Application of lubrication to the cutting region decreases the value of the radius of curvature R 1.5 − 2 times. Nevertheless, for lubricated cutting conditions the value of R is usually only insignificantly greater for UAT produced chips. An example case study, illustrating this kind of relationship, is shown in Table 5.3. In this case study, the following cutting conditions in turning Inconel 718 are used: $d = 0.2$ mm, $n = 40$ rev/min, $s = 0.03$ mm/rev.

Table 5.3 Radii of curvature of chips produced during CT and UAT in dry and lubricated conditions

	CT (Dry)	UAT (Dry)	CT (Lubricated)	UAT (Lubricated)
R, mm	3.6	3.7	2	2.5

The R-value depends also on the type of the lubricant applied in the cutting region. The effect of different lubrication is studied additionally for four various lubrication conditions when CT and UAT mild steel (cutting conditions being $n = 40$ rev/min, $s = 0.2$ mm/rev, $d = 0.1$ mm). The following cases are compared: (a) dry turning, (b) water used as lubricant, (c) silicon lubricant pre-applied to the workpiece surface as a very thin layer, and, finally, (d) commercially available cutting fluid (type HDC), sprayed onto the workpiece.

The result, which is noticed consistently for both CT and UAT, is a decrease in R for lubricated cutting conditions as compared to dry turning. The results of the tests with different lubricants are shown in Table 5.4.

Table 5.4 Radii of curvature of chips produced during UAT for various lubrication conditions

Material: mild steel	Dry turning	Water as lubricant	Silicon lubricant	Cutting fluid
Radius of curvature R, mm	5.9	5.5	3.5	5.0

Examination shows that ultrasonically machined chips are more brittle than conventionally machined ones, which witnesses greater degree of work hardening that can be attributed to higher strain rates during UAT.

In addition, various temper colours of chips produced by two cutting techniques indicate the difference in temperatures during the ultrasonic and conventional cutting processes, studied in infrared thermography experiments (Section 5.5).

SEM and light microscopy studies

SEM analysis is performed with whole samples of Inconel 718 and mild steel chips after CT and UAT. Although the microstructure of the chips cannot be studied with this kind of analysis, some information can be revealed on the macrostructural features of the chips and, consequently, provide one with more evidence on deformational processes in CT and UAT.

Chips produced with CT and UAT look similar to an unaided eye. They have similar helical shape and differentiate only by their radius of curvature R (discussed above) and smoothness of the edges. SEM observations of mild-steel chips demonstrate that chip edges are considerably more serrated in CT (Figure 5.20a) compared to relatively smooth edges obtained in UAT (Figure 5.20b).

The same observation is valid for Inconel 718 chips (Figure 5.21). The chip edges in UAT are much smoother compared to cracked edges in CT. No other differences are revealed with SEM of the whole chip fragments, and analysis of the chip microstructure is therefore performed.
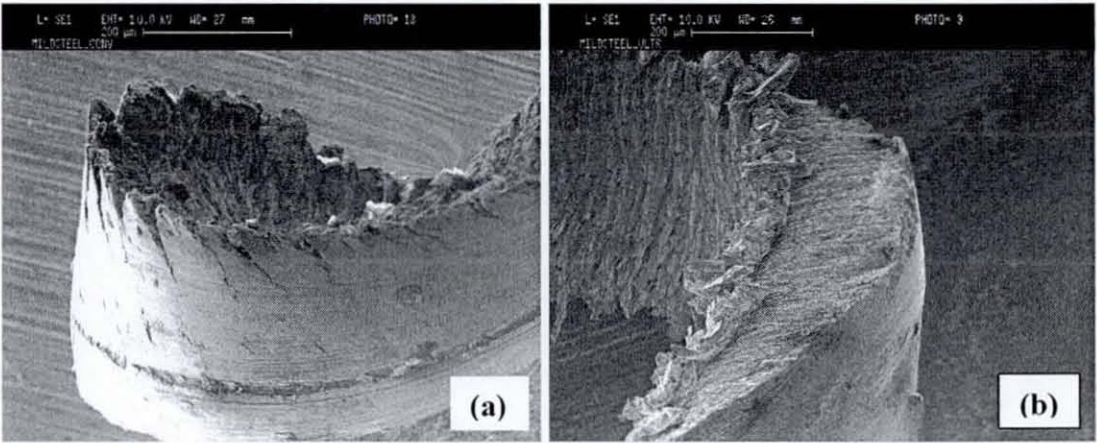
Figure 5.20 A mild-steel chip produced in CT (a) and UAT (b) tests
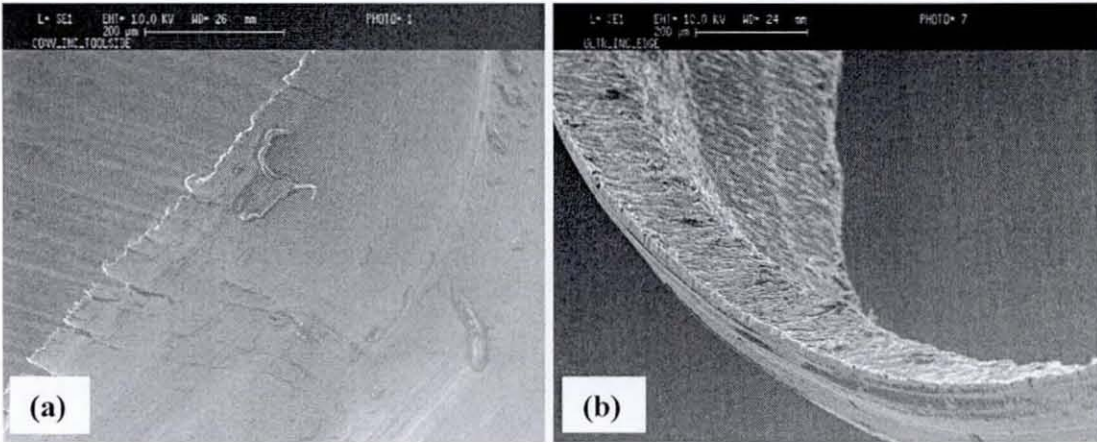
Figure 5.21 An Inconel 718 chip produced in CT (a) and UAT (b) tests

The difference between chips obtained in CT and UAT manifests itself in a different orientation angle of precipitates and various degrees of segmentation. As in the case of microscopic analysis of machined workpieces, it is considered that precipitates (seen as white lines in micrographs) are aligned along grain boundaries (Figure 5.22). Precipitates are lined up along one preferred direction at a certain angle to a chip face, different for chips obtained at CT and UAT. This angle shows a direction of deformation processes during turning and indicates different shear angles in the cutting process for CT and UAT. The shear angle φ can be calculated according to the following formula: $\varphi = \pi/2 - \alpha + \gamma$, where α is the angle between preferred orientation of precipitates and chip face and γ is the rake angle of the tool. The value of α for CT is 60° compared to significantly smaller 40° for UAT. Hence,

for $\gamma = 10°$ (the value of γ depends on the tool geometry and on the inclination angle of the ultrasonic transducer), the shear angle for UAT is about 60° compared to 40° for CT. This correlates well with a predicted increase in φ due to the improved lubrication ability of UAT described in Chapter 2.

Both chips in Figure 5.22 are continuous, although the degree of segmentation is definitely higher for the chip obtained in CT. The back surface of the chip obtained in CT is considerably more serrated, compared to that obtained in UAT. This is a strong manifestation of the significant differences in the chip formation processes between CT and UAT. Serrations on the backside of the chip obtained in CT (Figure 5.22a) indicate segmented chip formation during the CT process, which is observed in the high-speed filming experiments. The backside of the chip obtained when UAT (Figure 5.22b) demonstrates only minor serrations reflecting purely continuous chip formation with incremental chip growth at each impact of the ultrasonically vibrating cutter as opposed to the sliding processes in chip formation when CT. However, no shear bands are detected in either of the chips obtained when UAT or CT. It is possible that, in order to reveal probable shear band formation and other relevant information on deformation nature, a higher magnification technique, such as TEM, – giving at least 10 times higher resolution – should be applied.
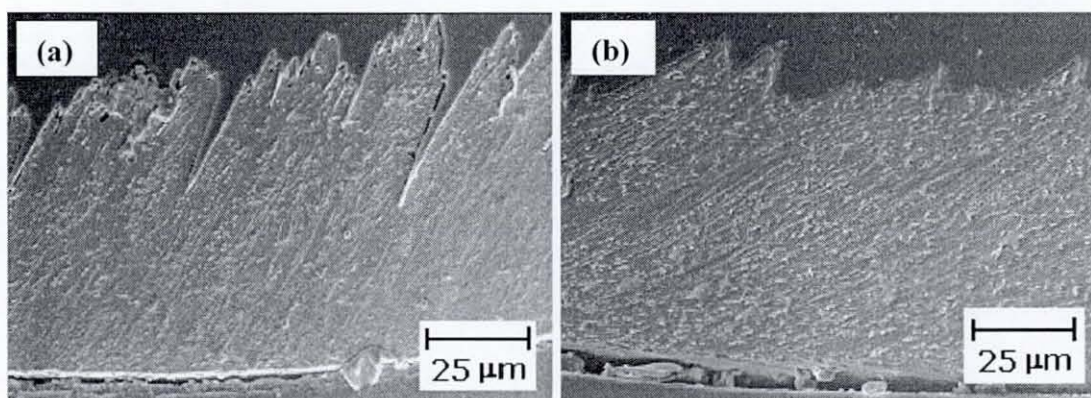
Figure 5.22 SEM of Inconel 718 chips obtained in CT (a) and UAT (b)

A highly deformed surface layer, similar to that found in the machined workpieces, is found in chips obtained both in CT and UAT. This layer possesses different properties compared to the rest of the chip and, consequently, is affected differently by the etching procedure. The thickness of this layer for CT is about 10

μm (Figure 5.23a). Unlike the thicker surface layer found in the workpieces machined with UAT, the highly deformed layer in chips obtained at UAT is much thinner than that found in chips obtained at CT, with the thickness of only about 2 μm, thus requiring quite high magnification to detect it (Figure 5.23b). In these highly deformed layers no alignment of precipitates can be seen, apparently because the precipitates are randomly distributed along the grain boundaries or grain refinement occurs due to high deformation levels. The much thinner layer observed in the chip obtained in UAT could be explained by the different character of the friction and thermal processes in UAT, caused by the intermittent contact between the chip and cutting tool, in contrast to the constant contact in CT. This difference in contact conditions leads to the shorter contact times in UAT, and, consequently, smaller influence on the structure of surface layers of the chip.
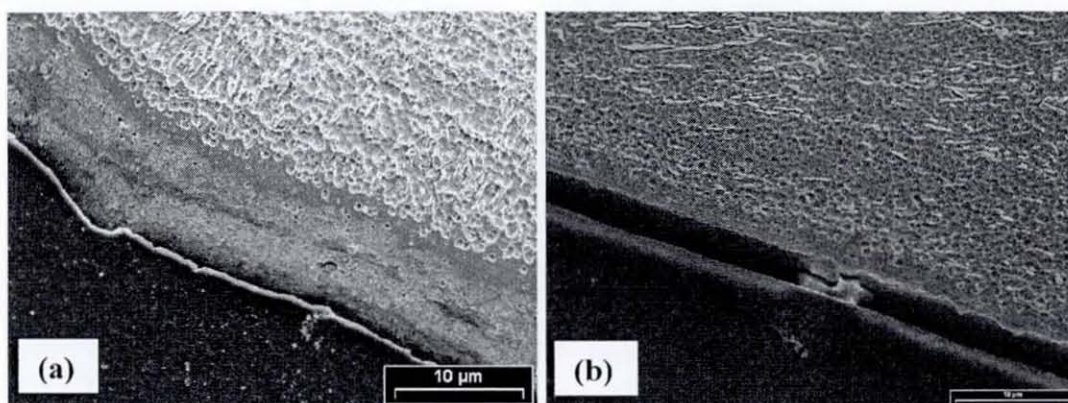
Figure 5.23 Highly deformed surface layer in the chips obtained in CT (a) and UAT (b) (SEM)

The main deformation patterns, i.e. alignment of precipitates and the mean grain size, in chips obtained in CT and UAT are quite similar and probably demonstrate comparable levels of plastic deformation in the chip material for both techniques (Figure 5.24). The smaller distance between precipitates in the chips compared to that in the workpiece material indicates grain refinement due to higher degree of plastic deformation caused by extensive shearing processes in the chips during cutting.
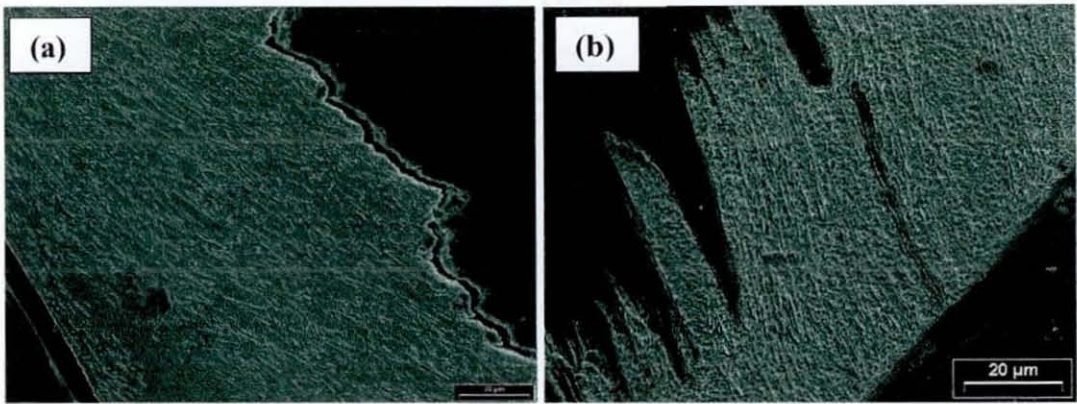
Figure 5.24 Observation of precipitates in the chips obtained in CT (a) and UAT (b) (SEM)

Cross-sections of chip produced by CT and UAT are also analysed with light microscopy (Figure 5.25). In addition to the information obtained with SEM tests, various colours are observed for the chip obtained in CT inside and on the boundaries between segments, as well as regular colour changes for the chip obtained in UAT. Different colours indicate different degree of deformation. However, grain boundaries cannot be revealed with the magnification, which is used in the test, and probably they cannot be found with light microscopy in this particular case due to the small grain size in the chips.
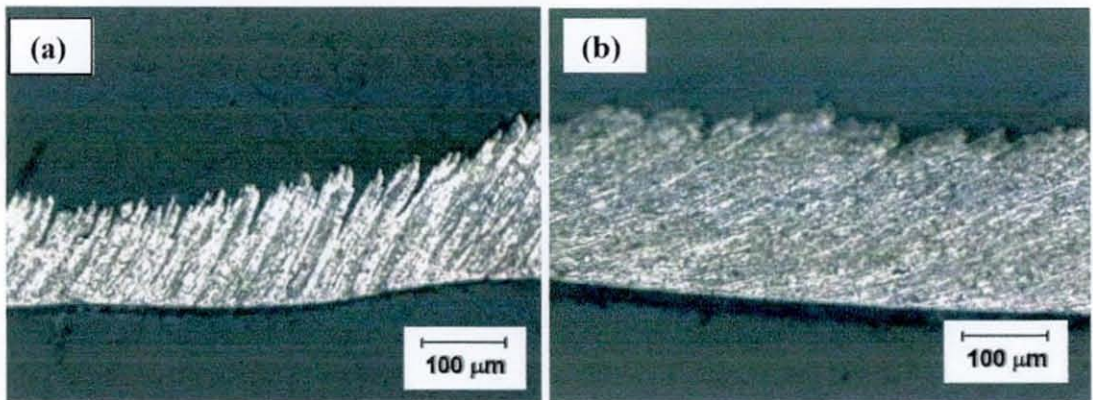
Figure 5.25 Light microscopy micrographs of the chips obtained in CT (a) and UAT (b) (SEM)

It is worth noticing that grain refinement found in the chips should be caused purely by deformation processes during turning, and not by the temperature

influence. The changes due to high temperature can be expected for Inconel 718 in the region of 800°C, thus lower temperatures, predicted by FEM and observed in the infrared thermography experiments, are not enough to cause any considerable grain refinement.

5.4.3 Nanoindentation tests

Overview of the nanoindentation technique

Nanoindentation tests are employed in this study in order to quantify differences between microstructures of surface layers of the workpieces treated with CT and UAT.

Nanoindentation is similar to conventional hardness testing, but it is performed on a much smaller scale. Recent improvements in indentation equipment allowed accurate measurements of load P down to micro-Newtons (μN) and penetration depth h down to nanometres (nm). To measure nanomechanical properties, a very small calibrated diamond probe is brought into contact with the sample surface at a specified applied load. The diamond probe is either Vickers or Berkovich indenter, the tip of which is a four-sided or three-sided pyramid, in contrast to the traditional sphere or a cone (a Rockwell indenter) usually used for hardness testing. The resultant displacement of this sharp diamond pyramid into the surface is monitored and displayed in real time as a function of load. Data is acquired, analysed and stored in ASCII format. Since depth resolution is on the scale of nanometres, it is possible to conduct indentation experiments even for very small surface areas. Two quantities, which can be extracted from nanoindentation experiments, are material's hardness and its Young's modulus. The hardness, in its turn, can be correlated to the yield strength. There is also some research, dedicated to applications of the nanoindentation tests to studies of residual stresses and strains in the surface layers of the material. However, the influence of the residual stress on the contact hardness is less than 10% of its value in the unstressed specimen, so such estimations for the residual stress are somewhat dubious [123]. (A standard technique, which is utilised for the measurement of residual stresses, is an X-ray diffractometry.)

Instrumentation

The tests are performed with the NanoTest Platform (Figure 5.26) made by Micro Materials Ltd, Wrexham, UK. The components of this device are shown in Figure 5.27. This instrument possesses the following features:

- A load is applied by means of a coil and magnet located at the top end of the pendulum.
- The penetration of the probe into the sample is monitored with a sensitive capacitive transducer.
- All instrument calibrations are performed automatically.
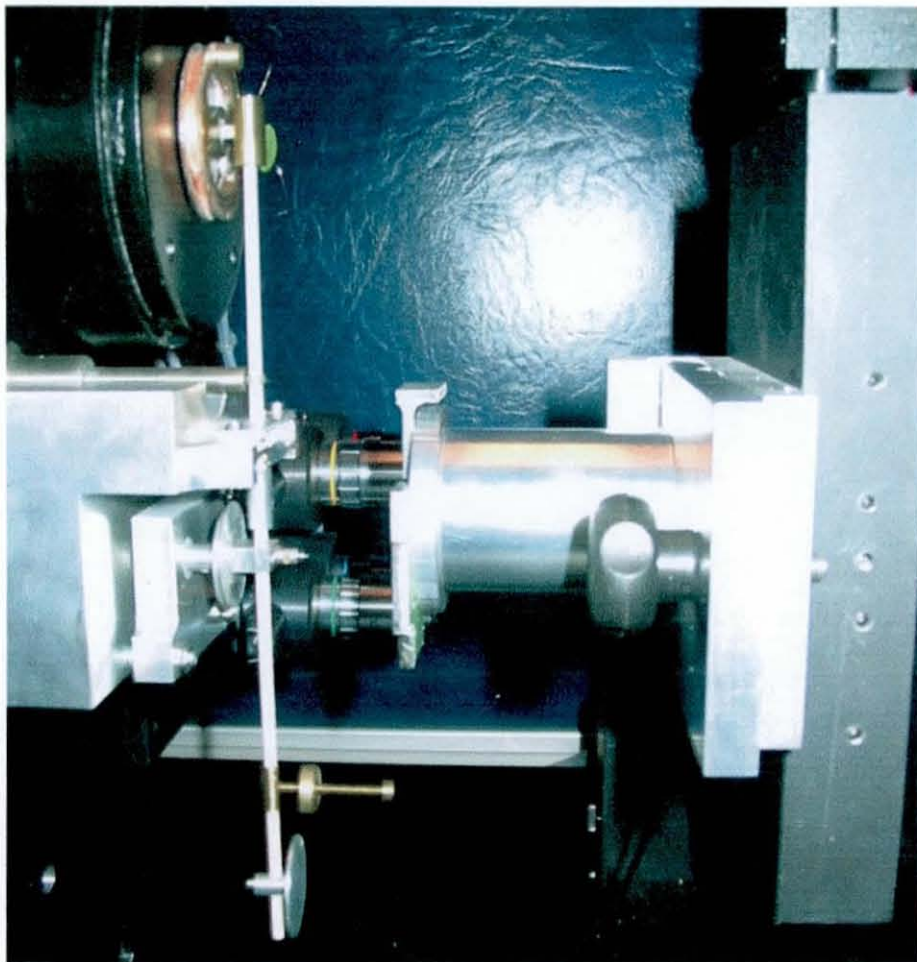
Figure 5.26 NanoTest Platform

The specification of the range and sensitivity for the displacement and load is shown in Table 5.5. The Berkovich indenter (Figure 5.28) is used in all the tests.

Table 5.5 Specification of the NanoTest Platform

Displacement range and sensitivity	
Range	0-50 μm
Noise-floor	0.025% of full-scale deflection
Theoretical resolution	0.04 nm
Load range and sensitivity	
Maximum resolution	better than 100 nN
Load ranges	up to 0-500 mN
X/Y/Z resolution/travel	0.02 mm/50 mm
Analysis area	50 mm x 50 mm
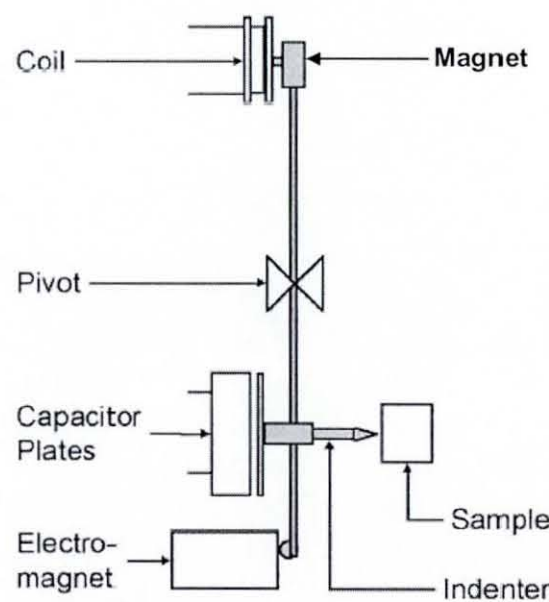
Figure 5.27 NanoTest Platform design
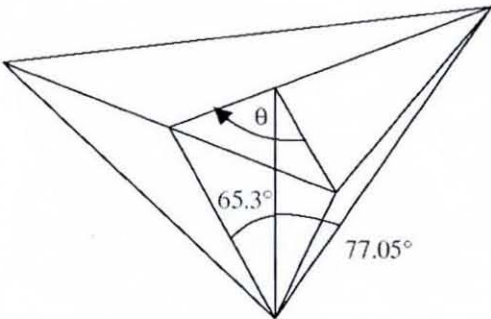
Figure 5.28 Berkovich three-faced pyramid

Nanoindentation data analysis

The NanoTest measures the penetration depth of a diamond probe as a function of the applied load during a loading-unloading cycle (Figure 5.29). On unloading, the elastic component of the displacement starts to recover producing a sloped rather than horizontal unloading curve. It is from this slope that the elastic properties can be derived. The hardness is derived from the residual depth of the unloading curve as described below.
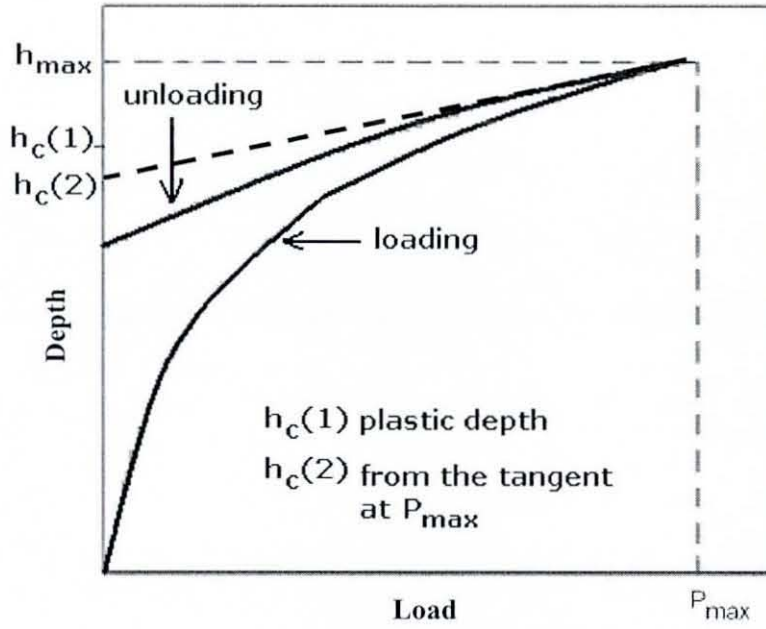
Figure 5.29 Plastic depth determination in nanoindentation

After frame compliance correction, the depth versus load unloading data is fitted to a power law function of the form.

$$P = a\left(h - h_f\right)^m,$$

where a, h_f and m are constants. The true contact depth of the diamond probe is determined from the expression:

$$h_c = h_{max} - \varepsilon S P_{max},$$

where h_{max} is the maximum penetration depth, P_{max} is the maximum load, S is the contact compliance equal to the tangent at the maximum load, and ε is a coefficient that depends on the indenter geometry.

Hardness H is determined from the peak load and projected indentation area, A:

$$H = P_{max}/A.$$

To obtain the Young's modulus, the unloading portion of the depth-load curve is analysed according to the following relation:

$$S = \pi^{0.5}/\left(2E_r A^{0.5}\right),$$

where E_r is the reduced modulus defined by

$$1/E_r = \left(1 - v_s^2\right)/E_s + \left(1 - v_i^2\right)/E_i. \tag{5.1}$$

Here E_s and v_s are the Young's modulus and Poisson's ratio for the sample, respectively, and E_i and v_i are those for the indenter ($E_i = 1141$ GPa and $v_i = 0.07$).

Specimen preparation and experimental procedure

Workpieces of Inconel 718 machined with CT and UAT with vibration in the tangential direction are examined in the tests. In order to prepare a specimen for the nanoindentation analysis, workpiece samples are placed facing each other and potted into epoxy resin as it is shown in Figure 5.30. Then the produced specimen is
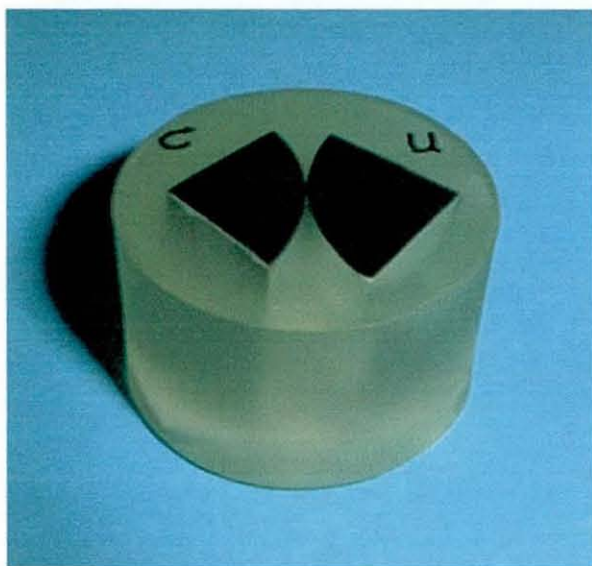
Figure 5.30 A specimen used in nanoindentation tests: Inconel samples placed face-to-face and mounted into epoxy resin
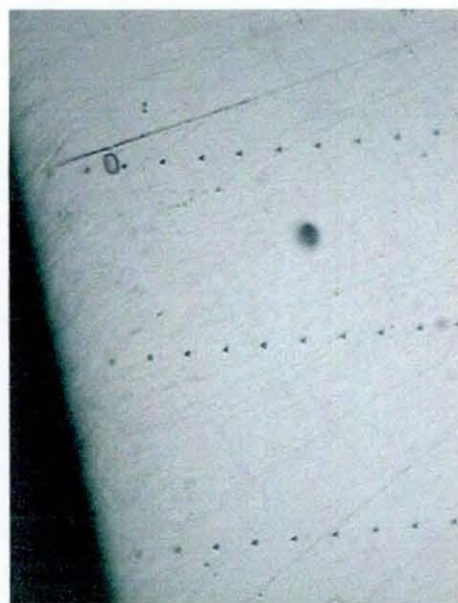
Figure 5.31 A photograph of the indentation points made with metallurgical microscope

polished and mounted into the NanoTest machine. The tests are carried out in an automatic mode with a total duration of two days. There are three runs A, B, and C, parallel to each other (vertical in Figure 5.32). Each of the lines A, B and C goes from the conventionally machined part of the specimen, crosses a thin separating layer of plastic between samples and then goes through the workpiece sample machined with UAT. Each run consists of three parts: coarsely placed indents (distance 50 μm between two neighbouring indentation points) in the regions distant

from machined surfaces and finely placed indents (10 μm between two neighbouring indentation points) in the direct vicinity of the machined surfaces (Figure 5.31).
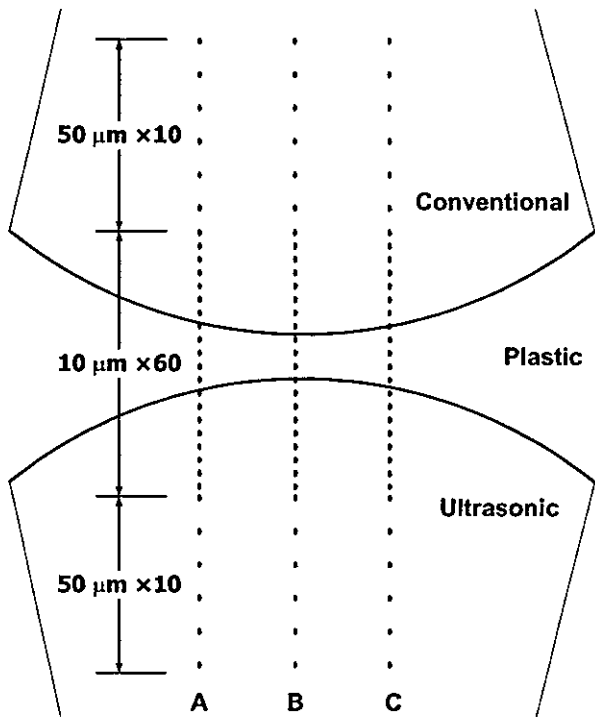
Figure 5.32 A diagram of the indentation points produced in nanoindentation tests

Each indentation point was produced with a constant load of about 10 mN applied to the probe tip. The difference in the residual depth of the crater produced with the probe is automatically recalculated into hardness and the Young's modulus of the corresponding indentation place as it is shown above. The complete data for these tests can be found in Appendix 1.

Results of the test and discussion

The following analysis is made for the indentation points along lines A,B and C, and the results for all three lines are consistent and show similar values for hardness and the Young's modulus in the corresponding places of the specimen.

Plotting hardness versus the indentation point number along line B, which is in the middle between lines A and C, the following graph is obtained (Figure 5.33). In the graph the area with significantly low hardness evidently corresponds to the layer of plastic between alloy samples.
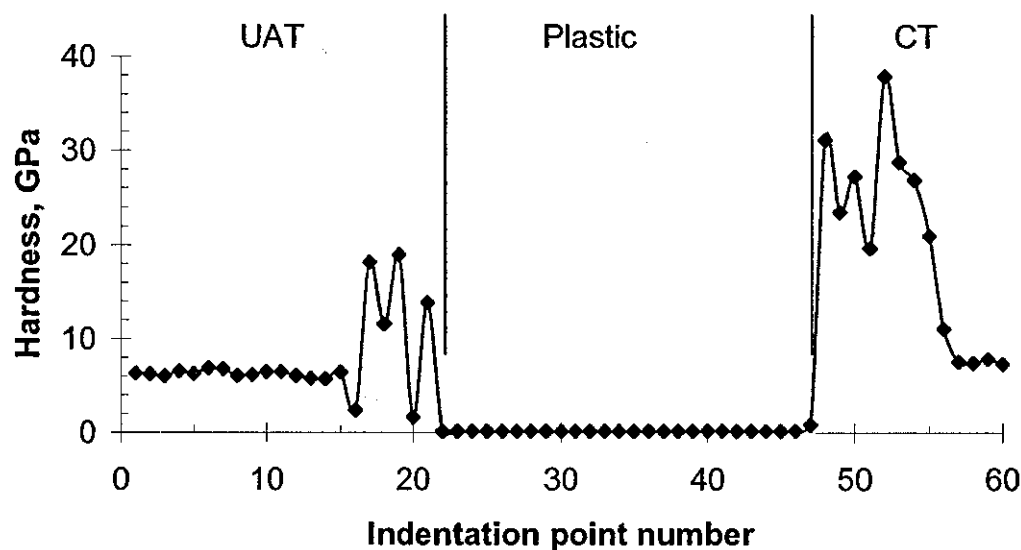
Figure 5.33 Measurements of hardness along line B

As mechanical properties of the plastic are out of the scope of the experiment, this graph can be replotted in the way it is presented in Figure 5.34 to compare hardness of the surface layers for alloy samples depending on the distance from the machined surface for two cutting processes.
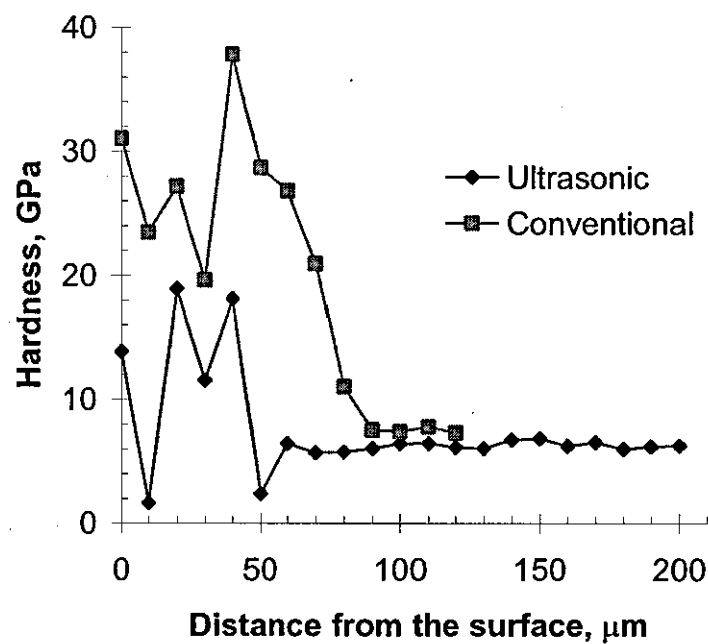
Figure 5.34 Comparative nanoindentation analyses of surface layers of Inconel 718 after ultrasonic and conventional turning

The scatter in hardness values, i.e. peaks/troughs found in the graph for both CT and UAT machined surfaces, can be explained by a combination of the following factors: (1) mechanical vibration of the testing machine, (2) roughness of the polished surface, and, finally, (3) indenting the microdefect, second phase / precipitate or carbides/nitrides. The mean values of hardness are therefore taken into consideration.

As it can be concluded from Figure 5.34, the hardened surface layer is observed for both treatments of the workpiece material (ultrasonic and conventional), however, the hardness of this layer and its width is significantly different for CT and UAT machined surfaces.

The comparative analysis of the hardened surface layer for CT and UAT was performed for all three lines A, B, and C. According to the results of this analysis (Table 5.6), the average width of this layer is 70 % higher for the conventionally machined specimen than for the ultrasonically machined one (85 μm and 50 μm, respectively). This result shows that the actual width of the hardened layer is greater than its visible value, observed with light microscopy and SEM.

Furthermore, the average hardness of the hardened surface layer for UAT (about 15 GPa) is about 60 % of that for CT (25 GPa) and considerably closer to the hardness of the untreated material (6.2 GPa). This indicates differences in thermal, deformation and chip formation processes between CT and UAT. It can be concluded that the UAT procedure is significantly more delicate to the machined material.

Table 5.6 Characteristics of the hardened surface layer for CT and UAT

Line	UAT		CT		Non-treated
	Hardness, GPa	Width, μm	Hardness, GPa	Width, μm	Hardness, GPa
A	13.9	55-60	25.3	80-90	6.1
B	15.6	40-50	25.2	80-90	6.3
C	16.7	40-50	24.2	80-90	6.2
Average value	15.4	50	24.9	85	6.2

In order to further analyse differences in the structure of the surface layers for CT and UAT, the X-ray diffractometry tests could be suggested. These tests would allow to compare values of the residual stresses in surface layers, as well as if the residual stresses/strains are tensile or compressive.

The Young's modulus of the material can be also deducted from nanoindentation tests as it is described above (Eq. 5.1). However, in this particular case the Young's modulus of the bulk material (Inconel 718) is known *a priori* – $E \approx 200\,\text{GPa}$ – and is in good agreement with nanoindentation results. It is worth noticing that anomalously high values for E observed in the hardened surface layers are due to an intrinsic error of the nanoindentation technique. The error in Young's modulus estimation for the hardened material is connected the increased values of "pile-ups" around the indent, resultant from material deformation during indentation of the probe. The pile-ups lead to underestimation in the values of the residual plastic depths h_c and, consequently, to overestimated E values. Thus, trustworthy information on E values for hardened surface layers cannot and should not be extracted from these particular tests.

5.5 Thermal analysis of ultrasonic and conventional turning

Temperature in turning is an important process parameter. It can affect properties of the workpiece material, such as thermal conductivity, specific heat, and the coefficient of thermal expansion. High temperatures also lead to thermal softening of the material, which is a reduction in its yield stress, leading to easier plastic deformation and shearing processes in chip formation. Excessive temperatures appearing when turning at high speeds or for high-strength materials can cause premature wear of the cutting edges. And even if temperatures are not high enough to significantly affect the properties of the workpiece, detailed experimental information on cutting temperatures can be valuable to validate the results of numerical simulations. Additional information on the nature of deformational processes can also be obtained with such thermal data, for example, mechanics of chip formation and the influence of friction and its mechanisms. In this case, it is important to know not only the value of temperature in the single point in the cutting

zone or mean value of temperature at the tool–chip interface, but rather a temperature distribution over the certain surface in the cutting region, such as along the rake face of the tool.

In order to study thermal processes during CT and UAT, and to verify results of FE simulations, infrared (IR) thermography tests are employed. As it was discussed in Section 2.5.2, although other methods can be used to obtain temperature distribution in the cutting tool, for example inserted tool-workpiece thermocouples, IR thermography is a considerably less laborious and straightforward way of getting such temperature data. It is worth noticing that inherent limitation of this technique is that temperature observation is possible only for exposed parts of the cutting tool.

5.5.1 Instrumentation

The experiments are performed with *ThermaCAM^{TM} SC3000* produced by FLIR Systems AB. The camera features the new Stirling-cooled Quantum Well Infrared Photon (QWIP). This IR detector has a spectral response between 8 and 9 μm and can measure temperature in a range of –20°C to 2000°C. The produced image has a resolution of 320×240 pixels with 14-bit digital image data. The camera comes with a built-in 20° lens, and close-up lens, attached to it, that allows to focus on the area of 34×26 mm^2. The data is acquired with the *Tracer Plus Package* real-time digital recording and temperature analysis system via a high capacity PC-card and then stored on the hard drive of a Windows-based PC.

The *ThermaCAM^{TM} SC3000* system has several operation modes: (i) frame mode, where a single IR image is taken at a certain moment of time and then stored in the memory individually, (ii) continuous filming mode, where continuous filming with a rate of 50 or 150 frames/s is carried out after the camera is triggered by the key stroke. Both modes cannot provide information on the dynamic temperature fluctuations within a cycle of ultrasonic vibration. Such a dynamic image would require the camera operating at a rate of about 10^5 frames/s, hence about 700 faster than the maximum speed of the camera in the line mode. The relatively slow operating rate of the camera is connected with a nature of thermal processes in the IR detector. High speeds of filming are, however, available with modern high-speed cameras, enabling real-time video recording of the dynamics of the UAT process, described above in Section 5.3. Consequently, temperature distribution frames taken

with the camera in a single-frame and continuous-filming modes used in the experiments are considered as quasistatic measurements. Most of the time the camera is operated in a continuous filming mode at rate of 50 frames/s, using a single-image format only during the calibration stage, however, the recording time is usually about four seconds at a time, as the stored data requires about 8 Mb per second of filming. Nevertheless, the total recording time is limited only by the PC hard drive space. The recording is conducted and recorded data is analysed by specialised software (ThermaCAM 2001 Researcher by FLIR Systems).

5.5.2 Experimental procedure

Camera calibration

The IR camera requires the values of the ambient temperature, distance to the object, relative humidity and object emissivity as input values set by the operator. The first three parameters are adjusted to the current values, and the only parameter that needed additional calibration is an emissivity of the cutting tool and that of the chip.

The emissivity factor ε describes emission from the body surface, being equal to unity for the ideal "black body" and less than 0.1 for polished surfaces. For oxidised or painted surfaces the value of ε is usually more than 0.9. The emissivity value depends in the experiment on the object material, temperature of the object and the angle of filming, thus making the precise measurement of absolute values of temperature extremely difficult. The measurements are further complicated by the presence of moving or vibrating parts in the filed of view.

The calibration of the emissivity value is performed with an electric heater, the steel top surface of which is heated to 450°C; this temperature is controlled by a thermocouple connected to the heater surface and thus can be considered as an accurate value (Figure 5.35). Inconel 718 chips and tungsten-carbide cutting tools, uncoated and tinned, are then placed on this surface plate. The sufficient time interval (about 15 min) is chosen for temperature of the tested objects to reach the temperature level of the heated surface (450°C). The IR image of the surface is then taken with the *ThermaCAM^{TM} SC3000* system (Figure 5.36).
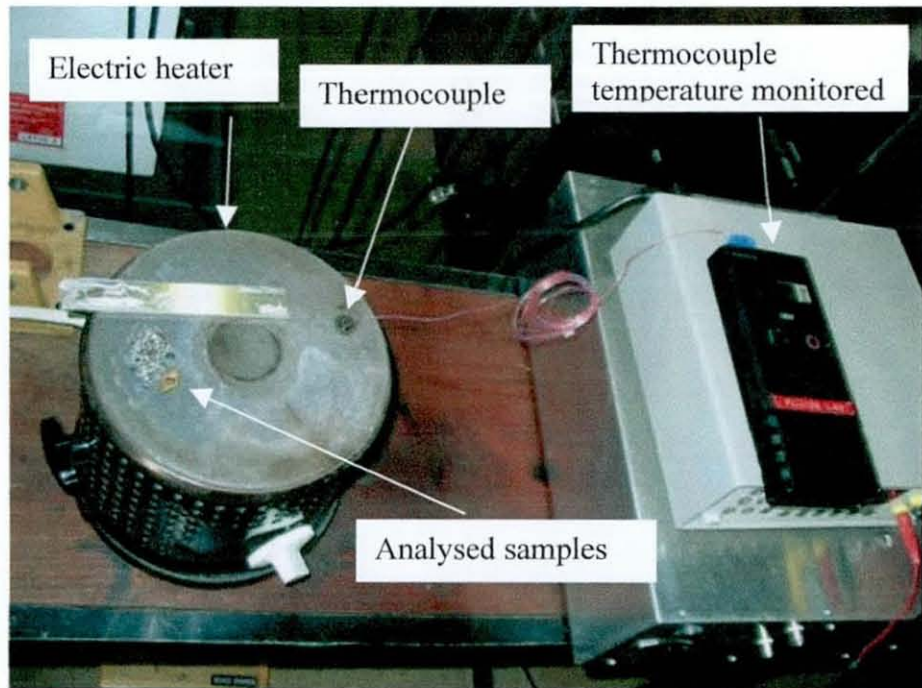
Figure 5.35 Electric heater and thermocouple system for IR camera calibration
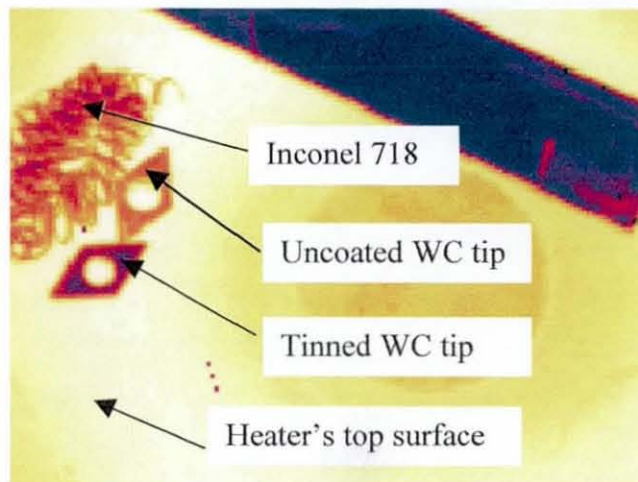
Figure 5.36 A magnified IR image for emissivity calibration

The automatic emissivity recalculation option is then utilized to adjust the emissivity levels for different materials (Inconel 718 and tungsten carbide) so that to obtain the same resultant temperature (450°) in the respective image areas. The calculated values of emissivity are 0.24 for Inconel 718 and 0.34 for the cutting tool. These calculated values are then applied for the analysis of the different areas in IR images, allowing calculate the levels of temperature corresponding either to the chip

or cutting tool materials. The error of emissivity calculation is estimated at ±0.1, which leads to error of ± 10° for the temperature measurement at the level of 500°C. Nevertheless, as the emissivity of the surface depends on the angle of filming, surface roughness and temperature level, the actual magnitude of the error in temperature measurement can be higher than this estimation. Still, relative difference between CT and UAT can be measured accurately in terms of cutting tool and chip temperatures, as well as distribution of temperature in the tool is observed for both cutting technologies. Additionally, levels of temperature, measured in the cutting tool, enable to set the correct value of the contact heat conduction coefficient H, which is a complex parameter and can be determined only experimentally.

Measurement procedure

The experimental set-up comprises the universal Harrison 300 lathe, ultrasonic transducer, tool holder with the tungsten carbide insert (grade H13A) attached to its end, infrared camera (*ThermaCAM^{TM} SC3000*), computer system and the monitor for real-time observation of the IR images (Figure 5.37).
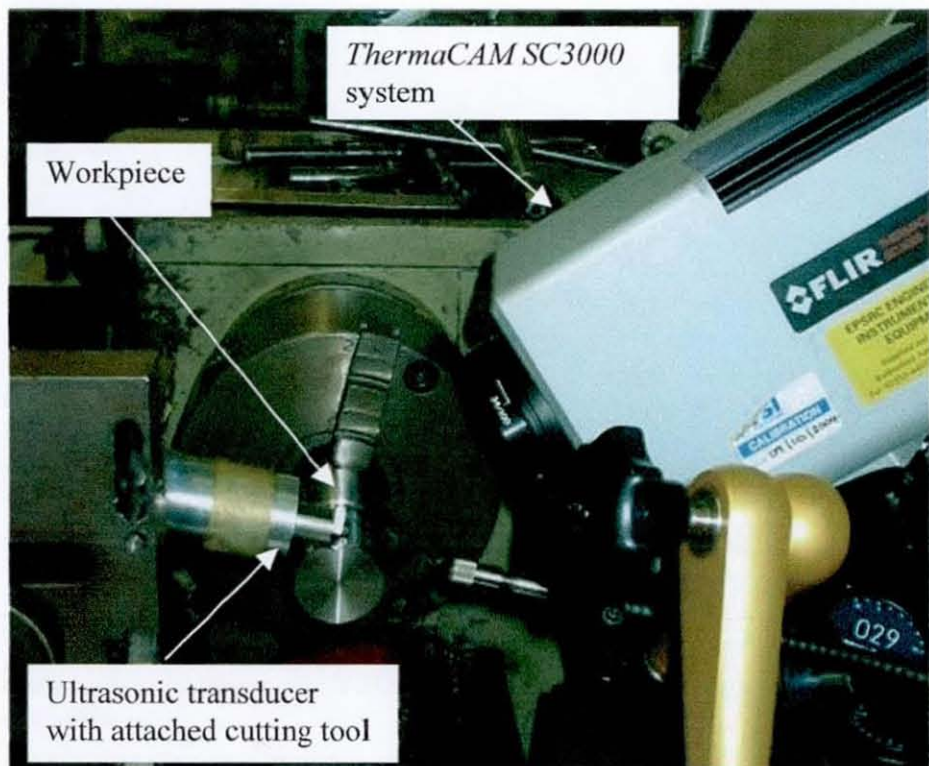
Figure 5.37 A photograph of the experimental set-up for infrared thermography

A lens of the *ThermaCAM*[TM] *SC3000* system is zoomed in and focused onto the tool area next to the cutting tip. The close-up lens supplied with the camera are designed for focal distances about 100 mm, allowing to focus onto the area of $34 \times 26\,\text{mm}^2$ with a very narrow depth of field of about 0.25 mm, leading to some objects, namely the chip, workpiece and distant parts of the cutting tool, being sometimes slightly off-focus.

Adjusting controls of the ThermaCAM 2001 Researcher, the range and scale of the measured temperature are set automatically to include all the temperatures in the field of view. Various colours on the IR images correspond to the temperature in the range between each two consecutive marks on the temperature scale. In case of the spot temperature being higher than the maximum temperature in the set range, this is indicated with white colour on the IR image for the chosen colour scheme.

For all considered cutting and lubrication conditions, runs are started with CT (i.e. with ultrasonic transducer switched off) and infrared images are taken after a minute or two of turning for each cut, in order to achieve a stable temperature mode of turning. After that, ultrasonic vibration is switched on and images are taken for UAT conditions, again allowing time to reach stable levels of temperature.

In IR images both the cutting tool and chip are seen. The emissivity of the camera during operation is set to 0.34 (cutting tool emissivity), thus the images show lower than factual temperatures for the chip (as calibrated emissivity of Inconel 718 is lower than that of the cutting tool). In order to obtain real magnitudes of the chip temperature, its emissivity level is adjusted during the analysis of the experimental results. Although changes in the chip geometry during cutting and, consequently, in the reflection angle could affect resultant readings, it is believed that this influence is averaged over the filming time, and thus relative differences in the chip temperatures between CT and UAT for various cutting conditions can be analysed. In some images, the chip, which temperature is higher than that of the cutting tool, obstructs the view: in this case temperatures in cutting tip are compared in the distant areas of the tool, usually several millimetres from the tool tip, where the measured temperatures are considerably less affected by the chip radiation and consequent reflections on the cutting tool.

The observation is done at two different angles: the position of camera is adjusted so that to observe the cutter along Z and X axes in Figure 5.6. The set-up for IR thermography along Z-axis can be also seen in Figure 5.37.

5.5.3 Experimental results and discussion

Initial measurements

The temperature of the cutting tip prior to the engagement with the workpiece is studied in CT and UAT. The temperature of the unloaded tip in CT is equal to the room temperature. However, when the ultrasonic vibration is switched on, the cutting tip begins to heat up, and the maximum temperature registered after the temperature stabilises in several minutes, attaining an average level of about 75°C (Figure 5.38). The temperature distribution in the cutting tool for UAT in no-load operation mode is shown in Figure 5.39. Apparently, the increase in the temperature of the cutting tip for UAT in no-load operation is connected with the dissipation of the ultrasonic energy.
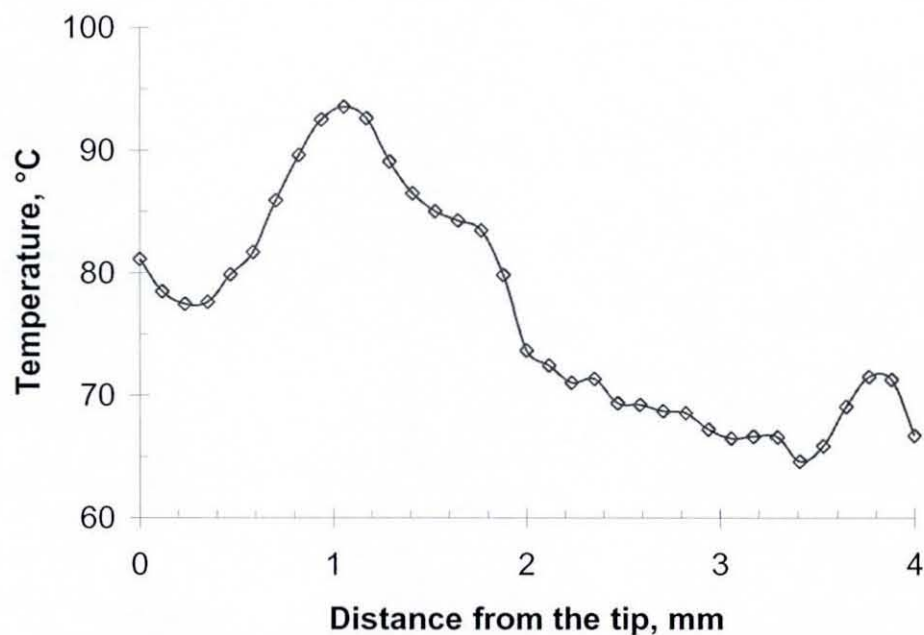
Figure 5.38 Temperature distribution in the vibrating cutting tool in no-load operation along line 2 (see Figure 5.39)

The experiments are performed with Inconel 718 and mild steel for various cutting and lubrication conditions, and various angles of filming, giving consistent results for various combinations of process parameters.
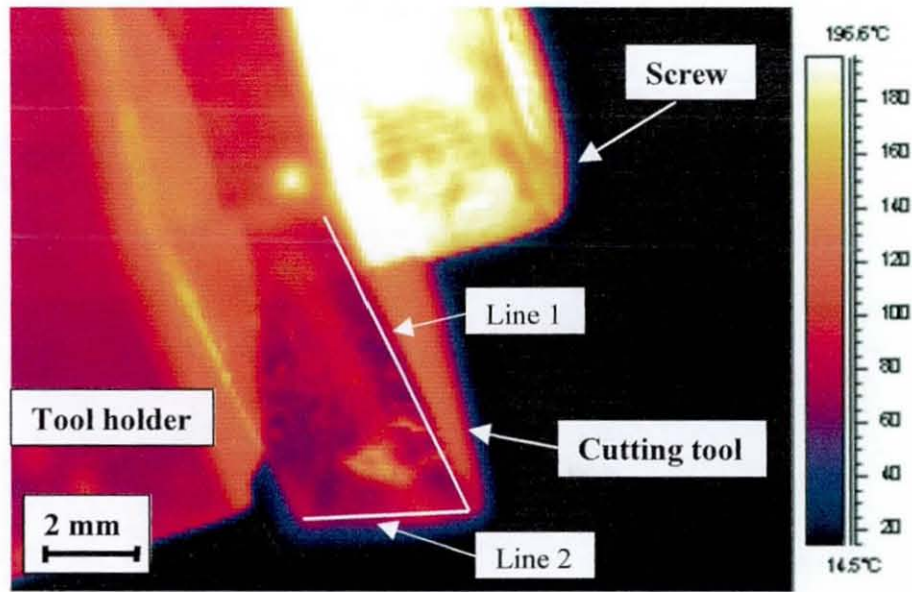
Figure 5.39 Temperature distribution in the cutting tool for UAT in no-load operation mode

Initial turning tests

For the tests described in this section, the temperature levels are observed in the cutting tool and chip prior to the proper camera calibration, thus absolute magnitudes of temperature cannot be given here. Still, some useful data is obtained from these trial runs.
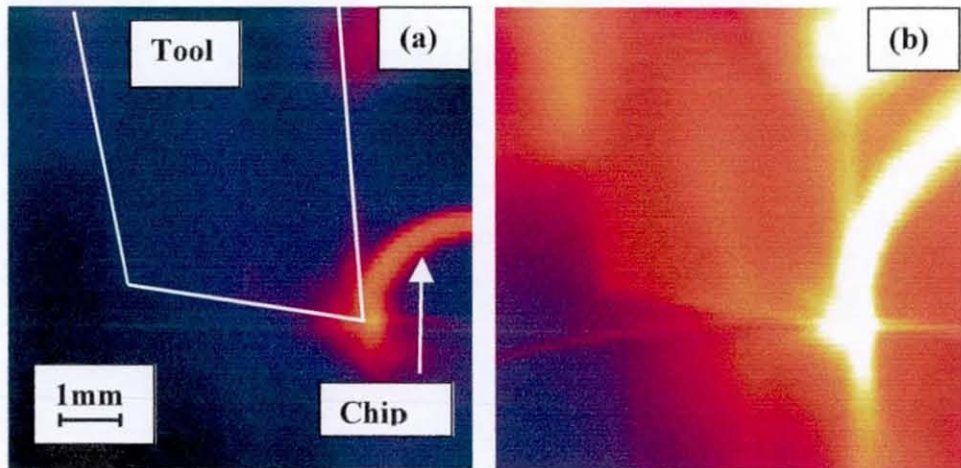
Figure 5.40 IR images of the cutting tool in CT (a) and UAT (b) of mild steel

Infrared images of the cutting tool, as observed along X-axis in Figure 5.6, are compared for CT and UAT of mild steel for the following cutting conditions: $n = 40$ rev/min, $s = 0.2$ mm/rev, $d = 0.1$ mm, workpiece diameter $D = 50$ mm without lubrication (Figure 5.40). Mild steel workpieces that are easily machined are used in order to gain hands-on experience prior to temperature measurements in turning of Inconel workpieces. Relatively low temperatures obtained in this test are due to low cutting speed, small depth of cut and mild steel being a soft and ductile material.

The effect of lubrication on cutting temperatures is studied for various lubrication conditions in CT and UAT of mild steel for the same cutting conditions. The following four cases are compared: (1) dry turning, (2) water used as lubricant, (3) silicon lubricant pre-applied to the workpiece surface as a very thin layer, and, (4) commercially available cutting fluid (type HDC) sprayed onto the workpiece. (The study of the chips produced in this experiment is given in Section 5.4.2). Each run starts under the dry turning conditions, and IR images are taken for CT and UAT. After that lubrication is introduced into the cutting region, and IR measurements are performed again. The measured temperature is invariably higher for ultrasonically vibrating tool for all lubrication conditions. Surprisingly, the only lubricant to reduce the temperature in the cutting region for both CT and UAT is water, whereas silicon lubricant and cutting fluid either do not affect the temperature or increase it. Such results apparently show that the influence of reduction in the friction forces at the tool–chip interface on the cutting temperature is less than the insulation effect of reduced heat conduction to the environment due to the presence of the lubricant in the cutting region. Temperatures in the chip demonstrate the same trend as in the cutting tool with slight decrease in the chip temperature for water-lubricated conditions and temperature growth for all other lubrication conditions compared to dry turning.

The influence of the depth of cut on the temperature in the cutting tool and chip is also studied. The following cutting conditions are used when machining Inconel 718: $n = 85$ rev/min, $s = 0.2$ mm/rev, workpiece diameter $D = 40$ mm and d is varied from 0.05 to 0.1 mm. The infrared images illustrating the temperature growth in the tool and chip with the increase in the depth of cut d are shown in Figure 5.41 (the observation is performed along Z-axis in Figure 5.6).

An increase in cutting temperatures is explained by greater amount of the material removed per unit time for greater values of d, and consequently greater values of the work of plastic deformation and friction at the tool–chip interface.
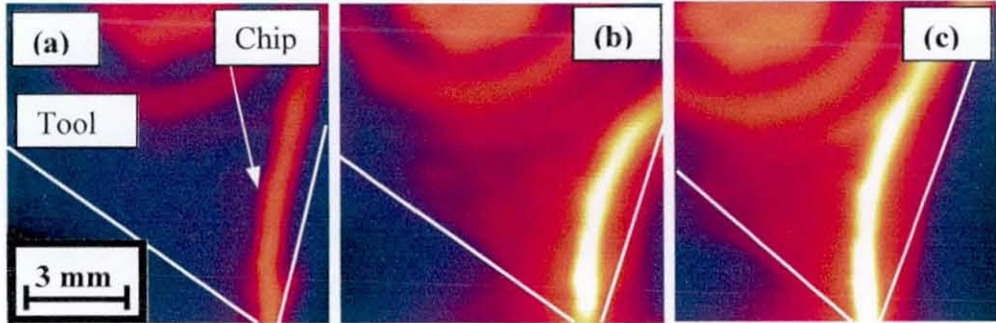
Figure 5.41 Temperature distribution in the cutting tool for different depths of cut in CT of Inconel 718: (a) $d = 0.05$ mm, (b) $d = 0.08$ mm, (c) $d = 0.1$ mm.

Turning of Inconel 718

Infrared images of the end clearance face of the cutting tool as observed along X-axis in Figure 5.6 are compared for CT and UAT of Inconel 718 (Figure 5.42). The following cutting conditions are used: $n = 40$, 85 and 125 rev/min, $s = 0.03$, 0.05 and 0.1 mm/rev, $d = 0.1$ mm, workpiece diameter $D = 4$ mm, and no lubrication is applied. The rotational speeds of 40, 85 and 125 rev/min correspond to cutting speeds V_C of 0.08, 0.18 and 0.26 m/s, which are calculated according to the following formula:

$$V_C = \frac{\pi n D}{60}.$$

The observed temperature is consistently higher for the ultrasonically vibrating tool and for the chip in UAT compared to those in CT for all studied cutting conditions. In order to make a quantitative comparison between IR images, the temperature is measured along two lines on the end clearance face of the cutting tool. The lines start from the tool tip and go along the intersection between the end clearance face and either rake face or flank of the tool (see lines 1 and 2, respectively, in Figure 5.39). Figure 5.43 shows the evolution of the surface temperature in the cutting tool with the distance from the tool tip along these lines.
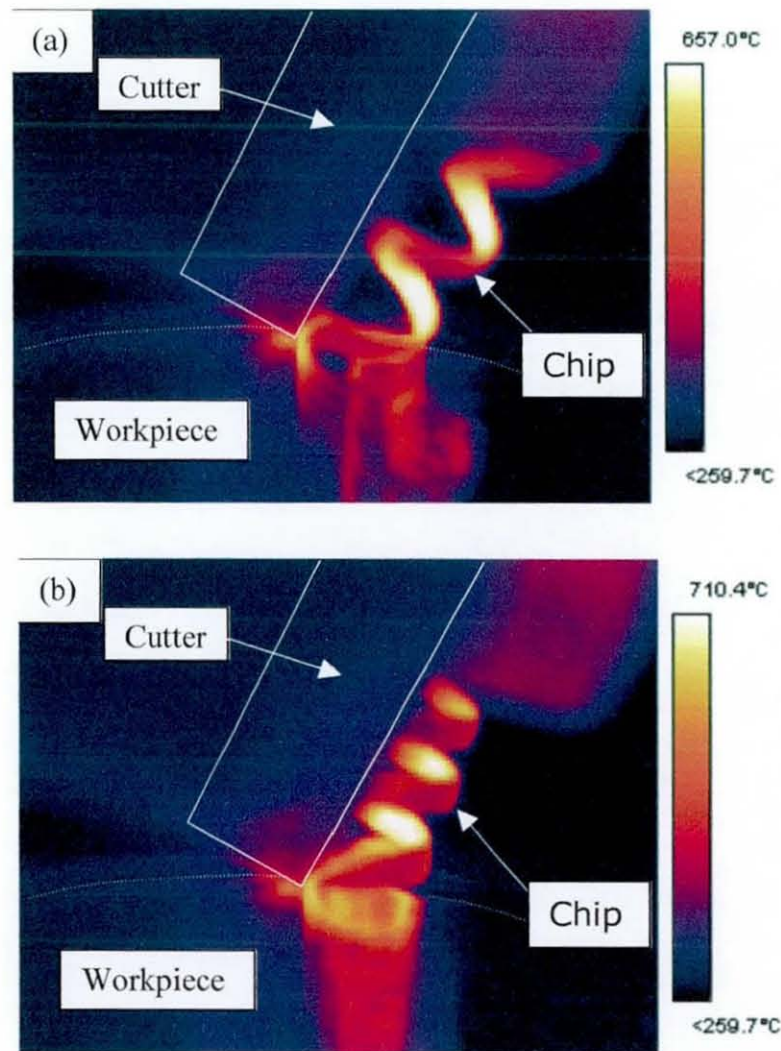
Figure 5.42 IR images of the cutting tool – workpiece interaction in CT (a) and UAT (b) of Inconel 718 ($n = 125$ rev/min, $s = 0.1$ mm). The emissivity of the image is adjusted to depict temperature magnitudes in the chip ($\varepsilon = 0.24$).

A steady exponential decrease in the temperature magnitudes is observed along both lines for UAT and CT. The temperature in the ultrasonically vibrating tool is greater compared to that in CT near the cutting tip, as well as in the distant parts of the tool. The relative difference in the tip temperature between CT and UAT varies from 20 to 70°C, depending on the cutting conditions. This is equivalent to the 4÷8 % difference when temperatures in °K are used for relative comparison. This difference is bigger for more severe cutting conditions (i.e. higher cutting speeds or feed rates), when greater overall temperatures are attained in the chip and tool volumes (see Table 5.7). The difference between maximum temperature in the chip in the processing zone and

temperature in the tool tip is quite significant and ranges between 10 and 20 % for both CT and UAT. Increase in either feed rate or cutting speed leads to temperature growth in the chip and tool for both cutting techniques.
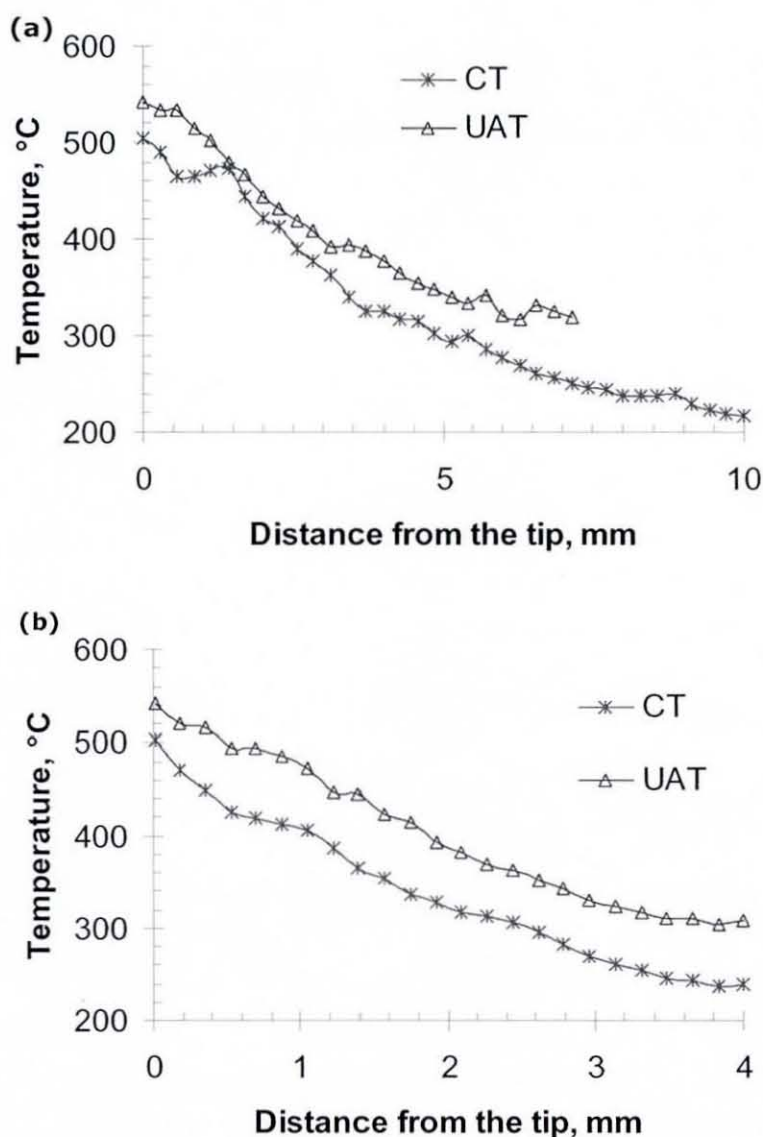
Figure 5.43 Temperature distribution in the cutting tool during CT and UAT of Inconel 718 along the lines 1 (a) and 2 (b) (experimental data)

For $V_c = 0.25$ m/s, $s = 0.1$ mm (these cutting conditions are close to those used in FE simulations in Chapter 7), the temperature of the tool's surface rapidly drops by nearly 300°C along both lines and for both cutting techniques (Figure 5.43), thus creating sharp temperature gradients in the tool. The maximum attained temperature

levels are 540 and 500°C for UAT and CT, respectively; hence the absolute temperature in the tool for UAT is 5 % higher than that for CT.

Table 5.7 Maximum temperatures in the cutting tool and chip when cutting Inconel 718

Cutting conditions	CT		UAT	
	Chip	Tool tip	Chip	Tool tip
n = 40 rev/min, s = 0.03 mm/rev	270	220	290	240
n = 40 rev/min, s = 0.05 mm/rev	300	240	>300	260
n = 85 rev/min, s = 0.1 mm/rev	530	380	580	420
n = 125 rev/min, s = 0.1 mm/rev	660	510	720	580

It may also be interesting to study the relative temperature growth in the cutting tool as compared to the temperature levels in no-load operation mode. This is performed in Figure 5.44, which indicates that the relative temperature increase in
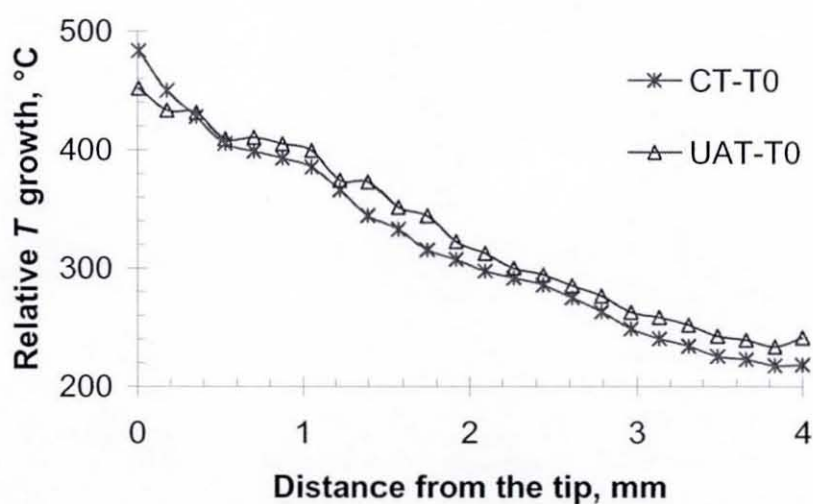
Figure 5.44 Temperature growth in the cutting tool relative to temperature levels in no-load operation mode when CT and UAT of Inconel 718 (along the line 2)

the tool is very similar for both cutting techniques with the maximum difference between the curves for CT and UAT being about 30 °C. In fact, relative temperature growth for the tool tip may be even higher in the case of CT.

An interesting phenomenon is registered during infrared thermography experiments. Under certain cutting regimes, the chip radius of curvature grows dramatically and practically straight chip is produced (Figure 5.45). This effect is observed for both CT and UAT and for the same cutting conditions when the usual, curled chip is produced. Hence, this phenomenon cannot be explained purely by combination of process parameters, but rather complex processes at the tool tip and can be connected with tool wear or certain tool vibration modes. This observation reminds one that metal cutting is a very complex material shaping process, where observed macroscopic phenomena result from interplay of a wide range of micromechanical mechanisms.
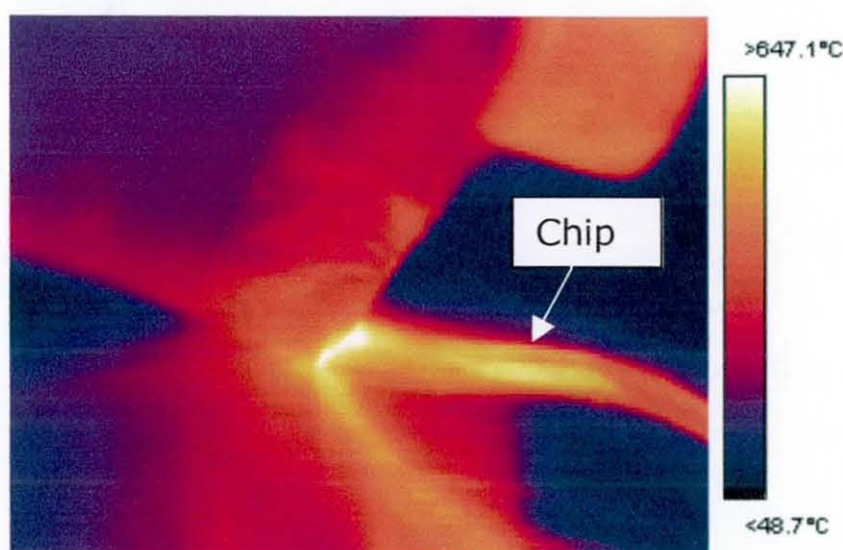
Figure 5.45 Chip formation with a big radius of curvature registered in UAT of Inconel 718 ($n = 125$ rev/min, $V_C = 0.26$ m/s, $s = 0.1$ mm) under some cutting regimes

Higher temperatures observed in the UAT cutting procedure can be explained by additional energy supplied into the system due to ultrasonic vibration, the different chip formation mechanism and the increased yield strength level of the material due to higher strain rates. This experimental result obtained with the high-precision equipment is quite surprising, since previous estimations [85] indicated lower

temperatures for UAT. Kumabe does not provide any information on how the temperature in UAT and CT was measured, however, infrared thermography was not yet used at the end of 1970s, hence it can be assumed that tool-workpiece thermocouple methods are likely to have been used. Markov [18] argues that thermocouple methods are not sufficiently reliable under conditions of dynamic load, when the cutting tool periodically moves away from the chip. Consequently, it is believed that present results are more reliable than previous temperature estimations for UAT.

It should be pointed out that infrared measurements of temperature in turning are limited to the surface temperature distribution. Additionally, the rake face of the tool cannot be seen due to chip separation processes. Numerical (FE) simulations are, therefore, an important tool, which allows an in-depth look at the details of transient thermal properties inside the workpiece and cutting tip. A comparison between experimental and numerical results will be presented in Chapter 7, although significantly different size and time scales of temperature measurements in the cutting tool and its numerical estimations make a direct quantitative comparison difficult to perform.

5.6 Cutting force measurements

5.6.1 Introduction

A significant reduction in cutting forces in UAT was reported by many researchers (for example, [2, 89, 105, 124]) and it is a well-established phenomenon. Such data, however, considerably depends on the specific features of the ultrasonic cutting system, materials used in turning, types of cutting edges, use of lubrication, and cutting parameters. No research has been found, which contains a systematic study of force reduction in UAT depending on all above-mentioned parameters. Above all, there were no experiments performed before with a particular UAT test rig, designed at Loughborough University. Hence, investigations of cutting forces in comparison between CT and UAT were considered as an important part of the full-scale study of the UAT technique.

5.6.2 Instrumentation

The quartz three-component Dynamometer (Type 9257A) produced by Kistler Instruments AG is used in the experiments. This piezoelectric dynamometer bolted to the cross-slide of the Harrison 300 lathe is used for turning tests, and the ultrasonic system is mounted on the top of the dynamometer.

The general description of piezoelectric dynamometers is given in Chapter 2. The dynamometer comprises four three-component force sensors, hence all three force components can be measured. The output voltage of the built-in charge amplifier is proportional to the applied force. A high rigidity of the system provides measurements practically without displacement; thus the dynamometer does not noticeably affect the stiffness of the tool – workpiece system. The cut-off frequency of the built-in filter is 200 Hz and the charge amplifier possesses a big time constant, consequently leading to the elimination of the high frequency component of the force during turning. Hence, the force measured with the dynamometer is an average cutting force, which in the case of UAT is averaged over a large number of cycles of ultrasonic vibration.

A Philips PM8043 analog X-Y recorder is connected to the output of the dynamometer and provides with cutting force component versus time graphs plotted with a pen on A4-format paper. Only one component of the cutting force can be recorded at a time. The difference between main cutting force component, tangential to the surface of the workpiece and perpendicular to its axis, and the component of the cutting force acting in the feed direction is about an order of magnitude, therefore in all the case studies only the main component of the cutting force is considered to compare CT and UAT. The X-Y recorder is calibrated with a spring balance in the quasistatic mode prior to dynamic force measurements in turning. A smoothing system in the X-Y recorder allows to register only low-frequency oscillations in the cutting force.

5.6.3 Experimental procedure

The X-Y force scale is adjusted before each run to accommodate the cutting force for specific turning conditions. The following cutting conditions are varied in tests: $d = 0.1 \div 0.3$ mm, $s = 0.03 \div 0.1$ mm/rev, $n = 40 \div 125$ rev/min. The present design of the mounting attachment does not allow precise setting of depth of cut, thus it

contributes as an additional error factor in the experiment. Except for the several runs, where lubrication effect was studied and thus dry cutting conditions are needed, a lubricant Hocut B60 is applied on the surface of the workpiece. All the runs start with CT, with ultrasonic vibration switched off; the force in CT is measured for 40-80 s, and after that ultrasonic vibration is switched on. Then cutting conditions are adjusted, for example lubrication is applied with a brush onto the surface of the workpiece or feed rate is adjusted. The run continues in the UAT mode for sufficient time (typically some 60 s) to obtain the stable magnitude of the cutting force. After that, vibration is switched off and the force is measured under new cutting conditions for CT. Tests with different rotation speeds require stopping the lathe, adjusting lathe controls and restarting the spindle.

There is a number of error factors in the force measurement experiments, such as the change in the behaviour of the autoresonant control system, wear of the cutting edges and the amount of lubrication applied. These factors and impossibility to set the depth of cut with a high precision in the current design of the testing rig lead to a certain scatter in the force measurements. However, the general tendencies discovered and described below allow a number of consistent conclusions to be drawn.

5.6.4 Experimental results and discussion

The cutting force on the X-Y plots oscillates with a low frequency of about 1.5 – 3 Hz. Higher frequency oscillations are not seen on X-Y plots because of the chosen time scale (from 5 to 10 s/cm) and smoothing analog system of the X-Y recorder. When connecting an oscilloscope directly to the output of the sensors in the dynamometer, the cutting force oscillations with a frequency of some hundred Hz are registered for CT. Switching on ultrasonic vibration leads to the superimposition of the high-frequency oscillations on this signal.

Cutting forces are studied in turning two different metals: mild steel and Inconel 718. There are a lot of parameters influencing the cutting force and complicating its precise measurements, such as the depth of cut, tool wear, the angle of tip orientation (depending on the transducer orientation), and the amount of applied lubrication. These parameters are not controlled accurately in the experiment, and they are therefore sources of error in the measurements. Nevertheless, consistent data has

been collected in these tests, indicating some general dependencies for cutting forces in CT compared to UAT.

The following tests are carried out on Inconel 718 workpieces of about 40 mm in diameter. Dependence of the main cutting force on the feed rate in turning is studied. The following cutting parameters are used: n = 40 rev/min, d = 0.1 mm. The cutting force in UAT (F_{UAT}) is invariably much lower than the cutting force in CT (F_{CT}). This correlates well with observations given in different studies (see Section 4.2.3). The ratio F_{CT} / F_{UAT} is considerably greater at low feed rate (3-4 times), and stabilizes at about 1.6 times at higher feed rates. With an increase in the feed rate from 0.03 rev/min to 0.1 rev/min, the cutting force in CT doubles, whereas that in UAT grows about fivefold (Table 5.8), but still remains much lower than F_{CT}. The increase in the cutting force with a growth in the feed rate is obviously explained by an increase in the material removal rate, i.e. amount of the material removed in unit time. The difference in the ratio F_{CT} / F_{UAT} for the lowest and highest feed rates can be attributed to the change in the contact area and separation line between the cutter and workpiece material.

Table 5.8 Cutting forces in CT and UAT of Inconel 718 for different feed rates

Feed rate s, mm/rev	F_{CT}, N	F_{UAT}, N	F_{CT} / F_{UAT}
0.03	120	30-40	3-4
0.05	170	100	1.7
0.08	205	120	1.7
0.1	255	160	1.6

The influence of the lubrication on the cutting force is also studied (Figure 5.46). The workpiece is degreased with alcohol before turning. The following cutting conditions are used: n = 40 and 85 rev/min (i.e. 0.08 and 0.18 m/s, respectively), s = 0.03 rev/min, d = 0.2 mm. The reduction in the cutting force with application of the lubricant onto the surface of the workpiece for UAT is from 15 to 45 % for different test runs, which is about double the reduction observed for CT. The ratio F_{CT} / F_{UAT} in dry turning is about 5 and 3 for n =40 and 85 rev/min, respectively.
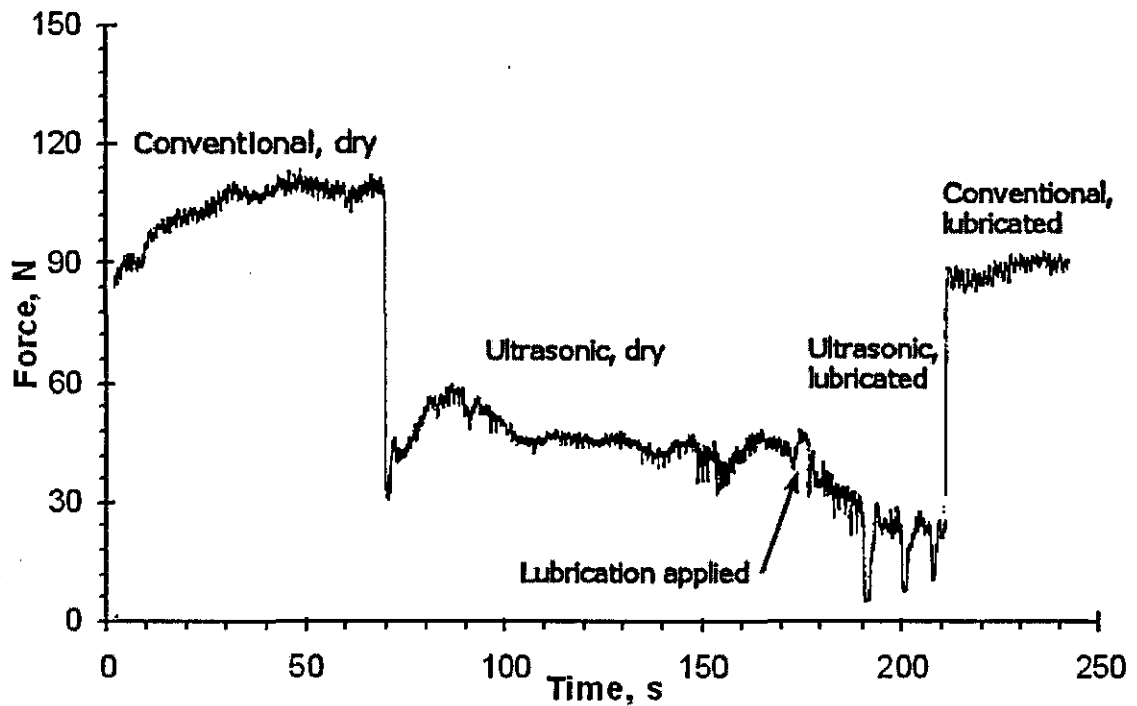
Figure 5.46 Study of the lubrication effect on cutting forces in UAT in comparison to CT

The influence of the cutting speed on the cutting forces is analysed. With an increase in n from 40 to 125 rev/min, the force in CT slightly decreases from 140 to 130 N, whereas the force in UAT grows from 60 to 95 N. A drop in the CT force is explained by the lower fracture toughness of the workpiece material at higher strain rates resulted from greater cutting speeds. An increase in the UAT force is caused by the increased time of the contact between the cutting tool and chip, with the cutting speed getting closer to its critical value ($v_t = 2\pi af$).

Mild steel workpieces (D = 50 mm) are also tested in the experiments. This material is much easier to cut than Inconel 718 and cutting forces are therefore about 5 times smaller for similar cutting conditions. Higher rotation speeds are studied (up to 370 rev/min or surface speed about 1 m/s). For n = 370 rev/min the ratio F_{CT} / F_{UAT} is around 1.5, and for slower rotation speeds increases to about 2.5. The difference in the force reduction at high cutting speeds for Inconel 718 and mild steel can be explained by significantly lower toughness of mild steel, leading to greater amplitudes of ultrasonic vibration during turning compared to those in UAT of Inconel 718.

To sum up, the decrease in the cutting force largely depends on the process parameters, such as the depth of cut, rotational speed of the spindle and feed rate. The cutting force in machining Inconel 718 and mild steel ranges for tested combinations of the process parameters from about 1.5 to 5 times lower values for UAT compared to CT, and varies for UAT from about 100 to 250 N for Inconel 718 and from 25 to 160 N for mild steel. The force consistently increases with an increase in cutting speed, feed rate or depth of cut, and it decreases by 15-40 % for lubricated cutting conditions compared to dry turning.

Chapter 6 Finite element simulations: separation-type model

6.1 Introduction

As it was already noticed above, an adequate computational analysis of the UAT process should take into consideration the geometry of chip formation, elasto-plastic material properties with strain-rate effects and thermal softening, contact interaction and friction at the tool–chip interface, and thermomechanical coupling. Incorporating all these features into a single FE model is a challenging task that should be implemented gradually increasing the complexity extent in order to validate the model at every stage of its development. A purely mechanical FE model of contact interaction between the elasto-plastic workpiece material and cutting tool is considered in this chapter. The model of both CT and UAT is built using MSC Marc/Mentat general FE code [13].

6.2 Model description

An orthogonal turning process with vibration in the tangential direction (direction of cutting velocity) is considered. Figure 6.1 shows a scheme of relative movements of the workpiece and cutting tool; the rotation axis of the cylindrical workpiece is directed along Y-axis. Dimensions of the part of the workpiece used in FE simulations are 1.25 mm by 0.5 mm with the uncut chip thickness t_1 being 0.1 mm. The model is developed under the plain strain assumption and initially consists of approximately 1000 four-node isoparametric elements with bilinear interpolation of displacements; the number of elements increases to about 1700 during the simulation due to remeshing in the process zone. The characteristic size of the element in the process zone is 10 μm (Figure 6.2).

In the model the workpiece moves with a constant velocity, which corresponds to

the cutting speed V_C and equals 300 mm/s. Kinematic boundary conditions providing this type of movement are applied to the left, right and bottom sides of the workpiece, whereas its top surface is free:

$$V_x\big|_{AH} = V_C, \quad V_x\big|_{FG} = V_C, \quad V_x\big|_{HG} = V_C, \quad V_y\big|_{AH} = 0, \quad V_y\big|_{FG} = 0, \quad V_y\big|_{HG} = 0. \qquad (6.1)$$
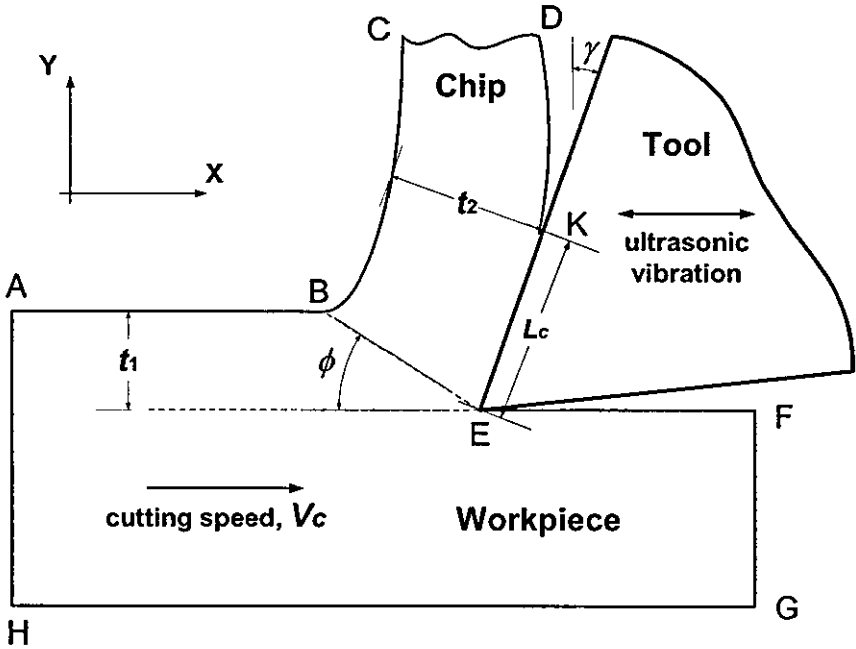
Figure 6.1 A scheme of relative movements of the workpiece and cutting tool in orthogonal UAT simulations. The magnitudes of cutting parameters are given in the text
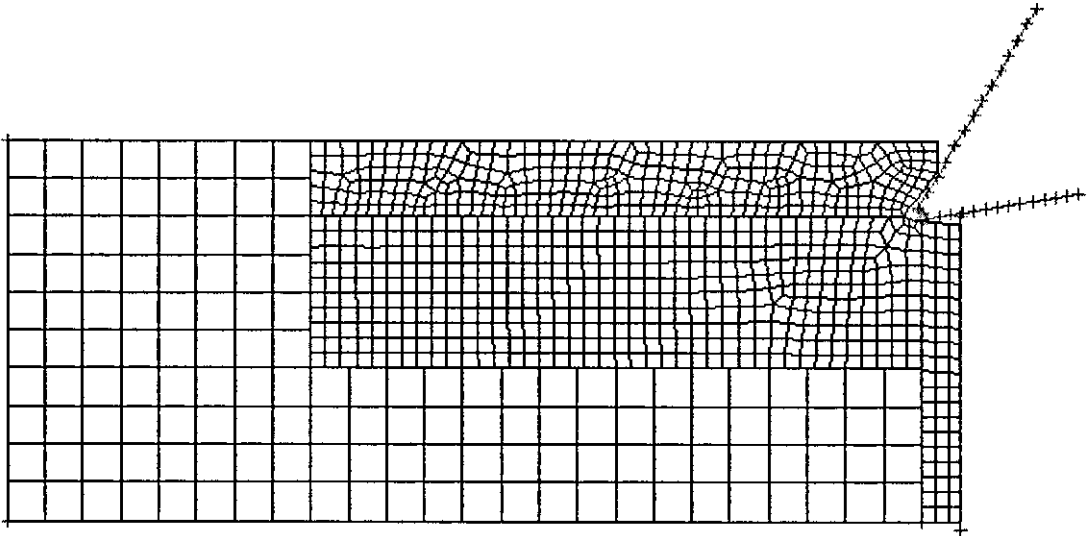
Figure 6.2 Finite element mesh for the workpiece in the initial configuration (before engagement with the cutting tool)

The cutting tool (rake angle $\gamma = 30°$) is rigid and immovable (in simulations of the CT process) or vibrates harmonically in the tangential direction in UAT simulations:

$$u_x = -a\cos\omega t, \quad u_y = 0, \tag{6.2}$$

where $\omega = 2\pi f$, the frequency f = 20 kHz and amplitude a = 13 μm.

The velocity of the cutting-tip vibration is described by the relation $\dot{u}_x = v_t \sin\omega t$, where $v_t = 2\pi a f \approx 1600$ mm/s. Thus $v_t > V_C$, providing a condition for separation of the cutter from the chip within each cycle of ultrasonic vibration.

The material modelled in all simulations is Inconel 718, which elasto-plastic behaviour – in terms of the stress-strain relation – is described by the Ramberg-Osgood constitutive equation [120] (see also Section 5.2.3):

$$\sigma_Y = \sigma_{Y_0} + K_Y \left(\varepsilon^p\right)^{1/M_Y}, \tag{6.3}$$

where ε^p is plastic strain, σ_{Y_0} is initial yield stress, K_Y is a coefficient of plastic resistance, and M_Y is the hardening exponent. The stress-strain curve for Inconel 718 used in simulations is shown in Figure 6.3 [120]. In this model, the thermal
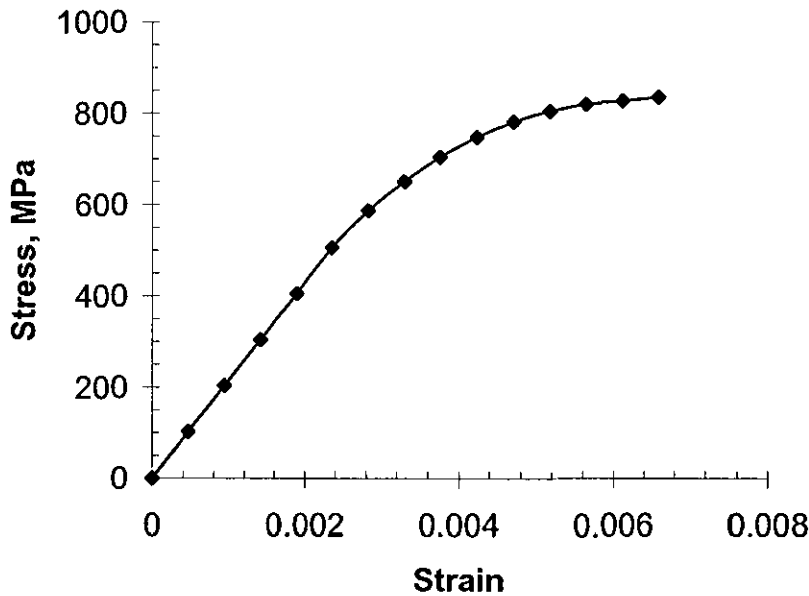
Figure 6.3 The Ramberg-Osgood stress-strain relation for Inconel 718

dependence of material properties, strain-rate sensitivity and thermal softening of Inconel 718 are neglected; these will be included in the coupled thermomechanical analysis at the next stage of modelling (see Chapter 7).

A frictionless contact interaction is considered between the cutting tool and workpiece in the current model; frictional effects are studied in the advanced model described in Chapter 7. The FE model also presupposes formation of the continuous chip, which is in good agreement with the results of high-speed filming experiments and analyses of chip microstructure, demonstrating a considerable reduction in chip segmentation for transition from the CT to UAT.

6.3 Results of simulations and discussion

The chip formation process in CT simulations is modelled from the initial contact between the cutting tool and workpiece at $t=0$ to a state of the fully formed chip $t = 0.00125$ s (Figure 6.4). The contour bands in the figure represent von Mises (equivalent) stresses:

$$\sigma_{eq} = \left(\frac{3}{2} s_{ij} s_{ij}\right)^{1/2}, \quad s_{ij} = \sigma_{ij} - \frac{1}{3}\sigma_{kk}\delta_{ij}, \quad i,j,k = x,y,z, \tag{6.4}$$

where σ_{ij} and s_{ij} are components of the Cauchy stress tensor and its deviatoric part, respectively, and δ_{ij} is the Kronecker delta. The stress distribution changes during the initial stage of the simulation: the region occupied by stresses exceeding the yield strength propagates gradually along the surface of the workpiece and moves into the depth of the workpiece in the vicinity of the cutting tip. However, a steady-state stress distribution (as in Figure 6.4d) is observed as soon as the chip is fully formed.

The time increment, chosen for the CT simulations is $2.5 \cdot 10^{-6}$ s, thus the entire analysis till the transition to the steady-state behaviour (in terms of stress levels in the process zone) requires 500 increments and takes about two hours of CPU time on HP 9000 workstation with 1 Gb RAM.

Due to the high levels of deformation in the process zone in the direct vicinity of the cutting edge, the local magnitudes of equivalent plastic strain

$$\bar{\varepsilon}^p = \int\left(\frac{2}{3}\dot{\varepsilon}^p_{ij}\dot{\varepsilon}^p_{ij}\right)^{1/2} dt, \quad i,j = x,y,z \quad \text{exceed unity, and elements in this zone could}$$

become highly distorted, leading to the accuracy degradation and even the premature termination of the analysis. To overcome this obstacle, an automatic remeshing procedure is used in the regions with a high degree of element distortion. The remeshing in such zones of the workpiece and chip material is carried out either periodically (usually each 5 increments), or in case of considerable changes in the aspect ratios or angles of finite elements.
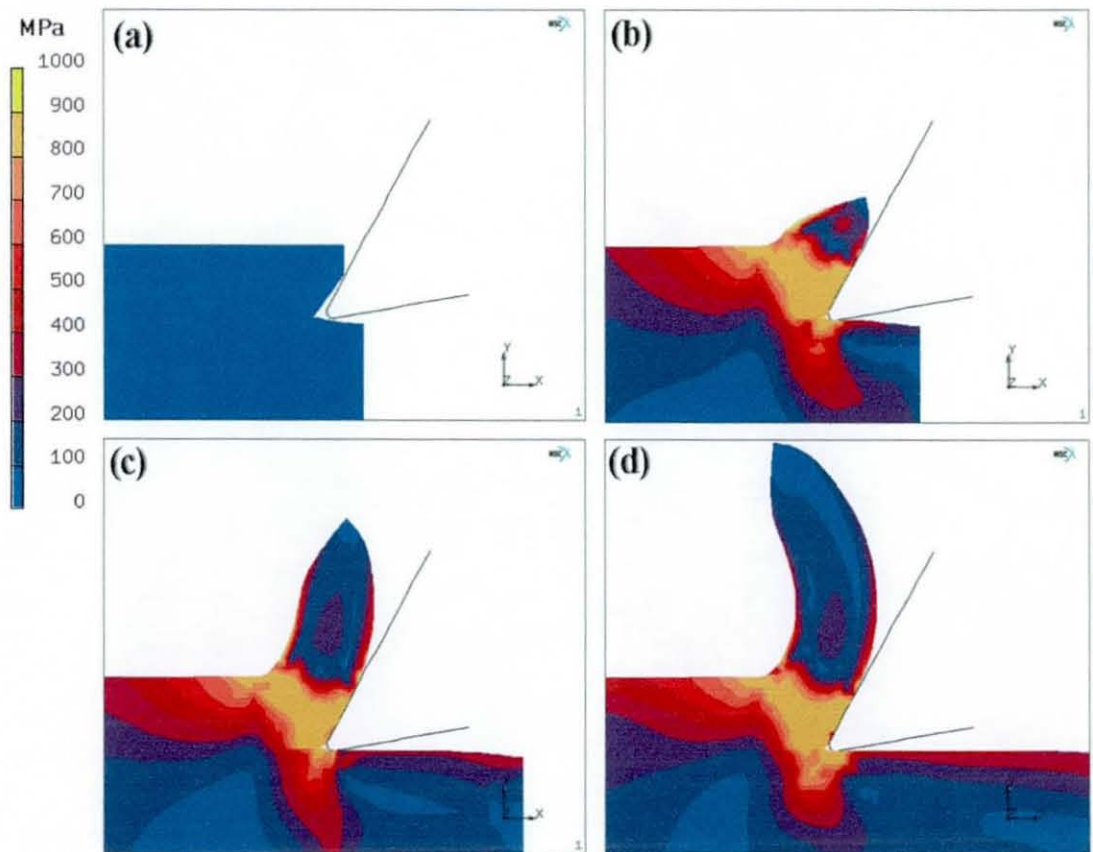
Figure 6.4 CT simulations: chip formation process and distribution of von Mises stresses: (a) $t = 0$, (b) $t = 0.00025$ s, (c) $t = 0.00075$ s, (d) $t = 0.00125$ s. The frame size is 0.7 mm by 0.6 mm. A notch of 50 μm is introduced (a) to improve the convergence at the beginning of the simulations

Contrary to modelling the general cases of crack propagation in solids with *a priori* unknown paths, the separation of the material in the turning process occurs in the vicinity of the cutting edge, which moves along the kinematically prescribed line in two-dimensional simulations. Hence, the material separation in front of the cutting edge can be considered along a predefined line and is subject to a critical stress

criterion, i.e. material fails when nodal stresses reach a specified critical value. Models of cutting with separation along a predefined line are reviewed in Chapter 3.

Ultrasonic vibration is "switched on" at the stage of the fully formed chip, i.e. the CT simulation is restarted with the ultrasonically-vibrating cutting tool. Figure 6.5 shows characteristic stages of a single cycle of vibration, which modelling takes 40
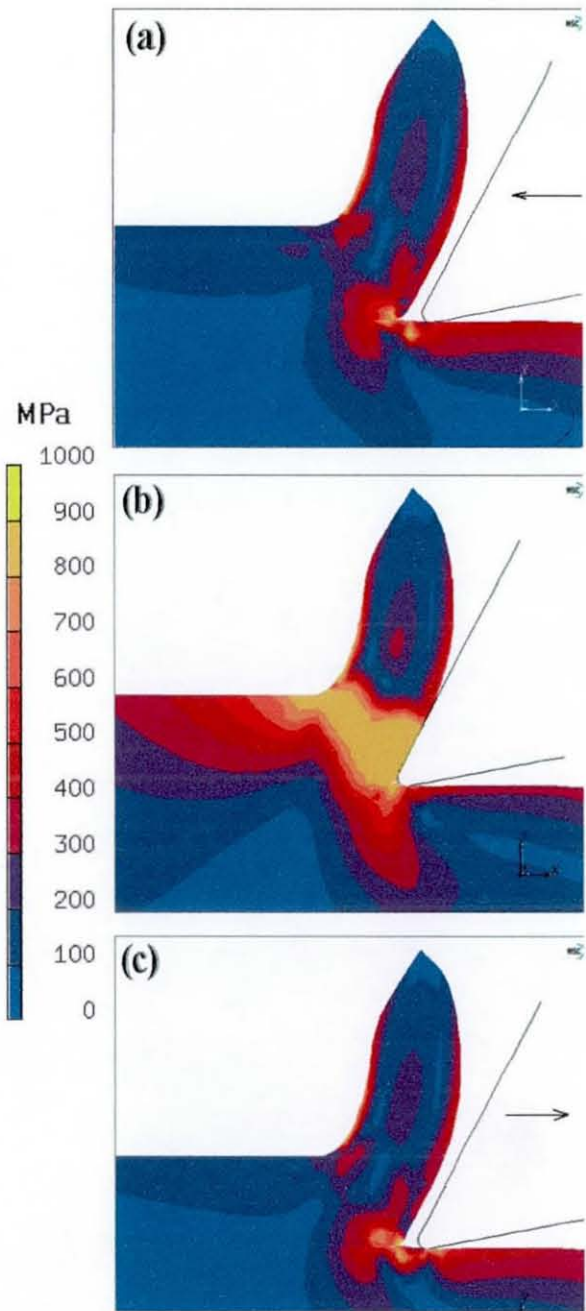
Figure 6.5 Distribution of von Mises (equivalent) stresses for UAT simulations at different moments of a single cycle of vibration: (a) cutter approaching the chip, (b) cutter in full contact with the chip, and (c) cutter moving away from the chip

time increments ($1.25 \cdot 10^{-6}$ s each) for $f = 20$ kHz. The cutting process during the cycle of vibration could be divided into four main stages. During the first stage the cutter approaches the chip, in the second stage the cutter contacts the chip and starts penetrating into the workpiece causing the chip separation. The attainment of the maximum penetration depth is characterized by highest levels of generated stresses in the process zone and marks the end of the second stage. The following stage is unloading: the tool moves backwards and remains in contact with the chip even after the moment when the tool speed exceeds the cutting speed (due to the elastic spring-back effect). During this phase, the relaxation of elastic stresses in the process zone takes place. The last stage, starting with the full separation of the cutting edge from the chip, is the withdrawal of the cutter from the chip. It is worth noticing that the cutting tip remains in contact with the newly-cut workpiece surface at all times.

In contrast to the steady-state stress distribution in CT simulations, a transient stress distribution is observed for UAT. During the approach and withdrawal stages of the ultrasonic cycle, the region with high stresses is situated in the vicinity of the separation point and between this point and the cutting tip. As soon as the cutter comes into the contact with the chip, the zone with equivalent stresses more than 800 MPa starts propagating from the cutting tip towards the chip's backside (along BE, Figure 6.1), forming a band with the mean thickness of 60 μm. At the beginning of the unloading stage of the cycle of vibration, the zone with high stresses begins shrinking in the direction of the cutting tip, gradually diminishing to the size it had at the approach stage (i.e. before the tool contacts the chip). During the withdrawal stage, the stress distribution in the process zone remains nearly unchanged. Hence, the greatest level of stresses during the cycle of vibration is attained within the penetration stage, whereas the stresses are significantly smaller in the rest of the cycle.

An important point is that the stress distribution in the process zone during the penetration phase of the cycle of ultrasonic vibration (Figure 6.5b) is similar to the steady-state stress distribution in CT (Figure 6.4d). Hence, during the considerable part of the ultrasonic cycle stresses are noticeably lower than those in CT. Consequently, mean magnitudes of stresses and, more generally, cutting forces are considerably lower in UAT. Figure 6.6 demonstrates levels of forces acting on the cutting tool when CT and within a single cycle of ultrasonic vibration when UAT:

the average force in CT is 65 N for a chosen material model and cutting conditions, whereas in UAT, by contrast, the average force is only 26 N. The cutting force in UAT reaches its maximum at the penetration stage of the cycle of ultrasonic vibration and rapidly declines at the withdrawal stage. The force magnitude is fluctuating between zero and small positive values when the cutter approaches or moves away from the chip; this is explained by the transient interaction between the cutter and the workpiece surface, as well as by the numerical error inherent in simulations. A reduction in average cutting forces correlates well with experimental measurements of cutting forces studied in Section 5.6 and with the reported experimental results (e.g. [18, 85]). It is also in good agreement with the behaviour of ductile materials under this kind of loading [125].
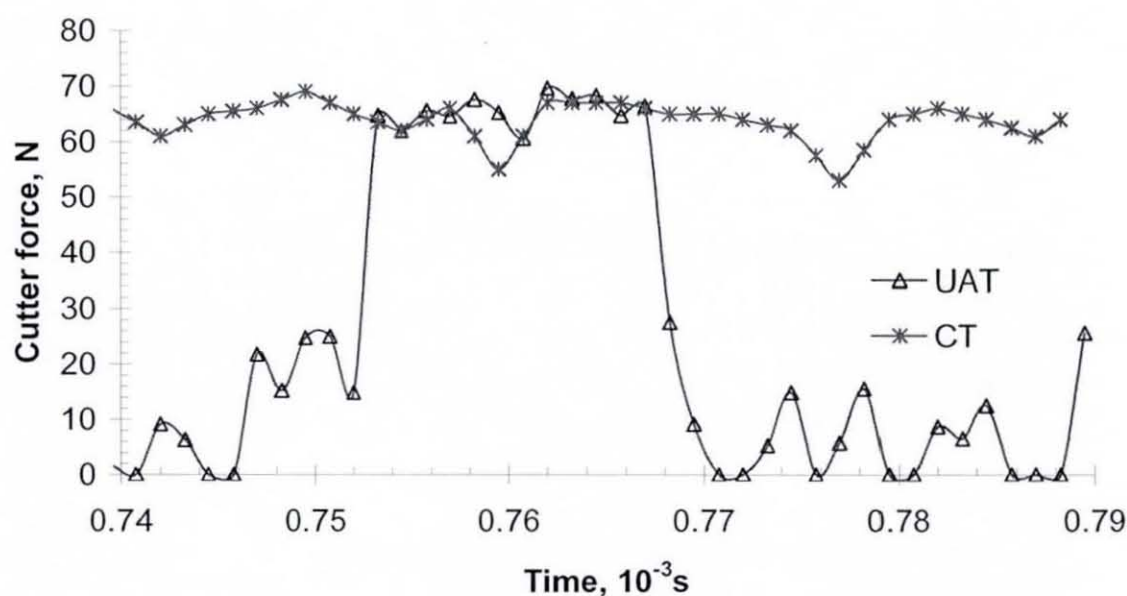
Figure 6.6 Forces acting on the cutting tool in CT and within a single cycle of ultrasonic vibration in UAT

Another important feature of UAT is the non-permanent character of the contact between the cutting tool and workpiece surface: the cutter remains in contact with the chip only during the penetration and unloading phases, making it about 40% of the cycle of vibration (Figure 6.7). Obviously, this amount depends on the ratio between the cutting speed and cutting tip velocity. The biggest attained length of the contact L_c (Figure 6.1) between the chip and the cutter within the cycle of vibration is 80 μm (Figure 6.7), which is equal to the steady-state value of L_c in CT. Different contact

conditions between the cutter and chip in UAT and CT influence thermal boundary conditions and friction.

The chip thickness ratio $R = t_1/t_2$ is approximately 0.8 for both CT and UAT simulations. Hence, the shear plane angle φ (Figure 6.1) can be estimated as $\varphi = \tan^{-1}\left(\dfrac{R\cos\alpha}{1 - R\sin\alpha}\right) \approx 50°$, providing fair agreement with the well-known Merchant equation [7] (which ignores material hardening effects): $\varphi = \pi/4 - (\lambda - \alpha)/2 = 60°$ (λ is the friction angle that vanishes for the frictionless contact).
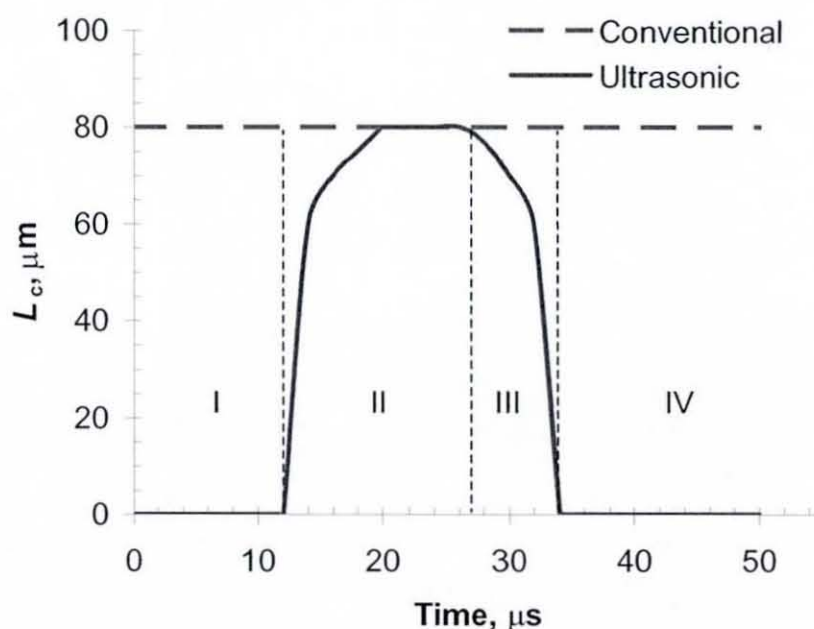
Figure 6.7 Simulated contact lengths L_c for CT and UAT. Stages of the cycle of vibration for UAT: approach (I), penetration (II), unloading (III) and withdrawal (IV)

The maximum magnitudes of equivalent plastic strains ($\bar{\varepsilon}^p$) observed in CT simulations are about the half of those in UAT simulations (Figure 6.8). However, the maximum plastic strains in UAT are concentrated within the vicinity of the cutting tip, whereas strains at the backside of the chip and along the rake face of the tool are similar to those attained in CT in the respective regions. The major difference between distributions of plastic strains in CT and UAT simulations is a presence of the area with a high level of plastic deformation along the newly formed

workpiece surface in the material machined with UAT, together with high levels of plastic strains in the vicinity of the vibrating cutting tip.
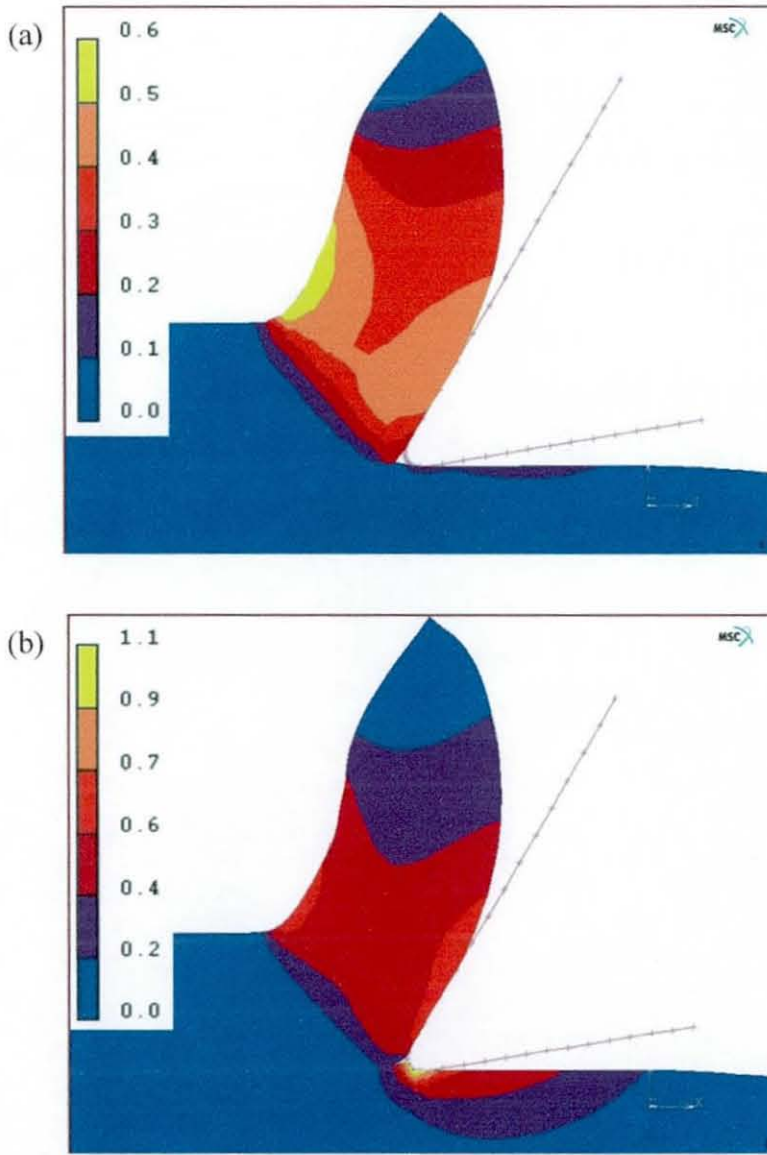
Figure 6.8 Distribution of equivalent plastic strains in (a) CT and (b) UAT simulations ($t = 0.76$ ms)

Residual strains in the machined layer are estimated after the end of CT simulations. Figure 6.9 shows the dependence of equivalent plastic strain $\bar{\varepsilon}^{\mathrm{p}}$ on the distance from the surface. Residual strains in the machined layer diminish more than fivefold within 100 μm from the surface. This agrees reasonably with the results of nanoindentation tests, indicating an 85 μm hardened layer for CT.

Equivalent plastic strain rates ($\dot{\bar{\varepsilon}}^p$) observed in CT simulations attain the highest magnitudes in the shear plane (BE in Figure 6.1) and occupy the band of the nearly constant width (30 μm) inclined at an angle $\varphi * = 55°$ to the X-axis. The maximum magnitude of $\dot{\bar{\varepsilon}}^p$ for CT is about 10^4 s^{-1}. For UAT simulations $\dot{\bar{\varepsilon}}^p$ are the largest during the penetration stage and they are also concentrated in the shear plane. The maximum level of $\dot{\bar{\varepsilon}}^p$ for UAT is observed in the vicinity of the cutting edge and attains approximately 10^5 s^{-1}. Hence, the maximum $\dot{\bar{\varepsilon}}^p$ levels are about an order of magnitude higher in UAT; this is explained by an increase in the maximum relative velocity between the chip and cutting tool due to the ultrasonic vibration of the latter.
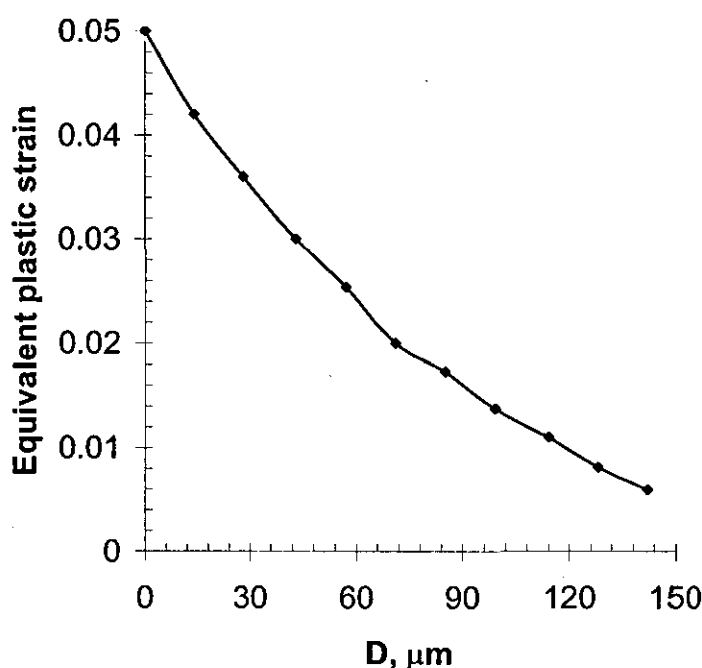
Figure 6.9 Residual plastic strains in the CT-machined surface layer (simulation results)

6.4 Concluding remarks

An elasto-plastic FE model for UAT is proposed as an enhancement of the model for CT to explore microstructural processes at the cutting tool–chip interface for both cutting techniques. A detailed comparison based on the numerical analysis of the transient stress distribution during the cycle of ultrasonic vibration and the steady-state stress distribution in CT has shown that the mean stress levels in the process

zone and, consequently, cutting forces are considerably lower for UAT, which correlates with known experimental results. In CT, the cutting tool stays in a permanent contact with the chip throughout the entire cutting process. In UAT, by contrast, the cutter remains in contact with the chip only about 40% of the time for chosen vibration parameters, according to FE simulations. Different contact conditions between the cutter and chip in UAT and CT influence evolution of thermal processes and the friction type, causing differences in the chip formation observed experimentally in high-speed filming experiments. The next stage of numerical investigations, described in Chapter 7, incorporates additional analysis features, such as thermomechanical coupling, frictional effects, and advanced material properties, into the FE model of the cutting techniques.

Chapter 7 Coupled thermomechanical simulations: deformation-type model

7.1 Introduction

A purely mechanical model of UAT was presented in the previous chapter. In the present chapter, a fully thermomechanically coupled model of the UAT is developed. It incorporates a range of other enhancements compared to the initial model. It includes a description of the advanced material behaviour, taking into consideration nonlinear hardening and strain-rate sensitivity effects of the material during cutting. It also takes into account various heat-transfer, friction and cooling conditions at the tool–chip interface. The description of this model, results of various numerical case studies and comparison with experiments are given in the following sections.

7.2 Contact heat transfer

Temperature in the cutting zone is one of the most important factors in metal turning. High temperatures can significantly affect the cutting process, leading to material softening (i.e. reduction in the yield stress) and influencing other material properties, such as the coefficient of thermal expansion, specific heat and thermal conductivity.

Thermal processes in turning comprise heat generation in the workpiece material due to its plastic deformation and creation of new surfaces, frictional heating at the tool–chip interface, contact heat conduction between the chip and tool, and convective heat transfer from free surfaces of the workpiece, chip and tool to the environment. The mechanisms of the last three factors (frictional heating, contact heat conduction and convective heat transfer) and their consequent boundary conditions will be described in this section.

Obviously, contact heat transfer in UAT between the chip and tool occurs only during the time of their contact, in contrast to permanent contact heat transfer in CT. This contact is along the line OB in Figure 2.5 with a maximum contact length L_c in a vibration cycle, which is nearly equal to the constant contact length at CT (as obtained in FE simulations described in Chapter 6).

There is a number of surface conditions arising in the mathematical theory of heat conduction, several of which can be applied to turning: (i) prescribed surface temperature, (ii) linear heat transfer at the surface, (iii) the separation surface of two media with different conductivities K_1 and K_2, and (iv) radiation from the surface. Condition (iii) can be complicated in cases when there is a contact resistance between the media, or if there is a heat source between them, as in the case of frictional heating. Various surface conditions are described below according to Carslaw and Jaeger [126].

Condition (i) $T = T_0$ at the surface is the easiest, but, in practice, it is often difficult to prescribe the surface temperature, and such cases are therefore can be better represented by condition (ii) [126]. The case of linear heat transfer presupposes that the flux across the surface is proportional to the temperature difference between the surface temperature and temperature of the environment, i.e.

$$q = h(T - T_\infty),$$ (7.1)

where T_∞ is the temperature of the surrounding medium and h is a constant. Hence, the boundary conditions in this case can be written as:

$$-K \frac{\partial T}{\partial x} = h(T - T_\infty),$$ (7.2)

where K is thermal conductivity of the body and x-axis is normal to the interface between the media.

Such boundary conditions are not, however, entirely accurate for the case of natural convection from the surface, i.e. the process of heat conversion from hot body into the surrounding fluid or air. It is found experimentally that in this case the flux across the surface is proportional not to the difference $(T - T_\infty)$, but to $(T - T_\infty)^{5/4}$ [126]. Nevertheless, for extremely short times of natural convection into

the air numerically simulated for turning with FE (described below), the difference with linear convection is negligible. Thus, the boundary condition (7.2) is used in simulations.

Radiation from the body surface is proportional to the $\left(T^4 - T_\infty^4\right)$, i.e.

$$q = \sigma\varepsilon(T^4 - T_\infty^4),\tag{7.3}$$

where σ is the Stefan - Bolzmann constant and ε is emissivity of the surface, that is the ratio between the heat emitted by the body to that emitted by the black body at the same temperature. Radiation from the chip and tool surfaces is used in our infrared thermography experiments, however, this boundary condition is usually reduced to (7.1) in various analyses, and few exact solutions for problems with the radiation boundary condition (7.3) can be found [126].

The case (iii), i.e. of the separation surface of two media with different conductivities k_1 and k_2, can be subdivided into different subcases. The simplest is the subcase, when there is no thermal resistance between the media. In that case, the heat flux and temperature are continuous on the boundary between bodies, and as

$q_i = -K_i\dfrac{\partial T_i}{\partial x}$ for $i = 1, 2$, the boundary condition is:

$$\begin{cases} K_1 \dfrac{\partial T_1}{\partial x} = K_2 \dfrac{\partial T_2}{\partial x} \\ T_1 = T_2 \end{cases} \quad \text{at } x = 0,\ t > 0.\tag{7.4}$$

However, such a boundary condition is possible only for a very close contact between the surfaces of two adjacent bodies, such as soldered surfaces. Typically, there is thermal contact resistance between the media, such that:

$$q = H(T_1 - T_2),\tag{7.5}$$

where H is a contact heat transfer coefficient, and $R = \dfrac{1}{H}$ is a thermal resistance constant. Contact heat transfer coefficient H is a very complex parameter, which in the case of cutting depends on contact pressure, parameters of the workpiece and tool, the type of the lubricant, cutting temperature and surface roughness. Schneider [127] argues that the mechanism of heat transfer across a solid-to-solid thermal contact is difficult to describe analytically, since this process depends on the unit pressure and total force exerted on the contacting surfaces. According to

experimental data, the solid-type conductance constitutes a substantial part of the total conductance of the contact joint at high contact pressures, whereas it constitutes only a minor part of the total conductance at low pressures. The process is further complicated by the physical nature of the contact bond, i.e. the type and distribution of surface irregularities, material hardness and the possibility of plastic flow. Other influencing parameters are the quantity and physical properties of the fluid / lubricant trapped between the contacting surfaces and the mean temperature of the interface [127]. In this case, the heat flux can be still continuous across the boundary between the media, but the temperature is discontinuous, and the boundary condition takes the form:

$$\begin{cases} K_1 \dfrac{\partial T_1}{\partial x} = K_2 \dfrac{\partial T_2}{\partial x} \\ -K_1 \dfrac{\partial T_1}{\partial x} = H(T_1 - T_2) \end{cases} . \tag{7.6}$$

The last subcase can be further complicated if there is a heat source on the surface of separation, e.g. when there is friction between the contacting bodies. The full description of the mathematical solution for this subcase can be found in [128]. It is introduced here with the current notation.

The thermal flux q cannot be described in the case when heat is generated at the interface, unless a more specific model of the interface is considered. There are two different analytical models for lubricated and dry friction conditions (Figure 7.1). In the models, two media with thermal conductivities K_1 and K_2 are in contact along the plane $x = 0$, contact resistance is created by either air or a layer of lubricant, and heat is generated due to sliding friction at the interface.

For lubricated friction conditions, it is assumed that the heat source S is situated between two thermal contact resistances R_1 and R_2, with the total resistance $R = R_1 + R_2$. In this case, two solid surfaces are separated by a layer of lubrication, and the heat is generated within the lubricant and flows to each solid surface through a film contact resistance. Assuming that the temperature of the lubricant layer is T, according to Eq. (7.5) we can write:

$$q_i = H_i(T - T_i) \text{ or } q_i R_i = T - T_i \text{ for } i = 1, 2 .$$

Lubricant temperature T is eliminated using $R = R_1 + R_2$ and $q_1 + q_2 = S$, and the following condition is obtained:

$$T_1 - T_2 = R_2 S - Rq_1 = -(R_1 S - Rq_2) \text{ at } x = 0.$$

Introducing $N_i = 1 - R_i/R$, the following general form of the condition at the interface is obtained:

$$T_1 - T_2 = R(N_1 S - q_1) = -R(N_2 S - q_2), \quad N_1 + N_2 = 1. \tag{7.7}$$
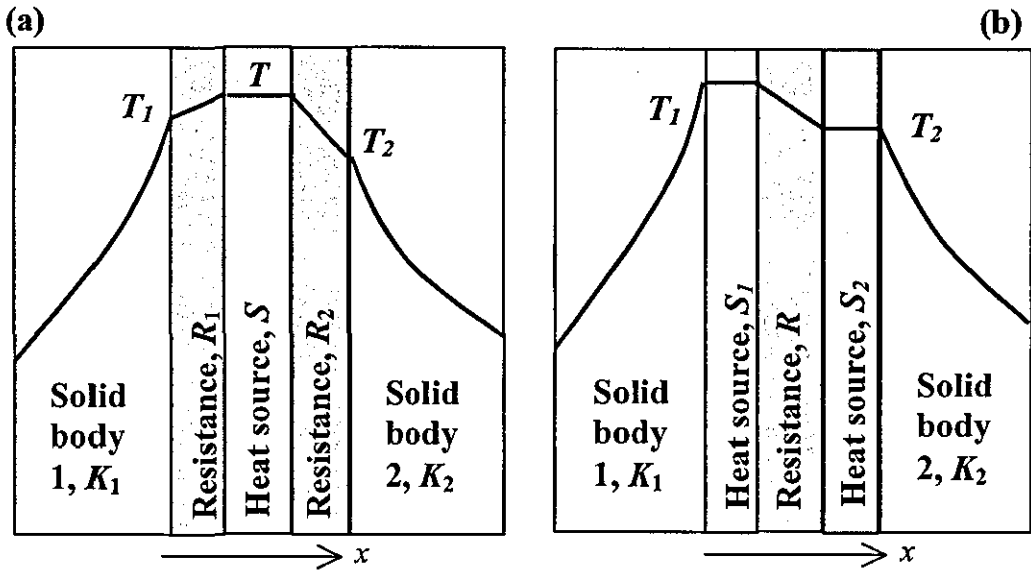
Figure 7.1 Models of heat generation and conductance for lubricated (a) and dry (b) friction conditions at the interface between two solid surfaces (adapted from [128])

For dry friction conditions, it is assumed that heat is generated on each of the solid surfaces by heat sources S_1 and S_2, with $S_1 + S_2 = S$, separated by single contact resistance R (Figure 7.1b). The physical explanation is that heat is generated on each of the sliding surfaces separated by a thin air layer, which constitutes a contact resistance. The total heat S is assumed to be divided between to sources proportionally:

$$S_1 = N_1 S, \quad S_2 = N_2 S, \quad N_1 + N_2 = 1,$$

where N_i is an empirical constant, depending on the surface roughness and the elastic and cohesive properties of the contact materials. As the heat flux flowing

from the body 1 to body 2 across the contact resistance is $S_1 - q_1$, according to Eq. (7.5) it can be written:

$$T_1 - T_2 = R(S_1 - q_1) = R(q_2 - S_2) \text{ at } x = 0, \text{ since } q_1 + q_2 = S = S_1 + S_2. \quad (7.8)$$

Eq. (7.8) for dry friction conditions is equivalent to Eq. (7.7), as $S_i = N_i S$.

Hence, Eq. (7.7) describes the boundary condition at the interface between two solid surfaces with the heat generation and thermal contact resistance for both dry and lubricated friction conditions.

Finally, the boundary value problem for heat transfer across the interface with contact resistance and friction can be formulated. Using $q_i = -K_i \dfrac{\partial T_i}{\partial x}$ for $i = 1, 2$ and Eq. (7.7), the boundary-value problem can be written as

$$\frac{\partial^2 T_i}{\partial x^2} = \frac{1}{\alpha_i} \frac{\partial T_i}{\partial t}, \quad (i = 1, 2), \quad x > 0, \ t > 0 \qquad (7.9)$$

$$T_i = T_0, \quad t = 0, \ x > 0$$

$$T_1 - T_2 = R\left(N_1 S(t) + K_1 \frac{\partial T_1}{\partial x}\right) = -R\left(N_2 S(t) + K_2 \frac{\partial T_2}{\partial x}\right), \ x = 0, \ t > 0, \ N_1 + N_2 = 1 \qquad (7.10)$$

where $\alpha_i = \dfrac{K_i}{\rho_i C_i}$, with ρ_i and C_i being material's density and specific heat, respectively.

A similar formulation is used in numerical (FE) simulations of cutting for the thermal contact with friction between the chip and the cutting tool described below.

7.3 Model description

Turning is accompanied by considerable heat generation in the cutting zone, affecting material properties of the treated workpiece. Hence, adequate computational schemes for turning processes should be fully thermomechanically coupled and take into account main factors affecting stress and strain generation: contact interaction and friction at the tool–chip interface, strain-rate effects, and temperature-dependent material properties. The two-dimensional thermomechanically coupled FE model developed for both CT and UAT is based on the MSC.Marc general FE code [13].

An orthogonal turning process is considered, i.e. the cutting tool edge is normal to both cutting and feed directions. Vibration is applied in the direction tangential to the surface of the workpiece. The same scheme of the modelled relative motion of the workpiece and cutting tool as in Chapter 6 is applicable (Figure 6.1), with the rotation axis of the cylindrical workpiece is orthogonal to the plane of the picture. The dimensions of a part of the workpiece used in plain-strain FE simulations are 2.5 mm in length by 0.5 mm in height with the uncut chip thickness t_1 being 0.1 mm. This part of the workpiece is initially discretized into approximately 2000 four-node isoparametric elements (see Figure 7.2); the number of elements increases during simulations to about 2500 due to remeshing in the process zone. The characteristic size of the element in the process zone is 20 μm, which corresponds to the mean grain size of Inconel 718.
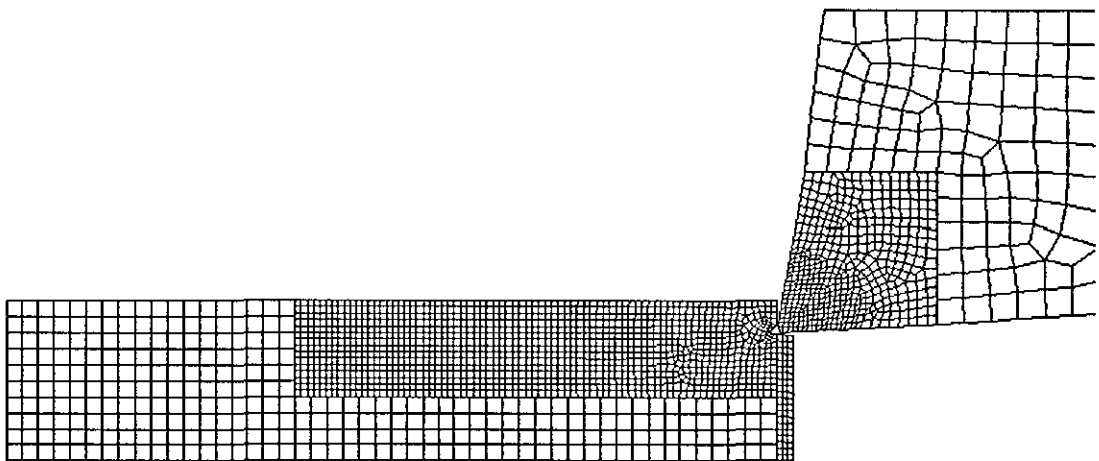
Figure 7.2 Finite element mesh for the workpiece and cutting tool in thermomechanically coupled FE model in the initial configuration (before engagement with the cutting tool)

The cutting tool with the rake angle $\gamma = 7.5°$ is simulated as a rigid body, as its stiffness is significantly higher than that of the workpiece (the tool material is tungsten-carbide). The part of the tool, modelled in FE simulations, is constructed from some 550 four-node, isoparametric, quadrilateral heat-transfer elements. Such elements, not experiencing deformation, allow the study of heat transfer in the tool during the cutting process.

Kinematic boundary conditions applied to the modelled workpiece part enable its translation in y-direction with the cutting speeds $V_c = 150$ mm/s and $V_c = 300$ mm/s, and are described by Eq. (6.1). In UAT simulations, the cutting tool vibrates harmonically around its equilibrium position with the frequency $f = 20$ kHz and amplitude $a = 15$ μm along y-direction (whereas it is immovable in simulations of CT). Such parameters of vibration provide separation of the tool from the chip at each cycle of ultrasonic vibration, as the maximum speed of the vibrating tool exceeds sixfold the cutting speed, thus transforming the constant contact at the tool–chip interface into an intermittent one. Such cutting and vibration parameters correspond to those employed in the turning tests with CT and UAT techniques.

Thermal boundary conditions include convective heat transfer from the workpiece, chip and tool free surfaces to the environment:

$$-K\frac{\partial T}{\partial n} = h(T - T_\infty),\tag{7.11}$$

where K is the conductivity of the workpiece or tool material, n is the outward normal to the surface, h is a convective heat transfer coefficient, and T_∞ is the ambient temperature. The thermal flux passing from the chip to the cutter at the contact length L_c (Figure 6.1) is described as follows:

$$q = H(T_{\text{chip}} - T_{\text{tool}}),\tag{7.12}$$

where H is a contact heat transfer coefficient, T_{chip} and T_{tool} are chip and tool surface temperatures, respectively.

Initial thermal conditions used in simulations are as follows:

$$\begin{aligned}&\text{CT}: T_{\text{work}}\big|_{t=0} = T_\infty; T_{\text{tool}}\big|_{t=0} = T_\infty;\\&\text{UAT}: T_{\text{work}}\big|_{t=0} = T_\infty; T_{\text{tool}}\big|_{t=0} = T_{\text{ultr}},\end{aligned}\tag{7.13}$$

where T_{work} is workpiece temperature and $T_{\text{ultr}} = 75\,°C$ is initial mean temperature of the tool in UAT, as found in infrared thermography experiments described in Section 5.5.

The Johnson-Cook model [26], accounting for the strain-rate sensitivity, is employed to describe the material behaviour of the aged Inconel 718:

$$\sigma_Y = \left(A + B\varepsilon_p^{\,n}\right)\left(1 + C \ln\left(\frac{\dot{\varepsilon}_p}{\dot{\varepsilon}_0}\right)\right)\left(1 - T^{*m}\right),\tag{7.14}$$

where σ_Y is the yield strength level, $T^* = \left(T - T_\infty\right)/\left(T_m - T_\infty\right)$, ε_p and $\dot{\varepsilon}_p$ are plastic strain and strain rate, and T_m is melting temperature. Parameters $n=0.6522$ and $C=0.0134$ are derived from dynamic tests and adapted from [116], with $A=1241$ and $B=622$ being calculated from quasistatic values of σ_Y, fracture strain and ultimate tensile strength (UTS) for the supplied Inconel 718 workpieces. A term T^{*m} is assumed zero in simulations, until reliable data on coefficient m is found. However, available data [119] for solution-treated and aged Inconel 718 shows that, within the temperature range modelled in FE simulations, maximum thermal softening of Inconel 718 is about $10\div15\%$. The described model is also modified to prevent unrealistically high stress values at high strains, so that maximum stress values are limited to UTS of Inconel 718 at corresponding strain rate (latter reaching 10^5 s^{-1} as FE simulations show), with quasistatic values of UTS being equal to 1450 MPa. As an illustration, the stress-strain diagram for Inconel 718 is shown in Figure 7.3 for strain rate $\dot{\bar{\varepsilon}}^p = 1$.
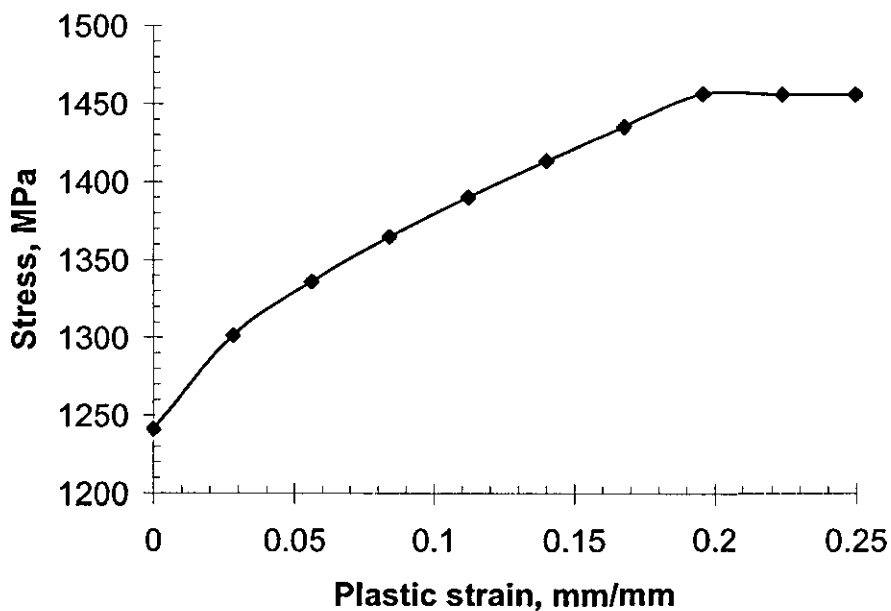
Figure 7.3 Stress – plastic strain relation for Inconel 718 (strain rate $\dot{\bar{\varepsilon}}^p = 1$)

The shear friction model [13] was chosen for simulations of turning, due to the high stress level at the tool–chip interface resulting from the high strength of Inconel 718. Contrary to the simple Coulomb friction model, the friction stress in the shear model depends on the equivalent stress in the material and not the normal force:

$$\sigma_{\mathrm{fr}} \le -\mu \frac{\overline{\sigma}}{\sqrt{3}} \frac{2}{\pi} \mathrm{sgn}(v_r) \arctan(\frac{v_r}{v_c}),$$ (7.15)

where μ is a friction coefficient, $\overline{\sigma}$ is the equivalent stress, v_r is a relative sliding velocity, and v_c is a critical sliding velocity below which sticking is considered. This resolves the problem of the unrealistically high friction force at high contact stresses inherent in the Coulomb model (see also Section 2.4 for the review of friction models in modelling of metal cutting).

During the simulations, elements in the process zone could become highly distorted, leading to degradation in solution accuracy and premature analysis termination. An automatic remeshing/rezoning procedure is used in the workpiece and chip volumes, providing the new mesh when element deviation from its rectangular shape reaches the critical value.

An important feature of the modelling of turning is a material separation criterion in front of the cutting tool. Different approaches can be used here, e.g. material separation along a predefined line, element deletion in the vicinity of the cutting tip, etc. (see Section 3.3 for a detailed description). In the initial FE model of UAT (see Chapter 6), the separation was based on the critical-stress condition. In this Chapter, however, the deformation method, using a plastic flow of the material under the action of the moving cutting tool as a separation criterion, was chosen for numerical simulations due to its better convergence properties (see also Sections 3.4.1 and 3.4.2 for the literature survey).

Continuous chip formation is considered in the simulations. According to the results of the light microscopy and SEM tests (see Chapter 5), chips produced by UAT are invariably continuous, as follows from microstructural analyses of the chip cross-sections. The degree of segmentation in chips was higher for CT, though no shear bands were discovered.

The coupled thermomechanical analysis is performed with a staggered solution procedure [13]: a heat transfer analysis is performed first, followed by a stress analysis at each time step (see Section 3.4.4 for more detailed description of the

staggered procedure). During the mechanical part of the analysis, heat generated by plastic deformation and friction is calculated. The fraction of mechanical energy converted into thermal energy β (Taylor-Quinney coefficient [74]) is equal to 0.9 in simulations; this fraction is suggested as appropriate for metal plasticity in different studies, for example [15]. Thermal conductivity K and specific heat C for Inconel 718 grow linearly from 12 W/m K and 440 J/kg K to 24 W/m K and 680 J/kg K, respectively, with an increase from room temperature T_∞ to 900°C (Figure 7.4). A coefficient of thermal expansion α increases nearly linearly from 12×10^{-6} °C^{-1} to 15×10^{-6} °C^{-1}, as temperature grows from T_∞ to 600°C, and then continues to grow up to 17×10^{-6} °C^{-1}, as temperature rises to 900°C [120].
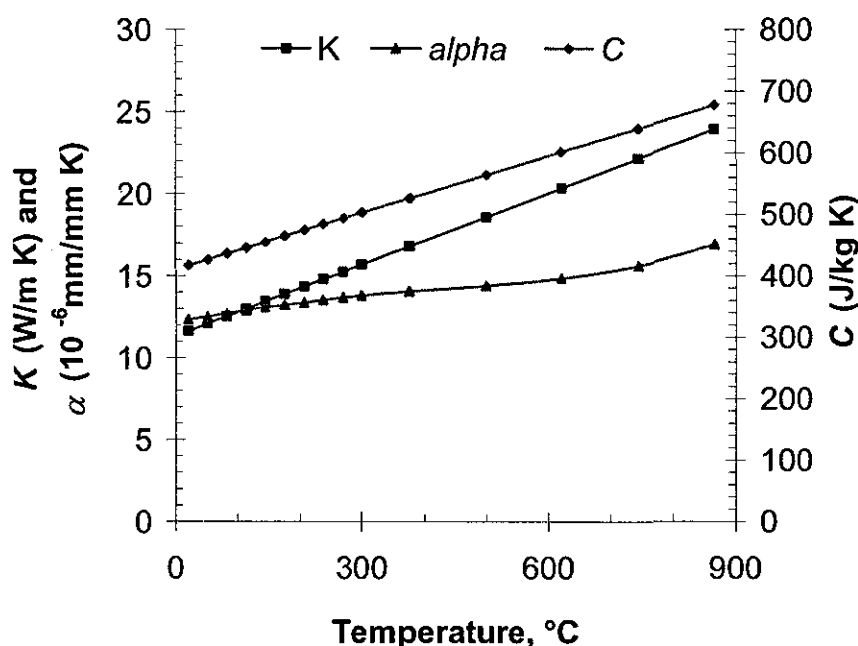
Figure 7.4 Effect of temperature on physical properties of Inconel 718

7.4 Results of simulations and discussion

The cutting process in simulations of CT and UAT is modelled from the moment of the initial contact between the cutter and workpiece until a fully formed chip has been generated. The simulated cutting time is 3 ms for both CT and UAT, and it comprises 60 periods of ultrasonic vibration in UAT simulations, with each period covered by 80 time steps of $6.25 \cdot 10^{-7}$ s. Hence, the total number of time increments

for a single UAT simulation is 4800, which requires in the case of the successful completion about 7 hours of calculation time on Pentium IV, 2 GHz workstation with 512 Mb RAM. The large number of time increments chosen to simulate each cycle of ultrasonic vibration is dictated by the need to limit the maximum rate of the contact interaction between the workpiece and cutting tool in order to ensure the analysis convergence and better accuracy of produced results. As the relative velocity of the workpiece and cutting tool in CT simulations is several times less than that in UAT, larger time steps can be implemented. The simulation time of 3 ms is therefore divided into 1200 time steps of $2.5 \cdot 10^{-6}$ in CT simulations that ensures significantly faster simulation times than those for the UAT model.

Several case studies are performed in order to examine the effect of different thermal and contact parameters on features of the turning process (stress, strain and temperature distributions in the cutting zone) and to investigate the formation process and geometry of the chip. Two contact conditions are studied at the tool–chip interface: (a) a frictionless contact, and (b) a contact with friction ($\mu = 0.5$). In the former case, corresponding to the well-lubricated cutting process, heat generation occurs only due to plastic deformation processes. The latter case accounts for both heat sources (plastic deformation and friction) and also introduces an additional stress-generating factor in the cutting region, which affects the process of chip formation, as it will be shown below. The influence of the change in heat transfer parameters of the workpiece / tool system are also studied: convective heat transfer coefficient h and contact heat transfer coefficient H are varied in the following range: $h = 50 \div 500$ W/m^{2}K and $H = 50,000 \div 500,000$ W/m^{2}K.

Four stages of a cycle of ultrasonic vibration have been described in the previous Chapter (see also [129]) for an uncoupled mechanical formulation of the problem, a different material law and chip separation criterion. These stages – approach, penetration, unloading and withdrawal – are also studied in the present model. The contact between the cutting tool and the chip is continuous for CT and intermittent for UAT, with the duration of the contact depending on the kinematic relation between the vibration parameters (f and a) and cutting speed V_c. For the current values of these parameters the cutting tool remains in contact with the chip 40% of the time.

As it was already described above in Section 7.2, temperature in the cutting zone is one of the most important factors in metal turning and can significantly influence the cutting process. Heat transfer processes are therefore studied in detail in the following paragraphs on a basis of comparison between CT and UAT.

Temperature distributions in the chip and process zone are very similar for both CT and UAT for different values of h, H and μ. A typical temperature distribution in the cutting region is shown in Figure 7.5 with the highest temperatures registered along the contact area at the tool–chip interface. This contact is along the line KE in Figure 6.1 at a contact length L_c, with the values of L_c observed in FE simulations also being similar for both UAT and CT. There is a range of parameters influencing temperature in the cutting tool, one factor is the ratio of the tool–chip contact time to the total process time. Other factors include friction at the tool–chip interface, contact heat conduction regulated by coefficient H, and, finally, the temperature distribution at the chip interface. The latter changes during the cycle of ultrasonic vibration due to the varying rate of plastic deformation caused by the rapidly changing strain rate for different stages of cutter – workpiece interaction. A steady increase in the temperature magnitude in the process zone, chip and cutting tool is caused by the work of plastic deformation and friction for both CT and UAT. Additional energy due to ultrasonic vibration causes higher levels of temperature for UAT, which can be explained at the micro level by the increased deformation rate linked to a growth in the interaction speed between the workpiece and tool. For the majority of cutting conditions, the chip and workpiece temperature stabilises at about 2.5 ms after the simulation commence for both UAT and CT (Figure 7.7). Hence, analyses of temperatures in the cutting region are performed after this moment. However, the full saturation has not been observed within the simulation time for the cutting tool temperatures. This is understandable, since the full saturation of the tool temperatures, experimentally observed in the infrared thermography tests (see Chapter 5), occurs only after about a minute or two of turning, as compared to a much shorter (3 ms) simulation time.

The temperature data for UAT simulations is given for time instants in the approach stage of the cycle of ultrasonic vibration just before the penetration stage, i.e. with the cutting tool not being in contact with the chip yet. It is important to point out that temperature of the cutting tip and in the cutting region attains somewhat higher levels in the penetration part of the cycle of vibration. Figure 7.6 demonstrates

evolution of the maximum temperature in the cutting region within a single cycle of ultrasonic vibration in UAT simulations with friction. The difference between the peak temperature at penetration and temperature levels just before the tool–chip contact reaches nearly 50 °C. After the rapid temperature increase in the penetration stage, the temperature in the cutting region gradually declines in the unloading, withdrawal and approach stages of the cycle until reaching the lowest levels just before penetration. A similar behaviour is observed in the cutting tip, with temperature levels fluctuating considerably during the cycle of ultrasonic vibration in a similar manner. Here, the temperatures in CT and UAT are compared when the cutter does not contacts the chip, as there is a high chance of the numerical error in the temperature estimation for the cutting tip at other time moments, due to the otherwise insignificant overlap of the tool and chip nodes.
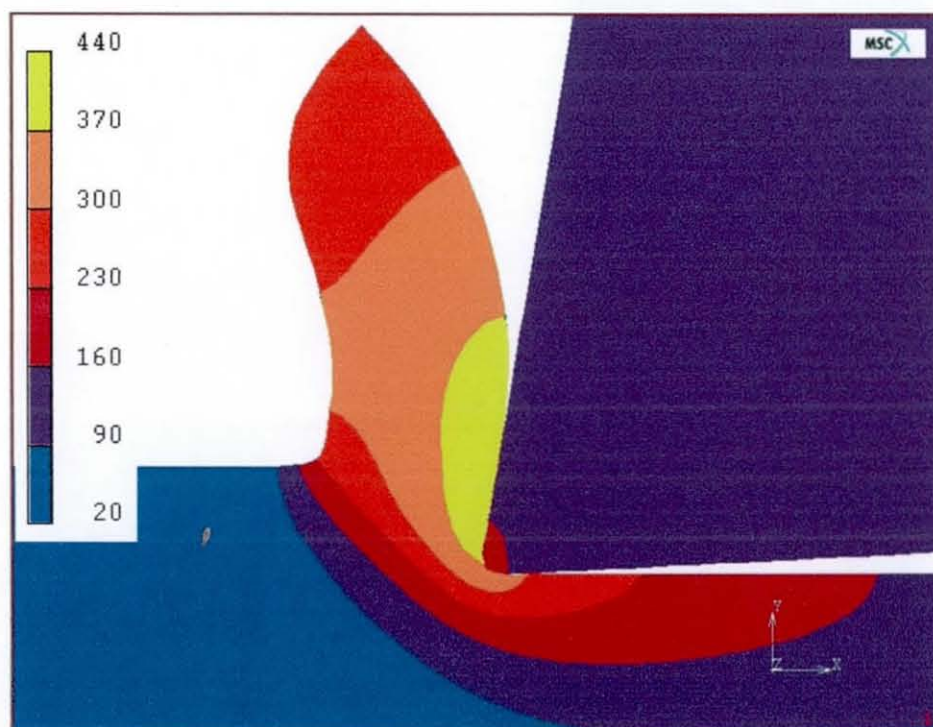
Figure 7.5 Temperature distribution in the cutting region in UAT ($h = 0.5$ W/m^{2}K, H $= 50,000$ W/m^{2}K, $\mu = 0.5$, $t = 2$ ms)

Contact heat transfer coefficient H is a complex parameter that depends on contact pressure, parameters of the workpiece and tool, type of the lubricant, cutting temperature and surface roughness. The interval from 50,000 to 500,000 W/m^{2}K,

considered in this thesis, covers various magnitudes of H for studied cutting conditions and allows investigation of its influence on temperature distributions in the chip, workpiece and tool. Figure 7.7a and Figure 7.7b show temperature evolution in the cutting region for various values of H for UAT and CT, respectively. A tenfold change in contact heat transfer coefficient H – from 50,000 to 500,000 W/m^{2}K – produces significant alterations in temperatures in the cutting region. For $H = 50,000$ W/m^{2}K, the maximum temperature levels, reached in the process zone of cutting, are 440°C and 410°C for UAT and CT, respectively, whereas for $H = 500,000$ W/m^{2}K these temperatures are 395°C and 300°C, respectively. This result could be naturally explained by increased heat flux from the chip into the tool with an increase in H.
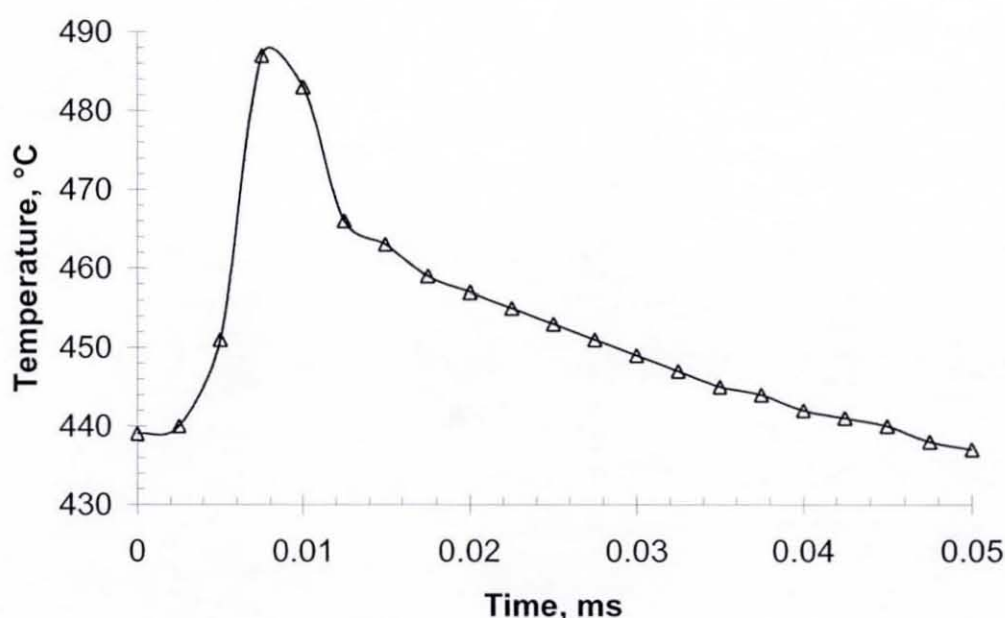
Figure 7.6 Evolution of the maximum temperature in the cutting region within a single cycle of ultrasonic vibration in UAT simulations with friction (after temperature saturation in the cutting region)

The case of free convection (without any coolant) corresponds to the value of convective heat transfer coefficient $h = 50$ W/m^{2}K. With application of coolants the value of h grows and could reach 500 W/m^{2}K for studied cutting conditions, with the value of h depending on properties of coolants and the rate of their supply to the cutting region. Coefficient h insignificantly affects the temperature distribution in the

cutting zone for both types of turning in a similar way, as it is demonstrated in Figure 7.7. The maximum magnitudes of temperature decrease by 15÷20 °C for CT and UAT, respectively, for the increase in h from 50 to 500 W/m²K. Altering coefficient
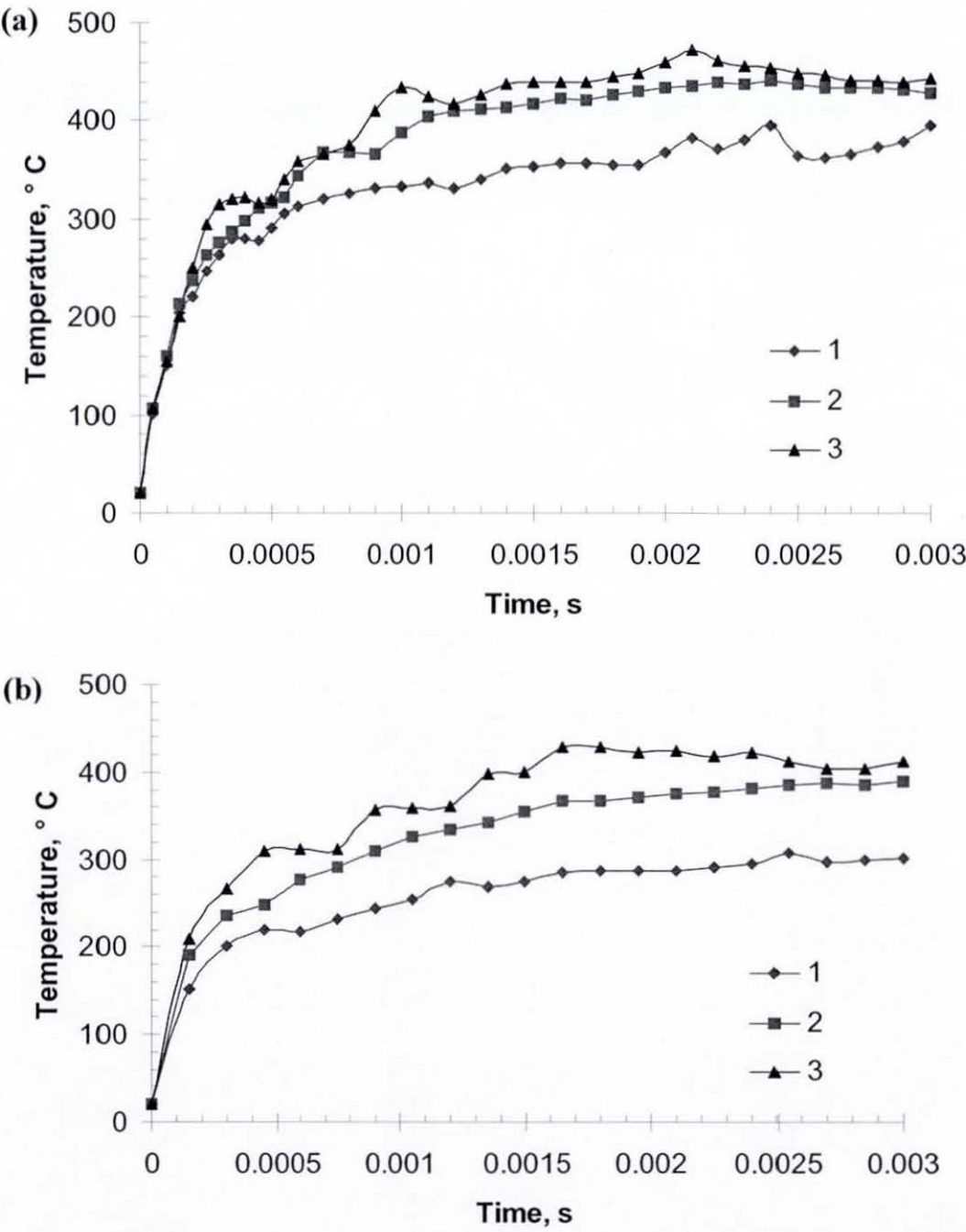
Figure 7.7 Evolution of the maximum temperature in the cutting region in simulations of UAT (a) and CT (b) with friction for different combinations of heat transfer parameters: (1) $h = 0.05$ W/m²K, $H = 500,000$ W/m²K; (2) $h = 0.5$ W/m²K, $H = 50,000$ W/m²K; (3) $h = 0.05$ W/m²K, $H = 50,000$ W/m²K

h in this range does not affect temperatures in the cutting tool, as it will be shown below. The influence of parameter h on simulation results is so negligibly small only due to extremely short simulation time. As an increase in the coefficient h corresponds to introduction of coolant in the cutting region, it should influence temperatures in both the chip and tool considerably more for larger cutting times. The only way to increase the influence of h on temperature levels within short simulation times is to use otherwise unrealistically high magnitudes for it.

The obvious decrease in the workpiece temperature is obtained in simulations of frictionless conditions (Figure 7.8), as heat generation due to friction is removed, with temperatures reaching approximately 380°C and 350°C compared to 440°C and 410°C for UAT and CT, respectively, in the analyses with friction. Still, temperature levels in UAT are higher than those in CT, demonstrating that this temperature difference cannot be attributed to only frictional effects. It is worth mentioning that the nature of friction and, consequently, the friction law is assumed in this thesis to be the same for both CT and UAT.
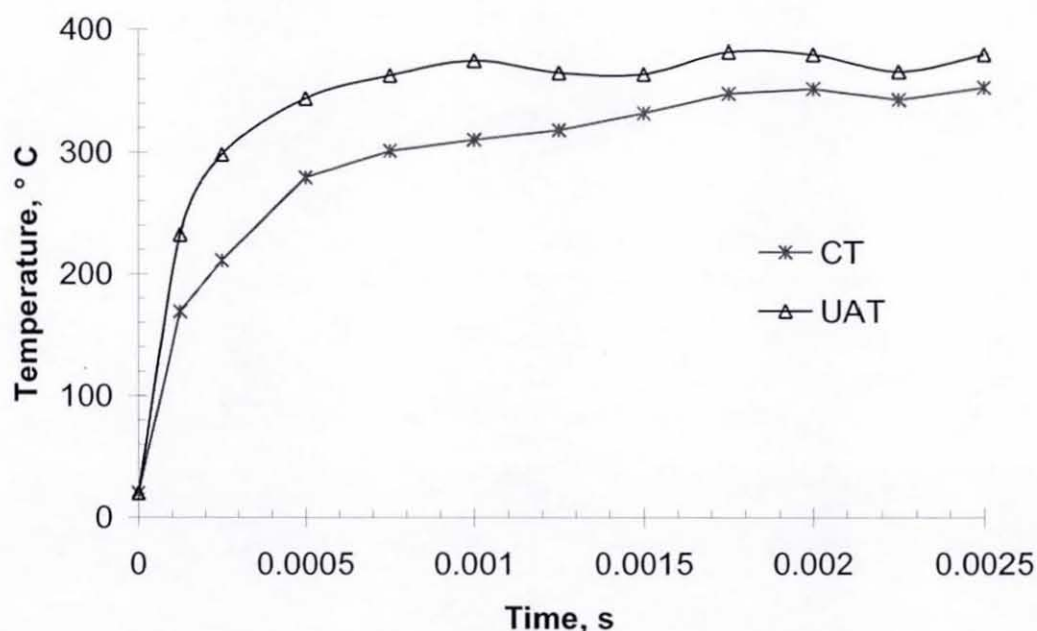
Figure 7.8 Evolution of the maximum temperature in the cutting region in frictionless CT and UAT simulations ($\mu = 0$, $h = 0.05$ W/m^{2}K, $H = 50,000$ W/m^{2}K)

Maximum temperature levels in the process zone and chip invariably higher in UAT simulations for various combinations of the coefficients for convective heat transfer (h), contact heat transfer (H) and friction (μ) than those in CT simulations.

It is, however, discovered that the relative temperature difference between UAT and CT depends on the value of H in FE simulations, growing from 5 % to 17 % for an increase in H from 50,000 to 500,000 W/m²K. The relative temperature difference is nearly insensitive to changes in the convective heat transfer coefficient or absence/presence of friction at the tool–chip interface, varying within 1 %. The results for values of $H = 50,000$ W/m²K are in good agreement with the infrared thermography data: experimental tests indicate 4÷6% increase in temperatures for the process with superimposed ultrasonic vibration compared to CT.

The study of cutting tool temperatures is also carried out in terms of FEA for both CT and UAT. The maximum temperature in the tool is obtained in the cutting tip (point E in Figure 6.1). A nearly steady increase in the cutting-tip temperature is observed in simulations from the moment of the initial contact between the tool and workpiece to the final moment of simulations ($t = 3$ ms) (Figure 7.9). The final temperature magnitudes are about 160°C and 140°C for UAT and CT, respectively.
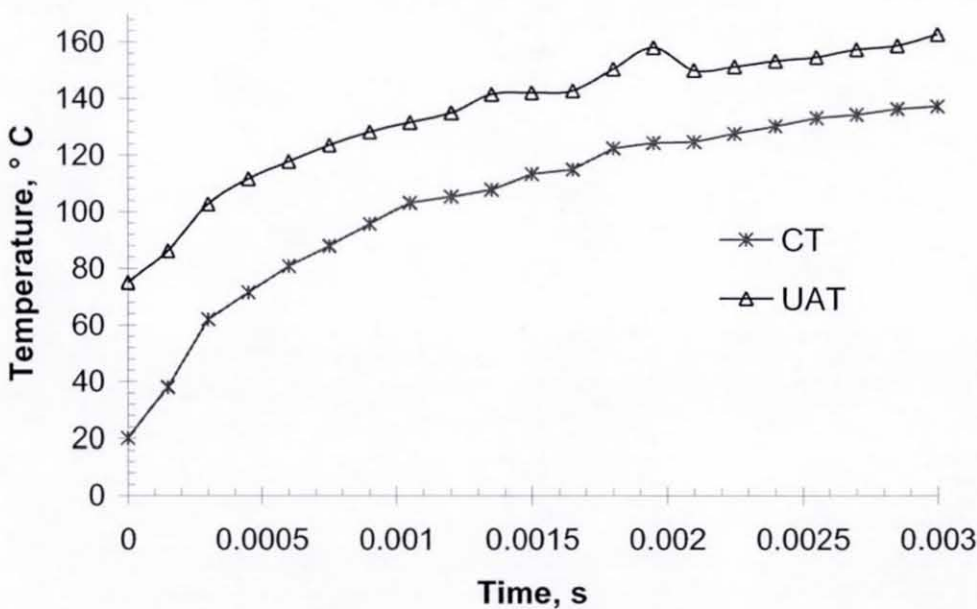
Figure 7.9 Evolution of the cutting-tip temperature in simulations of CT and UAT with friction ($\mu = 0.5$, $h = 0.05$ W/m²K, $H = 50,000$ W/m²K)

Nevertheless, it is worth noticing that the relative temperature difference between the initial and final levels is by 35 % larger in CT simulations, with final UAT temperatures being higher only due to the initial heating of the tool at UAT. Still, FE simulations are in good agreement with our experimental results, also indicating insignificantly higher temperatures for the UAT tool.

The absolute magnitude of the cutting-tip temperature is probably not as important as this qualitative result, because it depends on the friction and contact heat transfer coefficient, with the latter affected by the nature of the contact, type of materials and use of lubricants, thus its specific magnitude can be obtained only by laborious experiments for given cutting conditions. In addition, the simulation time is by several orders of magnitude lower than the time required for temperature in the cutting tool to reach the steady state. The latter time is several seconds as observed in infrared thermography experiments described in Section 5.5.

The evolution of cutting tip temperatures is also analysed for the frictionless case (Figure 7.10). Simulations demonstrate only a marginal increase in the tip temperatures for both UAT and CT (specifically, by 10°C and 35°C for UAT and CT, respectively). This shows that the temperature increase in the cutting tool is largely due to frictional interaction between the tool and chip (at least, for the
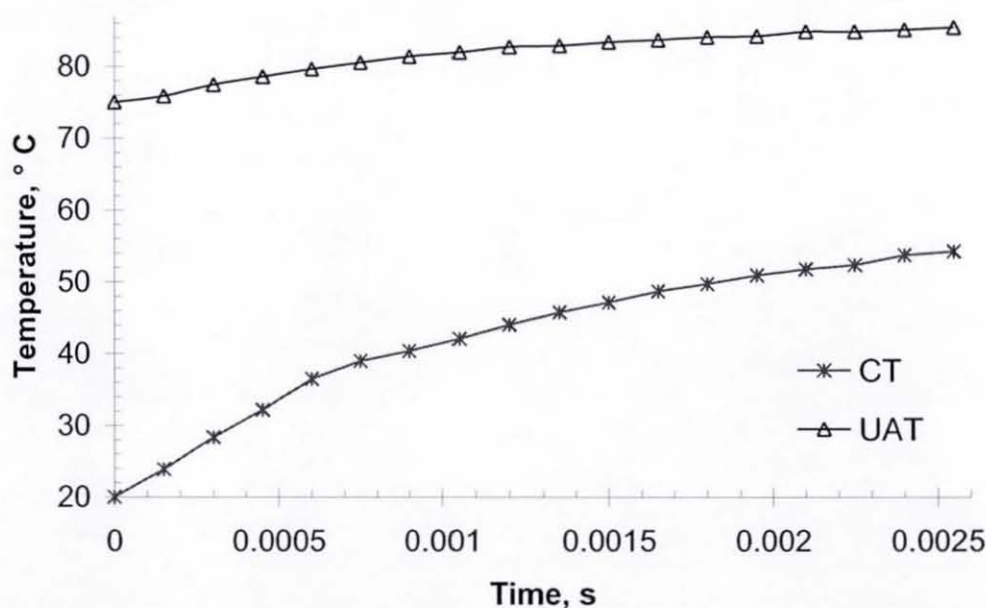
Figure 7.10 Evolution of the cutting-tip temperature in frictionless simulations of CT and UAT (the same conditions as in Figure 7.9)

used $H = 50{,}000$ W/m^{2}K). As in simulations with friction, the tip temperature in CT grows faster than that in UAT, in spite of the final temperature being higher for UAT.

The distribution of temperature in the cutting tool is examined after 2.5 ms of cutting for both UAT and CT along the clearance face of the tool (in the direction tangential to the workpiece surface). A steady exponential decrease from the maximum at the cutting tip to nearly room temperature (in the case of CT) or initial tool temperature $T_{ultr} = 75\,^\circ$C (in the case of UAT) in distant parts of the tool is observed (Figure 7.11). The rate at which temperature diminishes in the cutting tool
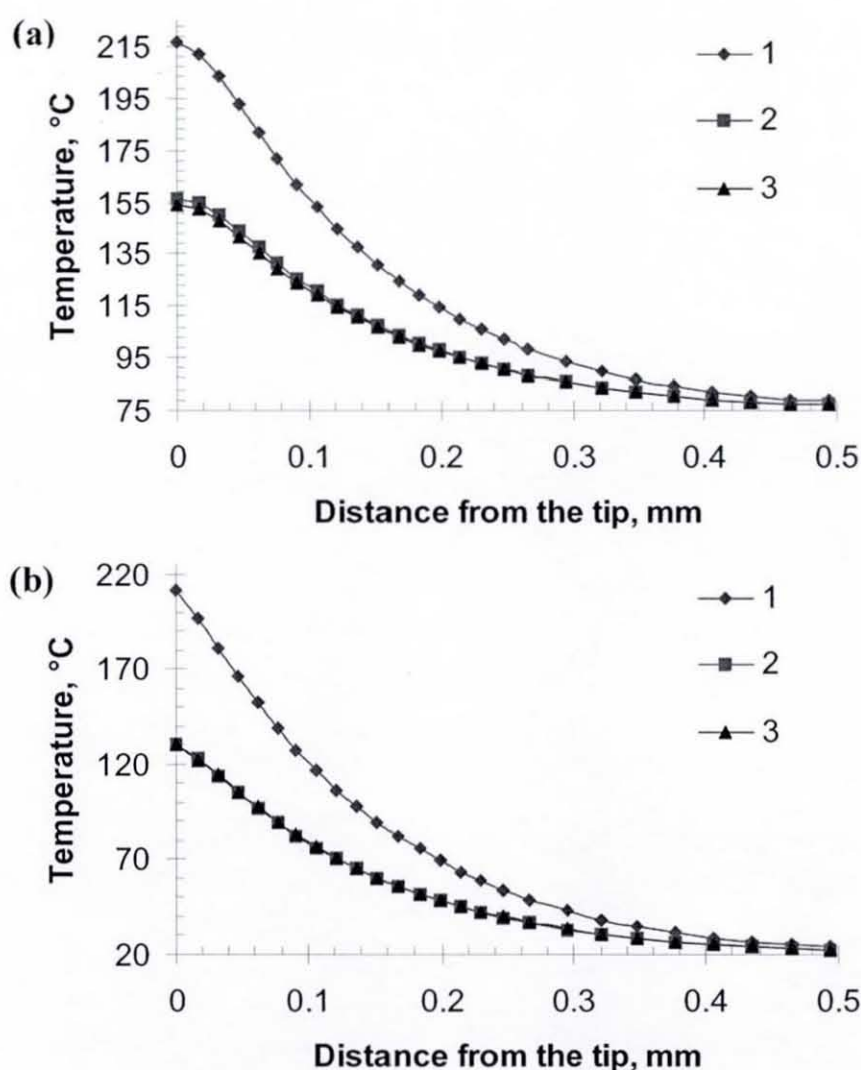
Figure 7.11 Temperature distribution in the cutting tool along the clearance face of the tool starting from the tool tip in simulations of UAT (a) and CT (b) with friction ($t = 2.5$ ms) (the same conditions as in Figure 7.7)

is noticeably higher than that in the workpiece material due to a substantially higher value of the thermal conductivity of tungsten carbide (about 60 W/m^{2}K) compared to that of Inconel 718 (about 15 W/m^{2}K). Figure 7.11 also illustrates the dependence of the temperature level in the tool on magnitudes of the heat transfer parameters h and H. A tenfold increase in the convective heat transfer coefficient h from 0.05 to 0.5 W/m^{2}K does not affect tool temperature magnitudes, whereas a rise in the contact heat transfer coefficient H from 50,000 to 500,000 W/m^{2}K leads to a significant temperature growth in the tool. This is in good agreement with the theory since parameter H regulates the value of the thermal flux between the chip and tool, with heat conduction increasing with its growth. The relative difference between maximum temperature levels for CT and UAT vanishes in the case of H = 500,000 W/m^{2}K

A comparison of the temperature distributions in the cutting tool along the rake face of the tool (in the direction radial to the workpiece surface) shows results similar to those along the clearance face. The temperature rapidly diminishes with the distance from the cutting tip reaching its initial levels at about 0.5 mm from the tip for both UAT and CT (Figure 7.12a and Figure 7.12b, respectively). Nonetheless, for CT the temperature curve is considerably flatter in the first 0.1 mm from the tip. This difference should be attributed to different contact conditions at the tool–chip interface for CT and UAT.

The effect of the feed rate on the cutting-tool temperatures in CT and UAT is also studied with FE simulations: uncut chip thickness (t_1) is reduced from 0.1 mm to 0.05 mm (other parameters of simulation being $h = 0.05$ W/m^{2}K, $H = 50,000$ W/m^{2}K, $\mu = 0.5$). Such a reduction leads to a decrease in the maximum temperature levels in the cutting region from 440°C to 400°C and from 410°C to 375°C for UAT and CT, respectively, as compared to simulations with $t_1 = 0.1$ mm. A drop in the cutting-tool temperature is also observed: it diminishes at $t = 2.5$ ms from 155°C to 125°C and from 130°C to 100°C for UAT and CT, respectively. This temperature reduction reproduces experimental results and is naturally explained by the decrease in the amount of material being removed per unit time.

Heat transfer between the chip and tool in UAT obviously occurs only during the time of their intermittent contact, compared to permanent-contact heat transfer in CT. Such a contact leads to a reduction in the total time of thermal conduction between

the cutter and chip, and, consequently, cooling due to the convective heat transfer to the environment. However, as both experiments and FE results show, this cooling does not play as significant role as the increase in cutting-tool's temperature during the contact time, which results in higher tool temperatures in UAT as compared to those in CT.
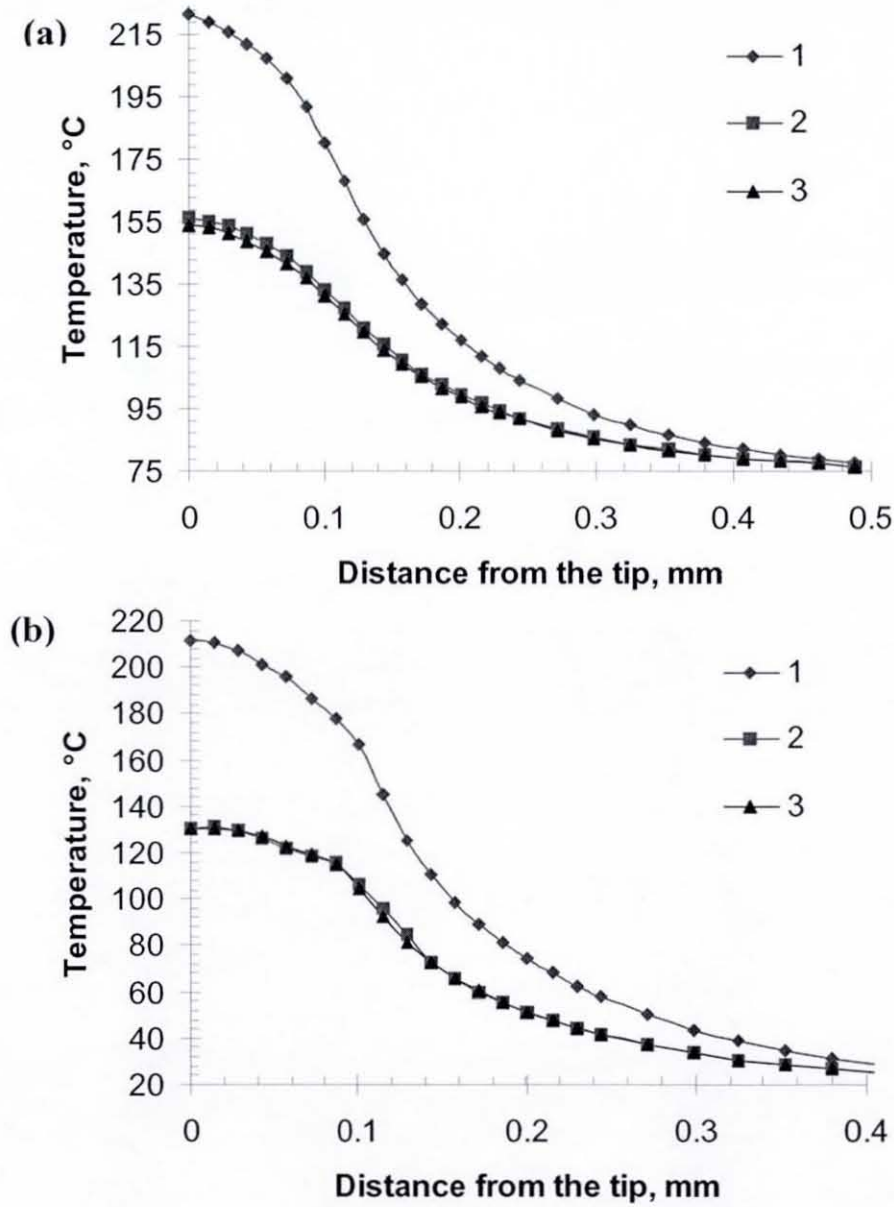
Figure 7.12 Temperature distribution in the cutting tool along the rake face of the tool starting from the tool tip in simulations of UAT (a) and CT (b) with friction ($\mu = 0.5$, $t = 2.5$ ms) (the same conditions as in Figure 7.7)

Noticeable differences are observed between chip shapes obtained in FE simulations with and without friction for both CT and UAT. Chips in simulations with friction are found to be thicker than those in simulations without friction. The chip thickness ratio $r = t_1/t_2$, that is the ratio of thickness of the uncut chip to that of the deformed one, equals 0.6 and 0.7, respectively, for simulations with and without friction, for both modelled cutting techniques. Thus, no significant differences between CT and UAT are found in the value of r for the same friction conditions. This numerical result coincides with experimental studies showing only insignificant variations in chip thickness for both cutting schemes. The chip formation process demonstrates a larger (20%) radius of curvature of the chip for CT compared to UAT in simulations with and without friction. In addition, the radius of curvature under the
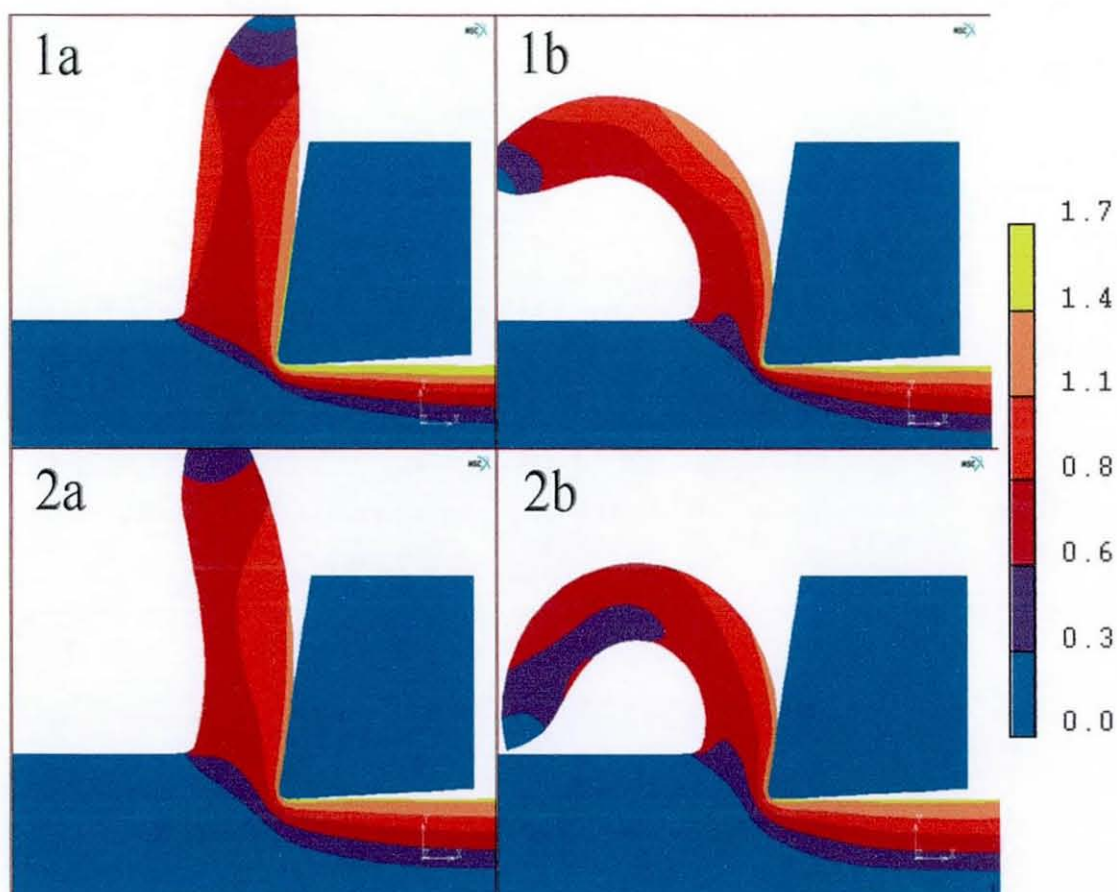
Figure 7.13. Equivalent plastic strains in the cutting region in simulations of CT with (1a) and without (1b) friction, and UAT with (2a) and without (2b) friction

frictionless contact condition at the tool–chip interface is approximately two and a half times smaller than that for the contact with friction in both cutting processes (Figure 7.13); this is supported by turning experiments with different lubricants, showing higher values of the radius of curvature for dry turning.

An equivalent plastic strain ($\bar{\varepsilon}^{p}$) is compared for CT and UAT simulations since it represents an important feature of the deformation processes. The maximum magnitudes of $\bar{\varepsilon}^{p}$ observed in the cutting region in UAT simulations range from 1.5 to 1.7 (Figure 7.13), which is about 15-20 % higher than in CT simulations for all friction and thermal conditions. A comparison between simulations with and without friction shows somewhat higher magnitudes of equivalent plastic strains (by 5-7 %) for the frictionless conditions. This may demonstrate the higher deformation levels for the frictionless analyses for both CT and UAT leading to more curled chips, i.e. chips with a smaller radius of curvature. This phenomenon is observed both in frictionless numerical simulations and well-lubricated cutting tests for both CT and UAT.

In order to compare the influence of the conventional and ultrasonically assisted cutting processes on properties of the treated workpiece, residual plastic strains are estimated in the newly formed workpiece surface in areas situated sufficiently behind the separation region to exclude the effect of transient conditions in the process zone. Figure 7.14 illustrates the distribution of the equivalent plastic strains along the radial direction starting from the workpiece surface. A fast exponential decrease in $\bar{\varepsilon}^{p}$ levels from maximum magnitudes at the workpiece surface to practically zero levels at the 200 µm depth is detected for both treatments, with the level of $\bar{\varepsilon}^{p}$ at the surface being 20-25 % higher for UAT in comparison to CT. Starting from a certain depth (100 µm and 75 µm for simulations with and without friction, respectively), the levels of $\bar{\varepsilon}^{p}$ are nearly the same for both cutting techniques.

Numerically calculated plastic strain rates $\dot{\bar{\varepsilon}}^{p}$ attain a maximum value of approximately 10^{5} s^{-1} in the process zone in UAT simulations during the penetration part of the cycle of ultrasonic vibration, when the cutter moves in the direction opposite to the rotating workpiece, thus separating a chip. However, due to the intermittent nature of the contact between the chip and cutting tool (discussed in detail in [129]), $\dot{\bar{\varepsilon}}^{p}$ drops down to zero at the unloading stage of the cycle and stays at that level till the next penetration stage commences. On the contrary, the

magnitude of $\dot{\bar{\varepsilon}}^{p}$ in CT simulations is nearly constant and equals about $2 \cdot 10^4\,\mathrm{s}^{-1}$. Obviously, this difference in strain rates increases the value of yield strength σ_Y by 15% and 13%, respectively, for UAT and CT, compared to the quasistatic σ_Y, due to the Johnson-Cook material model used in simulations. Rise in the σ_Y magnitude,
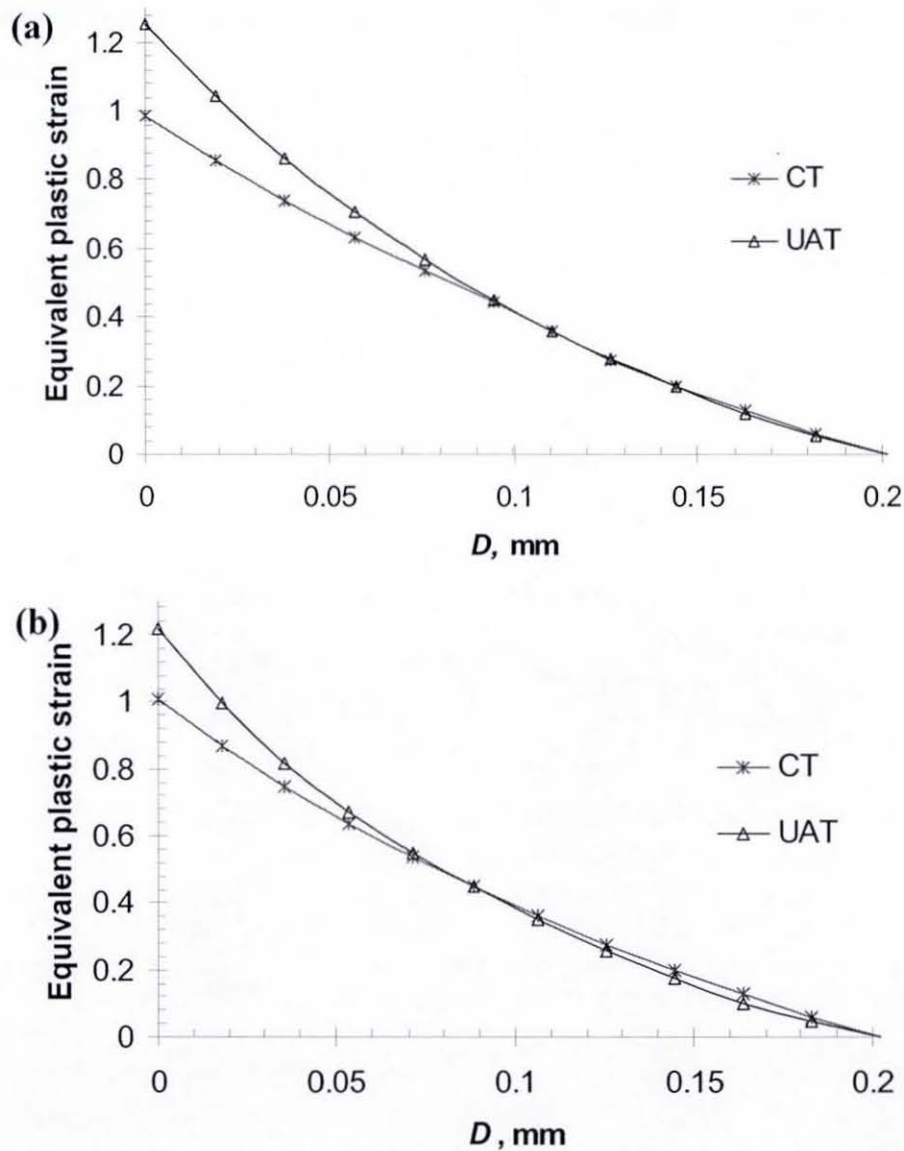
Figure 7.14 Residual equivalent plastic strains in the machined layer (0.5 mm behind the cutting tip) in CT and UAT simulations (a) with and (b) without friction. Distance D is counted from the workpiece surface in the radial direction.

in its turn, leads to greater levels of work required for the cutting tool to perform the separation of the chip, and, consequently, to greater amounts of heat generated in the

cutting region due to plastic deformation within the penetration stage of the cycle of ultrasonic vibration in simulations of UAT. However, nearly no heat is produced in other stages of the vibration cycle that eventually leads to approximately equal overall heat generation for both techniques, as soon as the final difference in temperatures between CT and UAT is about the initial difference of 40° C in the cutting tip temperature.

The intermittent character of the chip – cutting tool interaction determines the main differences in the stress distribution for CT and UAT. The modelled stress state during CT (Figure 7.15) is nearly quasistatic with the highest equivalent (von Mises) stresses concentrated in the primary and secondary shear zones, i.e. zones around line BE (Figure 6.1) and next to the rake face EK, and attaining magnitude up to 1600÷1700 MPa. The width of the region along the shear plane with the equivalent stress exceeding 1350 MPa is about 60 μm.

On the contrary, the stress state in UAT is inherently transient and changes for different stages of the cycle of ultrasonic vibration. The stress distribution in the penetration stage of the cycle (Figure 7.15c) is somewhat analogous to that of CT with the maximum equivalent stress also reaching some 1600 MPa. The stresses exceeding 1350 MPa are, however, concentrated in the narrower stripe of about 40 μm, propagating from the back side of the chip in the direction of the tool tip, but not reaching it. This zone of the highest stresses does not occupy the region in the secondary shear zone as that in CT either. When the unloading stage of the cycle of ultrasonic vibration commences, the magnitudes of the equivalent stress rapidly decline; the zones with high stress levels start to shrink in the directions of the tool tip E and towards the chip's back side B. After this quick transitional process that takes place at the unloading stage of the cycle, the stress distribution in the process zone remains fairly quasistatic within the withdrawal and approach stage of the cycle (Figure 7.15d and Figure 7.15b, respectively). This distribution is characterised by low levels of the highest stresses concentrated in the direct vicinity of the tool tip with their magnitudes not exceeding about 1000 MPa. The highest equivalent stress at the withdrawal and approach stages is situated at the chip's back side (around point B) occupying only marginal area with their levels hardly reaching 1200 MPa. As soon as the tool comes into contact with the chip again at the next penetration stage, the maximum stress levels quickly regain the high levels of about 1600 MPa,

and the cycle repeats. Hence, the maximum stress magnitude is considerably lower and areas occupied by high stresses are significantly smaller at the withdrawal and approach stages of the cycle of ultrasonic vibration than those at the penetration stage. Consequently, as these two stages comprise about 60 % of the total cycle duration (for chosen cutting speed and the vibration parameters), the mean values of stresses obtained in UAT simulations are significantly lower than those in CT, leading to lower mean cutting forces in the cutting process. The cutting forces in simulations of CT and UAT will be described below.
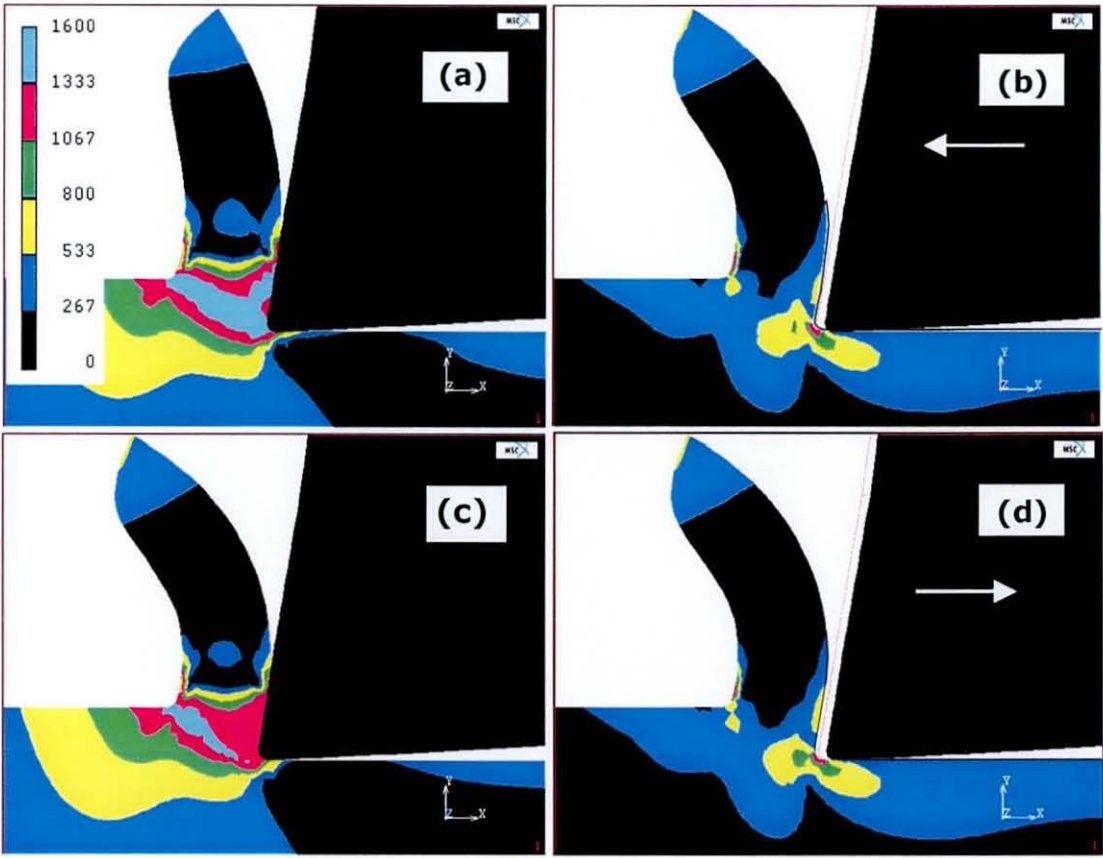
Figure 7.15 Distribution of equivalent (von Mises) stresses in CT (a) and UAT at different moments of a single cycle of vibration: tool approaches the chip (b), tool in full contact with the chip (c), and tool moves away from the chip (d)

The distribution of shear stresses (σ_{xy}) is studied in CT in comparison with UAT. As it is with equivalent stresses, the shear-stress distribution is quasistatic throughout CT simulations (after the initial transient stage) with highest levels of negative shear stresses concentrated in the vicinity of the tool tip and at the back side of the chip

next to the shear plane and reaching −800 MPa (Figure 7.16a). The area with negative stresses below −270 MPa is situated somewhere below the shear plane (BE in Figure 6.1) and extends by 350 μm in the direction normal to it. Maximum levels
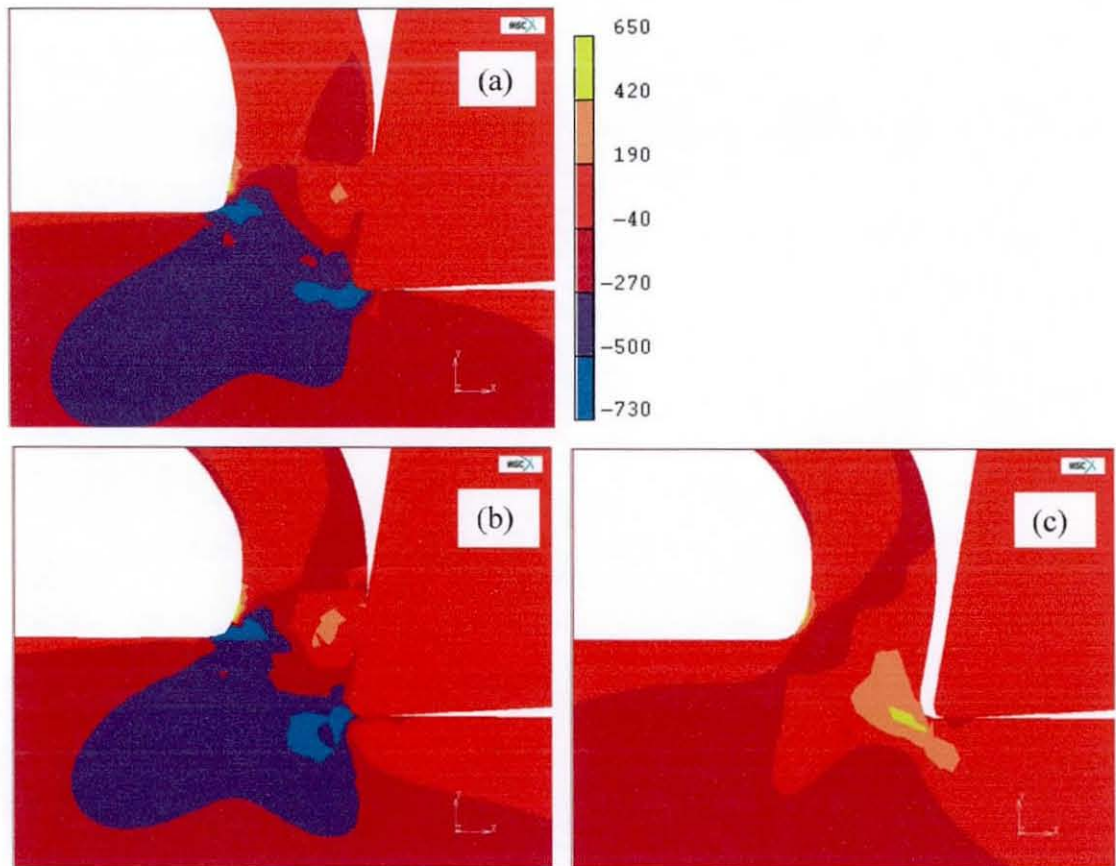
Figure 7.16 Distribution of shear stresses in CT (a) and UAT at the penetration stage of the cycle of ultrasonic vibration (b) and when the tool in not in contact with the chip (c)

of positive shear stresses are situated at the back side of the chip occupying only a small area, however, their appearance may be caused by the numerical error of FE simulations. The distribution of the shear stresses in UAT is essentially transient and changes drastically for various parts of the cycle of ultrasonic vibration depending on whether the cutting tool is in contact with the chip or not. At the penetration stage of the cycle the distribution of shear stresses is very similar to that in CT with their maximum magnitudes (for negative shears) attaining 800 MPa. The zone with shear stresses below −270 MPa is somewhat smaller than that in CT and extends by some 250 μm in the direction normal to the shear plane. As soon at the cutting tool starts to

withdraw from the chip, shear stresses in the cutting region change their direction, and thus their negative part disappears. Positive σ_{xy} ranges at these non-contact stages from 0 to 650 MPa with its maximum magnitudes situated in the vicinity of point E (see Figure 6.1). When the cutting tool re-engages with the chip, the sign of σ_{xy} changes again and the UAT cycle repeats.

A comparison of minimum principal stresses (σ_3) between CT and UAT simulations once again shows a similarity between the stress distribution in CT and at the penetration stage of the cycle of ultrasonic vibration (Figure 7.17). Maximum
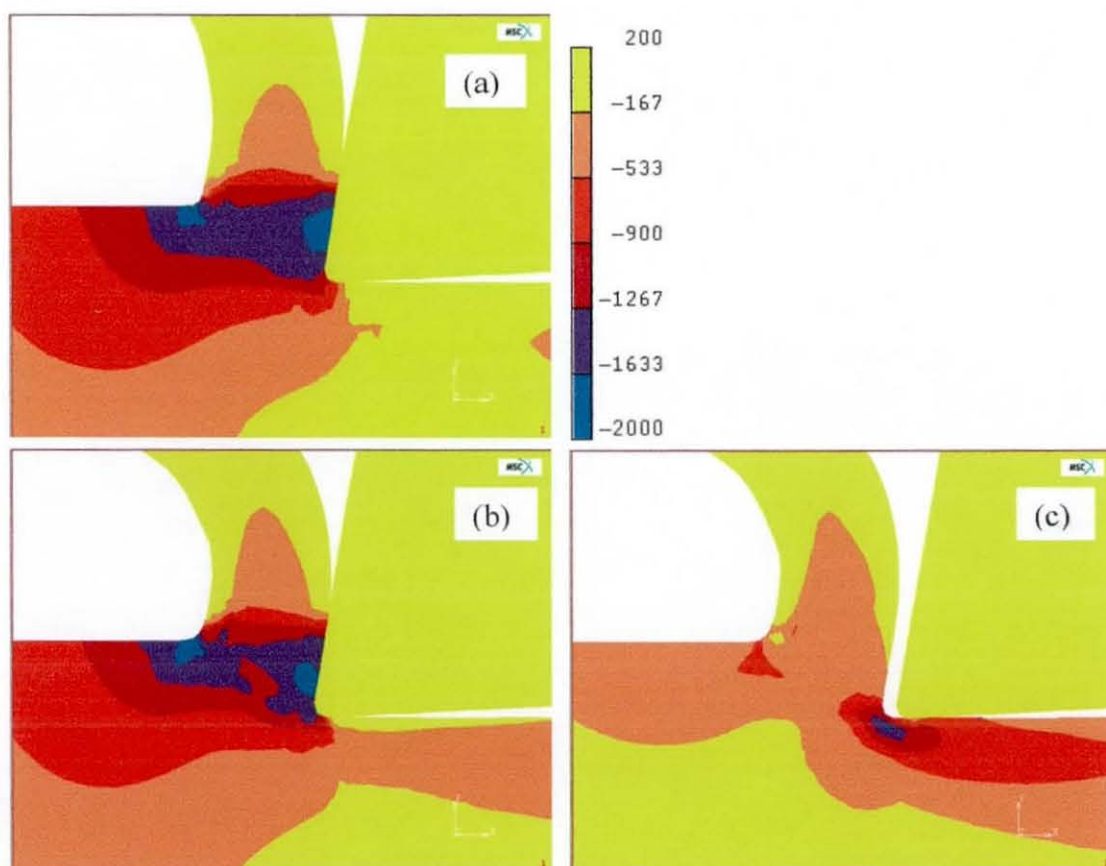
Figure 7.17 Distribution of minimum principal stresses in CT (a) and UAT at the penetration stage of the cycle of ultrasonic vibration (b) and when the tool in not in contact with the chip (c)

magnitudes of compressive stresses are situated next to the point B and along the contact length. The zone with high compressive principal stresses lower than 1270 MPa occupies an area roughly of a triangle formed by the points B, E and K (see Figure 6.1). Maximum magnitudes of the principal stress reach about –2000 MPa for

both CT and UAT. A big difference is again observed for the stages of the UAT cycle when the cutting tool does not contact the chip: principal stresses lower than 1270 MPa occupy only a small area next to the point E, with their maximum levels reduced to −1300 MPa.

Cutting forces are studied within a single cycle of ultrasonic vibration (Figure 7.18). The magnitudes of cutting forces at each time instant depend on the intensity of the stresses normal to the rake face of the tool. Logically, the force level increases when the penetration stage of the cycle of ultrasonic vibration begins. The cutting force grows until the moment of the maximum penetration, attaining levels somewhat higher than average forces in CT. The force magnitude starts to decline at the unloading stage until it vanishes when the cutter separates from the chip and starts to move away from it. The force stays close to the zero level until the cutter comes into contact with the chip again at the next cycle of ultrasonic vibration. Low-level fluctuations of the cutting force at the withdrawal and approach stages of the cycle are explained by the remaining contact between the cutter and freshly formed workpiece surface, as well as by the numerical error of the FE simulations.
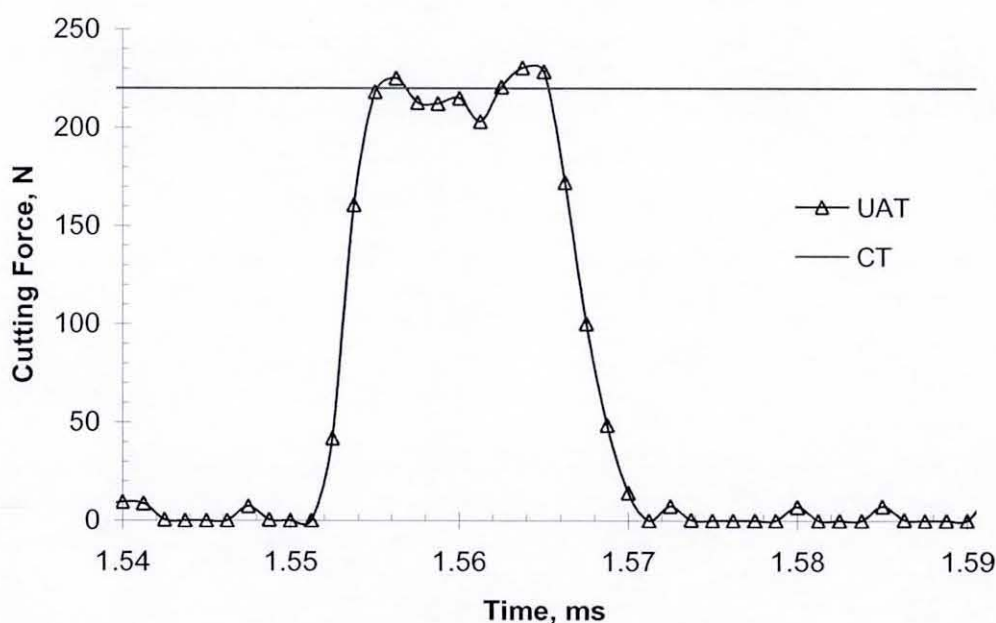
Figure 7.18 Evolution of forces acting on the cutting tool within a single cycle of ultrasonic vibration in UAT and average cutting forces in CT ($t_1 = 0.1$ mm, $V_C = 310$ mm/s, $h = 50$ W/m^{2}K, $H = 50,000$ W/m^{2}K, $\mu = 0.5$)

The mean values of cutting forces are estimated for various heat transfer, contact and cutting conditions for both CT and UAT. Theoretically, the cutting forces are proportional to the contact area between the chip and the cutting tool. The contact area, in its turn, should be proportional to both uncut chip thickness (that corresponds to the feed rate) and cutting edge engagement length (that corresponds to the depth of cut). In two-dimensional simulations, the latter parameter corresponds the workpiece thickness (w). This thickness is varied between 0.1 and 10 mm in order to study its influence on the results of simulations. As expected, w does not influence stress distributions in the cutting region or cutting temperatures. In fact, w affects only cutting forces, which are decreasing proportionally when w is reduced in simulations. This allows to keep constant $w = 1$ mm in all simulations, as the cutting forces can be easily recalculated for various w, thus enabling to estimate forces acting on the tool for different feed rates in real turning tests. In order to compare simulated and experimentally produced cutting forces, experimentally obtained chip cross-sections were analysed and the parameter w was chosen so that the simulated cross-sectional area $A = w \cdot t_2$ equates the experimentally obtained one.

The mean magnitudes of cutting forces in UAT are 60 N for $\mu = 0.5$ and 45 N for frictionless contact, respectively (other simulation parameters are $t_1 = 0.1$ mm, $V_C = 310$ mm/s, $h = 50$ W/m²K, $H = 50,000$ W/m²K). The respective magnitudes mean cutting forces in CT simulations for contact with and without friction are 220 and 175 N. Hence, superimposition of ultrasonic vibration leads to 3.5÷4 times reduction in the cutting forces for various friction conditions. Once again, the reduction in mean cutting forces for UAT as compared to those in CT is in good agreement with the experimental results described in Section 5.6, as well as with other reported results (for example, [18, 85]).

The simulations with various magnitudes of heat transfer parameters do not produce significant changes in the cutting force. Varying contact heat transfer coefficient H from 50,000 to 500,000 W/m²K and convective heat transfer coefficient h from 50 to 500 W/m²K results in less than 5% changes in the cutting force. The decrease in the cutting speed from 310 mm/s to 155 m/s increases the cutting force in CT simulations by 6%, which correlates well with experimental results (Section 5.6), indicating a similar drop in cutting forces for higher rotational speeds. The uncut chip thickness (t_1) was varied between 0.1 and 0.05 mm, in order

to simulate the effect of the changing feed rate in turning tests. A reduction in t_1 from 0.1 to 0.05 mm results in a decrease in the cutting force from 220N to 140 N in CT simulations, i.e. by 1.6 times. This is in very good agreement with experimental results demonstrating 1.5 times decrease in the cutting force when the feed rate is changed from 0.05 mm to 0.1 mm. Finally, the influence of the rake angle on the cutting force is studied. The rake angle in UAT simulations is increased from $\gamma = 7.5°$ to 30°, leading to natural decrease (by 25%) in the level of cutting forces.

The distribution of the stresses normal to the rake face of the tool are analysed at the penetration stage of the cycle of ultrasonic vibration in a UAT simulation and at an arbitrary time instant in a CT simulation (Figure 7.19). Normal stresses grow starting from the tip of the cutting tool, attain the maximum levels somewhere in the middle of the contact length, and then gradually decrease towards the end of the contact length where the chip separates from the cutting tool. The magnitudes of L_C
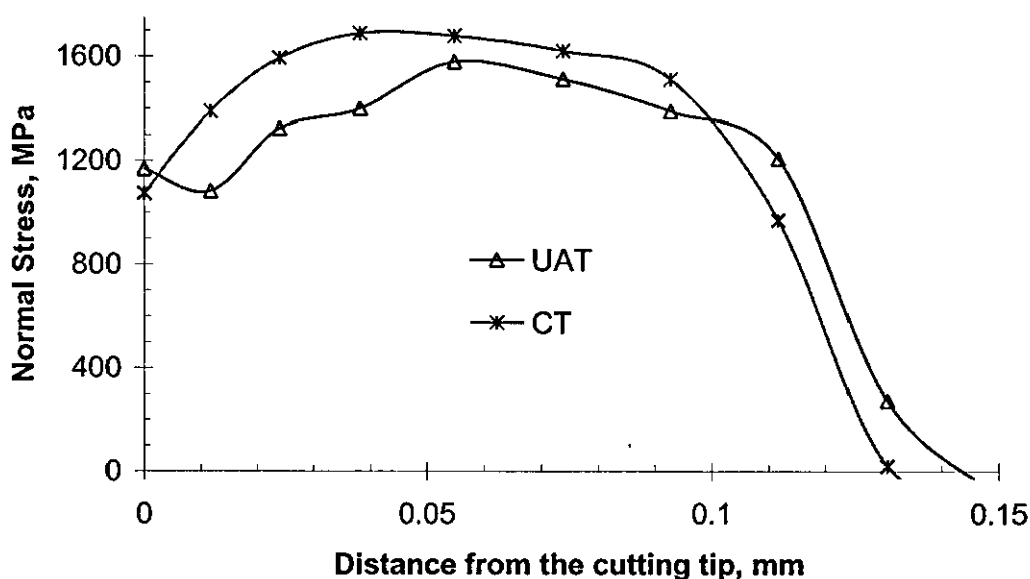
Figure 7.19 Distribution of normal stresses along the contact length L_C at the rake face of the tool in CT and at the moment of maximum penetration in UAT (the same parameters as in Figure 7.18)

fluctuate during the FE simulations, however, on average, they are somewhat similar for both CT and UAT and equal about 0.15 mm. In the frictionless case ($\mu = 0$), the

value of L_C decreases to 0.1 mm for both UAT and CT, which correlates well with a decrease in the chip's radius of curvature in this case in comparison to simulations with friction.

It is worth noticing that changing stress distributions for UAT observed in current simulations are similar to those obtained with separation-type model described in detail in Chapter 6 and [129].

The imposed due to ultrasonic vibration fatigue loading conditions can cause premature wear of the cutting tool, as reported in [2]. Additional FE research with a deformable cutting tool can be useful to analyse this issue, thus the possible model development would be also accounting for deformation processes in the tool.

7.5 Concluding remarks

A thermomechanically-coupled FE model of UAT and CT are used to investigate the influence of various cutting, heat-transfer and friction parameters on thermal and mechanical features of these cutting processes. The model incorporates a number of enhancements compared to the uncoupled mechanical model for turning presented earlier in Chapter 6. These improvements include an advanced material model for Inconel 718 accounting for strain-rate effects, nonlinear hardening and temperature-dependent material properties, friction at the tool–chip interface and heat conduction into the tool as well as convective heat transfer.

Simulations demonstrate considerable differences in the stress state, deformation processes and thermal characteristics between two machining techniques. Experimentally observed drastic changes in cutting forces are reproduced in simulations. The calculated stress distribution in the cutting region is studied for CT and different stages of the cycle of ultrasonic vibration for UAT. The similar maximum values of stresses are observed for both technologies. Nevertheless, unlike the quasistatic stress distribution during CT, the stress state at UAT changes significantly within a cycle of ultrasonic vibration, with the highest values of stresses attained only during a part of it. As a result, average cutting forces are up to four times smaller for UAT.

It is shown that an increase in contact heat conduction between the chip and cutting tool leads to a significant growth in the cutting-tip temperature and a decrease in temperatures in the chip and workpiece. Frictionless analyses result in a very small

rise in the tool's temperature, justifying the significant effect of friction on resultant temperatures in the tool. The relative temperature difference between CT and UAT is insensitive to changes in convective heat transfer and friction. An increase in contact heat conduction, however, results in the change of temperatures at UAT from 5% to 15% as compared to ones at CT. The former number is in good agreement with the infrared thermography data.

The maximum magnitudes of equivalent plastic strains observed in the cutting region in UAT simulations are about 15-20% higher than those in CT simulations for all combinations of friction and thermal conditions. No significant difference between CT and UAT in terms of plastic strains is discovered in simulations with and without friction. Residual plastic strains in the machined layer decrease exponentially from the workpiece surface, with the level of $\bar{\varepsilon}^p$ at the surface being 20-25 % higher for UAT in comparison to CT. Starting from about 100 μm from the workpiece surface, levels of $\bar{\varepsilon}^p$ are nearly the same for both cutting techniques. A conclusion is drawn that a proper analysis of the influence of machining on the surface structure requires introduction of additional microstructural features into FE simulations.

Chips, formed during simulations of cutting, are compared for cases with and without friction. A larger (by 20%) radius of curvature of the chip is found in CT as compared to UAT in simulations in both cases. It is noted that the chip thickness ratio attains higher values and that the radius of curvature of the chip is about two and a half times smaller in the frictionless case than that in the analysis with friction for both CT and UAT.

Chapter 8 Conclusions and recommendations for future work

8.1 Conclusions

The thesis was aimed at improving the understanding of the mechanics of the UAT process. The means of achieving this aim were the literature survey, experiments and numerical simulations. Various experiments have been carried out in order to study mechanical and heat-transfer processes involved in UAT, including microstructural analyses of machined workpieces and produced chips, high-speed filming and infrared thermography as well as real-time force measurements of cutting. These experiments were also used to validate the developed two-dimensional FE models for both UAT and CT. These numerical models allow predictions of the stress-strain distributions in the cutting region, cutting forces, and heat-transfer processes in both the workpiece material and the tool. Most importantly, the developed models adequately reflect experimental results. Following the list of objectives set in Introduction (see Chapter 1), the PhD research study has brought the results described below.

The historical development of UAT and state of the art in this area

The literature survey has shown that various practical attempts have been made to apply UAT for cutting various types of materials, including plastics, composites, structural steels, and intractable alloys. It was also discovered that the majority of the research on UAT has been focused on technological aspects of the problem, such as design of the UAT system, and on the influence of vibration and cutting parameters on the system performance. However, there was little information found on thermomechanical processes involved in UAT, justifying the objectives set for this thesis.

Experimentation

1. *Thermomechanics of deformation processes and dynamics of the tool–workpiece interaction*

- High-speed filming experiments showed that the area of the visible process zone for UAT and its width in the radial direction were considerably smaller than those for CT. Deformation processes in UAT were localized in the direct vicinity of the cutting edge along the surface of the workpiece and were not observed underneath the clearance face of the tool at the newly formed surface layer, in contrast to the CT process. This result was in good agreement with nanoindentation tests, indicating a much thinner hardened layer formed in workpieces machined with UAT compared to those machined with CT.

- High-speed filming also showed that the chip formed in UAT was formed nearly in the radial direction very close to the cutting tool surface, whereas the chip in CT shifted much further from the cutting tool that leads to a more curled chip. This correlates well with a subsequent chip analysis, which indicated that the chip radius of curvature was up to 2 times higher for UAT than for CT for dry cutting conditions. The explanation for this macroscopically observed behaviour is the difference in chip-formation mechanisms: continuous for UAT and step-like for CT.

- Application of ultrasonic vibration significantly reduced the level of chip segmentation compared to that of CT.

- The value of the shear angle in UAT was by 20° greater than that in CT as discovered from SEM of produced chips. Hence, the length of the shear plane was smaller in UAT as compared to that in CT; this led to easier shearing of the material along the shear plane in UAT and, consequently, to smaller cutting forces in UAT. This was another factor contributing to the experimentally observed force reduction in UAT.

- A highly deformed surface layer of 10 and 2 µm for CT and UAT, respectively, was discovered along the tool side of chips with SEM. The difference indicated more spatially localised effect of the UAT process in comparison to CT. It also can be explained by the different character of the friction and thermal processes in UAT, caused by the intermittent contact between the chip and cutting tool, in contrast to the constant contact in CT.

2. *Influence of the cutting process on the properties of treated materials*

- Light microscopy tests showed an affected subsurface layer, some 15 μm thick, for in the case of UAT. There were no visible alterations in the grain structure of the surface layers for the workpiece machined with CT.

- SEM tests detected an affected subsurface layer of about 30 to 40 μm in workpieces machined with UAT. There were no visible changes observed in the microstructure of CT-machined workpieces apart from a thin layer of about 3 μm.

- Nanoindentation tests indicated that the average thickness of the hardened subsurface layer is by 70 % higher for the CT-machined workpiece than that for the UAT-machined one (85 μm and 50 μm, respectively). The average hardness of this subsurface layer for UAT (about 15 GPa) was about 60 % of that for CT (25 GPa) and closer to the hardness of the untreated material (about 6.5 GPa). This result demonstrated that the actual thickness of the hardened layer was greater than visually observed with light microscopy and SEM.

3. *Heat transfer in the workpiece material and into the cutting tool*

- The initial temperature of the cutting tip in UAT prior to the engagement with the workpiece was higher than room temperature and measured to be about 75°C. This can be explained by the dissipation of the ultrasonic-vibration energy.

- The relative difference in the cutting-tip temperature between CT and UAT while cutting Inconel 718 varied insignificantly (4÷8 %, depending on the cutting conditions) and could largely be attributed to the initial preheating of the cutting tool in UAT and not to the result of cutting itself. In fact, in some cases the relative difference between final and initial (before engagement with the workpiece) temperature was even larger for CT.

- An experimentally obtained difference between maximum temperature in the chip in the processing zone and temperature in the tool tip was significant and ranged between 10 and 20 % for both CT and UAT. This was also reproduced is FE simulations and attributed to the thermal contact resistance between the tool and the chip.

4.   *Cutting forces*

- The cutting force in UAT of Inconel 718 ranged from 100 to 250 N for various combinations of the process parameters. The force in UAT was from 1.5 to 4 times lower compared to that in CT.

- Cutting force measurements also demonstrated that:
  - ➢ Higher cutting speeds led to lower cutting forces. This can be explained by the reduced dynamic fracture toughness of the machined material for higher strain rates resulting from higher cutting speeds.
  - ➢ Higher feed rates resulted in greater cutting forces due to increased material removal rates.
  - ➢ Sharper tools (with a larger rake angle) led to lower cutting forces
  - ➢ Cutting forces decreased by 15-40 % for lubricated cutting conditions as compared to dry turning

Numerical (FE) simulations of UAT

The two-dimensional FE models of UAT and CT have been developed. The results of simulations correlate well with the experimental results. The numerical models include such advanced modelling features as thermomechanical coupling, dynamic transient formulation and contact interaction with friction at the tool–chip interface, as well as an account for non-linear material hardening and strain-rate sensitivity.

1. Thermomechanics of the of the tool–chip interaction

- The following main stages of the cutting process during a single cycle of ultrasonic vibration were observed: approach, penetration, unloading and withdrawal. During the approach and withdrawal stages (that take 60 % of the cycle time for chosen vibration and cutting parameters) the cutting tool did not contact the chip, but still remained in contact with the workpiece. At the penetration stage the cutter contacted the chip and penetrated into the workpiece causing the chip separation. At the unloading stage the tool moved in the opposite to cutting direction, but remained in contact with the chip for about 10-15% of the cycle time due to the elastic spring-back effect until the tool finally withdrew from the chip.

- FE results indicated a nearly twofold increase in the radius of curvature of the chip under the frictionless contact condition at the tool–chip interface. This is in good agreement with the experimental results showing that application of lubrication to the cutting region increased the value of the radius of curvature in up to 2 times for both techniques, and confirms the dominant influence of friction on the radius.

- The magnitude of the contact length between the chip and the cutting tool changed in simulations of UAT between a zero and maximum level within a cycle of ultrasonic vibration. The maximum magnitude of the contact length in UAT was similar to its quasistatic value in CT. In the frictionless case, the value of contact length decreased by 30 % for both UAT and CT, which correlates well with a decrease in the chip's radius of curvature in this case in comparison to simulations with friction.

- No significant differences between CT and UAT were found in the chip thickness for the same friction conditions. This numerical result coincides with experimental studies showing only insignificant variations in chip thickness for both cutting techniques.

2. *Stress-strain distributions in the cutting region*

- The intermittent character of the chip – cutting tool interaction determined the main differences in the stress distribution for CT and UAT. The modelled stress state in UAT was inherently transient as compared to nearly quasistatic one in simulations of CT. The stress state in UAT changed for different stages of the cycle of ultrasonic vibration. The stress distribution in the penetration stage (that takes 25% of the cycle time) was somewhat analogous to that of CT with maximum achieved stresses being slightly higher than those in CT. However, stress levels in UAT were considerably lower than those in CT for about 60% of the cycle time. As a result, the mean values of stresses obtained in simulations of UAT were significantly lower than those in CT.

- The maximum magnitudes of equivalent plastic strain observed in the cutting region in simulations of UAT were about 15-20 % higher than those in simulations of CT for all friction and thermal conditions. A comparison between simulations with and without friction showed slightly higher magnitudes of equivalent plastic strains (by 5-7 %) for the frictionless

conditions. This demonstrates the higher deformation levels for the frictionless analyses for both CT and UAT leading to more curled chips (i.e. chips with a smaller radius of curvature) registered in the frictionless case.

- Numerically calculated plastic strain rates attained a maximum value of approximately 10^5 s^{-1} in the process zone in simulations of UAT during the penetration part of the cycle of ultrasonic vibration, whereas strain rates practically vanished at the other stages of the cycle. The magnitude of strain rates in simulations of CT was nearly constant and equalled about $2 \cdot 10^4 s^{-1}$. Greater strain rates normally lead to a higher reduction in the dynamic fracture toughness of the workpiece material in UAT, leading to easier material separation and, consequently, lower cutting forces in UAT in comparison to CT.

3. *Cutting forces*

- Lower values of average stresses in simulations of UAT naturally resulted in smaller forces acting on the cutting tool. Ultimately, FE simulations showed that superimposition of ultrasonic vibration led to the fourfold reduction in the cutting forces for various friction conditions as compared to those in CT. This was in good agreement with the experimental force-measurement results.

- FE simulations indicated smaller forces acting on the shear plane in UAT than those in CT, thus reflecting the reduced possibility of large slips along the shear plane for UAT. This correlates well with experimental results showing a reduced level of chip segmentation in UAT compared to that in CT.

4. *Heat-transfer in the workpiece material and into the cutting tool*

- Temperature levels in the chip, obtained in FE simulations, were similar to those observed in infrared thermography experiments. This is another validation of the developed FE models.

- FE results showed that temperature of chips obtained at UAT was by 5 % higher than that at CT. This correlates well with an experimentally observed 6 % difference in the chip temperature between two techniques.

- Frictionless FE simulations (corresponding to conditions of well-lubricated cutting) showed only a marginal temperature increase in the tool for both CT and UAT indicating a dominant role of friction in the temperature growth in the tool.

- An exponential temperature decrease from the maximum at the cutting tip to nearly room temperature (in the case of CT) or initial tool temperature (in the case of UAT) in distant parts of the tool was observed in both the numerical simulations and infrared thermography tests experiments, thus once again confirming a good correlation between them.

8.2 Further work

The present study has indicated several areas were further work would be useful. These areas are outlined below.

- It would be of interest to carry out the high-speed filming experiments with higher magnification to resolve smaller details of the chip formation mechanisms. A valuable insight into the UAT cutting process can also be given with the use of the higher filming rate (10^5 frames/s or higher), as this would allow to observe different stages of the cycle of ultrasonic vibration. High-speed filming of Inconel 718 would be of significant interest, in order to ensure that the main features of the chip formation mechanism in UAT of Inconel 718 are the same as those observed in machining mild steel.

- Ultrasonic vibration was applied in the tangential direction in all experiments described in this thesis. For this kind of vibration, the cutting speed should not exceed its critical magnitude (see Section 2.2.1). All experiments can be repeated with ultrasonic vibration applied in the feed direction and for higher cutting speeds, i.e. under conditions suitable for industrial turning requiring high material removal rates.

- A comparison between the efficiency of tangential and feed vibrations can be performed either experimentally or numerically. As the case of feed vibrations is essentially three-dimensional, a FE model should also be extended into three-dimensional one.

- As one of the biggest problems of the UAT process in machining intractable materials is a significantly reduced (due to micro-cracking and chipping) tool life, a FE model with a deformable tool could study this issue and, potentially, resolve it.

- A FE model with a finer mesh in the process zone could allow to study chip segmentation processes in CT and explain reduced segmentation in UAT. Different/upgraded software and/or hardware with a higher computational capacity is required for this purpose.

- Thermal softening of the workpiece material can be included into the constitutive equations, which would probably influence deformation mechanisms in chip formation and improve the overall accuracy of the FE model.

- Residual stress analysis with X-ray diffractometry or other techniques would reveal the details of residual stresses in the machined surface layer. This may be another means to validate numerical simulations, as well as to clarify suitability of surfaces produced at UAT for particular applications.

- Transmission electron microscopy (TEM) or other techniques can be applied to study in detail the structure and specific features of thin hardened layers on the workpiece and chip surfaces. As TEM allows higher levels of magnification, it could reveal more data than SEM tests. Such an analysis may give an invaluable insight into the nature of the UAT and CT effect on the treated material.

References

1. Babitsky, V., A. Kalashnikov, A. Meadows and A. Wijesundara, *Ultrasonically assisted turning of aviation materials.* Journal of Materials Processing Technology, 2003, **132** (1-3), pp. 157-167.

2. Sharman, A.R., P. Bowen, D.K. Aspinwall and C. Dewes, *Ultrasonic assisted turning of gamma titanium aluminide.* 2001, Rolls-Royce plc.

3. Boothroyd, G. and W.A. Knight, *Fundamentals of machining and machine tools.* 1989, New York and Basel: Marcel Dekker.

4. Trent, E.M. and P.K. Wright, *Metal Cutting.* 2000: Butterworth-Heinemann, London.

5. Childs, T.H.C., K. Maekawa, T. Obikawa and Y. Yamane, *Metal Machining: Theory and Applications.* 2000: Arnold, London.

6. Atkins, A.G., *Modelling metal cutting using modern ductile fracture mechanics: quantitative explanations for some longstanding problems.* Int. J. Mech. Sci., 2003, **45** (2), pp. 373-396.

7. Merchant, M.E., *Mechanics of the metal cutting process.* J. Appl. Phys., 1945, **16**, pp. 318-324.

8. Oxley, P.L.B., *Mechanics of Machining.* 1989: Chichester: Ellis Horwood.

9. Rowe, G.W. and P.T. Spick, Trans ASME, 1967, **89B**, pp. 530.

10. Mallock, A., *The action of cutting tools.* Proc. Roy. Soc. Lond., 1881-82, **33**, pp. 127-139.

11. Shaw, M.C., *Metal Cutting Principles.* 1984, Oxford: Clarendon Press.

12. Shirakashi, T. and E. Usui, *Friction characteristics on tool face in metal machining.* J. JSPE, 1973, **39**, pp. 966-972.

13. *MSC.Marc User's Guide, Version 2001.* 2001: MSC Software Corporation, Los Angeles.

14. Zorev, N.N., *Metal Cutting Mechanics.* 1966, Oxford: Pergamon Press.

15. *Thermomechanical Fatigue and Fracture (Advances in Fracture Mechanics),* ed. M.H. Aliabadi. 2001: Computational Mechanics.

16. Walley, S.M., W.G. Proud, P.J. Rae and J.E. Field, *Comparison of two methods of measuring the rapid temperature rises in split Hopkinson bar specimens.* Review of Scientific Instruments, 2000, **71** (4), pp. 1766-1771.

17. Ueda, T., M. Sato and K. Nakayama, *The temperature of a single crystal diamond tool in turning.* Annals CIRP, 1998, **47** (1), pp. 41-44.

18. Markov, A.I., *Ultrasonic Machining of Intractable Materials.* 1966, London: Iliffe Books Ltd.

19. Zienkiewicz, O.C. and R.L. Taylor, *The Finite Element Method.* 5th ed. Vol. 1. 2000, Oxford: Butterworth-Heinemann.

20. Behrens, A. and B. Westhoff, *Numerical simulation of chip forming processes.* Production Engineering, 2002, **9** (1), pp. 13-16.

21. Carroll, J.I. and J. Strenkowski, *Finite element models of orthogonal cutting with application to single point diamond turning.* Int. J. Mech. Sci., 1988, **30** (12), pp. 899-920.

22. Liu, C. and Y. Guo, *Finite element analysis of the effect of sequential cuts and tool - chip friction on residual stresses in a machined layer.* Int. J. Mech. Sci., 2000, **42** (6), pp. 1069-1086.

23. Yang, X. and C.H. Liu, *A new stress-based model of friction behavior in machining and its significant impact on residual stresses computed by finite element method.* Int. J. Mech. Sci., 2002, **44** (4), pp. 703-723.

24. Lin, Z. and Y. Lin, *Three-dimensional elastic-plastic finite element analysis for orthogonal cutting with discontinuous chip of 6-4 brass.* Theoretical and Applied Fracture Mechanics, 2001, **35** (2), pp. 137-153.

25. Lin, Z.-C. and Y.-Y. Lin, *A study of an oblique cutting modelling.* Journal of Materials Processing Technology, 1999, **86**, pp. 119-130.

26. Johnson, G. and W. Cook, *Fracture Characteristics of three metals subjected to various strains, strain rates, temperatures and pressures.* Eng. Fract. Mech., 1985, **2** (1), pp. 31-48.

27. Maudlin, P. and M. Stout, *Metal cutting simulation of 4340 steel using an accurate mechanical description of material strength and fracture.* Minerals, Metals and Materials Society, 1996, pp. 29-41.

28. Ng, E.-G. and D.K. Aspinwall, *Hard part machining AISI H13 (approx =50 HRC) using AMBORITE AMB90: a finite element modelling approach.* Industrial Diamond Review, 2000, **60** (587), pp. 305-310.

29. Ng, E.-G., T. El-Wardany, M. Dumitrescu and M. Elbestawi, *Physics-based simulation of high speed machining*. Machin. Sci. Technol., 2002, **6** (3), pp. 301-329.

30. Komvopoulos, K. and S. Erpenbeck, *Finite element modeling of orthogonal metal cutting*. J. Eng. Ind. (Trans. ASME), 1991, **113** (3), pp. 253-267.

31. Obikawa, T. and E. Usui, *Computational machining of titanium alloy--finite element modeling and a few results*. Journal of Manufacturing Science and Engineering, 1996, **118** (2), pp. 208-215.

32. Bäker, M., J. Rösler and C. Siemers, *A finite element model of high speed metal cutting with adiabatic shearing*. Computers and Structures, 2002, **80** (5-6), pp. 495-513.

33. Marusich, T. and M. Ortiz, *Modelling and simulation of high-speed machining*. International Journal for Numerical Methods in Engineering, 1995, **38** (21), pp. 3675-3694.

34. Bäker, M., J. Rosler and C. Siemers, *Finite element simulation of segmented chip formation of Ti6Al4V*. J. Manuf. Sci. Eng. (Trans. ASME), 2002, **124** (2), pp. 485-488.

35. Strenkowski, J.S. and J.T. Carroll III, *A Finite element model of orthogonal metal cutting*. J. Eng. Ind. (Trans. ASME), 1985, **107** (4), pp. 349-354.

36. Sandstrom, D. and J. Hodowany, *Modeling the physics of metal cutting in high-speed machining*. Machining Science and Technology, 1998, **2** (2), pp. 343-353.

37. Sekhon, G. and J. Chenot, *Numerical simulation of continuous chip formation during non-steady orthogonal cutting*. Engineering Computations, 1993, **10** (1), pp. 31-48.

38. Lei, S., Y. Shin and F. Incropera, *Thermo-mechanical modeling of orthogonal machining process by finite element analysis*. International Journal of Machine Tools & Manufacture, 1999, **39** (5), pp. 731-750.

39. Lin, Z.-C. and Y.-Y. Lin, *A study of oblique cutting for different low cutting speeds*. Journal of Materials Processing Technology, 2001, **115** (3), pp. 313-325.

40. Camacho, G., T. Marusich and M. Ortiz. *Modeling of high-speed machining and ballistic penetration*. In *Computational Plasticity: Fundamentals and Applications. II, Barcelona, Spain*. 1995: Pineridge Press Ltd.

41.   Ceretti, E., P. Fallbohmer, W.T. Wu and T. Altan, *Application of 2-D FEM to chip formation in orthogonal cutting.* Journal of Materials Processing Technology, 1996, **59**, pp. 169-181.

42.   Zienkiewicz, O.C., *The Finite Element Method in Engineering Science.* 2nd ed. 1971, London: McGraw-Hill.

43.   Shirakashi, T. and E. Usui, *Simulation analysis of orthogonal metal cutting process.* J. Japan Soc. Prec. Eng., 1976, **42** (5), pp. 340-345.

44.   Dirikolu, M.H., T.H.C. Childs and K. Maekawa, *Finite element simulation of chip flow in metal machining.* Int. J. Mech. Sci., 2001, **43**, pp. 2699-2713.

45.   Iwata, K., K. Osakada and Y. Terasaka, *Process modelling of orthogonal cutting by the rigid-plastic finite element method.* Trans ASME J. Eng. Mat. Tech., 1984, **106**, pp. 132-138.

46.   Maekawa, K. and M. Maeda, *Simulation analysis of three dimensional continuous chip formation process (1st report) - FEM simulation and a few results.* J. Japan Soc. Prec. Eng., 1993, **59** (11), pp. 1827-1833.

47.   Maekawa, K., H. Ohhata and T. Kitagawa. *Simulation analysis of cutting performance of a three-dimensional cut-away tool.* In *Advancement of Intelligent Production. Tokyo:Elsevier.* 1994.

48.   Marusich, T. *Finite element modeling of the machining of non-ferrous metals.* In *1st International Non-Ferrous Processing and Technology Conference.* 1997. St. Louis, Missouri, USA: ASM International (USA).

49.   Marusich, T.D. and M. Ortiz, *A finite element study of chip formation in high-speed machining.* J. Manuf. Sci. Eng. (Trans. ASME), 1995, **3** (1), pp. 245-258.

50.   Marusich, T. and M. Ortiz, *Simulation of chip formation in high-speed machining.* American Society of Mechanical Engineers, 1995, pp. 127-139.

51.   Sloan, S.W., *A fast algorithm for constructing Delaunay triangulations in the plane.* Adv. Eng. Software, 1987, **9**, pp. 34-55.

52.   Cheng, J.-H. and C.-C. Liao, *Developing automatic and adaptive 2-D remeshing capabilities for commercial finite element programs.* Journal of the Chinese Society of Mechanical Engineers, 2000, **21** (5), pp. 515-525.

53.   El-Wardany, T., D. Viens, G.C. Huang and J. Dierberger. *Finite element simulation of machining process with mesh adaptation.* In *Simulation of*

materials processing; theory, methods and applications International conference. 2001.

54. Marinov, V.R., *Hybrid analytical-numerical solution for the shear angle in orthogonal metal cutting - Part II: experimental verification.* Int. J. Mech. Sci., 2001, **43** (2), pp. 415-426.

55. Marinov, V.R., *Hybrid analytical-numerical solution for the shear angle in orthogonal metal cutting - Part I: theoretical foundation.* Int. J. Mech. Sci., 2001, **43** (2), pp. 399-414.

56. Bailey, T., M. Elbestawi, T. El-Wardany and P. Fitzpatrick, *Generic simulation approach for multi-axis machining, Part 1: Modeling methodology.* J. Manuf. Sci. Eng. (Trans. ASME), 2002, **124** (3), pp. 624-633.

57. Bailey, T., M. Elbestawi, T. El-Wardany and P. Fitzpatrick, *Generic simulation approach for multi-axis machining, Part 2: Model calibration and feed rate scheduling.* J. Manuf. Sci. Eng. (Trans. ASME), 2002, **124** (3), pp. 634-642.

58. Leopold, J., G. Schmidt and K. Hoyer, *Safety of high-speed tools.* Werkstatt und Betrieb, 1998, **131** (1-2), pp. 82-84, 86.

59. Maekawa, K., A. Kubo and T.H.C. Childs, *A friction model for free-machining steels and its applicability to machinability analysis.* Key Engineering Materials, 2001, **196**, pp. 79-90.

60. Childs, T.H.C., K. Bezas and M.H. Dirikolu, *The sensitivity of finite element predicted machining parameters to small variations in flow stress behaviour.* International Journal of Forming Processes, 2000, 3 (1/2), pp. 99-114.

61. Arrazola, P.J., F. Meslin and S. Marya, *Numerical cutting sensitivity study of tool-chip contact.* Materials Science Forum, 2003, **426-432** (5), pp. 4519-4524.

62. Subramanian, S.V., H.O. Gekonde, G. Zhu and X. Zhang, *Role Of Microstructural Softening Events In Metal Cutting.* Machin. Sci. Technol., 2002, 6 (3), pp. 353-364.

63. Ghosh, R., O.W.J. Dillon and I.S. Jawahir, *An investigation of 3-D curled chip in machining. II. Simulation and validation using FE techniques.* Machining Science and Technology, 1998, 2 (1), pp. 117-135.

64.   Fischer, C.E., J.T. Jinn, P. Chigurupati and G. Li, *Computer Simulation of the Chip Forming Process in Metal Cutting.* Technical Papers - Society Of Manufacturing Engineers -All Series, 2002 (308).

65.   Hayashi, M., M. Jin, S. Thipprakmas, M. Murakawa, J. Hung, Y. Tsai and C. Hung, *Simulation of ultrasonic-vibration drawing using the finite element method (FEM).* J. Mater. Process. Technol., 2003, **140** (1-3), pp. 30-35.

66.   Obikawa, T., H. Sasahara, T. Shirakashi and E. Usui, *Application of computational machining method to discontinuous chip formation.* Journal of Manufacturing Science and Engineering, 1997, **119** (4B), pp. 667-674.

67.   Ceretti, E., M. Lucchi and T. Altan, *FEM simulation of orthogonal cutting: serrated chip formation.* Journal of Materials Processing Technology, 1999, **95** (1-3), pp. 17-26.

68.   Bäker, M., *An investigation of the chip segmentation process using finite elements.* Technische Mechanik, 2003, **23** (1), pp. 1-9.

69.   Bäker, M., J. Rösler and C. Siemers, *The influence of thermal conductivity on segmented chip formation.* Comput. Mater. Sci., 2003, **26**, pp. 175-182.

70.   Nishioka, T., H. Tokudome and M. Kinoshita, *Dynamic fracture-path prediction in impact fracture phenomena using moving finite element method based on Delaunay automatic mesh generation.* Int. J. Solids Structures, 2001, **38** (30-31), pp. 5273-5301.

71.   Moes, N. and T. Belytschko, *Extended finite element method for cohesive crack growth.* Eng. Fract. Mech., 2002, **69** (7), pp. 813-833.

72.   Fassi, H.F., L. Bousschine, A. Chaaba and A. Elharif, *Numerical simulation of orthogonal cutting by incremental elastoplastic analysis and finite element method.* J. Mater. Process. Technol., 2003, **141**, pp. 181-188.

73.   Yen, Y.C., A. Jain and T. Altan, *A finite element analysis of orthogonal machining using different tool edge geometries.* J. Mater. Process. Technol., 2004, **146**, pp. 72-81.

74.   Taylor, G.I. and H. Quinney, *The plastic distortion of metals.* Philos. Trans. Roy. Soc. London, 1931, **A230**, pp. 323-362.

75.   El-Wardany, T., E. Mohammed and M. Elbestawi, *Cutting temperature of ceramic tools in high speed machining of difficult-to-cut materials.* International Journal of Machine Tools & Manufacture, 1996, **36** (5), pp. 611-634.

76.   Yen, Y.C., J. Söhner, B. Lilly and T. Altan, *Estimation of tool wear in orthogonal cutting using the finite element analysis.* J. Mater. Process. Technol., 2004, **146**, pp. 82-91.

77.   Koike, Y., K. Hiraizumi, J. Sakai, K. Nakamura and S. Ueha, *Finite element method aided power flow mapping of an ultrasonic vibration tool.* Jpn. J. Appl. Phys., 2000, **39** (5B), pp. 2995-2998.

78.   Macginley, T. and J. Monaghan, *Modelling the orthogonal machining process using coated cemented carbide cutting tools.* J. Mater. Process. Technol., 2001, **118** (1-3), pp. 293-300.

79.   Anagonye, A.U. and D.A. Stephenson, *Modeling cutting temperatures for turning inserts with various tool geometries and materials.* J. Manuf. Sci. Eng. (Trans. ASME), 2002, **124** (3), pp. 544-552.

80.   Wang, S., S. Choudhry and T. Wertheimer. *Comparison between the static implicit and dynamic explicit methods for FEM simulation of sheet forming processes.* In *NUMIFORM 98: Sixth International Conference on Numerical Methods in Industrial Forming Processes.* 1998. Enschede, Netherlands: A.A. Balkema Publishers, Simulation of Materials Processing: Theory, Methods and Applications (USA).

81.   Dam, H., P. Quist and M.P. Schreiber, *Productivity, surface quality and tolerances in ultrasonic machining of ceramics.* Journal of Materials Processing Technology, 1995, **51**, pp. 358-368.

82.   Thoe, T.B., D.K. Aspinwall and M.L.H. Wise, *Review on ultrasonic machining.* Int. J. Mach. Tools Manuf., 1998, **38** (4), pp. 239-256.

83.   Isaev, A. and V. Anochin, Vestnik Mashinostroenia (in Russian), 1961, **5**, pp. 56.

84.   Kubota, M., J. Tamura and N. Shimamura, Bull. Jap. Soc. Prec. Engng, 1977, **11**, pp. 127.

85.   Kumabe, J., *Vibratory Cutting.* 1979: Dzikke Sjuppan, Tokyo (in Japanese).

86.   Markov, A.I., *Ultrasonic Machining of Hard Materials.* 2nd ed. 1968, Moscow: Machinostroenie (in Russian).

87.   Markov, A.I., *Optimal ultrasonic cutting of hard-to-work materials.* Russian Engineering Research C/C Of Vestnik Mashinostroeniia And Stanki Instrument, 1996, **16** (10), pp. 26-31.

88.   Markov, A., *Process organization and control for ultrasonic cutting of hard-workable materials*. Vestnik Mashinostroeniya (Russia), 1996, **10**, pp. 19-22.

89.   Weber, H., J. Herberger and R. Piltz, *Turning of machinable glass ceramics with an ultrasonically vibrated tool*. Annals of the CIPR, 1984, **33** (1), pp. 85-87.

90.   Moriwaki, T., E. Shamoto and K. Inoue, *Ultraprecision ductile cutting of glass by applying ultrasonic vibration*. CIRP Annals, 1992, **41** (1), pp. 141-144.

91.   Shamoto, E., C.X. Ma and T. Moriwaki, *Ultraprecision ductile cutting of glass by applying ultrasonic elliptical vibration cutting*. Precision Engineering Nanotechnology, 1999, **1**, pp. 408-411.

92.   Moriwaki, T. and E. Shamoto, *Ultraprecision diamond turning of stainless steel by applying ultrasonic vibration*. CIRP Annals, 1991, **40** (1), pp. 559-562.

93.   Wang, L.-J., *The three states of unseparating zone in ultrasonic vibration cutting*. Science in China (Series A), 1992, **35** (9), pp. 1110.

94.   Yang, J., Y. Zhang and S. Yang. *Ultrasonic vibration turning of aluminum matrix composites*. In *Progress of Cutting and Grinding; with Some Topics in Advanced Manufacture Technology*. 1998: Progress of Cutting and Grinding.

95.   Kim, J.-D. and E.-S. Lee, *A study of ultrasonic vibration cutting of carbon fibre reinforced plastics*. International Journal of Advanced Manufacturing Technology, 1996, **12**, pp. 78-86.

96.   Kim, J.-D. and I.-H. Choi, *Micro surface phenomenon of ductile cutting in the ultrasonic vibration cutting of optical plastics*. Journal of Materials Processing Technology, 1997, **68** (1), pp. 89 - 98.

97.   Kim, J.-D. and I.-H. Choi, *Characteristics of chip generation by ultrasonic vibration cutting with extremely low cutting velocity*. International Journal of Advanced Manufacturing Technology, 1998, **14** (1), pp. 2-6.

98.   Jin, M. and M. Murakawa, *Development of a practical ultrasonic vibration cutting tool system*. Journal of Materials Processing Technology, 2001, **113** (1-3), pp. 342-347.

99.   Xiao, M., K. Sato, S. Karube and T. Soutome, *The effect of tool nose radius in ultrasonic vibration cutting of hard metal*. Int. J. Mach. Tools Manuf., 2003, **43**, pp. 1375-1382.

100. Klocke, F. and O. Rübenach, *Ultrasonic-assisted diamond turning of glass and steel.* Industrial Diamond Review, 2000, **60** (586), pp. 227 - 239.

101. Devine, J., *Ultrasonically assisted metal removal.* SAMPE Quarterly, 1979, **10**, pp. 485-496.

102. Takeyama, H. and N. Iijima, *Machinability of glassfiber reinforced plastics and application of ultrasonic machining.* Annals CIRP, 1988, **37** (1), pp. 93-96.

103. Kremer, D., *Ultrasonically assisted machining.* Mec. Ind. Mater., 1995, **48** (1), pp. 15-21.

104. Kumabe, J., K. Fuchizawa, T. Soutome and Y. Nishimoto, *Ultrasonic superposition vibration cutting of ceramics.* Precision Engineering Nanotechnology, 1989, **11** (2), pp. 71--77.

105. Astashev, V.K., *Effect of ultrasonic vibrations of a single point tool on the process of cutting.* Journal of Machinery Manufacture and Reliability, 1992, **5** (3), pp. 65-70.

106. Astashev, V.K. and V.I. Babitsky, *Ultrasonic cutting as a non-linear (vibro-impact) process.* Ultrasonics, 1998, **36**, pp. 89-96.

107. Babitsky, V.I., A. Kalashnikov and F. Molodtsov, *Autoresonant control of ultrasonically assisted cutting.* Mechatronics, 2004, **14**, pp. 91-114.

108. Ji, Z., W. Li-Jiang and L. Hua, *A new side-clamped ultrasonic vibration cutting system with two-stage amplification.* International Journal of Machine Tools and Manufacture, 1991, **31** (3), pp. 249-256.

109. Han, L., W. Xu and S. Tso, *Ultrasonically assisted and piezoelectric actuators integrated cutting tool.* Japanese Journal of Applied Physics, 1998, **37** (8), pp. 4616-4619.

110. Babitsky, V.I., *Autoresonant mechatronic systems.* Mechatronics, 1995, **5** (5), pp. 483-495.

111. Babitsky, V.I., A.V. Mitrofanov and V.V. Silberschmidt, *Ultrasonically Assisted Turning of Aviation Materials: Simulations and Experimental Study.* Ultrasonics, 2004, Vol. **42** (1-9), pp. 81-86.

112. Skelton, C., *Effect of ultrasonic vibration on the turning process.* Int. J. Mach. Tool Design Res., 1969, **9**, pp. 363-374.

113. DeMange, J., J. Pereira, B. Lerch and V. Prakash, *Ballistic impact behavior of Ni-based super alloys with applications to engine fan-blade containment.*

Proceedings of the SEM IX International Congress on Experimental Mechanics (USA), 2000, pp. 344-347.

114.   Jawaid, A., S. Koksal and S. Sharif, *Cutting performance and wear characteristics of PVD coated and uncoated carbide tools in face milling Inconel 718 aerospace alloy.* J. Mater. Process. Technol., 2001, **116** (1), pp. 2-9.

115.   Ezugwu, E. and A. Jawaid. *The effect of coatings on the performance of carbide cutting tools when machining a nickel base, Inconel 718, superalloy.* In *Proceedings of the Fifth International Manufacturing Conference with China (IMCC'91).* April 1991.

116.   Pereira, J.M. and B.A. Lerch, *Effects of heat treatment on the ballistic impact properties of Inconel 718 for jet engine fan containment applications.* International Journal of Impact Engineering, 2001, **25** (8), pp. 715-733.

117.   Sciuva, M.D., C. Frola and S. Salvano, *Low and high velocity impact on Inconel 718 casting plates: ballistic limit and numerical correlation.* International Journal of Impact Engineering, 2003, **28** (8), pp. 849-876.

118.   Lee, M., D. Flom and W.J. Reed, *High strain rate deformation behavior of Inconel 718 alloy and its effect on machining.* Second International Conference on Mechanical Behavior of Materials. ASM, Metals Park, Ohio, 1976, pp. 283-287.

119.   Brinkman, C. and G. Korth, *Strain fatigue and tensile behavior of Inconel 718 from room temperature to 650 C.* ASTM J. Testing Eval., 1974, **2** (4), pp. 249-259.

120.   *Military Handbook: Metallic Materials and Elements for Aerospace Vehicle Structures.* 1997: Department of Defense, USA.

121.   Lemaitre, J. and J.-L. Chaboche, *Mechanics of Solid Materials.* 1990: Cambridge University Press.

122.   Lissenden, C., C. Gil and B. Lerch, *A methodology for determining rate-dependent flow surfaces for Inconel 718.* ASTM Journal of Testing and Evaluation (USA), 1999, **27** (6), pp. 402- 411.

123.   Lee, Y.-H., J.-I. Jang and D. Kwon, *Influence of biaxial surface stress on mechanical indenting deformations.* Materials Science Forum, 2004, **449-452**, pp. 93-96.

124. Shamoto, E. and T. Moriwaki, *Study on elliptical vibration cutting.* CIRP Annals, 1994, **43** (1), pp. 35-38.

125. Blaha, F. and B. Langenecker, *Dehnung von Zink-Einkristallen unter Ultraschalleinwirkung.* Die Naturwissenschaften, 1955, **20**, pp. 556.

126. Carslaw, H.S. and J.C. Jaeger, *The conduction of heat in solids.* 2nd ed. 1959, Oxford: Oxford University Press.

127. Schneider, P.J., *Conduction Heat Transfer.* revised ed. 1974: Addison-Wesley.

128. Schaaf, S.A., *On the superposition of a heat source and contact resistance.* Quaterly of Appl. Maths, 1947, **5**, pp. 107-111.

129. Mitrofanov, A.V., V.I. Babitsky and V.V. Silberschmidt, *Finite element simulations of ultrasonically assisted turning.* Comput. Mater. Sci., 2003, **28** (3-4), pp. 645-653.

Appendices

Appendix 1 Complete data for nanoindentation tests

Scan	Line A (10 μm × 60 indents)					Line B (10 μm × 60 indents)					Line C (10 μm × 60 indents)				
	Depth h (nm)		Load	Hardness	E_r	Depth h (nm)		Load	Hardness	E_r	Depth h (nm)		Load	Hardness	E_r
#	Max.	Plastic	Max (mN)	(GPa)	(GPa)	Max.	Plastic	Max (mN)	(GPa)	(GPa)	Max.	Plastic	Max (mN)	(GPa)	(GPa)
1	241	214	10	7.13	206.3	253	230	9.99	6.28	228.5	256	234	10	6.1	231.6
2	259	233	10.03	6.16	195.4	256	231	10	6.2	209.2	256	234	10.01	6.1	222.9
3	251	229	9.99	6.33	232.3	260	236	10.01	6	213.4	256	232	10.03	6.23	215
4	245	219	10	6.84	210.4	254	225	10.01	6.53	183.2	254	231	10.02	6.23	225.7
5	249	223	9.99	6.58	209.4	256	231	10.04	6.25	208.3	265	242	10.03	5.75	222.3
6	262	241	10	5.8	226.3	245	219	10	6.85	208.8	254	230	10.01	6.28	227.6
7	265	242	10.03	5.77	227.3	245	221	10.02	6.75	217.9	260	237	10.04	5.99	219.3
8	257	234	10.01	6.08	226.6	262	236	10.01	6.03	201.9	262	238	10.01	5.93	203.5

9	268	246	10.01	5.6	218.9	258	233	10.04	6.15	208.7	263	240	10.01	5.83	218.3
10	263	238	10	5.91	204.5	252	227	10.03	6.45	206.2	259	234	9.96	6.05	215.3
11	255	231	10.03	6.25	220.2	252	227	9.99	6.44	204.3	246	218	10.01	6.89	208.8
12	265	240	10.04	5.83	207.1	259	235	10.02	6.04	211	252	225	10.06	6.54	195.6
13	260	236	10.02	6.02	214.7	268	242	10.02	5.77	191.1	255	230	10.05	6.33	209.4
14	271	246	9.98	5.56	199.7	270	243	10.02	5.71	191.5	216	188	10.01	8.96	223.8
15	268	242	10.02	5.79	191.5	254	227	10	6.42	199.8	170	137	10.02	15.26	228.9
16	270	243	10.02	5.69	190.5	425	393	9.98	2.38	97.8	181	151	10	12.99	253.6
17	250	221	10.01	6.71	191.4	159	123	10.01	18.14	238.8	156	125	10.03	17.67	277.7
18	155	120	9.99	18.91	242.6	197	162	10.03	11.55	194.1	153	127	10.01	17.37	316.4
19	180	152	10.03	12.92	247.1	153	120	10.03	18.92	262.7	156	115	10.06	20.37	211
20	168	140	10.01	14.64	268.9	516	484	10.02	1.62	78.5	518	489	10.01	1.59	86.2
21	218	188	10.01	8.93	196.6	177	146	10.06	13.84	235.5	1877	1637	10.01	0.15	3.3
22	152	119	10.02	19.24	266.3	2118	1883	9.99	0.11	2.9	1882	1642	10.02	0.15	3.3
23	222	192	10	8.61	193	1958	1721	10.02	0.14	3.2	1914	1674	10.03	0.14	3.2
24	1792	1557	9.99	0.17	3.5	1927	1682	9.99	0.14	3.1	1945	1711	10.01	0.14	3.3
25	1857	1611	10.02	0.16	3.3	1877	1632	10.02	0.15	3.3	1953	1716	10.01	0.14	3.2
26	1892	1644	10.01	0.15	3.2	1905	1661	10.03	0.15	3.2	1918	1679	10.01	0.14	3.2
27	1904	1666	10.02	0.15	3.3	1892	1646	10.04	0.15	3.2	1921	1683	10.04	0.14	3.3

28	1799	1557	10.02	0.17	3.4	1869	1627	10.04	0.15	3.3	1861	1621	10	0.15	3.4
29	1831	1589	10.01	0.16	3.4	1890	1644	10.01	0.15	3.2	1848	1606	10.02	0.16	3.3
30	1892	1647	10.03	0.15	3.2	1884	1642	10.02	0.15	3.3	1844	1609	10	0.16	3.4
31	1887	1648	10	0.15	3.3	1895	1652	10.03	0.15	3.3	1855	1616	10.01	0.16	3.4
32	1869	1623	10.02	0.15	3.3	1889	1642	9.99	0.15	3.2	1835	1592	10	0.16	3.4
33	1876	1622	10	0.15	3.2	1966	1734	10.06	0.14	3.3	1863	1618	10.02	0.15	3.3
34	1912	1665	10.03	0.15	3.2	1918	1686	10.01	0.14	3.3	1895	1663	10.03	0.15	3.4
35	1851	1606	10.02	0.16	3.3	1910	1681	10.03	0.14	3.4	1895	1653	10.02	0.15	3.3
36	1855	1612	10.03	0.16	3.3	1882	1651	10	0.15	3.4	1901	1657	10.01	0.15	3.2
37	1846	1610	9.99	0.16	3.4	1958	1718	10.02	0.14	3.2	1908	1658	10.02	0.15	3.1
38	1849	1605	10.02	0.16	3.3	1918	1681	10	0.14	3.3	1860	1620	10.02	0.15	3.4
39	1865	1619	10.04	0.16	3.3	1910	1669	10.01	0.15	3.2	1835	1580	10	0.16	3.2
40	1834	1595	10.03	0.16	3.4	1852	1606	10.01	0.16	3.3	1814	1564	10	0.17	3.3
41	1840	1600	10.04	0.16	3.4	1861	1608	9.99	0.16	3.2	1845	1598	10.01	0.16	3.3
42	1841	1590	9.98	0.16	3.2	1923	1679	9.97	0.14	3.2	1835	1590	10	0.16	3.3
43	1848	1606	9.98	0.16	3.3	1909	1668	10	0.15	3.2	1827	1579	10.01	0.16	3.3
44	1852	1605	10.01	0.16	3.3	1882	1640	10.02	0.15	3.3	992	968	9.98	0.43	56.1
45	1886	1636	10.03	0.15	3.2	1907	1659	10.01	0.15	3.2	122	99	10.02	25.73	438.7
46	1830	1577	10.04	0.16	3.3	1860	1611	10.02	0.16	3.2	139	113	10.03	20.81	378.7

47	1832	1580	10.01	0.16	3.3	717	692	10.02	0.83	75.3	133	111	10.02	21.67	408.9
48	1836	1589	10.01	0.16	3.3	112	88	9.98	31.07	508.9	125	100	10	25.25	422.2
49	1848	1593	10.05	0.16	3.2	130	105	9.99	23.49	389	123	101	10.01	24.94	463.5
50	134	111	10.02	21.49	449.6	121	96	10.01	27.2	439.1	118	96	10.02	27.27	468.3
51	126	102	10	24.62	434.8	143	118	10.03	19.65	368.3	124	105	10.04	23.54	519.1
52	108	80	9.99	35.78	431.7	101	77	10.01	37.86	532.9	116	97	10.04	26.76	545.9
53	110	84	9.99	33.13	447.5	115	92	10.01	28.71	498.3	127	110	9.98	21.71	545.9
54	127	102	10	24.57	401	119	97	10.05	26.83	499.1	213	189	9.99	8.81	263.8
55	123	95	10	27.36	402	136	113	9.99	20.97	397.8	236	214	10.02	7.15	262.8
56	125	98	10.01	25.94	407.7	191	166	10.02	11.04	278	234	211	10.01	7.31	248.1
57	128	104	10.03	23.78	423.9	231	207	10.05	7.55	251.6	238	216	10	7.03	246.4
58	122	98	10.03	25.98	463	233	209	10	7.41	232.9	239	216	9.96	6.97	246.4
59	202	176	9.98	9.93	260.4	226	203	10	7.81	253.4	236	216	10.03	7.02	285.1
60	227	205	10.01	7.67	265.3	237	211	10	7.3	222.3	238	215	10.02	7.08	245